Fast Multi-Core CEM Solvers and Flux Trapping Analysis for Superconducting Structures

by

Kyle Jackman

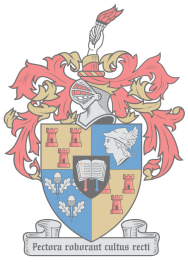

Dissertation presented for the degree of Doctor of Philosophy in Electrical and Electronic Engineering in the Faculty of Engineering at Stellenbosch University

Supervisor:

Prof. Coenrad J. Fourie
Electrical and Electronic Engineering
Stellenbosch University

Marc 2018

The financial assistance of the National Research Foundation (NRF) towards this research is hereby acknowledged. Opinions expressed and conclusions arrived at, are those of the author and are not necessarily to be attributed to the NRF.

Declaration

By submitting this dissertation electronically, I declare that the entirety of the work contained therein is my own, original work, that I am the sole author thereof (save to the extent explicitly otherwise stated), that reproduction and publication thereof by Stellenbosch University will not infringe any third party rights and that I have not previously in its entirety or in part submitted it for obtaining any qualification.

This dissertation includes one original paper published in peer-reviewed journals or books and 0 unpublished publications. The development and writing of the papers (published and unpublished) were the principal responsibility of myself and, for each of the cases where this is not the case, a declaration is included in the dissertation indicating the nature and extent of the contributions of co-authors.

Signature: K. Jackman

Date: 2017/10/27

Abstract

Fast Multi-Core CEM Solvers and Flux Trapping Analysis for Superconducting Structures

K. Jackman

Department of Electrical and Electronic Engineering,
University of Stellenbosch,
Private Bag X1, Matieland 7602, South Africa.

Dissertation: PhD

October 2017

The dissertation presents the development of a numerical field solver, called TetraHenry (TTH), for inductance extraction and flux trapping analysis of superconducting integrated circuits. The solver uses tetrahedral elements to model multidirectional current flow in complex three-dimensional superconducting volumes; whereas two dimensional triangular elements are used for sheet currents in thin superconducting films. Triangular meshing significantly reduces the number of unknowns and provides the capability to analyse chip-scale superconducting layouts. Support for piecewise homogenous dielectric materials are implemented, which enables frequency-depended impedance extraction. The Fast Multipole Method for the Biot-Savart law, which enables the simulation of magnetic materials, is derived. The effects of external magnetic fields on the performance of superconducting circuits are analysed. The amount of flux through each hole or moat can be specified using the Volume Loop basis function; enabling flux trapping analysis and inductance extraction around holes. The full derivation of the integral equations for volume and sheet currents are discussed. The Method of Moments is used to obtain a system of linear equations, which is solved with a preconditioned GMRES solver. Matrix-vector multiplication is accelerated with the Fast Multipole method. The accuracy and performance of the numerical solver are evaluated, by comparing simulated results to existing software.

Uittreksel

Vinnige Multi-Kern Elektromagnetiese Veldoplosser en Vloed-Vasvang Analise vir Supergeleidende Strukture

("Fast Multi-Core CEM Solvers and Flux Trapping Analysis for Superconducting Structures")

K. Jackman

Departement Elektriese en Elektroniese Ingenieurswese,
Universiteit van Stellenbosch,
Privaatsak X1, Matieland 7602, Suid Afrika.

Proefskrif: PhD

Oktober 2017

Die dissertasie bied aan die ontwikkeling van 'n numeriese veldoplosser, genaamd TetraHenry (TTH), vir induktansie onttrekking en vloed-vasvang analise van supergeleier geïntegreerde stroombane. Die veldoplosser gebruik tetrahedraal elemente om stroomvloei binne komplekse driedimensionele supergeleidende volumes te modelleer; terwyl tweedimensionele driehoekige elemente gebruik word vir stroomvloei in dun supergeleier filamente. Driehoekige elemente verminder die aantal onbekendes aansienlik en bied die vermoë om supergeleier uitlegte op groot skaal te analiseer. Ondersteuning vir stuksgewyse homogene diëlektriese materiale word geïmplementeer, wat frekwensie-afhanklike impedansie onttrekking moontlik maak. Die "Fast Multipole" metode vir die Biot Savart wet, wat die simulering van magnetiese materiale moontlik maak, word afgelei. Die effekte van eksterne magnetiese velde op supergeleier stroombane word ontleed. Vloed-vasvang analise en induktansie onttrekking rondom gate word uitgevoer met behulp van Volume Lus funksies. Die volledige afleiding van die integraalvergelykings vir volume en oppervlakstrome word bespreek. Die Metode van Momente word gebruik om 'n stelsel van lineêre vergelykings te verkry, wat opgelos word met 'n voorafbepaalde GMRES iteratiewe oplosser. Matriks-vektor vermenigvuldiging word versnel met die "Fast Multipole" metode. Die akkuraatheid en spoed van die numeriese enjin word geëvalueer deur gesimuleerde resultate te vergelyk met bestaande sagteware.

Acknowledgements

I would like to express my sincere gratitude to the following people:

I am most grateful to my supervisor, Professor Coenrad J. Fourie. Thank you for all the expert advice and support through the last four years. Thank you for introducing me to the field of applied superconductivity, for teaching me the fundamentals in superconducting circuits, and taking me to various international conferences. I could not have wished for a better supervisor.

To Ruben Van Staden and Johannes A. Delport, thank you for all the motivational speeches and support through the last four years.

To Professor Pascal Febvre, thank you for your expert advice on Josephson Junctions.

I am also grateful to the National Research Foundation (NRF) for financing my post-graduate studies.

Lastly, I want to thank my parents. Without your love, support and understanding I could not have achieved what I have.

Contents

List of Figures

List of Tables

Chapter 1

Introduction

1.1 Motivation

The improvement of existing silicon-based devices is reaching its limit as the physical structures approach atomic dimensions. Energy efficiency has become the new limiting factor defining processor performance [8]. It is also a dominant metric for the next generation of supercomputers [9]. The high energy requirements of complementary metal-oxide-semiconductor (CMOS) devices make it an impractical technology for the next generations of high-end computing systems [9].

Alternatively, superconducting electronics outperforms semiconductors with respect to both speed and power dissipation. The use Josephson Junctions devices [10] as ultra-fast switching devices, allows superconducting digital circuits to operate at clock frequencies exceeding 40 GHz and can be boosted to approximately 300 GHz for low critical temperature circuits [11]. Superconducting technologies, such as Adiabatic Quantum Flux Parametron (AQFP) circuits [12, 13], can reduce energy dissipation by several orders when used for parallel pipelining [14], compared to CMOS circuits, and is estimated to be the most energy efficient technology for computations [15].

For superconducting electronics to reach the computational complexities of CMOS processors, very-large-scale integration (VLSI) is required. Before large-scale superconducting integrated circuits can be implemented on physical wafers, several design steps must be followed. One of the design steps is the extraction of circuit parameters from the circuit's layout. These extracted parameters are then used to verify that the layout corresponds to the circuit schematic.

Inductance plays an important role in superconducting circuit design. Accurate inductance extraction is crucial for accurate circuit simulation of single flux quantum (SFQ) circuits. The lack of accurate and fast computational electromagnetics (CEM) solvers for superconducting structures, limits the capabilities for VLSI superconducting circuit design.

1.2 Inductance Extraction

Accurate inductance calculations are crucial when designing superconducting integrated circuits. During the fabrication process, several layers are deposited on top of each other, resulting in irregular topography. Fabrication processes that use planarization methods, such as complemented caldera planarization [16, 17, 18, 19], do not necessary planarize the top layers. The result is complex curvatures that are difficult to model with existing numerical solvers, such as FastHenry [20], that uses rectangular uniaxial filaments. Corners, stacked vias and non-Manhattan structures such as spiral coils are also not easily modelled with rectangular uniaxial filaments.

To overcome this limitation, software, such as InductEx [21, 2], has been developed to extract inductance from complex superconducting circuit layouts [22]. The inductance solver, FastHenry, was modified to support superconductivity [23] and forms the back-end of InductEx. InductEx generates three-dimensional (3D) meshes, consisting of cuboid filaments, as input to FastHenry. Although this approach is efficient for Manhattan layouts, cuboid filaments lack the ability to accurately model uneven multi-directional current flow along curved structures.

FastHenry is a magnetoquasistatic solver and, therefore, lacks the ability to capture distributed capacitance and inductance simultaneously. Modifications have been made to support the full quasistatic Maxwell's equations [3, 24], but the source code of these versions are not readily available. An impedance extraction program, FastImp [25], which uses a surface integral formulation and the precorrected fast Fourier transform (pFFT), is capable of perform full 3-D electromagnetic analysis over a wide-band of frequencies. Unfortunately, the surface integral formulation makes it difficult to accurately analyse the effects of high current density near the surface of a volume. This is especially important within superconductor, since the London penetration depth determines the distance a magnetic field will penetrate the superconductor [26].

Another significant drawback of superconducting integrated circuits, is the sensitivity to external magnetic fields and fluxons trapped in superconducting films. These trapped fluxons, in the form of Pearl vortices [27], magnetically couples with surrounding superconducting elements; degrading the circuit's performance. Previous work [28, 29, 30] has demonstrated techniques for analysing trapped fluxons and most require the extraction of inductance around holes, formed by trapped fluxons. The software package, 3D-MLSI [31, 32], is capable of extracting self- and mutual-inductance around holes; however, it is limited to two-dimensional superconducting films. The method discussed in [33], can simulate trapped fluxons in Josephson-junction arrays, but this method was only developed for geometries consisting of rectangular filaments.

Although several tetrahedral modeling methods [34, 35, 36] have already been developed for non-superconducting structures; these methods have not

yet been adapted and implemented for superconducting structures.

1.3 Objectives of dissertation

In this work, we propose a numerical solver, called TetraHenry (TTH), that uses tetrahedral elements to model multi-directional current flow in complex three-dimensional superconducting structures. The numerical solver will be used to perform inductance calculations and flux trapping analysis on large superconducting integrated circuits. The solver, including all the algorithms mentioned in this dissertation, is implemented in C/C++. The accuracy and performance of the numerical engine is evaluated, by comparing simulated results to existing software. The objectives of this dissertation requires several features to be added to the numerical solver:

1. Enabling full-chip simulation and inductance extraction, using hybrid meshes that consisting of both triangular and tetrahedral meshes.
2. Simulating piecewise homogenous dielectric materials, which enables frequency-depended impedance extraction.
3. Simulating piecewise homogenous magnetic materials, used in superconducting memory devices.
4. Adding support for external magnetic fields, to evaluate their effect on the performance of superconducting circuits.
5. Implementing support for hole/moat excitation, which will be used for flux trapping analysis.
6. Implementing numerical techniques, such as iterative solvers with preconditioning and the Fast Multipole Method (FMM), to speed up the numerical engine.

In the next Chapter, Chapter 2, the full implementation of the numerical solver, TetraHenry (TTH), is discussed. The full derivation of the current density integral equation (VJIE), with support for superconducting currents, is derived from Maxwell's equations. A system of linear equations is obtained from the VJIE, using a special Volume Loop (VL) basis function (consisting of SWG functions) and the Method of Moments (MoM). Analytical solutions are derived for the integration over tetrahedrons. The system of linear equations is solved with the GMRES iterative solver and accelerated with preconditioning matrices. The Fast Multipole method is used to accelerate the computation of matrix-vector products. Finally, the performance and accuracy of TTH is compared to FastHenry, for small and large superconducting circuits.

In Chapter 3, the implementation of the two-dimensional triangular method is discussed. An integral equation is derived for the two-dimensional sheet current model. The Surface Loop (SL) basis function, consisting of RWG functions, is introduced. Analytical solutions are derived for the integration over triangles. The advantages of triangular meshing for large superconducting circuit layouts, consisting of thin superconducting films, are demonstrated. The the performance and accuracy of the triangular method is compared to the tetrahedral method.

The full derivation of the integral equations for electric and magnetic currents, inside inhomogeneous dielectric and magnetic materials, is discussed in Chapter 4. Special Half-SWG basis function are used to account for electric and magnetic charge accumulation on material interfaces. The interaction between magnetic and electric currents is accelerated, using the Biot-Savart FMM (BiotFMM) derived in Chapter 6. Preconditioners are developed to accelerate the iterative solver. The impedance of several test structures are extracted, using both electro-magneto-quasi-static (EMQS) analysis and Full-Wave analysis. The effects of magnetic materials on non- and superconducting structures are evaluated. The accuracy of TTH is compared to existing software packages, such as FastImp and *CST Studio*.

The implementation of uniform external magnetic fields is discussed in Chapter 5. The magnetic vector potential of a predefined uniform magnetic field, with x-, y- and z-components, is derived and implemented into the existing VJIE formulation. An equivalent circuit model for the magnetic field is derived, which can be used to evaluated the effects of magnetic fields on the operating margins of SFQ circuits.

The full derivation of the FMM algorithm for the Biot-Savart law, referred to as BiotFMM, is discussed in Chapter 6. The BiotFMM algorithm replaces the direct multiplication of Biot-Savart law, which is used to calculate the interaction between electric and magnetic currents, see Chapter 4. The BiotFMM algorithm can also be implemented directly into the existing FastCap or FastHenry code. Finally, the accuracy and performance of BiotFMM are compared to the existing library, ExaFMM.

Appendix A contains the published article, *"Flux Trapping Analysis in Superconducting Circuits"* [37]. VL basis functions are used to specify the number of fluxons inside each hole or moat. The inductance of holes and the mutual-inductance between holes are extracted, including the energy of trapped fluxons in the presence of external magnetic fields. These extracted values are then used to calculate the probability of flux trapping.

Appendix B contains the published article, *"Fast Multicore FastHenry and a Tetrahedral Modeling Method for Inductance Extraction of Complex 3D Geometries"* [38]. In this article, the algorithmic improvements made to the numerical solver, FastHenry, are discussed.

Lastly, a user's manual for TTH is provided in Appendix C. All the input commands and file requirements are specified, including the geometry files

(Gmsh format) of two single layer superconducting structure.

Chapter 2

3D Tetrahedral Modelling Method

2.1 Introduction

In this chapter, a detailed description of the newly developed numerical solver, called TetraHenry (TTH), is provided. TTH uses tetrahedral volume elements to discretize complex geometries and is capable of modeling multidimensional current flow in superconducting structures. The volume electric current integral equation (VJIE), used in [39, 40, 41, 42, 36], was chosen as the most suitable method for modeling superconducting currents. The VJIE formulation is similar to the VIE used in FastHenry and requires less iterations when using an iterative method [40]. It is also more stable for extremely anisotropic materials [41] compared to the electric flux density formulation (VDIE) [34].

The VJIE formulation is derived for superconducting structures, starting with the magneto-quasistatic (MQS) Maxwell's equations and assuming sinusoidal steady-state. Volume Loop (VL) basis functions [35], a combination of Schaubert-Wilton-Glisson (SWG) functions [34], are used to discretize the VJIE. The Method of Moment (MoM) [43] is used to construct a linear system of equations from the VJIE, which is solved using the GMRES iterative method [44]. The matrix-vector product in the GMRES is accelerated using the Fast Multipole Method (FMM) [45]. Meshing is done by a third party finite element mesh generator, i.e. Gmsh [46, 47]. Algorithmic improvements and parallelization methods developed in [38], see Appendix B, have also been modified and implemented in TTH. The entire numerical engine, including the algorithms mentioned in this Chapter, was fully implemented in C/C++.

2.2 Background Formulation

The aim is to extract the inductance between several terminals by computing the complex frequency-dependent impedance matrix of a multi-terminal sys-

tem, similar to the method used in FastHenry. The problem is solved under the magnetoquasistatic (MQS) approximation, described in [20]. This will require solving the following linear equation at a given excitation frequency ω:

$$Z_m(\omega)I_m(\omega) = V_m(\omega) \tag{2.2.1}$$

where $I_m(\omega), V_m(\omega) \in \mathbb{C}^m$ are vectors containing the current and voltage phasors at the terminals, respectively [20]. The complex impedance matrix $Z_m \in \mathbb{C}^{m\times m}$ for the two conductor example, shown in Fig. 2.2.1, will be of the form:

$$Z_m(\omega) = R_m(\omega) + j\omega L_m(\omega) = \begin{bmatrix} R_{11}(\omega) + j\omega L_{11} & R_{12}(\omega) + j\omega L_{12} \\ R_{21}(\omega) + j\omega L_{21} & R_{22}(\omega) + j\omega L_{22} \end{bmatrix} \tag{2.2.2}$$

where $R_m, L_m \in \mathbb{C}^m$ are the resistance and inductance matrix, respectively. The value L_{11} is the self-inductance of conductor 1 and $L_{12} = L_{21}$ is the mutual inductance between the two conductors. If the vectors I_m and V_m are known, the i column of Z_m can be calculated by setting the value at index i in I_m equal to 1 and the rest to zero.

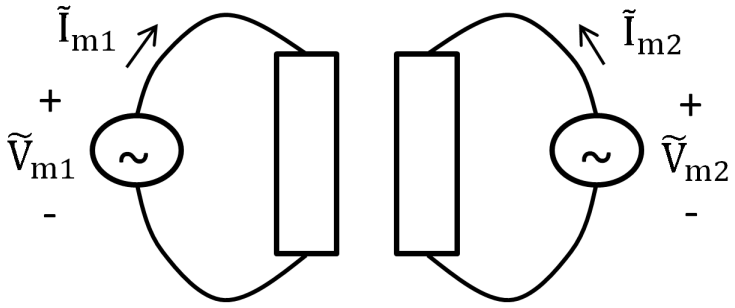

Figure 2.2.1: Two conductors with sinusoidal excitation voltages at given frequency.

2.3 Derivation of Volume Integral Equation

Several volume integral equation (VIE) formulations exist for inhomogeneous dielectric problems; either based on electric flux density [34, 48], electric field intensity [48, 49] or current density [36, 40, 41]. In order to calculate the inductance between two terminals, both the current and voltage at each terminal is required. The VIE formulation described in [36] is ideal, since it the uses the volume electric current integral equation (VJIE) and is similar to the method used by FastHenry. The VJIE require less iteration when using an iterative method [40] and is more stable [41] compared to the electric flux density formulation (VDIE) [34].

The finite element method (FEM) is used to model the non-uniform current density within the superconducting volumes. To implement the FEM method, the current carrying volumes are discretized using tetrahedral elements; whereas the free-space regions between structures are not discretized. The material properties of each individual tetrahedral element can be specified, allowing for variation in material properties, which is ideal for piecewise homogeneous bodies.

In addition to the FEM method, the Method of Moments (MoM) [43] is used to solve a volume integral equation (VIE), which will be derived in this Chapter. The Method of Moment is a powerful numerical technique for solving open-region electromagnetic problems [50]. The MoM transforms a boundary-value problem into a matrix equation and does not required the free-space regions to be discretized [50]. This makes the MoM ideal for simulating large superconducting integrated circuits, since the dielectric materials surrounding the superconductors do not require meshing. This is a valid assumption, if the displacement currents, $j\omega\mathbf{E}$, are to be assumed negligible compared to the currents within the superconductors. However, this assumption is not valid at high frequencies, which requires discretizing the dielectric regions, as will be discussed in Chapter 4. In this Chapter, it is assumed that frequency is relatively low and that the displacement current is negligible.

Starting with Maxwell's equations and assuming sinusoidal steady-state,

$$\nabla \times \mathbf{E} = -j\omega\mu\mathbf{H}, \tag{2.3.1}$$
$$\nabla \times \mathbf{H} = j\omega\epsilon\mathbf{E} + \mathbf{J}, \tag{2.3.2}$$
$$\nabla \cdot (\epsilon\mathbf{E}) = \rho, \tag{2.3.3}$$
$$\nabla \cdot (\mu\mathbf{H}) = 0, \tag{2.3.4}$$

the VJIE formulation can be derived. The displacement current is assumed negligible, i.e. magnetoquasistatic (MQS) approximation, since the conductivity is large within the conductors. From Ohm's law the volume electric current, $\mathbf{J}(\mathbf{r})$, within the conductor can be expressed as:

$$\mathbf{J}(\mathbf{r}) = \sigma(\mathbf{r})\mathbf{E}(\mathbf{r}). \tag{2.3.5}$$

where $\sigma(\mathbf{r})$ is the conductivity. Under the quasistatic assumption, the divergence of the current becomes:

$$\nabla \cdot \mathbf{J}(\mathbf{r}) = 0, \tag{2.3.6}$$

and for ideal current sources:

$$\nabla \cdot \mathbf{J}(\mathbf{r}) = I_m(r). \tag{2.3.7}$$

From Maxwell's equations it can be shown that:

$$\mathbf{E}(\mathbf{r}) + j\omega\mathbf{A}(\mathbf{r}) = -\nabla\phi(\mathbf{r}). \tag{2.3.8}$$

where $\mathbf{A}(\mathbf{r})$ is the magnetic vector potential:

$$\mathbf{A}(\mathbf{r}) = \frac{\mu}{4\pi} \int_{V'} \frac{\mathbf{J}(\mathbf{r}')}{|\mathbf{r} - \mathbf{r}'|}\, dv. \tag{2.3.9}$$

From (2.3.5), (2.3.8) and (2.3.9), the following integral equation can be derived:

$$\frac{\mathbf{J}(\mathbf{r})}{\sigma(\mathbf{r})} + \frac{j\omega\mu}{4\pi} \int_{V'} \frac{\mathbf{J}(\mathbf{r}')}{|\mathbf{r} - \mathbf{r}'|}\, dv' = -\nabla\phi(\mathbf{r}), \tag{2.3.10}$$

where $\phi(\mathbf{r})$ is the scalar potential. The conductivity, $\sigma(\mathbf{r})$, can vary within the conductors and the permeability is considered constant: $\mu = \mu_0$.

2.3.1 Superconductivity

For a material in superconducting state, the total current consists of a normal- and super component:

$$\mathbf{J} = \mathbf{J_n} + \mathbf{J_s}, \tag{2.3.11}$$

where $\mathbf{J_n}$ is the normal current, i.e. the flow of normal electrons, and $\mathbf{J_s}$ is the superconducting current, i.e. the flow of Cooper-pairs [26]. The relation between the total current and the electric field resembles Ohm's law [26]. This relation can be expressed in the sinusoidal steady state as:

$$\mathbf{J} = \mathbf{J_n} + \mathbf{J_s} = \left(\tilde{\sigma_0} + \frac{1}{j\omega\mu\lambda^2}\right)\mathbf{E}, \tag{2.3.12}$$

where $\lambda = \lambda(T)$ is the temperature depended London penetration depth of the superconductor with critical temperature T_C:

$$\lambda_L(T) = \frac{\lambda_L(0)}{\sqrt{1 - \left(\frac{T}{T_C}\right)^4}}, \tag{2.3.13}$$

and $\tilde{\sigma_0} = \tilde{\sigma_0}(T)$ is the temperature-dependent conductivity of the normal channel [26]. The London penetration depth determines the depth a magnetic field will penetrate a superconducting volume from the surface. Section 2.6.1 provides a detailed description of the penetration depth and how meshing is adapted to account for this penetrating field. Support for superconductivity can now be added to (2.3.10) by substituting $\sigma(\mathbf{r})$ with $k(\mathbf{r})$:

$$\frac{\mathbf{J}(\mathbf{r})}{k(\mathbf{r})} + \frac{j\omega\mu}{4\pi} \int_{V'} \frac{\mathbf{J}(\mathbf{r}')}{|\mathbf{r} - \mathbf{r}'|}\, dv' = -\nabla\phi(\mathbf{r}), \tag{2.3.14}$$

where

$$k(\mathbf{r}) = \tilde{\sigma_0}(\mathbf{r}) + \frac{1}{j\omega\mu\lambda(\mathbf{r})^2}. \tag{2.3.15}$$

2.3.2 Discretization

A special basis function was developed for tetrahedral meshes, known as the SWG function [34], which can be used to discretize the VIE. The SWG function can also modified into Half- and Full-SWG functions for piecewise homogeneous dielectrics [36], as will be discussed in Chapter 4. It was shown in [36] that the Full-SWG and Half-SWG basis functions (JSWG) are as accurate as the DSWG basis method used in [34].

Figure 2.3.1 shows an arbitrary body with piecewise constant electrical parameters, discretized using Full-SWG functions. Figure 2.3.2 and 2.3.3 show the definition of the Full-SWG basis function, with constant electrical parameters in each tetrahedron. The two tetrahedrons, T_n^+ and T_n^-, are associated with the nth face of the discretized volume. The vectors, ρ_n^+ and ρ_n^-, represent the position vectors in T_n^+ and T_n^-, respectively. In tetrahedron T_n^+, the position vector ρ_n^+ is defined with respect to the free vertex and in T_n^- towards the free vertex [34], see Fig.2.3.3. The signs of the two tetrahedrons depend on the choice of the direction of current flow through the nth face.

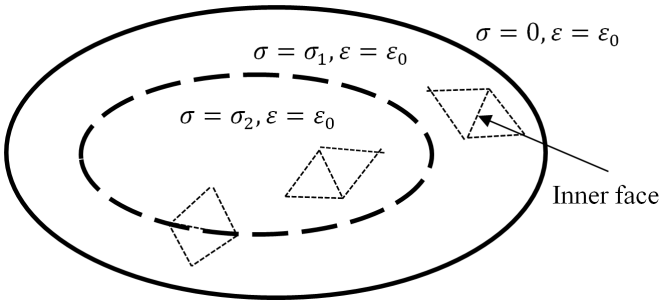

Figure 2.3.1: Full-SWG basis functions in arbitrary body with piecewise constant electrical parameters.

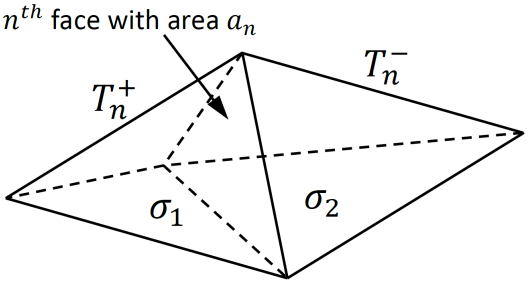

Figure 2.3.2: Full-SWG basis function at material interface ($\sigma_1 \neq \sigma_2$).

Since $\mathbf{J}(\mathbf{r})$ is not continuous across material interfaces of inhomogeneous dielectric bodies, surface charges will accumulate at material interfaces. For piecewise homogeneous dielectric objects, the Half-SWG function should be

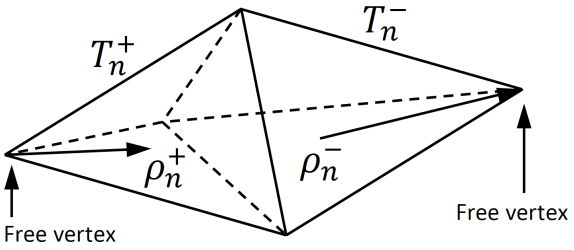

Figure 2.3.3: Full-SWG basis function.

used at material interfaces, as discussed in Chapter 4. To simplify the problem, the entire volume is first assumed to be a homogeneous dielectric body, preventing surface charges accumulation. The Full-SWG function can then be used within the entire volume:

$$\mathbf{f_n}(\mathbf{r}) = \begin{cases} \frac{1}{3|v_n^+|}\rho_{\mathbf{n}}^+(\mathbf{r}), & \text{if } \mathbf{r} \in T_n^+ \\ \frac{1}{3|v_n^-|}\rho_{\mathbf{n}}^-(\mathbf{r}), & \text{if } \mathbf{r} \in T_n^- \\ 0, & \text{otherwise} \end{cases}, \tag{2.3.16}$$

where $|v_n^\pm|$ represents the volume of tetrahedron $T_n^\pm$. This function differs from the basis functions used in [34] and [36], which uses the area of the face to normalize $\mathbf{f_n}(\mathbf{r})$. Using Full-SWG functions, the volume electric current density, $\mathbf{J}(\mathbf{r})$, can be expanded as follow:

$$\mathbf{J}(\mathbf{r}) = \sum_{n=1}^{N} i_n \mathbf{f_n}(\mathbf{r}), \tag{2.3.17}$$

where N is the number of faces that make up the entire volume and i_n is the *branch* current through the nth face. The total volume electric current within the tetrahedron, T_q, can be calculated by summing the four linear independent basis functions, associated with each face of the tetrahedron [34],

$$\mathbf{J_q}(\mathbf{r}) = \sum_{n=1}^{4} i_n \mathbf{f_n}(\mathbf{r}),\ \mathbf{r} \in T_q. \tag{2.3.18}$$

Following the Method of Moments [50], the VIE can be solved by defining the equation:

$$\mathcal{L}\left(\mathbf{J}(\mathbf{r})\right) = \mathbf{v}, \tag{2.3.19}$$

where $\mathcal{L}$ denotes the linear operator, which will be left-hand side of (2.3.14). The vector function $\mathbf{v}$ is known, whereas $\mathbf{J}(\mathbf{r})$ needs to be solved. Next, a set of weighting functions, $\mathbf{w_1}(\mathbf{r}), \mathbf{w_2}(\mathbf{r}), .., \mathbf{w_m}(\mathbf{r})$, in the range of $\mathcal{L}$ are defined. The weighting functions, $\mathbf{w_m}(\mathbf{r})$, are defined as Full-SWG functions, as given in (2.3.16). To obtain a system of linear equations, the inner products between (2.3.14) and the weighting functions are used:

$$\sum_{n=1}^{N} < \mathbf{w_m}(\mathbf{r}), \mathcal{L}\left(\mathbf{f_n}(\mathbf{r})\right) > = < \mathbf{w_m}(\mathbf{r}), \mathbf{v} >, \tag{2.3.20}$$

where $< \cdot >$ denotes the inner product of two vector functions [50]. Equation can now be written in matrix format:

$$ZI_{branch} = V_{branch}, \tag{2.3.21}$$

where

$$Z = \begin{bmatrix} < \mathbf{w_1}, \mathcal{L}(\mathbf{f_1}) > & \dots & < \mathbf{w_1}, \mathcal{L}(\mathbf{f_n}) > & \dots & < \mathbf{w_1}, \mathcal{L}(\mathbf{f_N}) > \\ < \mathbf{w_2}, \mathcal{L}(\mathbf{f_1}) > & \dots & < \mathbf{w_2}, \mathcal{L}(\mathbf{f_n}) > & \dots & < \mathbf{w_2}, \mathcal{L}(\mathbf{f_N}) > \\ \vdots & \ddots & \vdots & \ddots & \vdots \\ < \mathbf{w_m}, \mathcal{L}(\mathbf{f_1}) > & \dots & < \mathbf{w_m}, \mathcal{L}(\mathbf{f_n}) > & \dots & < \mathbf{w_m}, \mathcal{L}(\mathbf{f_N}) > \\ \vdots & \ddots & \vdots & \ddots & \vdots \\ < \mathbf{w_N}, \mathcal{L}(\mathbf{f_1}) > & \dots & < \mathbf{w_N}, \mathcal{L}(\mathbf{f_n}) > & \dots & < \mathbf{w_N}, \mathcal{L}(\mathbf{f_N}) > \end{bmatrix}, \tag{2.3.22}$$

and

$$I_{branch} = \begin{bmatrix} i_1 \\ \vdots \\ i_n \\ \vdots \\ i_N \end{bmatrix}, \qquad V_{branch} = \begin{bmatrix} < \mathbf{w_1}, \mathbf{v_1} > \\ < \mathbf{w_2}, \mathbf{v_2} > \\ \vdots \\ < \mathbf{w_m}, \mathbf{v_m} > \\ \vdots \\ < \mathbf{w_N}, \mathbf{v_N} > \end{bmatrix}, \tag{2.3.23}$$

From (2.3.22) the matrix Z can be decomposed into its real and imaginary components:

$$Z = R + j\omega L, \tag{2.3.24}$$

where R and L are respectively the resistance and inductance matrices. The entries of the resistance matrix are computed as follow:

$$R_{m,n} = \int_{v_m} \frac{1}{k(\mathbf{r})} \mathbf{w_m}(\mathbf{r}) \cdot \mathbf{f_n}(\mathbf{r})\, dv, \tag{2.3.25}$$

and the entries of the inductance matrix:

$$L_{m,n} = \frac{\mu}{4\pi} \int_{v_m} \int_{v_n} \frac{\mathbf{w_m}(\mathbf{r}) \cdot \mathbf{f_n}(\mathbf{r}')}{|\mathbf{r} - \mathbf{r}'|}\, dv' dv. \tag{2.3.26}$$

The values $R_{m,n}$ and $L_{m,n}$ correspond to the Full-SWG basis functions m and n. The volumes v_m and v_n represent the volumes of the SWG-basis functions, which are a combination of $(T_m^+ + T_m^-)$ and $(T_n^+ + T_n^-)$, respectively. The voltage over each face is stored in the vector, V_{branch}, and can be computed as follow:

$$(V_{branch})_m = < \mathbf{w_m}, \mathbf{v_m} > = -\int_{v_m} \mathbf{w_m}(\mathbf{r}) \cdot \nabla\phi(\mathbf{r})\, dv, \tag{2.3.27}$$

given the vector function, $\mathbf{v_m} = \nabla\phi(\mathbf{r})$, over face m.

Using the basis function defined in (2.3.16), it is difficult to apply boundary conditions to (2.3.27), e.g. excitation voltage between two terminals. Using the volume loop (VL) basis function, discussed in Section 2.3.3, it is possible to restrict current flow to a solenoidal subspace in which Kirchhoff's voltage law (KVL) is enforced.

2.3.3 Volume loop basis function

The divergence of the electric flux within homogeneous dielectric bodies, including superconducting volumes, is zero. This poses a problem, since the divergence of the SWG basis function is non-zero [34],

$$\nabla \cdot \mathbf{f_n}(\mathbf{r}) \begin{cases} \frac{1}{3|v_n^+|}, & \text{if } \mathbf{r} \in T_n^+ \\ \frac{1}{3|v_n^-|}, & \text{if } \mathbf{r} \in T_n^- \\ 0, & \text{otherwise} \end{cases}. \tag{2.3.28}$$

From the continuity equation,

$$\nabla \cdot \mathbf{J}(\mathbf{r}) = j\omega\rho(\mathbf{r}), \tag{2.3.29}$$

it is clear that the charge density is constant within each tetrahedron [35]. Several schemes have been developed to ensure divergence free currents within tetrahedral meshes, such as the basis reduction scheme [51], edge-based solenoidal basis functions [52, 53, 35], and volume loop (VL) basis set consisting of SWG functions [42].

The basis reduction scheme enforces divergence free current within each tetrahedron. The sum of the 4 basis functions associated with each face of the tetrahedron must equal zero [35]. Although the basis reduction scheme reduces the number of unknowns, it results in a matrix equation with a large condition number, making it difficult to solve with an iterative method [35].

The volume loop (VL) basis is a solenoidal basis function that restricts current flow to a solenoidal subspace and enforces Kirchhoff's voltage law. This approach is similar to the methods used in [20] and [54]. VL basis functions are constructed around the edges of a tetrahedral mesh, which ensures divergence free current within a homogeneous dielectric body. Figure 2.3.4 and 2.3.5 illustrate the closed and unclosed volume loop (VL) basis functions around an edge, respectively. The VL basis function around edge m can be defined as a combination of SWG functions, $\mathbf{f_n}(\mathbf{r})$,

$$\mathbf{o_m}(\mathbf{r}) = \sum_{n=1}^{N} M_{m,n}\mathbf{f_n}(\mathbf{r}), \tag{2.3.30}$$

where $M_{m,n} = \pm 1$, depending on the direction of $\mathbf{f_n}(\mathbf{r})$ within loop m [42]. The value of $M_{m,n}$ is zero, if $\mathbf{f_n}(\mathbf{r})$ does not form part of loop m. The value N is the total number faces inside the tetrahedral mesh.

The volume electric current density, $\mathbf{J}(\mathbf{r})$, can now be expanded in terms of VL basis functions:

$$\mathbf{J}(\mathbf{r}) = \sum_{m=1}^{M} i_m \mathbf{o_m}(\mathbf{r}) = \sum_{m=1}^{M} i_m \left\{ \sum_{n=1}^{N} M_{m,n}\mathbf{f_n}(\mathbf{r}) \right\}, \tag{2.3.31}$$

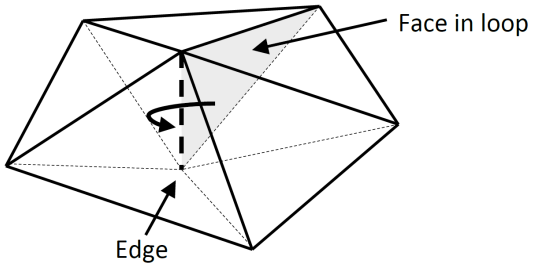

Figure 2.3.4: Close volume loop basis function.

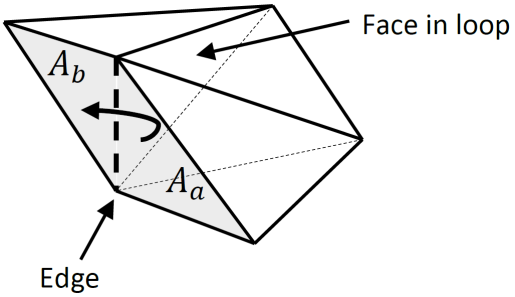

Figure 2.3.5: Unclosed volume loop basis function.

where i_m is defined as the *mesh* current circulating around loop m, which is a combination of several *branch* currents, i_n:

$$i_m = \sum_{n=1}^{N} M_{m,n} i_n. \tag{2.3.32}$$

The *mesh* currents are stored within the vector, I_{mesh}, and can be computed from the current vector, I_{branch}, defined in (2.3.23):

$$I_{mesh} = M I_{branch}. \tag{2.3.33}$$

The entries of matrix M at indexes (m, n) are equal to the values, $M_{m,n}$, given in 2.3.32. Each row of M represents a single VL basis function. The column index of M determines which currents from I_{branch}, i.e. SWG functions $\mathbf{f_n}(\mathbf{r})$, form part of the VL basis function. The system of equations given in (2.3.24) can now be transformed as follows:

$$MZI_{branch} = MV_{branch}, \tag{2.3.34}$$

and replacing I_{branch} with I_{mesh},

$$\left(MZM^T\right) I_{mesh} = V_{mesh}. \tag{2.3.35}$$

The vector, V_{mesh}, contains the voltages across each VL basis function and is defined as,

$$V_{mesh} = MV_{branch}. \tag{2.3.36}$$

It is shown in [42] that the values of the vector V_{mesh} will become zero for closed VL basis functions and will be equal to the voltage difference across the ends of unclosed VL basis functions:

$$(V_{mesh})_m = \begin{cases} 0, & \text{for closed loop } m \\ \phi(\xi)_{|\xi \in A_a} - \phi(\xi)_{|\xi \in A_b}, & \text{for unclosed loop } m \end{cases}. \tag{2.3.37}$$

The functions $\phi(\xi)_{|\xi \in A_a}$ and $\phi(\xi)_{|\xi \in A_b}$ represent the constant voltage potential across the two faces at the ends of an unclosed loop, with area A_a and A_b, respectively.

Figure 2.3.5 illustrates the setup of the VL basis functions within a rectangular filament, with a voltage source connected to two terminals. The points represent edges viewed from above and the circles represent closed VL basis functions. Since displacement current is assumed negligible, current will not flow across the boundary and SWG basis functions are not required for boundary faces. However, the faces connected to the terminals require SWG basis functions, since current can exit these faces. Closed VL basis functions around the terminal edges ensure that the terminal faces are shorted electrically. An unclosed VL basis function is defined between the two terminals and represents the voltage difference between the two terminals, as shown in (2.3.37).

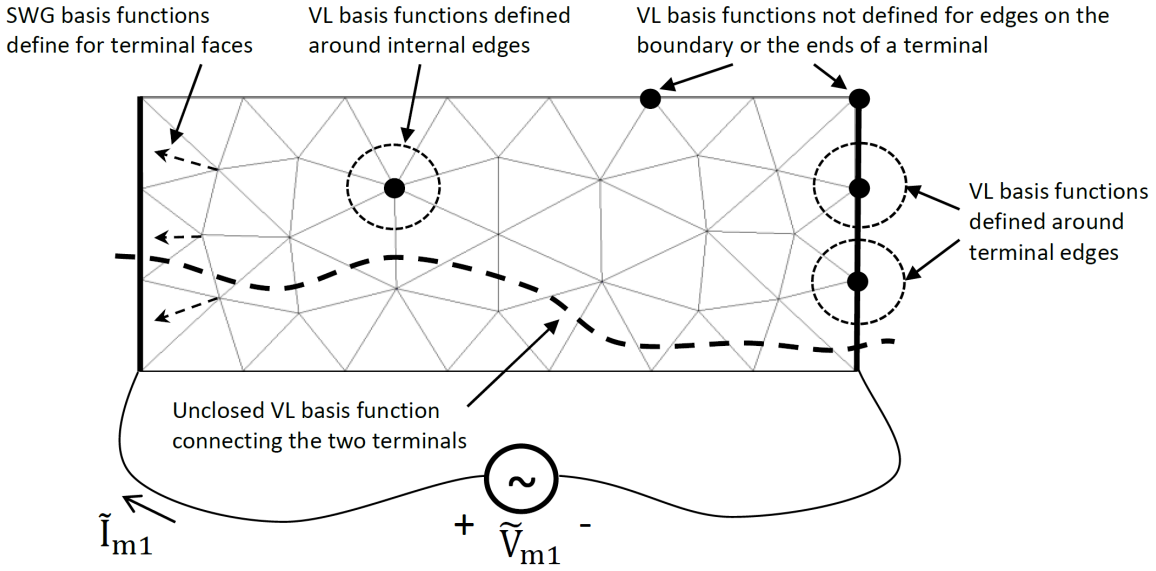

Figure 2.3.6: Top view of tetrahedral mesh of rectangular filament with two terminals.

2.3.4 Fundamental Set of Basis Functions

If VL basis functions are expanded to each possible edge, the basis functions will no longer be independent, resulting in a null space in the matrix equation.

It is shown [35] that this null space is not detrimental when using iterative solvers. However, this is not the case when preconditioners are used to improve the convergence rate of the iterative solver, which will be discussed in Section 2.5.2. A set of independent (fundamental) VL basis functions can be obtained, using the generating (spanning) tree scheme described in [35]. The basis reduction scheme [35] can also be used to reduce the number of loops, but this approach results in a poorly-conditioned matrix, due to many overlaps between loops.

Using the generating tree scheme, an undirected graph is constructed from the geometrical (tetrahedral) mesh. The tetrahedrons and faces represent the nodes and edges of the undirected graph, respectively. If displacement current is taken into account, as discussed in Chapter 4, an additional node must be used for the outer space. A spanning tree is then constructed from this undirected graph and the remaining edges, i.e. edges that do not form part of the spanning tree, are used to obtain a set of independent VL basis functions. This approach (hereafter referred to as the *tetrahedral tree* scheme) is equivalent to finding a set of fundamental circuits in a graph [55].

The nodes and edges of the tetrahedral mesh can also be used to construct an undirected graph [35]. An independent VL basis set can be obtained by constructing VL basis functions around the edges that do not form part of the spanning tree. This method (hereafter referred to as the *edge tree* scheme) can be easily implemented, but it is limited to simply connected regions that do not contain any holes [35]. If a structure contains a hole, an addition VL basis function must be constructed around the hole, resulting in a null space in the matrix equation. As mentioned before, the null space in the matrix equation is not detrimental when using iterative solvers. However, it can limit the ability to perform LU decomposition, which is necessary for preconditioning.

One advantage of the *tetrahedral tree* scheme, is that multiple VL basis functions are automatically constructed around holes. This can also be considered a disadvantage, because it is difficult to identify the VL basis functions surrounding each hole. To perform flux trapping analysis, see Appendix A, the voltage of these VL basis functions must be specified in order to induce current around specific holes. Another disadvantage of the *tetrahedral tree* scheme is the large VL basis functions, created by the spanning tree, which increase the number of non-zero values in the sparse matrix, MZM^T.

The *edge tree* scheme reduces the number of non-zero values in the sparse matrix, MZM^T, since the size of each VL basis function depends only on the number of faces connected to each edge. The disadvantage of this approach is that the VL basis functions must be specified manually by the user for each hole, which can also be detrimental to LU decomposition. Since the VL basis functions around each hole are manually specified, it reduces the complexity of inducing current around holes and makes it ideal for flux trapping analysis.

The *tetrahedral tree* scheme is suitable for most problems described in this dissertation; whereas the *edge tree* scheme will be used for hole excitations and

flux trapping analysis.

2.3.5 Port Excitations

Ports are defined between two terminals, one positive and the other negative, as shown in Fig. 2.3.8. To extract the current through the ports, an excitation voltage must be applied to one of the ports. Each port has to be excited independently, while the remaining ports are electrically shorted. This step has to be repeated for each port. If N ports are defined, N^2 currents will be extracted. The excitation voltages are specified in the vector V_{mesh}, i.e. the right-hand side of (2.3.35). The *mesh* currents, I_{mesh} in (2.3.35), have be solved for each excited port. Once all the *mesh* currents are obtained, the inductance matrix can be calculated, as discussed in Section 2.2.

First, closed VL basis functions have to be constructed around internal and terminal edges, as discussed in Section 2.3.3. The *mesh* voltages, corresponding to the closed VL basis functions, have to be set equal to zero in the vector V_{mesh}. If a closed VL basis functions is constructed around a hole, the corresponding voltage in vector V_{mesh} will depend on the flux through the hole, see Appendix A.

To construct unclosed VL basis functions between the terminals of each port, an undirected graph is constructed from the topological structure of the mesh. Figure 2.3.7 illustrates the constructed graph of two conductors with two excitation ports. The centroid of each tetrahedron represents a node in the graph, while the connections between a tetrahedron and its neighbouring tetrahedrons represent edges in the graph. A *pseudo* tetrahedron is used to represent each port, i.e. a connection between two terminals.

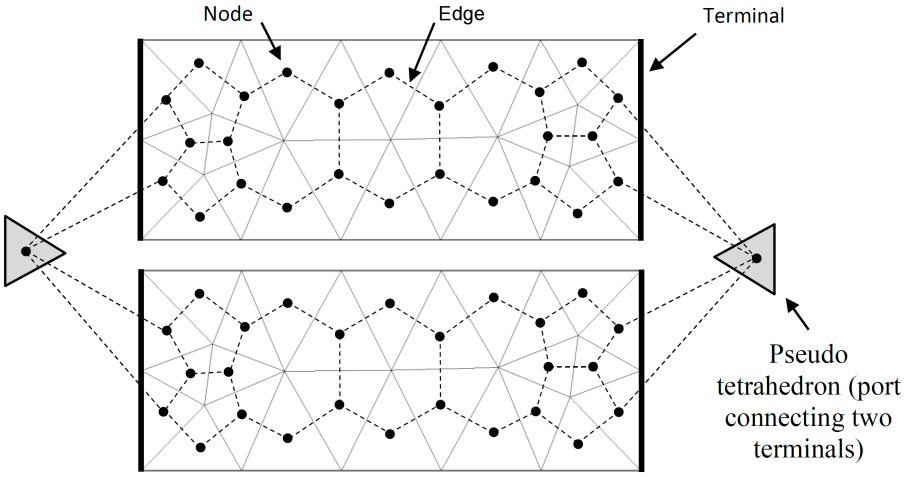

Figure 2.3.7: Meshing graph of two conductors with two ports.

This graph can now be used to determine the shortest path (VL basis function) between two terminals. The shortest path between two nodes in a graph can be obtained using Dijkstra's algorithm [56]. When determining the shortest path between two terminals, all the other ports are electrically shorted, using a *pseudo* tetrahedron. The *pseudo* tetrahedrons add additional nodes to the graph; forming connections between positive and negative terminals.

Each port must have a unique path that connects its two terminals. If two identical paths are created, the linear system in (2.3.35) will be ranked deficient and unsolvable. The two port example in Fig. 2.3.7 will result in two identical paths, but their direction will be reversed. The magnitude of the current through these two ports will be identical, but in the opposite direction. To overcome this, paths are compared with each other and duplicate paths are removed from the matrix M, given in (2.3.35).

When a path (VL basis function) crosses several ports, those ports must be taken into account when specifying the mesh voltages in V_{mesh}. Figure 2.3.8 illustrates three ports with two paths. Path 1 is the unclosed VL basis functions of port A, while path 2 is the unclosed VL basis function of both port B and C. When port A is excited, the terminals of both port B and C are electrically shorted and path 2 will become a closed VL basis function.

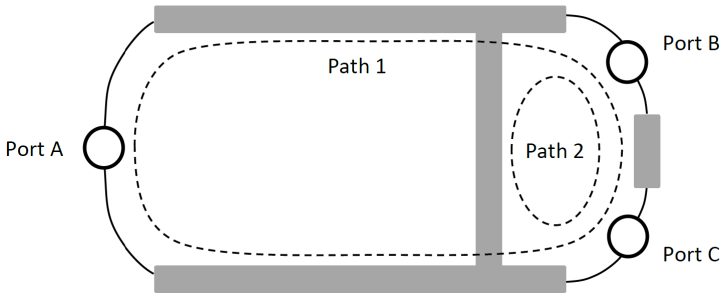

Figure 2.3.8: Three port example with paths through multiple ports.

It is important to note that when either port B or C is excited, path 1 will remain an unclosed VL basis function. Therefore, the voltage difference over the unclosed VL basis function (path 1) will not be zero, since it is crossing an excited port (either port B or C). If port B or C is excited, the voltage of the unclosed VL basis function (path 1) will be either $\pm(V_{mesh})_B$ or $\pm(V_{mesh})_C$, depending on the direction of path 1 and the polarity of the port B and C.

2.4 Resistance and Inductance Matrices

To obtain the currents inside each VL basis function, the system of linear equations in (2.3.35) has to be solved. Before this can be accomplished, the entries of the resistance and inductance matrices, given in (2.3.25) and (2.3.26),

have to be calculated. Luckily, existing numerical methods can be used to evaluate single integrals over tetrahedrons.

In this section, it will be shown that the resistance matrix, R, is mostly sparse, containing only a few non-zero values; whereas the inductance matrix, L, is dense. An analytical solution can be derived for each entry of the resistance matrix, which can be computed and stored directly. However, the inductance matrix cannot be computed and stored directly, due to the size of the matrix. To compute of the inductance matrix, the electrostatic analogy, described in [20], is used and accelerated with the Fast Multipole Method (FMM) [45].

2.4.1 Resistance Matrix

Since each Full-SWG basis function stretches over two tetrahedrons, T_m^+ and T_m^-, each entry of the resistance matrix, given in (2.3.25), can be separated into two components:

$$R = R^+ + R^-. \tag{2.4.1}$$

The entries of matrix R^+, corresponding to the positive tetrahedron, T_m^+, can now be written as,

$$(R^+)_{m,n} = \frac{1}{k_m^+} \int_{T_m^+} \mathbf{w_m}(\mathbf{r}) \cdot \mathbf{f_n}(\mathbf{r})\, dv, \tag{2.4.2}$$

and the entries of matrix R^-, corresponding to the negative tetrahedron, T_m^-,

$$(R^-)_{m,n} = \frac{1}{k_m^-} \int_{T_m^-} \mathbf{w_m}(\mathbf{r}) \cdot \mathbf{f_n}(\mathbf{r})\, dv. \tag{2.4.3}$$

The conductivity within each tetrahedron is assumed constant:

$$k_m^+ = k(\mathbf{r}),\ r \in T_m^+, \tag{2.4.4}$$
$$k_m^- = k(\mathbf{r}),\ r \in T_m^-. \tag{2.4.5}$$

Substituting (2.3.16) into (2.4.2), the entries of the resistance matrix, R^+, can be computed as follow:

$$(R^+)_{m,n} = \begin{cases} \frac{1}{k_m^+} \int_{T_m^+} \left(\frac{1}{3|v_m^+|} \rho_{\mathbf{m}}^+(\mathbf{r}) \right) \cdot \left(\frac{1}{3|v_n^+|} \rho_{\mathbf{n}}^+(\mathbf{r}) \right) dv, & \text{if } T_m^+ = T_n^+ \\ \frac{1}{k_m^+} \int_{T_m^+} \left(\frac{1}{3|v_m^+|} \rho_{\mathbf{m}}^+(\mathbf{r}) \right) \cdot \left(\frac{1}{3|v_n^-|} \rho_{\mathbf{n}}^-(\mathbf{r}) \right) dv, & \text{if } T_m^+ = T_n^- \\ 0, & \text{if } T_m^+ \neq T_n^\pm \end{cases}. \tag{2.4.6}$$

Although not discussed here, the entries of matrix R^- can be computed similarly.

From (2.4.6) it is evident that the majority of the values in matrix R^+ will be zero, except when $T_m^+ = T_n^\pm$. For rest of this section, it is assumed that $T_m^+ = T_n^+$ and $v_m^+ = v_n^+$, unless stated otherwise. The position vectors, $\rho_{\mathbf{m}}^+(\mathbf{r})$ and $\rho_{\mathbf{n}}^+(\mathbf{r})$, are defined with respect to their free vertices, see Fig. 2.3.3. If $\mathbf{r}_{\mathbf{m}}^+$ and $\mathbf{r}_{\mathbf{n}}^+$ are respectively the free vertices of $\rho_{\mathbf{m}}^+(\mathbf{r})$ and $\rho_{\mathbf{n}}^+(\mathbf{r})$, (2.4.6) can be written as:

$$\begin{aligned}(R^+)_{m,n} &= \frac{1}{9k_m|v_m^+||v_n^+|}\int_{T_m^+}(\mathbf{r}-\mathbf{r}_{\mathbf{m}}^+)\cdot(\mathbf{r}-\mathbf{r}_{\mathbf{n}}^+)\,dv \\ &= \frac{1}{9k_m|v_m^+||v_n^+|}\int_{T_m^+}\begin{bmatrix}x-x_m^+\\ y-y_m^+\\ z-z_m^+\end{bmatrix}\cdot\begin{bmatrix}x-x_n^+\\ y-y_n^+\\ z-z_n^+\end{bmatrix}\,dv \\ &= (R_x^+)_{m,n}+(R_y^+)_{m,n}+(R_z^+)_{m,n},\end{aligned} \tag{2.4.7}$$

where $(R_x^+)_{m,n}$ represents the contributions of the x-components:

$$\begin{aligned}(R_x^+)_{m,n} &= \frac{1}{9k_m|v_m^+||v_n^+|}\int_{T_m^+}(x-x_m^+)\cdot(x-x_n^+)\,dv \\ &= \frac{1}{9k_m|v_m^+||v_n^+|}\int_{T_m^+}(x^2+x_m^+x+x_n^+x+x_m^+x_n^+)\,dv.\end{aligned} \tag{2.4.8}$$

Taking the origin of the coordinates at the centroid of T_m^+ and using the integration formula for a tetrahedron [57], the analytical solution for (2.4.8) is as follow:

$$(R_x^+)_{m,n} = \frac{1}{9k_m|v_m^+||v_n^+|}\left\{\frac{1}{20}(x_1^2+x_2^2+x_3^2+x_4^2)+x_m^+x_n^+\right\}, \tag{2.4.9}$$

where $x_1,...,x_4$ are the 4 vertices (x-coordinates) of tetrahedron T_m^+. It is important to note that origin of the coordinates ($x_1,...,x_4, x_m^+$ and x_n^+) are at the centroid of T_m^+. The analytical solution of $(R_y^+)_{m,n}$ and $(R_z^+)_{m,n}$ can be obtained from (2.4.9), by replacing the x-coordinates with the y- and z-coordinates, respectively. Equation (2.4.9) is an exact solution and can be easily implemented in code.

2.4.2 Electrostatic Analogy

Computing the entries of the inductance matrix, given in (2.3.26), is difficult since it requires the evaluation of a double integral over two tetrahedrons. An analytical solution for (2.3.26) has not yet been derived. However, analytical expressions have been derived for potential integrals of linear source distributions on polyhedral domains [1]. Also, numerical quadrature schemes [58] are available to evaluate the outer integral, while using the analytical expressions for the inner integral.

As demonstrated in [20], the FMM can be used to evaluate the matrix-vector product, ZI_{branch}, without explicitly forming Z. The matrix-vector product, ZI_{branch}, can be separated into a real and imaginary part:

$$ZI_{branch} = RI_{branch} + j\omega LI_{branch}. \tag{2.4.10}$$

The evaluation of RI_{branch} is not computationally expensive, since R is a sparse matrix, as shown in Section 2.4.1. However, L is a dense matrix and LI_{branch} is computationally expensive to compute directly.

Using the electrostatic analogy, it is possible to compute LI_{branch} by evaluating the electrostatic potential, produced by surrounding charges, at each tetrahedron [20]. Each entry of the matrix-vector product, LI_{branch}, can be evaluated as follows:

$$(LI_{branch})_m = \sum_{n=1}^{N} \left(\frac{\mu}{4\pi} \int_{T_m^{\pm}} \int_{T_n^{\pm}} \frac{\mathbf{w_m}(\mathbf{r}) \cdot \mathbf{f_n}(\mathbf{r}')}{|\mathbf{r} - \mathbf{r}'|} \, dv' dv, \right) i_n, \tag{2.4.11}$$

where i_n is the *branch* current through face n, i.e. the coefficient in (2.3.17). Note that the integration in (2.4.11) is performed over the tetrahedrons $T_m^{\pm}$ and $T_m^{\pm}$, and not over the volumes v_m and v_n, as given in (2.3.26). Equation (2.4.11) can also be written in terms of the magnetic vector potential, $\mathbf{A}(\mathbf{r})$,

$$(LI_{branch})_m = \int_{T_m^{\pm}} \mathbf{w_m}(\mathbf{r}) \cdot \mathbf{A}(\mathbf{r}) \, dv \tag{2.4.12}$$

where

$$\begin{aligned} \mathbf{A}(\mathbf{r}) &= \frac{\mu}{4\pi} \sum_{n=1}^{N} \left(\int_{T_n^{\pm}} \frac{\mathbf{f_n}(\mathbf{r}')}{|\mathbf{r} - \mathbf{r}'|} \, dv' \right) i_n \\ &= \frac{\mu}{4\pi} \sum_{n=1}^{N} \left(\int_{T_n^{\pm}} \frac{\rho_{\mathbf{n}}^{\pm}}{|\mathbf{r} - \mathbf{r}'|} \, dv' \right) \frac{i_n}{3|v_n^{\pm}|}. \end{aligned} \tag{2.4.13}$$

This decomposition shows that $(LI_{branch})_m$ can be evaluated by integrating the magnetic vector potential, $\mathbf{A}(\mathbf{r})$, over each tetrahedron. The vector potential can be decomposed into its x-, y-, and z-components. Each component can be considered a scalar electrostatic potential generated by a collection of charges [20]:

$$\psi_p(\mathbf{r}) = \frac{\mu}{4\pi} \sum_{n=1}^{N} \left(\int_{T_n^{\pm}} \frac{(\rho_{\mathbf{n}}^{\pm})_p}{|\mathbf{r} - \mathbf{r}'|} \, dv' \right) \frac{i_n}{3|v_n^{\pm}|}, \tag{2.4.14}$$

where $p \in \{1, 2, 3\}$ and the scalar potential, $\psi_p(\mathbf{r})$, denotes the pth component of $\mathbf{A}(\mathbf{r})$. The product $(i_n/3|v_n^{\pm}|)\,(\rho_{\mathbf{n}}^{\pm})_p$ can be interpreted as the charge density within $T_n^{\pm}$. If it is assumed that $\mathbf{A}(\mathbf{r})$ varies slowly across $T_n^{\pm}$, (2.4.14) can be approximated by taking the value at the centroid of the tetrahedron [34]:

$$\psi_p(\mathbf{r}) \approx \frac{\mu}{4\pi} \sum_{n=1}^{N} \left(\int_{T_n^{\pm}} \frac{1}{|\mathbf{r} - \mathbf{r}'|} \, dv' \right) \frac{i_n}{3|v_n^{\pm}|} (\rho_{\mathbf{n}}^{\mathbf{c}\pm})_p, \tag{2.4.15}$$

where $\rho_{\mathbf{n}}^{\mathbf{c}\pm}$ is the vector between the centroid of $T_n^{\pm}$ and the corresponding free vertex. Substituting $\mathbf{A}(\mathbf{r})$ with its scalar potentials, (2.4.12) can be decomposed into its x-, y-, and z-components:

$$(LI_{branch})_m = \sum_{p=1}^{3} \int_{T_m^{\pm}} \left(\frac{1}{3|v_m^{\pm}|} (\rho_{\mathbf{m}}^{\pm})_p \right) \psi_p(\mathbf{r})\, dv. \tag{2.4.16}$$

Once again it is assumed that $\mathbf{A}(\mathbf{r})$ varies slowly enough to approximate (2.4.16), by taking the value at the centroid of $T_m^{\pm}$:

$$(LI_{branch})_m \approx \sum_{p=1}^{3} \left\{ \left(\frac{1}{3|v_m^{\pm}|} (\rho_{\mathbf{m}}^{\mathbf{c}\pm})_p \right), \int_{T_m^{\pm}} \psi_p(\mathbf{r})\, dv \right\}. \tag{2.4.17}$$

where $\rho_{\mathbf{m}}^{\mathbf{c}\pm}$ is the vector between the centroid of $T_m^{\pm}$ and the corresponding free vertex. Substituting (2.4.15) into (2.4.17),

$$\begin{aligned}
(LI_{branch})_m &\approx \sum_{p=1}^{3} \left\{ \left(\frac{1}{3|v_m^{\pm}|} (\rho_{\mathbf{m}}^{\mathbf{c}\pm})_p \right) \int_{T_m^{\pm}} \left[\frac{\mu}{4\pi} \sum_{n=1}^{N} \left(\int_{T_n^{\pm}} \frac{1}{|\mathbf{r}-\mathbf{r}'|}\, dv' \right) \frac{i_n}{3|v_n^{\pm}|} (\rho_{\mathbf{n}}^{\mathbf{c}\pm})_p \right] dv \right\} \\
&= \sum_{p=1}^{3} \left\{ \left(\frac{1}{3|v_m^{\pm}|} (\rho_{\mathbf{m}}^{\mathbf{c}\pm})_p \right) \left[\frac{\mu}{4\pi} \sum_{n=1}^{N} \left(\int_{T_m^{\pm}} \int_{T_n^{\pm}} \frac{1}{|\mathbf{r}-\mathbf{r}'|}\, dv' dv \right) \frac{i_n}{3|v_n^{\pm}|} (\rho_{\mathbf{n}}^{\mathbf{c}\pm})_p \right] \right\} \\
&= \sum_{p=1}^{3} \left\{ (\rho_{\mathbf{m}}^{\mathbf{c}\pm})_p \left[\sum_{n=1}^{N} \left(\frac{\mu}{36\pi |v_m^{\pm}||v_n^{\pm}|} \int_{T_m^{\pm}} \int_{T_n^{\pm}} \frac{1}{|\mathbf{r}-\mathbf{r}'|}\, dv' dv \right) i_n (\rho_{\mathbf{n}}^{\mathbf{c}\pm})_p \right] \right\}.
\end{aligned} \tag{2.4.18}$$

Equation (2.4.18) can easily be accelerated using the FMM, since it involves the evaluation of electrostatic potential at tetrahedron m due to accumulative effect of n charges. Using the FMM, the matrix-vector product, LI_{branch}, can be computed in $O(m)$ operations [20].

2.4.3 Solving Double Integrals

Although the FMM prevents calculating the inductance matrix directly, a solution to the double integral in (2.4.18) is still required:

$$\int_{T_m^{\pm}} \int_{T_n^{\pm}} \frac{1}{|\mathbf{r}-\mathbf{r}'|}\, dv' dv \tag{2.4.19}$$

The inner integral over $T_n^{\pm}$ can be evaluated analytically, following the method described in [1]:

$$\begin{aligned}
\int_{T_n^{\pm}} \frac{1}{|\mathbf{r}-\mathbf{r}'|}\, dv' = \frac{1}{2} \sum_j d_j \Bigg\{ \sum_i \hat{\mathbf{P}}_{\mathbf{ij}}^{\mathbf{0}} \cdot \hat{\mathbf{u}}_{\mathbf{ij}} \Bigg[|d_j| \Bigg(\tan^{-1} \frac{P_{ij}^0 l_{ij}^+}{(R_{ij}^0)^2 + |d_j| R_{ij}^+} \\
- \tan^{-1} \frac{P_{ij}^0 l_{ij}^-}{(R_{ij}^0)^2 + |d_j| R_{ij}^-} \Bigg) P_{ij}^0 \ln \frac{R_{ij}^+ +^0 l_{ij}^+}{R_{ij}^- +^0 l_{ij}^-} \Bigg] \Bigg\},
\end{aligned} \tag{2.4.20}$$

where the double subscript ij denotes the ith edge on the jth face of the tetrahedron $T_n^{\pm}$. The vectors $\hat{\mathbf{P}}_{\mathbf{ij}}^{\mathbf{0}}$ and $\hat{\mathbf{u}}_{\mathbf{ij}}$ are defined on the three dimensional plane of the jth face, as shown in Fig 2.4.1. See [1] for the full derivation of the equation in (2.4.20).

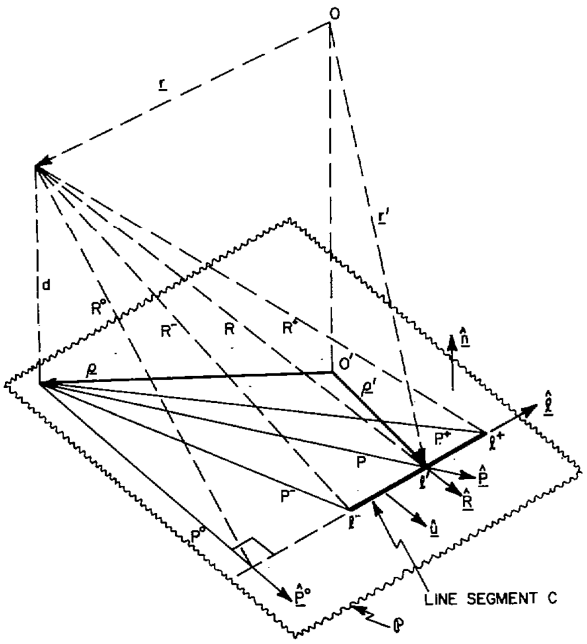

Figure 2.4.1: Geometrical quantities associated with the ith edge on the j^{th} face of the tetrahedron [1].

The outer integral over $T_m^{\pm}$ in (2.4.19) can be evaluated using numerical quadrature rules for tetrahedral elements [58]. Before numerical quadrature can be performed over a given tetrahedron, the global coordinates, $\mathbf{r}$, need to be expressed as a linear combination of natural coordinates,

$$\mathbf{r} = L_1\mathbf{r_1} + L_2\mathbf{r_2} + L_3\mathbf{r_3} + L_4\mathbf{r_4}. \tag{2.4.21}$$

where $\mathbf{r_1}, \mathbf{r_2}, \mathbf{r_3}$ and $\mathbf{r_4}$ are the 4 vertices of the tetrahedron. The natural coordinates, L_1, L_2, L_3 and L_4, are defined as [59],

$$L_1 = \frac{|v_1|}{|v_m^{\pm}|}, \qquad L_2 = \frac{|v_2|}{|v_m^{\pm}|}, \qquad L_3 = \frac{|v_3|}{|v_m^{\pm}|}, \qquad L_4 = \frac{|v_4|}{|v_m^{\pm}|}, \tag{2.4.22}$$

where v_i, $i \in \{1, 2, 3, 4\}$ are the sub-volumes formed between the point $\mathbf{r}$ and the other 4 vertices of the tetrahedron. The sum of the natural coordinates must satisfy:

$$L_1 + L_2 + L_3 + L_4 = 1. \tag{2.4.23}$$

Equation (2.4.19) can now be written in terms of natural coordinates [59]:

$$\int_{T_m^{\pm}} F_n(\mathbf{r})\, dv = \int^{1} \int^{1-L_1} \int^{1-L_1-L_2} G_n(L_1, L_2, L_3)\, dL_1\, dL_2\, dL_3, \quad (2.4.24)$$

where $F_n(\mathbf{r})$ represent the inner integral in (2.4.19),

$$F_n(\mathbf{r}) = \int_{T_n^{\pm}} \frac{1}{|\mathbf{r} - \mathbf{r}'|}\, dv', \quad (2.4.25)$$

and

$$G_n(L_1, L_2, L_3) = F_n(L_1\mathbf{r_1} + L_2\mathbf{r_2} + L_3\mathbf{r_3} + L_4\mathbf{r_4}). \quad (2.4.26)$$

Using the quadrature method, (2.4.19) can be evaluated as:

$$\iiint G_n(L_1, L_2, L_3)\, dL_1\, dL_2\, dL_3 \approx 6|v_m^{\pm}| \sum_{i=1}^{N_q} w_i G_n(L_1^{(i)}, L_2^{(i)}, L_3^{(i)}), \quad (2.4.27)$$

where N_q is the number of sampling points and w_i is the 'weight' of each sampling point [59]. The location of the sampling points within a normalised tetrahedron ($L_1^{(i)}, L_2^{(i)}$ and $L_3^{(i)}$) and the weights, w_i, are calculated with the algorithm described in [58].

Numerical quadrature can also be used to solve $F_n(\mathbf{r})$, instead of using the analytical solution, given in (2.4.20). However, numerical quadrature is less accurate than the analytical solution if the sampling points, N_q, is low.

2.5 Iterative Solver

Direct methods can be used to solve the linear system in (2.3.35), but will quickly become computationally intractable as the size of the matrix, MZM^T, increases. Instead, iterative methods can be used for solving large linear systems.

The most practical iterative solvers are based on projection processes onto Krylov subspaces [60], such as the Conjugate Gradient algorithm and the Generalized Minimum Residual Method (GMRES) [44]. The GMRES is theoretically equivalent to Generalized Conjugate Residual (GCR) method [61], but has several advantages over the GCR method. The GCR method is ideal for solving sparse linear systems that are symmetric positive definite; whereas the GMRES was specifically developed for solving non-symmetric linear systems [44].

Depending on the number of VL basis functions used for discretizing the VIE, as described in Section 2.3.4, the matrix MZM^T in (2.3.35) is not guaranteed to be symmetric positive definite. Iterative methods, such as the GCR method, can break down when the matrix is not symmetric positive definite; whereas the GMRES is guaranteed to not break down [44]. Therefore, the GMRES algorithm is chosen to solve the linear system in (2.3.35).

2.5.1 GMRES

The general form of the GMRES algorithm [60] is described in algorithm 1. The matrix $A = MZM^T$, $x = I_{mesh}$ and $b = V_{mesh}$. The dominant cost of the GMRES algorithm is the computation of the matrix-vector product, $Av_j = (MZM^T)I_{mesh}$, which requires $O(m^2)$ operations. In TetraHenry, the matrix A is not explicitly formed but approximated using the FMM, as discussed in Section 2.4.2. The FMM reduces the matrix-vector product, $(MZM^T)I_{mesh}$, to $O(m)$ operations. The dominant storage of the GMRES is the matrix V_{mesh}, which scales linearly with the number of iterations. Instead of allocating memory for all the m columns, the memory for each column is dynamically allocated as required [38].

Algorithm 1: Algorithm for solving linear system using GMRES [60]

Choose x_0 and the maximum number of iterations m. Set the all the values of the matrix H_m, with size $m \times (m+1)$, equal to zero.
Compute $r_0 = b - Ax_0$, $\beta = ||r_0||_2$ and $v_1 = r_0/\beta$
for $j = 1, 2, ..., m$ **do**
  Compute $w_j = Av_j$
  for $i = 1, 2, ..., j$ **do**
    $h_{ij} = (w_j, v_i)$
    $w_j = w_j - h_{ij}v_i$
  $h_{j+1,j} = ||w_j||_2$. Stop for-loop if $h_{j+1,j} = 0$
  $v_{j+1} = w_j/h_{j+1,j}$
Define $V_m := [v_1, v_2, ...]$
Compute $y_m = argmin_y||\beta e_1 - H_m y||_2$ and $x_m = x_0 + V_m y_m$, where $e_1 = [1, 0, ...]^T$.

2.5.2 Preconditioning

Preconditioning is a modification of the original linear system that reduces the convergence rate of the iterative solver [60]. The right preconditioned linear system is used:

$$(MZM^T)Px' = V_{mesh}, \tag{2.5.1}$$

where P is the preconditioning matrix. The aim is to make P^{-1} as close as possible to MZM^T. The vector I_{mesh} can then be obtained by solving the linear system:

$$P^{-1}I_{mesh} = x'. \tag{2.5.2}$$

The solution to I_{mesh} can easily be calculated, if P is known. Obtaining the solution for P is expensive, because the matrix MZM^T has to be factorized into its lower and upper triangular matrices, L and U:

$$P^{-1} \approx MZM^T = LU. \tag{2.5.3}$$

A common approach for approximating P^{-1}, is to use the values on/near the diagonal of the matrix:

$$P^{-1} = (MZM^T)_{\text{sparse}}. \tag{2.5.4}$$

Using incomplete LU (ILU) factorization to factorize the sparsified matrix $(MZM^T)_{\text{sparse}}$ is ineffective, since the diagonal values of MZM^T are not necessarily greater than the sum of the off-diagonal values [20]. Instead of sparsifying MZM^T, a better preconditioner is formed when sparsifying the matrix Z. This approach is less computationally expensive and has proven to be effective in FastHenry [20]. The preconditioning matrix is then formed using ILU factorization:

$$P^{-1} = M(Z_{\text{sparse}})M^T \approx LU. \tag{2.5.5}$$

where

$$Z_{\text{sparse}} = R + j\omega L_{\text{sparse}}. \tag{2.5.6}$$

The ILU factorization of P^{-1} is computed using routines from the SuperLU_MT library [62, 63, 64]. SuperLU_MT uses an "asynchronous parallel supernodal algorithm for sparse Gaussian elimination" [64]. The matrix L_{sparse} is the sparse inductance matrix of L, with most of its values set equal to zero. The non-zero pattern of L_{sparse} will determine the quality of the preconditioner.

The following two choices for L_{sparse} are assessed: using the diagonal values of L or using the non-zero pattern of matrix R. These two preconditioners will be referred to as the "*Diagonal-L*" and "*Pattern-R*" preconditioners, respectively. For a non-superconducting circuits ($k(\mathbf{r}) = \tilde{\sigma_0}$), the preconditioned system reduces to the following, as $\omega \to \infty$:

$$(MZM^T)P \to MLM^T(ML_{\text{sparse}}M^T)^{-1}. \tag{2.5.7}$$

It was shown in [20] that, as $\omega \to \infty$, the matrix L_{sparse} should be chosen as symmetric positive definite in order to be effective. For superconducting circuits, the values of R will be imaginary and, therefore, Z will only consist of imaginary values. To reduce the convergence rate, the matrix Z_{sparse} needs to be symmetric positive definite. Fortunately, both matrices R and L_{sparse} are symmetric positive definite for both the *Diagonal-L* and the *Pattern-R* preconditioners. Unfortunately, the VL basis functions are not always independent, as mentioned in Section 2.3.3; therefore, the matrix MZM^T is not always

symmetric positive definite. If the *tetrahedral tree* scheme is used, a set of independent VL basis functions can be obtained, as discussed in Section 2.3.3.

If MZM^T is symmetric positive definite, all its eigenvalues will be positive. The convergence rate of the GMRES solver depends on the eigenvalues of MZM^T, including the condition number:

$$\kappa(V) = ||V||_2||V^{-1}||_2 = \frac{\lambda_{max}(V)}{\lambda_{min}(V)}, \tag{2.5.8}$$

where V is the eigenvector matrix of MZM^T [20]. The values $\lambda_{min}(V)$ and $\lambda_{max}(V)$ are the minimum and maximum eigenvalues of V. The purpose of the preconditioner is to minimize the condition number of the original linear system, hence improving the convergence rate of the GMRES solver [20]. If the eigenvalues of the preconditioned system is spread over a smaller interval, the condition number will be reduced and the converge rate will be increased. If the eigenvalues are close to the origin, the convergence rate will be slowed down [20, 60].

Figure 2.5.1 shows the eigenvalues of MZM^T for the superconducting microstrip line example in Fig. 2.7.1. The *tetrahedral tree* scheme was used to obtain an independent set of VL basis functions, ensuring a symmetric positive definite matrix with positive eigenvalues. Figure 2.5.2 and 2.5.3 show the eigenvalue spectrum of the *Diagonal-L* and *Pattern-R* preconditioned matrices, respectively. Examining the eigenvalue spectrum of MZM^T and the *Diagonal-L* preconditioned matrix, it is evident that the eigenvalues of *Diagonal-L* are spread over a smaller interval and are further away from the origin. Therefore, the convergence rate of the preconditioned linear system in (2.5.1) will be faster, compared to the original linear system in (2.3.35). However, the *Pattern-R* preconditioned system will converge even faster, since its eigenvalues are spread over a smaller interval.

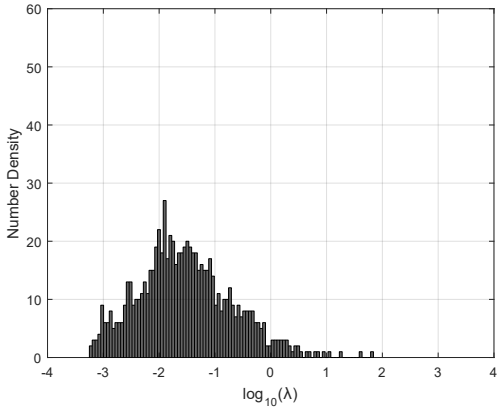

Figure 2.5.1: Eigenvalue spectrum of the matrix MZM^T.

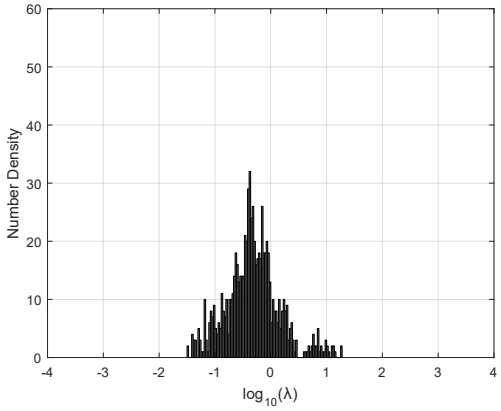

Figure 2.5.2: Eigenvalue spectrum of the *Diagonal-L* preconditioned matrix, $(MZM^T)P$.

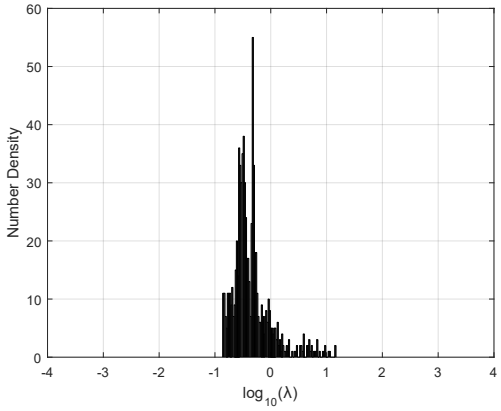

Figure 2.5.3: Eigenvalue spectrum of the *Pattern-R* preconditioned matrix, $(MZM^T)P$.

Figure 2.5.4 shows the convergence of the GMRES for the superconducting microstrip line example, when applying no preconditioner, the *Diagonal-L* and the *Pattern-R* preconditioners. Figure 2.5.5 shows the convergence of the multi-layer example in Fig. 2.7.2. From Fig. 2.5.4 and 2.5.5 it is evident that *Diagonal-L* preconditioning accelerates the convergence of the GMRES method, compared to the linear system with no preconditioning. Constructing the *Pattern-R* preconditioner is more computationally expensive than *Diagonal-L* preconditioner, but it delivers much faster convergence and reduces overall calculation time.

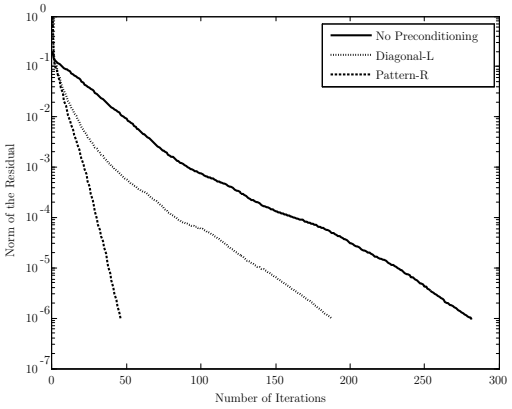

Figure 2.5.4: Convergence rate of GMRES for the microstrip line example.

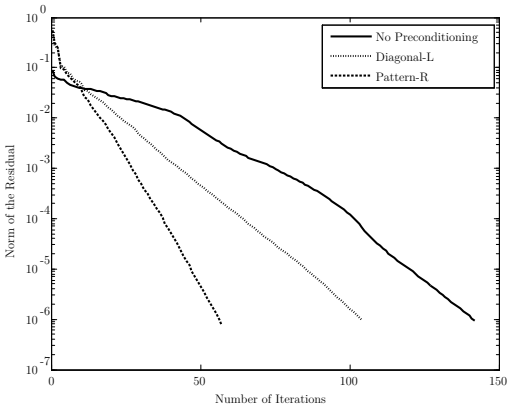

Figure 2.5.5: Convergence rate of GMRES for the multi-layer example.

2.6 Meshing

The numerical solver, TetraHenry (TTH), and mesh generation are two separate components. Meshing is done by third party finite element mesh generators, with sophisticated meshing algorithms. Gmsh [46, 47] was chosen as the primary mesh generator, since it is an open source mesh generator capable of generating both triangular (surface) and tetrahedral (volume) meshes for large geometries.

Figure 2.6.1 shows the process for generating an input mesh file for TTH. The geometry of the structure, including electrical parameters and terminal surfaces, are prescribed in an ASCII text file (.geo file), using Gmsh's own scripting language. A detailed description of the scripting language is available in Gmsh's reference manual [47]. Gmsh generates an output mesh file (.msh file), containing the properties each tetrahedron and surface, as shown in Fig. 2.6.2. Finally, the mesh file is given to TTH as input. A few examples (Gmsh input files) are provided in TTH user's manual, available in

Appendix C.

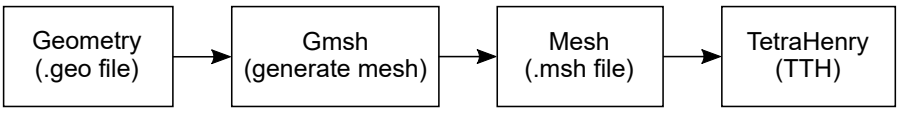

Figure 2.6.1: The process for generating an input mesh file for TTH.

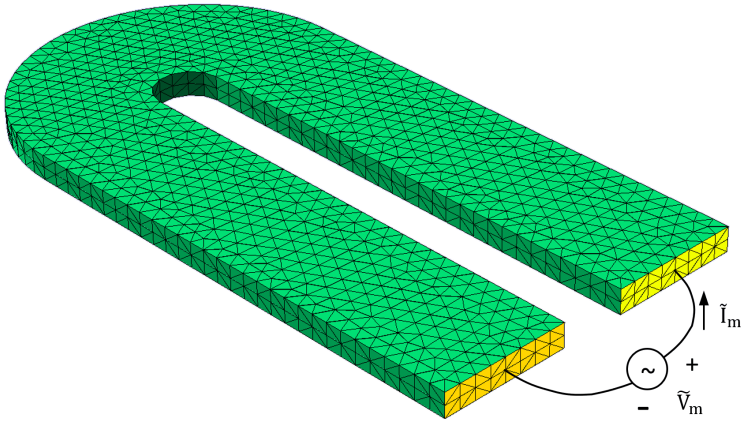

Figure 2.6.2: Tetrahedral mesh generated from geometrical circuit model.

2.6.1 Modeling Penetration Depth

High quality meshes are vital for accurate inductance extraction [65]. This is especially important for superconducting structures, since the current density within the superconductor depends on the London penetration depth, λ, given in (2.3.13). Therefore, the mesh has to be adapted to account for regions of high current density, which is usually near the surface of the superconductor.

When a superconducting slab is placed inside a magnetic field, the magnetic field will penetrate the superconductor to a depth of order λ [26]. The magnetic field inside a superconducting slab (with thickness $2a$ in the y-direction and of infinite extend in the x- and z-direction) will be as follows,

$$\mathbf{H} = Re\left\{H_0 \frac{\cosh(y/\lambda)}{\cosh(a/\lambda)} e^{j\omega t}\right\} \hat{\mathbf{z}}, \tag{2.6.1}$$

where H_0 is the amplitude of the applied magnetic field in the z-directed [26]. The current density inside the superconducting, due to the z-directed magnetic field, can be calculated as follow,

$$\mathbf{J} = Re\left\{H_0 \frac{1}{\lambda} \frac{\sinh(y/\lambda)}{\cosh(a/\lambda)} e^{j\omega t}\right\} \hat{\mathbf{x}}. \tag{2.6.2}$$

The distributions of the field in (2.6.1) and the current density in (2.6.2) are shown in Fig. 2.6.3. If the thickness of the slab is much smaller than the penetration depth. i.e. $a \ll \lambda$, the field will penetrate the entire slab and the current will be distributed throughout the slab [26]. If the thickness of the slab is much larger than the penetration depth, i.e $a \gg \lambda$, the current will flow near the surface of the slab [26], as shown in Fig. 2.6.3b. It is therefore important to take the penetration depth into account when meshing superconducting structures.

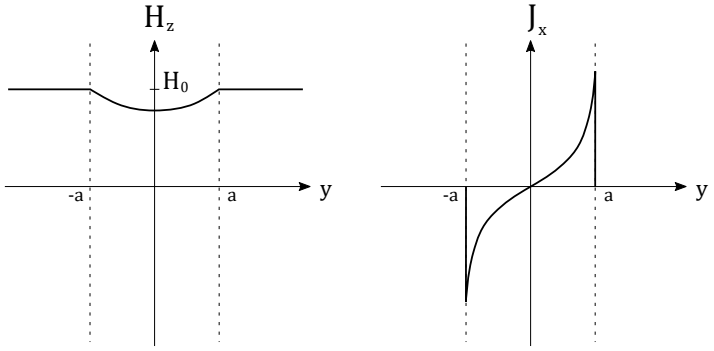

(a) ($a \ll \lambda$)

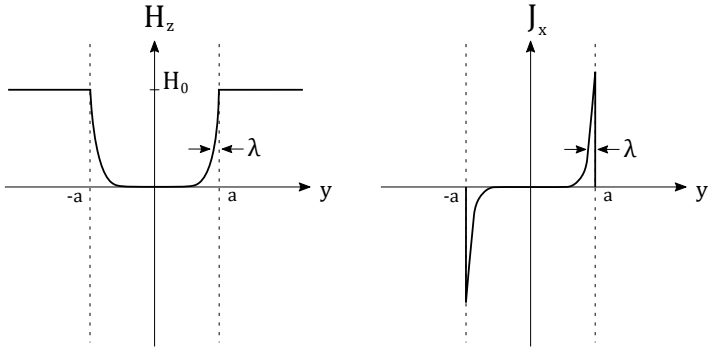

(b) ($a \gg \lambda$)

Figure 2.6.3: Magnetic field and current density inside a superconducting slab with thickness a.

To accurately model skin currents near the surface of bulk superconductors, i.e $a \gg \lambda$, several meshing layers near the surface are necessary. One option is to use a small mesh elements near the surface and gradually increase the size towards the interior, as shown in Fig. 2.6.4a. The disadvantage of this approach is the high number of elements generated near the surface. Since the current is flowing parallel to the surface, long thin mesh elements parallel to the surface would significantly lower the number of meshing elements, as shown in Fig. 2.6.4b.

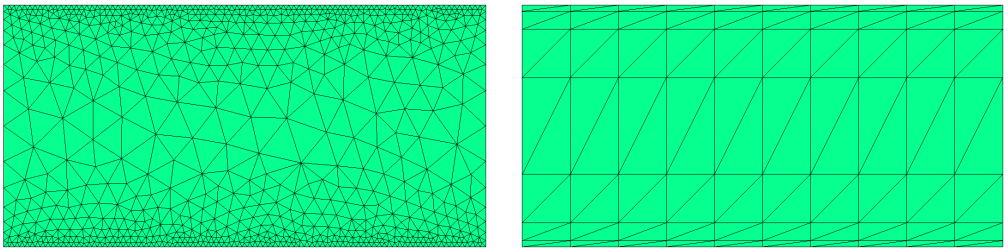

(a) Mesh size as a function of the distance from the boundary.

(b) Larger and thinner mesh elements along the boundary.

Figure 2.6.4: Adaptive meshing for modeling skin currents.

2.7 Results

2.7.1 Small Superconducting Structures

To evaluate the efficiency and performance of TTH, several test structures were simulated with TTH and the results were compared to Fast FastHenry (FFH) [38]. Figure 2.7.1 and 2.7.2 show the current density calculated with TTH for the microstrip line and the multilayer structure, respectively. The geometry in Fig. 2.7.2 was generated using InductEx [21, 2]. Table 2.7.1 shows the performance of TTH compared to FFH. The unknowns represent the number of SWG functions in TTH and filaments in FFH. Extracted values correspond with both FFH and the method used in [66] with less than 1% error. The running time and memory usage of TTH are lower than FFH; however, the number of SWG functions necessary for the same level of accuracy can be higher compared to FFH. For example, the structure in Fig. 2.7.2 does not model the London penetration depth accurately and, therefore, requires a lower discretization size compared to the structure in Fig. 2.7.1. In order to lower the number of unknowns, i.e. increase the discretization size, the number of layers near the edges must be increased, as discussed in Section 2.6.1.

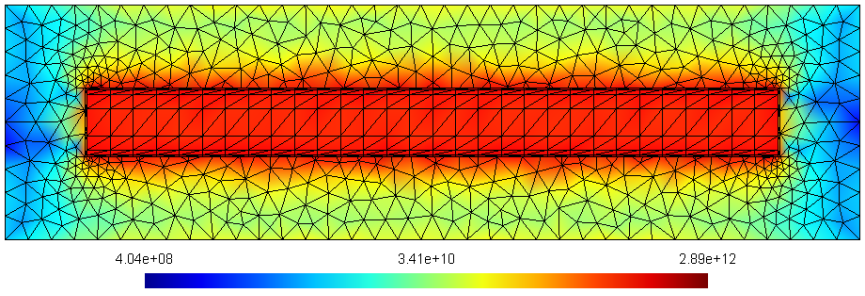

Figure 2.7.1: Current density of a $5\,\mu$m $\times$ $50\,\mu$m microstrip line (thickness = 220 nm and penetration depth = 137 nm) 177.5 nm above ground layer (overhang = $6\,\mu$m, thickness = 300 nm, and penetration depth = 86 nm). Note: segment size and height division is for illustration purposes only.

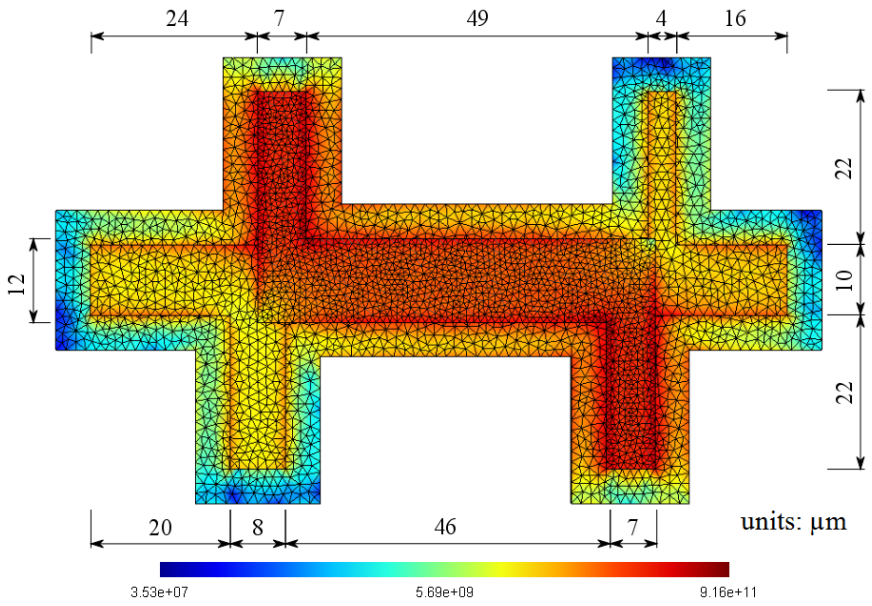

Figure 2.7.2: Current density of a multilayer example with coupled structures. Penetration depth is 90 nm and thicknesses are respectively 200 nm, 250 nm and 350 nm for top, middle and ground layers. Ground overhang is 5 μm.

Table 2.7.1: Performance comparison between TTH and FFH. Bench-marked performed on a Intel Core i7-3612QM @2.1 GHz, running Windows 8.1.

Layout model	Unknowns	Inductance	CPU Time	Memory
Strip line (TTH)	121104	4.421 pH	84 s	1.51 GB
Strip line (FFH)	119824	4.426 pH	87 s	2.92 GB
Multilayer (TTH)	108404	1.471 pH	67 s	1.45 GB
Multilayer (FFH)	105655	1.461 pH	144 s	2.71 GB

2.7.2 Coupling Between Two Moats

VL basis functions and the method discussed in [37], which is provided in Appendix A, are used to calculate the self- and mutual-inductance between two moats, within a superconducting ground layer. Results are compared with 3D-MLSI [32] using two examples; one large and one small. The small structure is a $16\mu m \times 11\mu m$ film containing two $5\mu m \times 2\mu m$ moats, shown in Fig. 2.7.3. Figure 2.7.4 shows the larger structure; a $50\mu m \times 30\mu m$ film containing two $4\mu m \times 1\mu m$ moats. The moats are separated by $8\mu m$ in both examples. The VL basis functions can also be used to specify the number of fluxons in each moat, including the polarity, as shown in Fig. 2.7.4a and 2.7.4b. Table 2.7.2 shows the comparison of the inductance values calculated with

TTH and 3D-MLSI. The results of the two-dimensional triangular method, discussed in Chapter 3, are also shown in Table 2.7.2. The results of TTH correspond with 3D-MLSI with less than 1% error, for both examples. As expected, the two-dimensional method correspond more closely with 3D-MLSI, since 3D-MLSI uses two-dimensional triangular meshing.

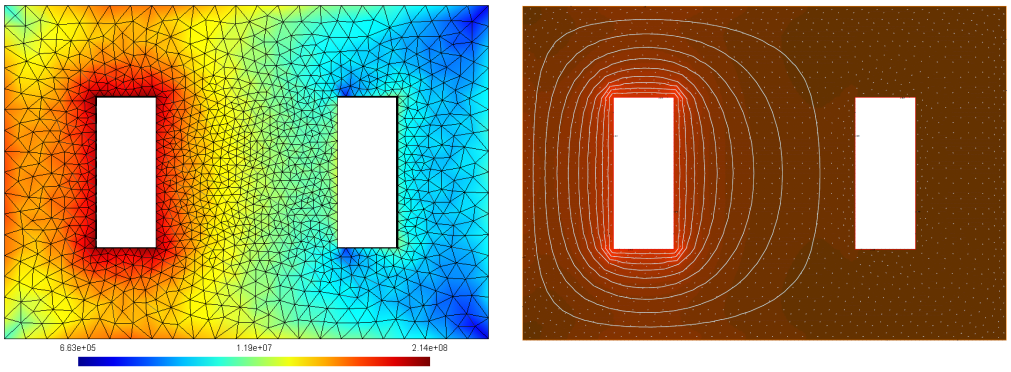

(a) Current density using TTH. (b) Current density using 3D-MLSI.

Figure 2.7.3: Current density (log-scale) of a superconducting film. A fluxon is trapped in the left hole and zero fluxons in the right hole. Dimensions: 16 μm $\times$ 11 μm with thickness of 0.4 μm and London penetration depth of 0.4 μm. Dimensions of holes: 5 μm $\times$ 2 μm separated by 8 μm.

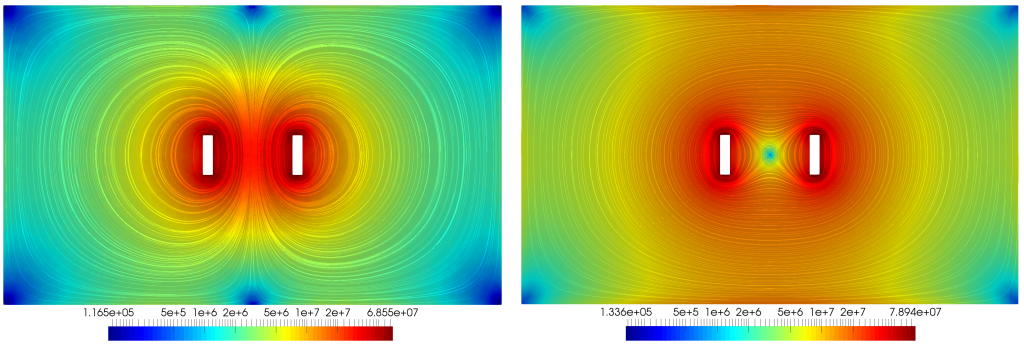

(a) Fluxons with opposing polarities. (b) Fluxons with same polarities.

Figure 2.7.4: The current density (log-scale) of two moats ($4\mu m \times 1\mu m$) in a $50\mu m \times 30\mu m$ film (thickness $100nm$ and $\lambda = 966.95nm$) calculated using TTH. The two moats are separated by $8\mu m$.

2.7.3 Large-scale Superconducting Circuits

To evaluate the performance of TTH on large-scale circuits, the SFQ pulse splitter [2] with multiple excitation ports was simulated, shown in Fig. 2.7.5.

Table 2.7.2: The extracted inductance values of the small structure in Fig. 2.7.3 and the large structure in Fig. 2.7.4

Inductance	3D-MLSI [pH]	TTH (3D) [pH]	TTH (2D) [pH]	% Difference (TTH 3D)	% Difference (TTH 2D)
Small - left moat	9.046	9.059	9.053	0.147%	0.073%
Small - right moat	9.047	9.060	9.056	0.148%	0.095%
Small - mutual	0.655	0.656	0.656	0.132%	0.066%
Large - left moat	38.260	38.061	38.330	0.523%	0.183%
Large - right moat	38.280	38.064	38.324	0.568%	0.167%
Large - mutual	9.865	9.779	9.866	0.879%	0.006%

First, the GDS layout of the SFQ splitter is converted into a three-dimensional geometry, using InductEx and the Hypres 4.5 kA/cm^2 Nb fabrication process [4]. InductEx automatically adds labels to each terminal surface, which is then used by TTH to identify excitation ports. Gmsh converts the geometry to a tetrahedral mesh and the mesh is send to TTH as input, as discussed in Section 2.6. Voltages are applied to each port, separately, and the currents through each port are extracted, see Fig. 2.7.6. The circuit netlist in Fig. 2.7.5b and the corresponding port currents are send to InductEx, which calculates the self-inductance of each component in the netlist.

The extracted inductance values of the SFQ splitter are given in Table 2.7.3, including the inductance values calculated with FFH. Three tetrahedral meshing types were tested: a large mesh consisting of a single layer, a large mesh with a boundary layer and a fine mesh with a boundary layer, as described in Section 2.6.1. The error between TTH and FFH is about 5% or less for the fine mesh with a boundary layer. The high error is due to the lack of accuracy when modeling the London penetration depth. The error can be improved by increasing the number layers near the surface, as will be shown in Section 3.4 of Chapter 3.

2.7.3.1 Coupling between moats and inductors

To evaluate the effects of moats on large-scale circuits, we start with a GDS layout of the SFQ pulse splitter with moats added at critical locations, as shown in Fig. 2.7.5a. Fluxons are inserted within each moat, using VL basis functions and the method described in Appendix A.

InductEx automatically adds labels to the interior surfaces of each moat (hole), which is then used to identify the perimeter of each moat. Gmsh converts the geometry to a tetrahedral mesh, as shown in Fig. 2.7.7a. The tetrahedral mesh is given to TTH as input and VL basis functions are constructed around each moat's perimeter. An illustration of the VL basis functions, around each moat and between the terminals of each port, is shown in Fig. 2.7.7c. The port and hole currents are computed with TTH, see Fig. 2.7.7b; whereas the self- and mutual inductance are calculated with InductEx,

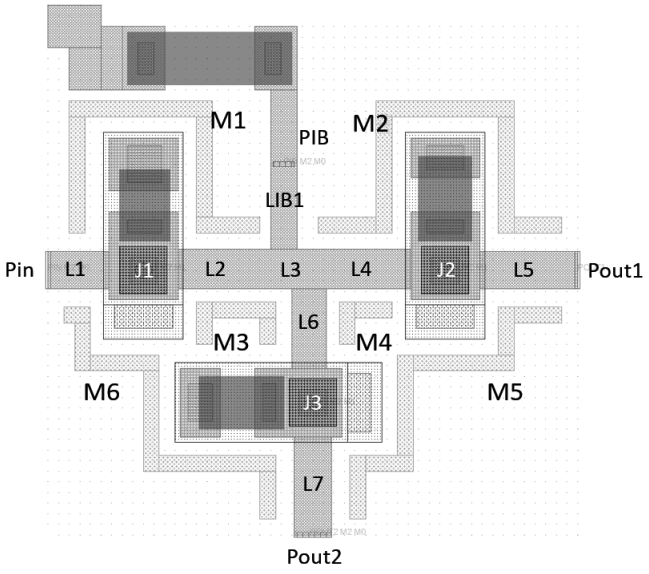

(a) GDS layout with ports (P_{Ib}, P_{in}, P_{out1} and P_{out2}) and moats (M1,M2,M3,...).

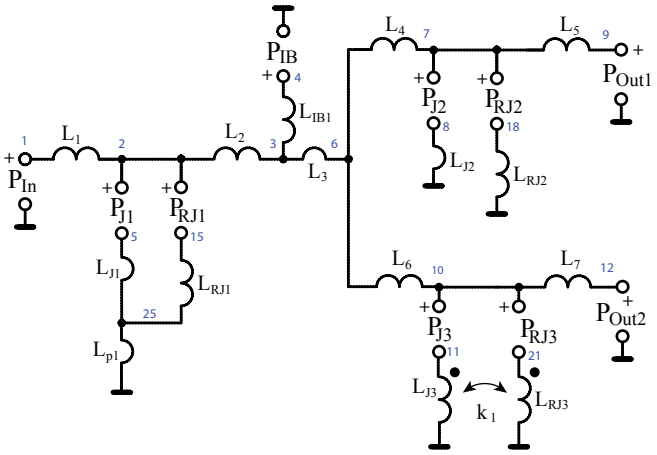

(b) Circuit netlist defining ports and inductors for InductEx [2].

Figure 2.7.5: SFQ pulse splitter example from InductEx website [2].

given in Table 2.7.4. The highlighted values in the Table 2.7.4 indicate the largest coupling factors for a specific moat. As expected, the coupling factors are higher for inductors closest to the moat.

The circuit schematic of the SFQ pulse splitter is shown in Fig. 2.7.8. Moats are modeled as inductors connected to current sources. The coupling factors between a moat and each inductor are specified within the circuit schematic. Operating margins and yield analysis can be performed by changing the number of fluxons through each moat. If coupling factors are too high or the operating margins are too low, the area of the moats can be reduced. Reducing the area of a moat has two advantages: the coupling factor and the magnetic flux density through the moat are reduced [37]. However, reducing the size of

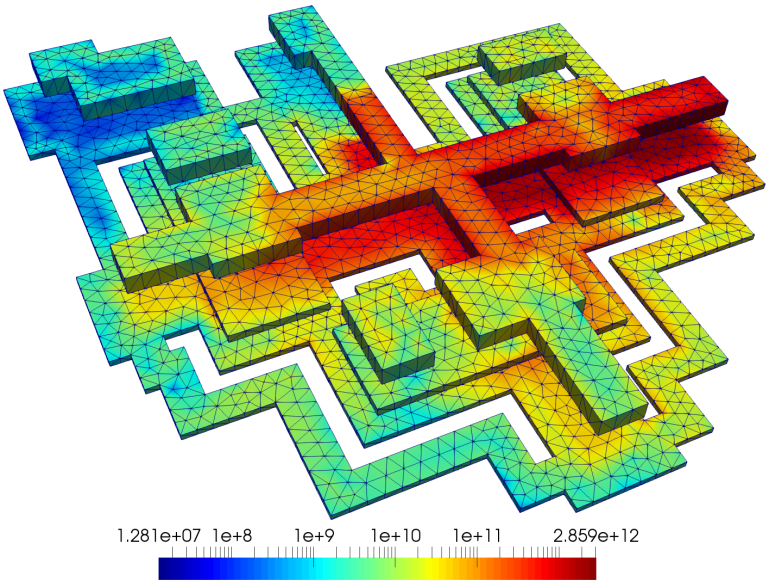

Figure 2.7.6: Current density of the SFQ pulse splitter, generated with TTH, with 1 V applied to port P_{Ib}.

Table 2.7.3: Inductance values of SFQ pulse splitter computed with TTH and FFH.

Inductor	TTH (large) [pH]	TTH (boundary) [pH]	TTH (fine mesh) [pH]	FFH [pH]	Error FFH vs TTH (fine mesh)
L1	1.7408	1.6341	1.6092	1.5601	3.14%
L2	2.5401	2.3764	2.3590	2.2507	4.81%
L3	0.5374	0.5017	0.5029	0.4746	5.95%
L4	2.4367	2.2684	2.2526	2.1738	3.62%
L5	2.5732	2.4349	2.4015	2.3009	4.37%
L6	2.4025	2.2298	2.2105	2.1456	3.02%
L7	2.5613	2.4272	2.4013	2.2830	2.30%
LJ1	0.1506	0.1405	0.1280	0.1251	4.72%
LJ2	0.1517	0.1422	0.1290	0.1232	4.32%
LJ3	0.1569	0.1469	0.1341	0.1285	4.32%
LIB1	2.6727	2.4961	2.4764	2.3806	4.02%

a moat will lower its ability to keep fluxons away from critical regions [67].

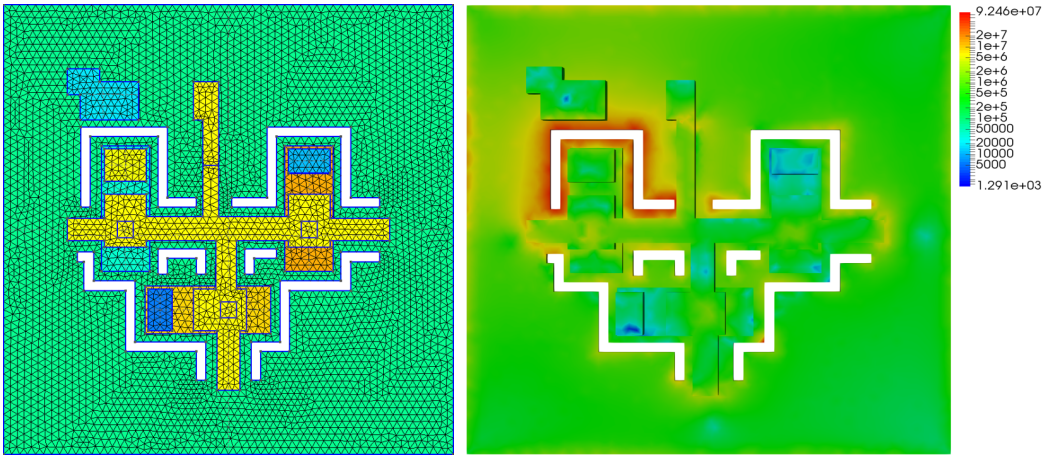

(a) (b)

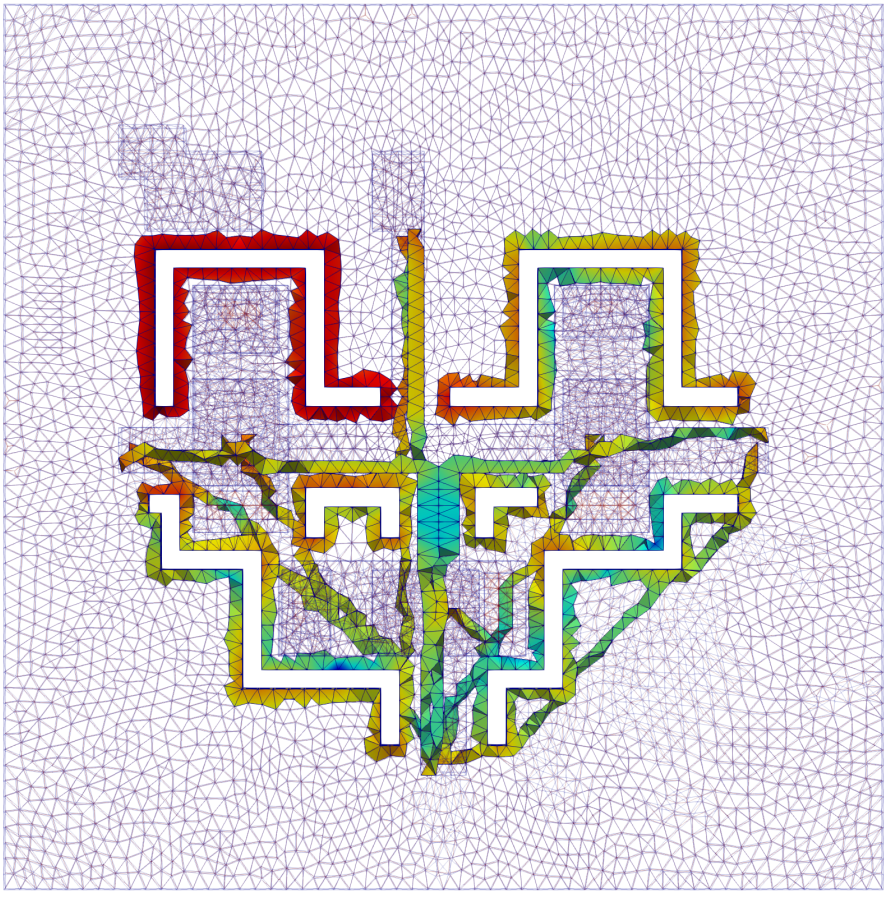

(c)

Figure 2.7.7: (a) Mesh generated from GDS layout using InductEx. (b) Current distribution of SFQ pulse splitter with a fluxon trapped in moat M1. (c) VL basis functions around moats and between port terminals.

Table 2.7.4: Coupling factors (k) between moats and inductors in SFQ splitter. Highlighted values indicate the highest coupling factors of each moat.

Inductor	Moat 1	Moat 2	Moat 3	Moat 4	Moat 5	Moat 6
L1	**0.0471**	-0.0019	**0.0307**	0.0033	0.0052	**0.0362**
L2	**0.0445**	0.0022	**0.0504**	0.0076	0.0067	**0.0229**
L3	-0.0043	**-0.0653**	**0.0838**	0.0101	0.0009	**0.0446**
L4	0.0029	**-0.0347**	0.0033	**0.0614**	**0.0339**	-0.0014
L5	0.0046	**-0.0413**	0.0005	**0.0307**	**0.0437**	0.0011
L6	-0.0049	0.0040	**0.0373**	**-0.0578**	**-0.0339**	**0.0227**
L7	-0.0056	0.0004	**0.0275**	**-0.0292**	**-0.0439**	**0.0345**
LIB1	**-0.0338**	**-0.0235**	-0.0082	-0.0022	-0.0045	-0.0017
LJ1	-0.0239	-0.0153	-0.1044	-0.0201	-0.0099	0.0293
LJ2	-0.0074	0.0309	0.0113	0.1226	-0.0445	-0.0100
LJ3	0.0034	0.0139	0.0345	-0.1075	0.0460	-0.0515

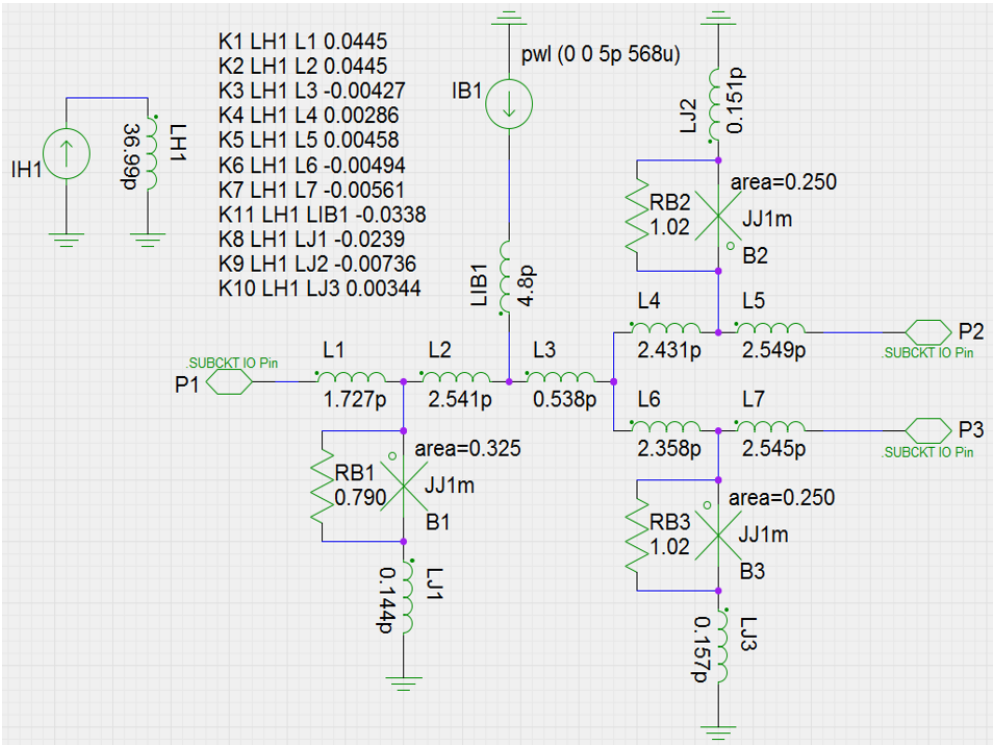

Figure 2.7.8: circuit schematic of SFQ Splitter with current source (IH1) and inductor (LH1) representing the fluxon in a moat coupling with the surrounding inductors.

2.8 Conclusion

A finite element numerical solver was developed, called TetraHenry (TTH), that uses tetrahedral volume elements to model current density within superconducting structures. Volume Loop (VL) basis functions, consisting of SWG basis functions, are used to discretize the volume electric current integral equation (VJIE). The Method of Moments (MoM) transforms the boundary-value problem into a matrix equation, which is solved using the GMRES iterative solver. Two types of preconditioners, *Diagonal-L* and *Pattern-R*, were developed to accelerate the convergence rate of the iterative solver. An analytical solution for the sparse resistance matrix was derived. The calculation of the dense inductance matrix is accelerated, using an electrostatic analogy and the FMM. Voltage sources are used to excite current through multiple ports in the superconducting structure, which can then be used to calculate the self- and mutual-inductance.

Calculation results of TTH correspond with FastHenry, for small and large scale superconducting circuits. Self- and mutual-inductance of holes and between holes, in a superconducting ground layer, was calculated and the results correspond with 3D-MLSI with less than 1 % error.

Segmentation of complex 3D structures is much easier with tetrahedral elements compared to the cuboid filaments used in FastHenry. The non-uniform segmentation capabilities of tetrahedral meshes also reduces the number of elements, when meshing curved structures, compared to cuboid filaments.

Chapter 3

2D Triangular Modelling Method

3.1 Introduction

Performing current distribution calculations on a chip-scale circuit layout, requires a large number of unknowns to be solved. Typically, superconducting circuit layouts consist of thin superconducting films. If the thickness of the superconducting films are on the same order as the London penetration depth, the three-dimensional volume current density can be restricted to two dimensions. This is also known as the sheet current model, which has proven to be efficient for simulating the current density in multilayer superconductor films [32, 68, 69, 70, 71].

Meshing thin superconducting films with two dimensional triangular elements, instead of tetrahedral elements, significantly reduces the number of unknowns. Modelling the current density inside a cuboid conductor requires at least six tetrahedral elements, whereas the same cuboid can be modelled with only two triangular elements. Furthermore, each tetrahedron requires four SWG basis functions, one for each face, whereas a triangle requires only three RWG basis functions [72], one for each edge. Theoretically, the number of unknowns can be reduced by a factor of $\frac{6\times4}{2\times3} = 4$, if triangular meshing is used instead of tetrahedral meshing. However, triangular meshing is limited to sheet current models; therefore, only practical for simulating thin superconducting films with finite thickness. The thickness of these films can be modelled with the special Green's functions defined in [32, 68, 69].

3.2 Derivation of Surface Integral Equation

The volume electric current integral equation (VJIE), with support for superconductivity, was derived in Section 2.3. For convenience, it is once again

stated here:

$$\frac{\mathbf{J}(\mathbf{r})}{k(\mathbf{r})} + \frac{j\omega\mu}{4\pi}\int_{V'}\frac{\mathbf{J}(\mathbf{r})}{|\mathbf{r}-\mathbf{r}'|}\,dv' = -\nabla\phi(\mathbf{r}), \tag{3.2.1}$$

where $k(\mathbf{r})$ represents the conductivity of the normal and superconductivity channel,

$$k(\mathbf{r}) = \tilde{\sigma_0}(\mathbf{r}) + \frac{1}{j\omega\mu\lambda(\mathbf{r})^2}. \tag{3.2.2}$$

The following can be assumed for a large class of digital circuits [70]:

$$t_m \ll l \qquad \text{and} \qquad \lambda_m \sim t_m, \tag{3.2.3}$$

where t_m and λ_m are respectively the thickness and penetration depth of film m. The value l is the size of the circuit in the x, y-plane. If it is assumed that $J_z(r) = 0$, the volume current density, $\mathbf{J}(\mathbf{r})$, can be reduced to a sheet current density in the x, y-plane [68],

$$\mathbf{J^s_m}(\mathbf{r}) = \int_{h^0_m}^{h^1_m}\mathbf{J}(\mathbf{r})\,dz, \tag{3.2.4}$$

where h^0_m and h^1_m is respectively the bottom and top z-coordinates of layer m. Taking the average of the current density over the height of film layer m,

$$\mathbf{J^s_m}(\mathbf{r}) = t_m\mathbf{J}(\mathbf{r}), \tag{3.2.5}$$

the integral equation, (3.2.1), can be written in terms of sheet currents,

$$\frac{\mathbf{J^s_m}(\mathbf{r})}{t_m k(\mathbf{r})} + \frac{j\omega\mu}{t_m 4\pi}\int_{S'_m}\mathbf{J^s_m}(\mathbf{r}')G_0(\mathbf{r},\mathbf{r}')\,ds' = -\nabla\phi(\mathbf{r}), \tag{3.2.6}$$

where $\mathbf{J^s_m}(\mathbf{r})$ is the sheet current and t_m is the thickness of film layer m. In the case of thin film superconducting materials with thickness,

$$t_m \ll \lambda_m, \tag{3.2.7}$$

the product $t_m k(\mathbf{r})$ effectively replaces the penetration depth, λ, with the perpendicular penetration depth [68, 31]:

$$\lambda_\perp = \frac{\lambda_m^2}{t_m}. \tag{3.2.8}$$

For single-layer problems, the free-space Green's function $G_0(\mathbf{r},\mathbf{r}')$ can be used:

$$G_0(\mathbf{r},\mathbf{r}') = \frac{1}{|\mathbf{r}-\mathbf{r}'|}. \tag{3.2.9}$$

However, for multi-layered films with finite thickness, the current density above and below the films have to be taken into account [68]. Figure 3.2.1 demonstrates the top and bottom surfaces of layer m, with a normal vector pointing in the z-direction. The integration is done over the two projected triangles parallel to T_m^+, at heights $z = h_m^0$ and $z = h_m^1$. The Green's function for the interacting films m and n can be calculated as,

$$G_{m,n}(\mathbf{r},\mathbf{r}') = \frac{1}{4}\sum_{k=0}^{1}\sum_{l=0}^{1}\left\{\left\|\left(\mathbf{r}+\mathbf{n_m}\frac{t_m}{2}(-1)^k\right)-\left(\mathbf{r}'+\mathbf{n_n}\frac{t_n}{2}(-1)^l\right)\right\|\right\}^{-1}, \tag{3.2.10}$$

where $\mathbf{n_m}$ and $\mathbf{n_n}$ are the unit normal vectors of layers m and n, respectively. The Green's function in (3.2.10) is similar to the one used in [68] for finite thickness films.

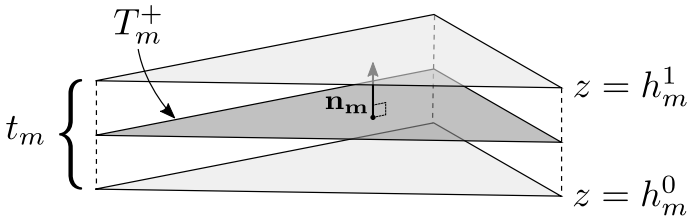

Figure 3.2.1: Triangle T_m^+ with projected triangles at heights h_m^0 and h_m^1.

3.2.1 Discretization

As discussed in Chapter 2, a system of linear equations can be obtained from the integral equation, (3.2.6), using the Method of Moments (MoM) [43]. The finite element method (FEM) is used to discretize the piecewise homogeneous superconducting films, using triangular elements instead of tetrahedral elements. Once again, it is assumed that the electrical parameters in each triangle are constant.

The integral equation in (3.2.6) is discretised using the RWG basis function, developed in [72]. Figure 3.2.1 shows the definition of the RWG basis function. The two triangles, T_n^+ and T_n^-, are associated with the nth edge of the discretize region. The position vectors, ρ_n^+ and ρ_n^-, represent points in T_n^+ and T_n^-, respectively. In triangle T_n^+, the positive position vector, ρ_n^+, is defined with respect to the free vertex and the negative position vector, T_n^-, towards the free vertex [72]. The signs of the two triangles depend on the direction of current flow through edge n.

To simplify the problem, the entire problem domain is assumed to be a homogeneous dielectric body, preventing surface charge accumulation at material interfaces. Although the RWG basis function is defined for infinitely thin

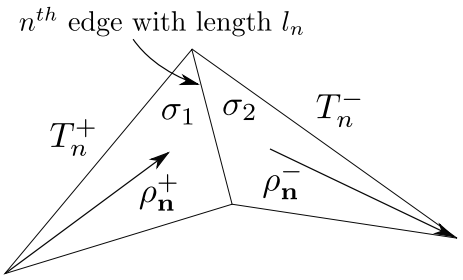

Figure 3.2.2: RWG basis function at material interface with different conductivities.

triangles, it is assumed to have finite thickness. The RWG function is defined as:

$$\mathbf{f_n}(\mathbf{r}) = \begin{cases} \frac{1}{2|a_n^+|}\rho_{\mathbf{n}}^+(\mathbf{r}), & \text{if } \mathbf{r} \in T_n^+ \\ \frac{1}{2|a_n^-|}\rho_{\mathbf{n}}^-(\mathbf{r}), & \text{if } \mathbf{r} \in T_n^- \\ 0, & \text{otherwise,} \end{cases} \tag{3.2.11}$$

where $|a_n^\pm|$ is the area of $T_n^\pm$. This function differs from the basis functions used in [72], which uses the length of the face to normalize $\mathbf{f_n}(\mathbf{r})$. Using the RWG function, the sheet current density, $\mathbf{J^s}(\mathbf{r})$, can be expanded as follows:

$$\mathbf{J^s}(\mathbf{r}) = \sum_{n=1}^{N} i_n \mathbf{f_n}(\mathbf{r}), \tag{3.2.12}$$

where N is the number of edges that make up the entire surface domain and i_n is the *branch* current through the nth edge. The sheet current density, within triangle q, can be calculated by summing the three linear independent basis functions, associated with each edge of the triangle [72],

$$\mathbf{J_q^s}(\mathbf{r}) = \sum_{n=1}^{3} i_n \mathbf{f_n}(\mathbf{r}),\ \mathbf{r} \in T_q. \tag{3.2.13}$$

The integral equation in (3.2.6) can be solved with the Method of Moments, as described in Chapter 2. Using the RWG function as weighting functions, $\mathbf{w_m}(\mathbf{r})$, a system of N linear equations can be obtained:

$$ZI_{branch} = V_{branch}. \tag{3.2.14}$$

The sheet impedance matrix Z can be decomposed into its real and imaginary parts:

$$Z = R + j\omega L. \tag{3.2.15}$$

where R and L are respectively the sheet resistance and inductance matrices. The entries of the sheet resistance matrix are computed as follow:

$$R_{m,n} = \int_{s_m} \frac{1}{t_m k_m} \mathbf{w_m}(\mathbf{r}) \cdot \mathbf{f_n}(\mathbf{r})\, ds, \tag{3.2.16}$$

and the entries of the sheet inductance matrix:

$$L_{m,n} = \frac{\mu}{4\pi} \int_{s_m} \int_{s_n} \frac{1}{t_m t_n} \mathbf{w_m}(\mathbf{r}) \cdot \mathbf{f_n}(\mathbf{r}') G_{m,n}(\mathbf{r}, \mathbf{r}') \, ds' ds, \tag{3.2.17}$$

where t_m and t_n are the thicknesses of surfaces s_m and s_n. The value k_m is calculated from (3.2.2),

$$k_m = k(\mathbf{r}), \; r \in s_m. \tag{3.2.18}$$

The values $R_{m,n}$ and $L_{m,n}$ correspond to the RWG basis functions m and n, respectively. The surfaces s_m and s_n represent the surfaces of the RWG-basis functions, which are a combination of $(T_m^+ + T_m^-)$ and $(T_n^+ + T_n^-)$, respectively. The voltage over each edge is stored in the vector, V_{branch}, and can be computed as follow:

$$(V_{branch})_m = -\int_{s_m} \mathbf{w_m}(\mathbf{r}) \cdot \nabla \phi(\mathbf{r}) \, ds \tag{3.2.19}$$

3.2.2 Surface loop basis function

Similar to the SWG basis function, discussed in Chapter 2, the divergence of the RWG basis function is also non-zero [72]. In order to ensure the divergence free condition, a surface loop (SL) basis function is used to discretize the integral equation in (3.2.6). This SL basis function is similar to the VL basis function, described in Section 2.3.3. Figures 3.2.3 and 3.2.4 illustrate how closed and unclosed SL basis functions are constructed around nodes (vertices).

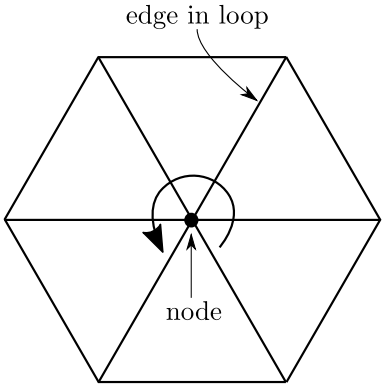

Figure 3.2.3: Closed surface loop basis function.

Following the same approach described in Section 2.3.3, the SL basis function can be defined as a combination of RWG functions around node m:

$$\mathbf{o_m}(\mathbf{r}) = \sum_{n=1}^{N} M_{m,n} \mathbf{f_n}(\mathbf{r}). \tag{3.2.20}$$

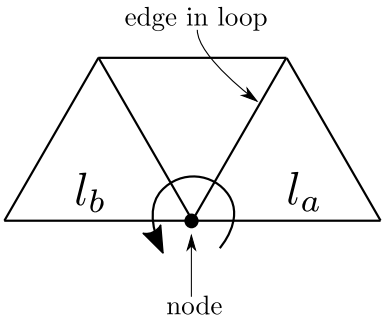

Figure 3.2.4: Unclosed surface loop basis function with two boundary edges of lengths l_a and l_b.

The value of $M_{m,n}$ is either 0 or ± 1, depending on the direction of the RWG function n in loop m. The value N is the total number of edges on the surface domain. Using the SL basis function, the sheet current can be expanded as follows:

$$\mathbf{J^s}(\mathbf{r}) = \sum_{m=1}^{M} i_m \mathbf{o_m}(\mathbf{r}) = \sum_{m=1}^{M} i_m \left\{ \sum_{n=1}^{N} M_{m,n} \mathbf{f_n}(\mathbf{r}) \right\}, \tag{3.2.21}$$

where i_m is defined as the *mesh* current circulating around node m. Once again, the MoM is used to obtain a matrix equation, see Section 2.3.3, using SL basis functions:

$$\left(MZM^T\right) I_{mesh} = V_{mesh}. \tag{3.2.22}$$

It can be shown that the values of V_{mesh} will become zero for closed SL basis functions and will be equal to the voltage difference across the ends of an unclosed SL basis function:

$$V_m = \begin{cases} 0, & \text{for closed loop } m \\ \phi(\xi)_{|\xi \in l_a} - \phi(\xi)_{|\xi \in l_b}, & \text{for unclosed loop } m \end{cases}. \tag{3.2.23}$$

The functions, $\phi(\xi)_{|\xi \in l_a}$ and $\phi(\xi)_{|\xi \in l_b}$, represent the constant voltage potential across the two edges at the ends of an unclosed SL basis function, with lengths l_a and l_b, respectively.

3.3 Numerical integration

The entries of the sheet resistance matrix, given in (3.2.16), can be computed using the same approach described in Section 2.4.1. Taking the origin of the coordinates at the centroid of triangle T_m^+ and using the integration formula for a triangle [57], the analytical solution for (3.2.16) becomes:

$$R_{m,n}^+ = \frac{1}{4t_m k_m |a_m^+||a_n^+|} \left\{ \frac{1}{12}(x_1^2 + x_2^2 + x_3^2) + x_m x_n \right\}, \tag{3.3.1}$$

where $x_1, ..., x_3$ are the 3 vertices (x-coordinates) of the triangle T_m^+. It is important to note that the origin of the coordinates ($x_1, ..., x_3, x_m$ and x_n) are at the centroid of T_m^+. Equation (3.3.1) is an exact solution and can be easily implemented in code.

The matrix-vector product, LI_{branch}, can be computed following the electrostatic approach, described in Section 2.4.2. Once again, it is assumed that $\mathbf{A}(\mathbf{r})$ varies slowly over T_m^+. Therefore, $(LI_{branch})_m$ can be approximated by taking the values at the centroids of the triangles:

$$(LI_{branch})_m \approx \sum_{p=1}^{3} \left\{ (\rho_{\mathbf{m}}^{\mathbf{c}\pm})_p \left[\sum_{n=1}^{N} \left(\frac{\mu}{16 t_m t_n \pi |a_m^\pm||a_n^\pm|} \cdot \int_{T_m^\pm} \int_{T_n^\pm} G_{m,n}(r, r')\, ds' ds \right) i_n (\rho_{\mathbf{n}}^{\mathbf{c}\pm})_p \right] \right\}, \tag{3.3.2}$$

where $\rho_{\mathbf{n}}^{\mathbf{c}\pm}$ is the vector between the centroid of triangle $T_m^\pm$ and the corresponding free vertex. The subscript p denotes the x, y, and z components of the vector. Equation (3.3.2) can be easily accelerated using the FMM, since it involves the evaluation of electrostatic potential at triangle m due to accumulative effect of n charges [20]. Using the FMM, the matrix-vector product, LI_{branch}, can be computed in m operations.

3.4 Results

3.4.1 Single-Layer Superconducting Films

The current densities of a single superconducting film, with a thickness of 500 nm and London penetration depth of 90 nm, are shown in Figure 3.4.1. An excitation voltage of 1 V was applied, as shown in Fig. 2.6.2, and the current densities were calculated using the triangular and tetrahedral methods.

Figure 3.4.1a shows the triangular mesh, with the average of the current density taken over the height of the structure. Since the thickness (height) of the layer is larger than the London penetration depth, the current density inside the superconductor is non-uniform. To account for non-uniform current density, the height of the tetrahedral mesh is subdivided into several layers, as can be seen in Fig. 3.4.1b and 3.4.1c. Subdividing the height into non-uniform layers will improve accuracy, as discussed in Section 2.6.1; however, the optimal thickness of these layers will depend on the London penetration depth and the number of layers used. Since the structures throughout this section have different London penetration depths; uniform layers are used to emphasize the effects the number of layers have on accuracy.

Figure 3.4.2a shows the extracted inductance of the 500 nm single film, using both the triangular and tetrahedral methods. The inductance of the tetrahedral method converge towards the inductance of the triangular method, as the number of layers in the tetrahedral mesh increase. This is due to the fact

that most of the current flows near the surface, if the dimensions of the superconductor is much larger than the penetration depth. Figure 3.4.2b shows the extracted inductance of the same film, but with a thickness of 150 nm. Since the 150 nm film is close to the penetration depth, the current density inside the superconductor is more uniform. Therefore, the 150 nm films requires fewer layers, compared to the 500 nm film. The number of layers can be reduce, if finer layers are used near the surface, as explained in Section 2.6.1. Using the Green's function in (3.2.10) for the triangular method, the current near the surface is taken into account. Therefore, the triangular method can deliver accurate results, even for superconducting films that are thicker than the penetration depth, while reducing the number of unknowns.

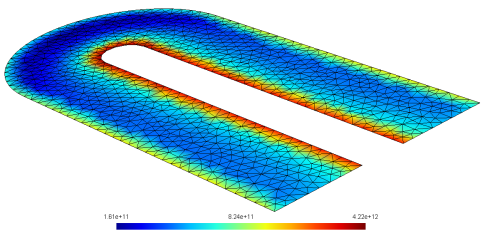

(a) 2D triangular method (average taken across height).

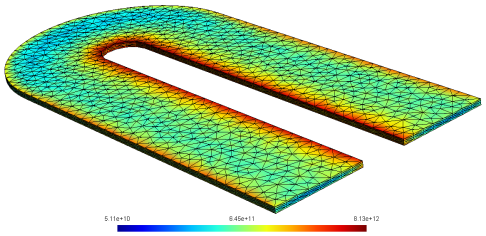

(b) 3D tetrahedral method (height subdivided int 4 layers).

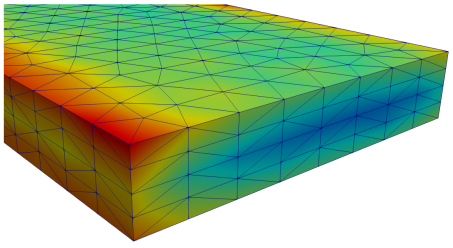

(c) Close-up of tetrahedral mesh with 4 uniform vertical subdivisions.

Figure 3.4.1: Current density (in log-scale) of a single-layer superconducting film. Each rectangular strips (30 μm $\times$ 8 μm, thickness = 500 nm, λ = 90 nm) are separated by 4 μm.

3.4.2 Multi-Layered Superconducting Films

Figure 3.4.3 shows the current distribution of a microstrip line above a ground layer, i.e. a multi-layered structure.[1] The current distribution, calculated with the triangular method, closely matches that of the tetrahedral method.

The extracted inductance of the microstrip line, using both the triangular and tetrahedral methods, is shown in Fig. 3.4.4. Once again, the inductance

[1]Note: segment size and height division is for illustration purposes only.

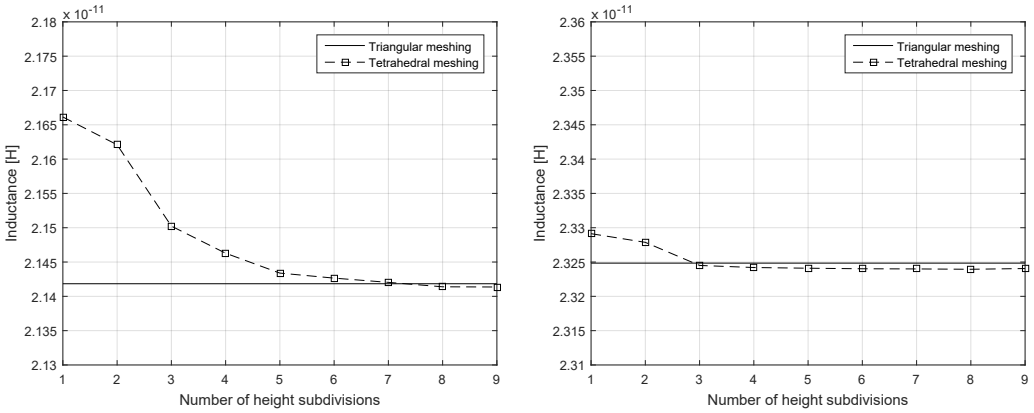

(a) $t_m = 500$ nm and $\lambda = 90$ nm. (b) $t_m = 150$ nm and $\lambda = 90$ nm.

Figure 3.4.2: Inductance of single-layer superconducting film as a function of the number of height subdivisions used for the tetrahedral mesh.

calculated with the tetrahedral method converge towards the inductance calculated with the triangular method.

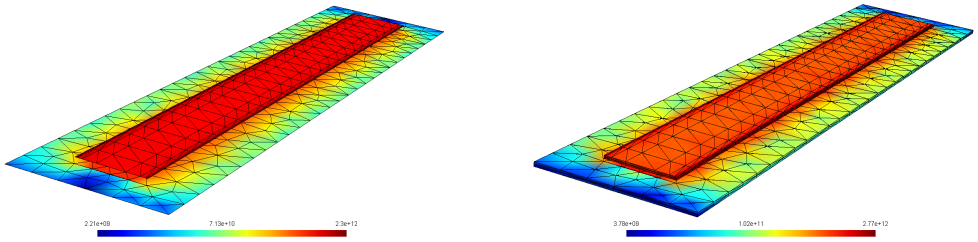

(a) 2D triangular method (average taken across height). (b) 3D tetrahedral method (height subdivided × 2).

Figure 3.4.3: Current density of a 50 μm × 5 μm microstrip line (thickness = 220 nm and penetration depth = 137 nm) 177.5 nm above ground layer (overhang = 6 μm, thickness = 300 nm, and penetration depth = 86 nm).

Figure 3.4.5 shows the number of mesh elements within the tetrahedral and triangular meshes of the microstrip line, as a function characteristic length (maximum distance between nodes). The height of the tetrahedral mesh was subdivided into two layers. It is evident that the triangular mesh contains significantly fewer elements, compared to the tetrahedral mesh. The number of unknowns (SL basis functions) of the triangular method is an order in magnitude less than the number of unknowns (VL basis functions) of tetrahedral method.

Table 3.4.1 shows the calculation time of the triangular and tetrahedral methods, for both the single- and multi-layered examples. The triangular

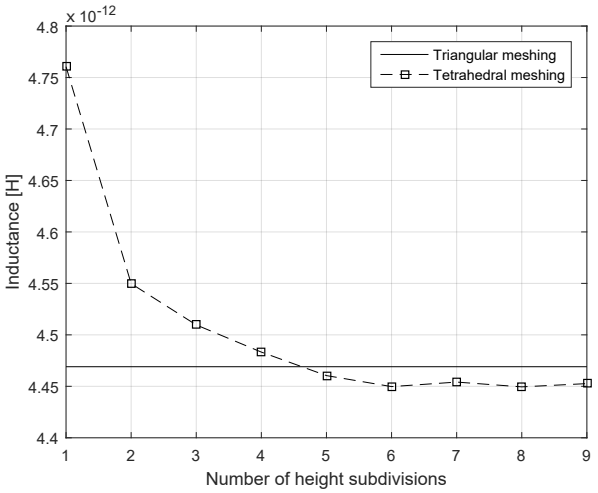

Figure 3.4.4: Extracted inductance of microstrip line as a function of the number of height subdivisions used for the tetrahedral mesh.

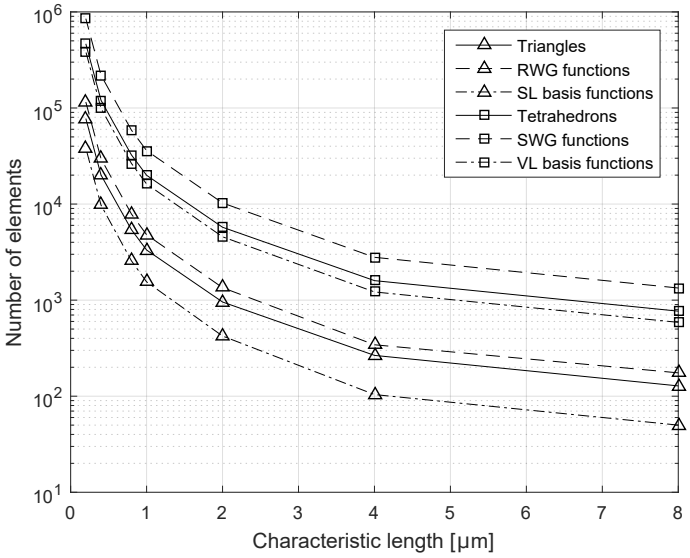

Figure 3.4.5: Number of elements and unknowns as a function of characteristic length (maximum distance between nodes).

method is at least 20 times faster compared to the tetrahedral method, when 4 or more layers are used for the tetrahedral mesh. The tetrahedral method (with a single height layer) requires at least twice the computation time, compared to the triangular method.

Table 3.4.1: Calculation time of triangular method compared to tetrahedral method with uniform subdivisions.

Example	Triangular	Tetra 1 layer	Tetra 2 layers	Tetra 3 layers	Tetra 4 layers	Tetra 5 layers
Single-layer	1.05 s	4.08 s	11.1 s	11.2 s	19.1 s	28.2 s
Multi-layer	2.05 s	5.08 s	14.1 s	15.1 s	24.4 s	39.1 s

3.5 Hybrid Meshes

Support for hybrid meshes, consisting of both triangles and tetrahedrons, have been implemented in TTH. Hybrid meshing can be used to improve calculations speeds by representing thin superconducting layers with triangles and complex inter-layer connections (vias) with tetrahedrons.

To use triangles and tetrahedrons simultaneously, both the volume loop (2.3.30) and surface loop (3.2.20) basis functions are implemented. Hybrid loop basis functions are used at the interface that connects triangles with tetrahedrons, as shown in Fig. 3.5.1. This hybrid loop basis function consists of both SWG and RWG functions depending on the type of element (triangle of tetrahedron) in the loop. The single integral equations, (2.3.25) and (3.2.16), remain the same; whereas the double integral equations, (2.3.26) and (3.2.17), are a combination of triangular and tetrahedral elements.

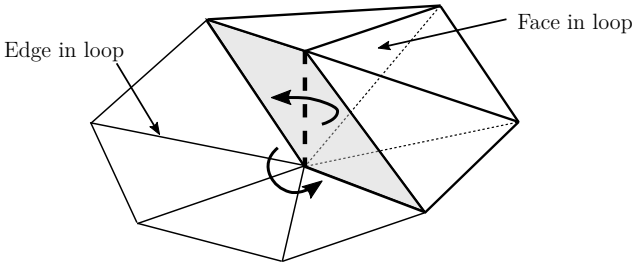

Figure 3.5.1: Hybrid loop basis function.

A example of a hybrid mesh is shown in Figure 3.5.2. The microstrip line is meshed using tetrahedrons, while the ground layer is meshed using triangles. The microstrip has the same dimensions as the one in Fig. 3.4.3. The extracted inductance is 4.466 pH; corresponding with the results in Fig. 3.4.4.

Figure 3.5.3 shows the current distribution of a microstrip line, connected to the ground layer though an inter-layer connection (via). The dimensions are the same as the microstrip in Fig. 3.4.3. Triangular meshing is used for both the microstrip line and the ground layer; whereas the via is meshed with tetrahedrons. The inductance, as a function of the number of height layers, is shown in Fig. 3.5.4. Two types of hybrid loop function are evaluated: the sheet current of each triangle enters a single face in the tetrahedral mesh

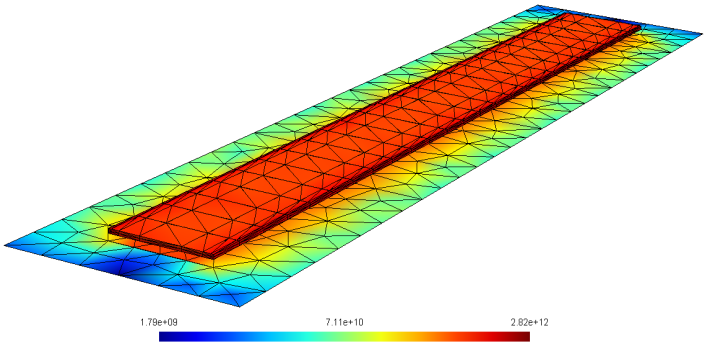

Figure 3.5.2: Microstrip line (tetrahedrons) above a groundplane (triangles). The height of the microstrip line is divided into 5 even layers

or multiple faces in the tetrahedral mesh. If each surface is connected to a single tetrahedral face, the inductance of the hybrid mesh is higher (1.6% error), compared to the tetrahedral method. This is expected, since the area through which the current can flow is reduced. If each surface is connected to multiple tetrahedral faces, the area of the interface is increased and the extracted inductance matches the tetrahedral method with less than 0.5% error, as can be seen in Fig. 3.5.4.

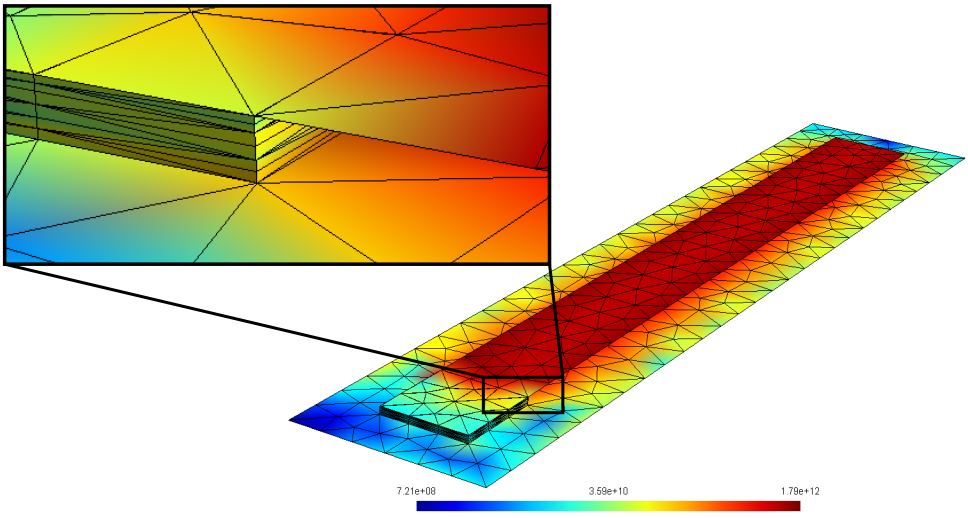

Figure 3.5.3: Current density of a 50 μm $\times$ 5 μm microstrip line (triangular meshing) with a via (tetrahedral meshing).

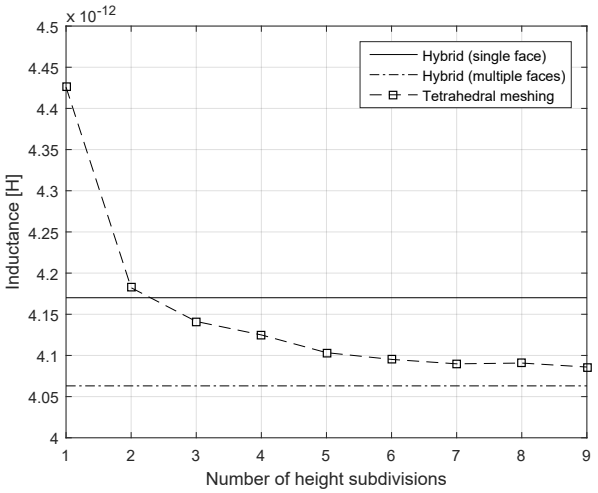

Figure 3.5.4: Extracted inductance values for the microstrip line with via.

3.6 Conclusion

Support for two-dimensional triangular meshes was implemented in TetraHenry (TTH). Surface loop basis functions, consisting of RWG functions, are used to model sheet currents in thin superconducting films. The triangular method delivers accurate results for both single- and multi-layered superconducting films, that are on the same order as the London penetration depth. Furthermore, it was shown that the triangular method can deliver accurate results for superconducting films that are thicker than the penetration depth, using a special Green's function. Triangular meshes (for thin superconducting films) and tetrahedral meshes (for complex inter-layer connections) can be simulated simultaneously, using hybrid loop basis functions.

The number of unknowns are significantly reduced and computational speed gains of one order of magnitude are obtained, by replacing tetrahedral meshes with triangular meshes. The triangular method, in combination with hybrid basis functions, provides the capability to analyze large-scale SFQ circuits.

Chapter 4

Inhomogeneous Dielectric and Magnetic Materials

4.1 Introduction

This Chapter discusses the modification made to TetraHenry (TTH) to support electric and magnetic currents inside inhomogeneous dielectric and magnetic materials, respectively. The derivation of the integral equations for both dielectric and magnetic materials are almost identical and, therefore, both topics are discussed in this chapter. However, the frequency-depended impedance extraction and the simulation of magnetic materials are regarded as two separate topics.

4.1.1 Impedance Extraction

As the frequencies at which VLSI superconducting circuits operate increase, accurate interconnected models become essential for accurate chip design. Although a lot of work has been directed towards solving inductance and capacitance separately, these two quantities are not necessarily decoupled. At high frequencies the coupled effects can create resonant peaks in the frequency response, reducing inductance significantly [3, 24, 73].

Techniques have been developed to generate guaranteed passive reduced order models that can be used in a circuit simulator, such as SPICE [74]. Simple transmission line circuit models, such as the Γ, π and T models, shown in Fig. 4.1.1, are accurate at low frequencies, but break down for higher frequencies [3].

Figure 4.1.2 shows the frequency response of a 2-pin structure calculated in [3]. It was shown that if the inductance and resistance are computed at low frequencies, f_{C1}, the circuit models will be accurate below some frequency, $f_{H1} \gg f_{C1}$. As the frequency increases, current will move to the surface of the conductor, increasing the resistance and resulting in the breakdown of the circuit model. If the inductance and resistance are computed at a relatively

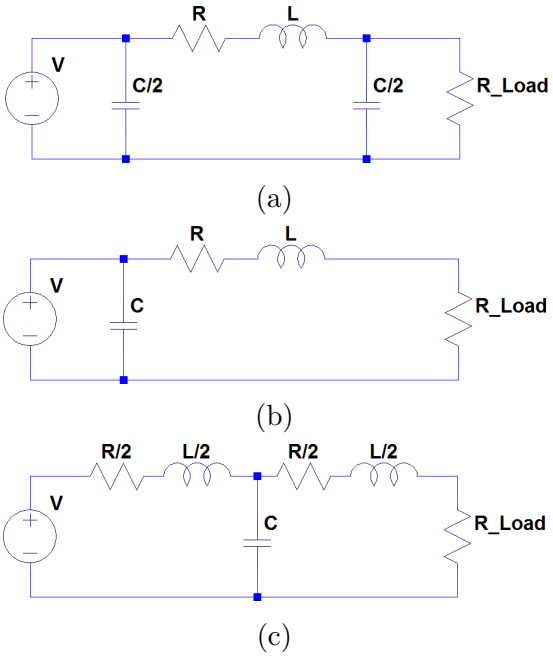

Figure 4.1.1: Simple transmission line circuit models. (a) π circuit model. (b) Γ circuit model. (c) T circuit model.

high frequency, f_{E2}, the models will be accurate above some frequency, $f_{L2} > f_{H1}$, but still below the extracted frequency, $f_{H2} \ll f_{E2}$ [3]. Therefore, the frequency that is used to extract inductance and resistance, will produce a circuit model that is only valid for a certain range of frequencies.

It was shown in [3], that the π model works best for capturing the first resonant peak of a 2-pin structure. However, all three circuit models can capture at most only one resonant and become inaccurate above the first resonant frequency [3]. Another disadvantage is the difficulty of designing simple models for complex 3D structures. Therefore, it is necessary to capture the coupled inductance and capacitance simultaneously, when extracting the impedance at frequencies above the first resonance, as shown in Fig. 4.1.2.

Existing numerical engines, such as FastHenry, have been modified to account for charge accumulating on the surface of conductors [3, 24, 73]. It was shown in [24], that electro-magneto-quasi-static (EMQS) analysis and the partial element equivalent circuit (PEEC) method [75] can be used for capturing distributed capacitance and inductance. The two methods discussed in [3] and [24], both use cuboid filaments to model current density; which is effective for long and uniform structures, such as microstrip lines. However, non-uniform structures, such as vias through ground planes, Josephson Junctions and chip-to-board wires, are difficult to model using cuboid filaments.

To account for these parasitic effects in superconducting integrated circuits, the numerical engine, TetraHenry (TTH), was modified to include EMQS impedance extraction; provided that the interconnected structures are smaller

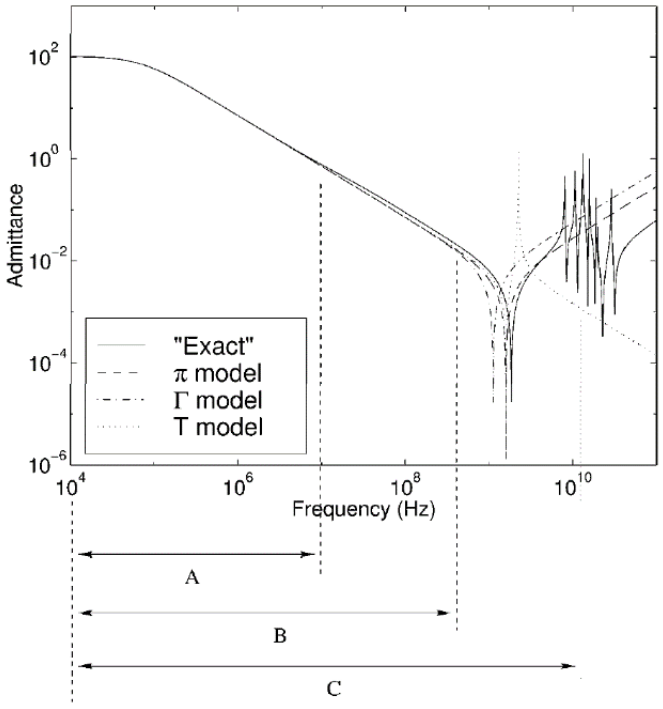

Figure 4.1.2: The different regimes for transmission line models [3]. (A) Single lumped inductance, (B) Frequency dependent inductance, (C) Coupled inductance and capacitance.

than the wavelength. The derivation of the integral equations, under EMQS approximation, are discussed in detail in this chapter. Charge accumulation (displacement current), at material interfaces of inhomogeneous dielectrics, are modelled using Half-SWG basis functions [36]. Support for Full-Wave analysis is added, using the ExaFMM library [76, 6]. Results, obtained with EMQS and Full-Wave analysis, are compared to the software package, FastImp [25].

4.1.2 Magnetic Materials

Superconducting-ferromagnetic (SFT) elements play a crucial role in the development of memory devices [77, 78, 79] for superconducting integrated circuits. These magnetic materials pose a challenge to accurate inductance and current distribution calculations. Several methods have already been developed [80, 81, 82, 83] for extracting inductance of non-superconducting structures, in the presence of magnetic materials. Although some of these methods have been demonstrated to be fast and effective, access to their implementations, i.e source code, is not readily available. Therefore, it was decided to develop support for permeable materials in TTH, from first principles, using methods that are applicable to the existing VJIE formulation, discussed in Chapter 2.

This chapter presents the modifications made to the numerical solver,

TTH, to analyze the effects of magnetic materials on superconducting and non-superconducting metals. Magnetic characteristics are taken into account by introducing displacement current, fictitious magnetic current density, and magnetic charge density to the VJIE formulation, discussed in Chapter 2. Computing the interaction between magnetic and non-magnetic volumes is accelerated using BiotFMM, a Fast Multipole Method (FMM) for the Biot-Savart law. The implementation of BiotFMM is discussed in Chapter 6. The accuracy and efficiency of the solver are evaluated, by comparing it to existing experimental and numerical results for non-superconducting structures.

4.2 Obtaining Volume Integral Equations

4.2.1 Maxwell's equations

Starting with the time-harmonic Maxwell's equations in phasor format:

$$\nabla \times \mathbf{E} = -j\omega\hat{\mu}\mathbf{H} - \mathbf{M_{inc}}, \tag{4.2.1}$$
$$\nabla \times \mathbf{H} = j\omega\hat{\epsilon}\mathbf{E} + \mathbf{J_{inc}}, \tag{4.2.2}$$
$$\nabla \cdot (\hat{\epsilon}\mathbf{E}) = \rho_e, \tag{4.2.3}$$
$$\nabla \cdot (\hat{\mu}\mathbf{H}) = \rho_m, \tag{4.2.4}$$

where $\hat{\mu}$ and $\hat{\epsilon}$ are respectively the complex permeability and permittivity of the dielectric and magnetic material, which are functions of space for inhomogeneous objects. The complex dielectric constant is defined as:

$$\hat{\epsilon}(\mathbf{r}) = \epsilon(\mathbf{r}) - j\sigma(\mathbf{r})/\omega, \tag{4.2.5}$$

where $\epsilon(\mathbf{r})$ and $\sigma(\mathbf{r})$ are respectively the permittivity and conductivity at position $\mathbf{r}$. For superconducting metals, the conductivity of the normal and superconducting channels must be taken into account, as stated in Section 2.3.1. Substituting $\sigma(\mathbf{r})$ with the conductivity defined in (2.3.15), the complex dielectric constant can be redefined as:

$$\hat{\epsilon}(\mathbf{r}) = \epsilon(\mathbf{r}) - \frac{j\tilde{\sigma_0}(\mathbf{r})}{\omega} - \frac{1}{\omega^2\mu_0\lambda^2(\mathbf{r})}, \tag{4.2.6}$$

where $\tilde{\sigma_0}(\mathbf{r})$ is the temperature depended conductivity of the normal channel and $\lambda(\mathbf{r})$ is the temperature depended London penetration depth of the superconductor [26].

Excitation is provided by the impressed electric and magnetic current sources, $\mathbf{J_{inc}}$ and $\mathbf{M_{inc}}$. The total electric and magnetic fields, $\mathbf{E}$ and $\mathbf{H}$, can be decomposed into scattered and incident fields,

$$\mathbf{E} = \mathbf{E_{inc}} + \mathbf{E_{scat}}, \tag{4.2.7}$$
$$\mathbf{H} = \mathbf{H_{inc}} + \mathbf{H_{scat}}. \tag{4.2.8}$$

The incident electric field, $\mathbf{E_{inc}}$, is due to the impressed electric current sources $\mathbf{J_{inc}}$; whereas the incident magnetic field, $\mathbf{H_{inc}}$, is due to the impressed magnetic current sources $\mathbf{M_{inc}}$.

4.2.2 Volume Equivalent Principle

The volume equivalent principle [84] is used to transform the original field problem into an equivalent problem, using field-dependent current sources. This method has proven to be effective when simulating the scattering of EM waves by dielectric and magnetic materials [85, 48]. First, (4.2.1) and (4.2.2) are rewriting as follow:

$$\nabla \times \mathbf{E} = -j\omega\mu_0\mathbf{H} - \mathbf{M_{inc}} - j\omega(\hat{\mu} - \mu_0)\mathbf{H}, \tag{4.2.9}$$
$$\nabla \times \mathbf{H} = j\omega\epsilon_0\mathbf{E} + \mathbf{J_{inc}} + j\omega(\hat{\epsilon} - \epsilon_0)\mathbf{E}. \tag{4.2.10}$$

Using the volume equivalent principle [84], (4.2.9) and (4.2.10) can be written in terms of equivalent current sources:

$$\nabla \times \mathbf{E} = -j\omega\mu_0\mathbf{H} - \mathbf{M_{inc}} - \mathbf{M}, \tag{4.2.11}$$
$$\nabla \times \mathbf{H} = j\omega\epsilon_0\mathbf{E} + \mathbf{J_{inc}} + \mathbf{J}, \tag{4.2.12}$$

with the equivalent sources defined as:

$$\mathbf{J} = j\omega(\hat{\epsilon} - \epsilon_0)\mathbf{E}, \tag{4.2.13}$$
$$\mathbf{M} = j\omega(\hat{\mu} - \mu_0)\mathbf{H}. \tag{4.2.14}$$

Equations (4.2.11) and (4.2.12) represent an equivalent problem, where $\mathbf{J}$ and $\mathbf{M}$ radiate in free space to generate the same scattered fields as in (4.2.1) and (4.2.2) [85]. Substituting (4.2.13) and (4.2.14) in (4.2.7) and (4.2.8), the following expressions are obtained [85],

$$\frac{\mathbf{J}(\mathbf{r})}{j\omega\kappa_e(\mathbf{r})\hat{\epsilon}(\mathbf{r})} = \mathbf{E_{inc}}(\mathbf{r}) + \mathbf{E_{scat}}(\mathbf{r}), \tag{4.2.15}$$
$$\frac{\mathbf{M}(\mathbf{r})}{j\omega\kappa_m(\mathbf{r})\hat{\mu}(\mathbf{r})} = \mathbf{H_{inc}}(\mathbf{r}) + \mathbf{H_{scat}}(\mathbf{r}). \tag{4.2.16}$$

where $\mathbf{r}$ is inside the electric and magnetic volumes, respectively. In (4.2.15) and (4.2.16), the material parameters for the electric and magnetic volumes are taken as:

$$\kappa_e(\mathbf{r}) = [\hat{\epsilon}(\mathbf{r}) - \epsilon_0]/\hat{\epsilon}(\mathbf{r}), \tag{4.2.17}$$
$$\kappa_m(\mathbf{r}) = [\hat{\mu}(\mathbf{r}) - \mu_0]/\hat{\mu}(\mathbf{r}). \tag{4.2.18}$$

4.2.3 Volume Integral Equations

By decomposing the electric and magnetic fields into fields due to electric and magnetic sources, it can be shown that the scattered fields can be calculated as [50, 86]:

$$\mathbf{E_{scat}}(\mathbf{r}) = -j\omega\mathbf{A}(\mathbf{r}) - \nabla\phi_e(\mathbf{r}) - \frac{1}{\epsilon_0}\nabla \times \mathbf{F}(\mathbf{r}), \tag{4.2.19}$$

$$\mathbf{H_{scat}}(\mathbf{r}) = -j\omega\mathbf{F}(\mathbf{r}) - \nabla\phi_m(\mathbf{r}) + \frac{1}{\mu_0}\nabla \times \mathbf{A}(\mathbf{r}), \tag{4.2.20}$$

where $\mathbf{A}(\mathbf{r})$ and $\mathbf{F}(\mathbf{r})$ are the magnetic and electric vector potentials, respectively. Substituting (4.2.15) and (4.2.16) in (4.2.19) and (4.2.20) and assuming zero incident fields, the following two volume integral equations (VIE) are obtained:

$$\frac{\mathbf{J}(\mathbf{r})}{j\omega\kappa_e(\mathbf{r})\hat{\epsilon}(\mathbf{r})} + j\omega\mathbf{A}(\mathbf{r}) + \frac{1}{\epsilon_0}\nabla \times \mathbf{F}(\mathbf{r}) = -\nabla\phi_e(\mathbf{r}), \tag{4.2.21}$$

$$\frac{\mathbf{M}(\mathbf{r})}{j\omega\kappa_m(\mathbf{r})\hat{\mu}(\mathbf{r})} + j\omega\mathbf{F}(\mathbf{r}) - \frac{1}{\mu_0}\nabla \times \mathbf{A}(\mathbf{r}) = -\nabla\phi_m(\mathbf{r}). \tag{4.2.22}$$

The electric scalar potential, ϕ_e, and the magnetic scalar potential, ϕ_m, can be obtained from the Lorenz gauge conditions,

$$\nabla \cdot \mathbf{A}(\mathbf{r}) = -j\omega\mu_0\epsilon_0\phi_e(\mathbf{r}), \tag{4.2.23}$$

$$\nabla \cdot \mathbf{F}(\mathbf{r}) = -j\omega\mu_0\epsilon_0\phi_m(\mathbf{r}). \tag{4.2.24}$$

Using (4.2.23) and (4.2.24), it can be show that the following set of Helmholtz equations for the potentials can be derived [50, 87]:

$$\nabla^2\phi_e(\mathbf{r}) + k_0^2\phi_e(\mathbf{r}) = -\frac{1}{\epsilon_0}\rho_e(\mathbf{r}), \tag{4.2.25}$$

$$\nabla^2\phi_m(\mathbf{r}) + k_0^2\phi_m(\mathbf{r}) = -\frac{1}{\mu_0}\rho_m(\mathbf{r}), \tag{4.2.26}$$

$$\nabla^2\mathbf{A}(\mathbf{r}) + k_0^2\mathbf{A}(\mathbf{r}) = -\mu_0\mathbf{J}(\mathbf{r}), \tag{4.2.27}$$

$$\nabla^2\mathbf{F}(\mathbf{r}) + k_0^2\mathbf{F}(\mathbf{r}) = -\epsilon_0\mathbf{M}(\mathbf{r}), \tag{4.2.28}$$

where $k_0^2 = \omega^2\mu_0\epsilon_0$. The scalar potential in (4.2.25)-(4.2.26), due to arbitrary electric charge distributions, $\rho_e(\mathbf{r})$, and magnetic charge distributions, $\rho_m(\mathbf{r})$, can be solved as follow:

$$\phi_e(\mathbf{r}) = \frac{1}{\epsilon_0}\int_{S_e} \rho_e(\mathbf{r})G_0(\mathbf{r},\mathbf{r}')\,dS', \tag{4.2.29}$$

$$\phi_m(\mathbf{r}) = \frac{1}{\mu_0}\int_{S_m} \rho_m(\mathbf{r})G_0(\mathbf{r},\mathbf{r}')\,dS'. \tag{4.2.30}$$

The vector potentials in (4.2.27)-(4.2.28), for arbitrary electric and magnetic currents, can be calculated as:

$$\mathbf{A}(\mathbf{r}) = \mu_0 \int_{V_e} \mathbf{J}(\mathbf{r}) G_0(\mathbf{r}, \mathbf{r}')\, dV', \tag{4.2.31}$$

$$\mathbf{F}(\mathbf{r}) = \epsilon_0 \int_{V_m} \mathbf{M}(\mathbf{r}) G_0(\mathbf{r}, \mathbf{r}')\, dV', \tag{4.2.32}$$

where $G_0(\mathbf{r}, \mathbf{r}')$ is the free-space Green's function, which can be defined for Full-Wave analysis as,

$$G_0(\mathbf{r}, \mathbf{r}') = \frac{e^{j\omega k_0 |r - r'|}}{|\mathbf{r} - \mathbf{r}'|}, \tag{4.2.33}$$

or for electro-magneto-quasi-static (EMQS) analysis, discussed in Section 4.5.1,

$$G_0(\mathbf{r}, \mathbf{r}') = \frac{1}{|\mathbf{r} - \mathbf{r}'|}. \tag{4.2.34}$$

4.3 VJIE and the Half-SWG Function

The two VIE's in (4.2.21) and (4.2.22) is similar to the volume electric current integral equation (VJIE), given in [36]. Discretizing these two VIE's with Full-SWG basis functions [36], requires normal continuity between neighboring tetrahedrons, see Section 2.3.2. However, for inhomogeneous dielectric and magnetic materials, the equivalent electric and magnetic currents, $\mathbf{J}(\mathbf{r})$ and $\mathbf{M}(\mathbf{r})$, are not continuous across material interfaces. It was suggested in [36] to use Full-SWG functions to expand $\mathbf{J}(\mathbf{r})$ in homogeneous regions and Half-SWG basis functions at material interfaces, as shown in Fig. 4.3.1.

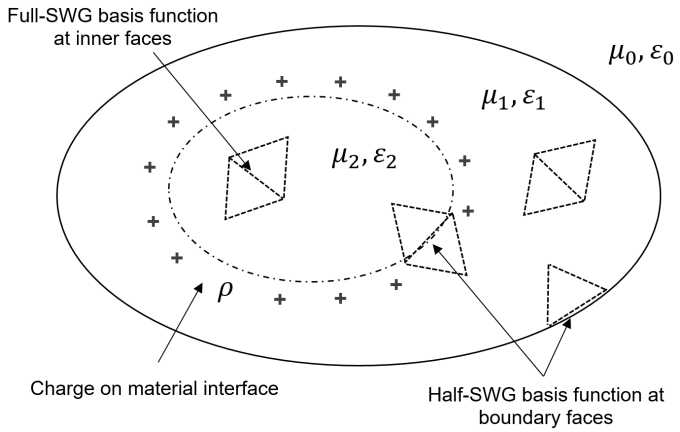

Figure 4.3.1: Piecewise homogeneous object with Full-SWG functions inside homogeneous regions and Half-SWG basis functions at material interfaces.

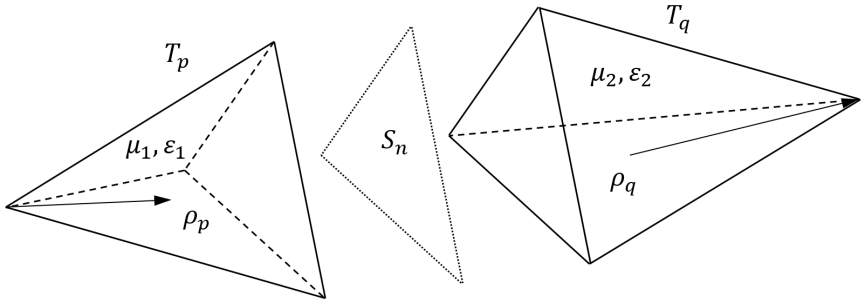

Figure 4.3.2: Definition of the Half-SWG basis functions.

Full-SWG function are defined for each "*inner*" face (within homogeneous regions) and Half-SWG basis functions are defined for each "*boundary*" face (on the material interfaces) [36]. Fig. 4.3.2 shows a *boundary* face, S_n, separating two tetrahedron, T_p and T_q, at a material interface. The Half-SWG basis function for the *boundary* face, S_n, can be defined as follow [36],

$$\mathbf{f_p}(\mathbf{r}) \begin{cases} \frac{1}{3|v_p|}\rho_{\mathbf{p}}(\mathbf{r}), & \text{if } \mathbf{r} \in T_p \\ 0, & \text{if } \mathbf{r} \notin T_q \end{cases}, \tag{4.3.1}$$

$$\mathbf{f_q}(\mathbf{r}) \begin{cases} 0, & \text{if } \mathbf{r} \in T_p \\ \frac{1}{3|v_q|}\rho_{\mathbf{q}}(\mathbf{r}), & \text{if } \mathbf{r} \notin T_q \end{cases}, \tag{4.3.2}$$

where $|v_p|$ and $|v_q|$ are the volumes of T_p and T_q, respectively. Full-SWG functions, within homogeneous regions, prevents charge accumulation on *inner* faces. Half-SWG functions allows for charge accumulation, due to the material discontinuity, on *boundary* faces. Using (4.3.1) and (4.3.2), the electric and magnetic current density inside the two tetrahedrons, T_p and T_q, can be expanded as follow,

$$\mathbf{J_p}(\mathbf{r}) = \sum_{k=1}^{4} J_{p_k} \mathbf{f_{p_k}}(\mathbf{r}), \tag{4.3.3}$$

$$\mathbf{J_q}(\mathbf{r}) = \sum_{k=1}^{4} J_{q_k} \mathbf{f_{q_k}}(\mathbf{r}), \tag{4.3.4}$$

$$\mathbf{M_p}(\mathbf{r}) = \sum_{k=1}^{4} M_{p_k} \mathbf{f_{p_k}}(\mathbf{r}), \tag{4.3.5}$$

$$\mathbf{M_q}(\mathbf{r}) = \sum_{k=1}^{4} M_{q_k} \mathbf{f_{q_k}}(\mathbf{r}), \tag{4.3.6}$$

where J_{p_k}, J_{q_k}, M_{p_k} and M_{q_k} are respectively the electric and magnetic currents across the 4 faces of tetrahedrons T_p and T_q. The electric surface charge density

on the *boundary* face, S_n, can now be calculated as:

$$\begin{aligned}\rho_{e_s}(\mathbf{r}) &= (j/\omega)\mathbf{n}\cdot[\mathbf{J_q}(\mathbf{r}) - \mathbf{J_p}(\mathbf{r})] \\ &= (j/\omega)\mathbf{n}\cdot\left[\sum_{k=1}^{4} J_{p_k}\mathbf{f_{p_k}}(\mathbf{r}) - \sum_{k=1}^{4} J_{q_k}\mathbf{f_{q_k}}(\mathbf{r})\right] \qquad \mathbf{r}\in S_n, \\ &= (j/\omega)\mathbf{n}\cdot[J_{p_1}\mathbf{f_{p_1}}(\mathbf{r}) - J_{q_1}\mathbf{f_{q_1}}(\mathbf{r})] \\ &= (j/\omega)\left(J_{p_1} - J_{q_1}\right),\end{aligned} \tag{4.3.7}$$

where J_{p_1} and J_{q_1} are the electric currents flowing across face S_n and $\mathbf{n}$ is a unit vector normal to S_n [36]. The same holds for the magnetic surface charge density,

$$\begin{aligned}\rho_{m_s}(\mathbf{r}) &= (j/\omega)\mathbf{n}\cdot[\mathbf{M_q}(\mathbf{r}) - \mathbf{M_p}(\mathbf{r})] \\ &= (j/\omega)\left(M_{p_1} - M_{q_1}\right),\end{aligned} \qquad \mathbf{r}\in S_n, \tag{4.3.8}$$

where M_{p_1} and M_{q_1} are the magnetic currents flowing across face S_n. The electric and magnetic charge densities can now be discretized using uniform basis functions:

$$\rho_e(\mathbf{r}) = \sum_{i=1}^{N_e^s} q_{e_i}, \tag{4.3.9}$$

$$\rho_m(\mathbf{r}) = \sum_{i=1}^{N_m^s} q_{m_i}, \tag{4.3.10}$$

where q_{e_i} and q_{e_i} are the uniform charges on *boundary* face i,

$$q_{e_i} = (j/\omega)\left(J_{p_i} - J_{q_i}\right), \tag{4.3.11}$$

$$q_{m_i} = (j/\omega)\left(M_{p_i} - M_{q_i}\right). \tag{4.3.12}$$

The constants, N_e^s and N_m^s, are the number of *boundary* faces on the electric and magnetic material interfaces, respectively.

4.3.1 Potential Fields

Using the Full- and Half-SWG functions, the electric and magnetic vector potentials in (4.2.31)-(4.2.32) can be expanded as follow,

$$\mathbf{A}(\mathbf{r}) = \mu_0 \int_{V_e} \sum_{n=1}^{N_e^v} J_n \mathbf{f_n}(\mathbf{r}) G_0(\mathbf{r},\mathbf{r}')\, dV', \tag{4.3.13}$$

$$\mathbf{F}(\mathbf{r}) = \epsilon_0 \int_{V_m} \sum_{n=1}^{N_m^v} M_n \mathbf{f_n}(\mathbf{r}) G_0(\mathbf{r},\mathbf{r}')\, dV'. \tag{4.3.14}$$

where N_e^v and N_m^v are the number of faces in the electric and magnetic volumes, respectively. The vector function, $\mathbf{f_n}(\mathbf{r})$, is either the Full-SWG function in

(2.3.17) or the Half-SWG function in (4.3.1)-(4.3.2). The electric and magnetic scalar potentials are a result of equivalent volume and surface charges [36],

$$\phi_e(\mathbf{r}) = \phi_e^v(\mathbf{r}) + \phi_e^s(\mathbf{r}), \tag{4.3.15}$$

$$\phi_m(\mathbf{r}) = \phi_m^v(\mathbf{r}) + \phi_m^s(\mathbf{r}). \tag{4.3.16}$$

The interior of each tetrahedron is considered homogenous with zero equivalent volume charge, i.e. $\phi^v(\mathbf{r}) = 0$. Therefore, the electric and magnetic scalar potentials in (4.2.29)-(4.2.30) can be expanded using only the equivalent surface charges defined in (4.3.7)-(4.3.8),

$$\begin{aligned}\phi_e(\mathbf{r}) &= \phi_e^s(\mathbf{r}) \\ &= \frac{1}{\epsilon_0}\int_{S_e} \rho_e(\mathbf{r}) G_0(\mathbf{r},\mathbf{r}')\, dS' \\ &= \frac{1}{\epsilon_0}\sum_{i=1}^{N_e^s} q_{e_i} \int_{S_{e_i}} G_0(\mathbf{r},\mathbf{r}')\, dS',\end{aligned} \tag{4.3.17}$$

and

$$\begin{aligned}\phi_m(\mathbf{r}) &= \phi_m^s(\mathbf{r}) \\ &= \frac{1}{\mu_0}\int_{S_m} \rho_m(\mathbf{r}) G_0(\mathbf{r},\mathbf{r}')\, dS' \\ &= \frac{1}{\mu_0}\sum_{i=1}^{N_m^s} q_{m_i} \int_{S_{m_i}} G_0(\mathbf{r},\mathbf{r}')\, dS'.\end{aligned} \tag{4.3.18}$$

The calculation of the vector potentials, (4.3.13)-(4.3.14), and the scalar potentials, (4.3.17)-(4.3.18), is accelerated using the FMM described in Section 2.4.2.

4.3.2 Obtaining Linear Set of Equations

Expanding the two VIE in (4.2.21) and (4.2.22) with Full- and Half-SWG weighting functions, $\mathbf{w_i}(\mathbf{r})$, and following the Method of Moments (MoM), a set of linear equations can be obtained,

$$\begin{bmatrix} R_e + j\omega L_e & F_e \\ F_m & R_m + j\omega L_m \end{bmatrix} \begin{bmatrix} J_i \\ M_i \end{bmatrix} = \begin{bmatrix} V_e \\ V_m \end{bmatrix} \tag{4.3.19}$$

and

$$\begin{bmatrix} P_e & 0 \\ 0 & P_m \end{bmatrix} \begin{bmatrix} q_e \\ q_m \end{bmatrix} = \begin{bmatrix} \phi_e \\ \phi_m \end{bmatrix}. \tag{4.3.20}$$

The matrices R_e and L_e represent the resistive and inductive properties of electric volumes (carrying electric current) and can be computed as follow:

$$(R_e)_{i,j} = \frac{1}{j\omega\kappa_{e_i}\hat{\epsilon}_i}\int_{v_{e_i}} \mathbf{w_i}(\mathbf{r}) \cdot \mathbf{f_j}(\mathbf{r})\, dv, \tag{4.3.21}$$

$$(L_e)_{i,j} = \mu_0 \int_{v_{e_i}}\int_{v_{e_j}} [\mathbf{w_i}(\mathbf{r}) \cdot \mathbf{f_j}(\mathbf{r}')]\, G_0(\mathbf{r},\mathbf{r}')\, dv' dv. \tag{4.3.22}$$

The matrices R_m and L_m represent the resistive and inductive properties of magnetic volumes (carrying magnetic current) and can be computed as follow:

$$(R_m)_{i,j} = \frac{1}{j\omega\kappa_{m_i}\hat{\mu}_i}\int_{v_{m_i}} \mathbf{w_i}(\mathbf{r})\cdot\mathbf{f_j}(\mathbf{r})\,dv, \tag{4.3.23}$$

$$(L_m)_{i,j} = \epsilon_0\int_{v_{m_i}}\int_{v_{m_j}} [\mathbf{w_i}(\mathbf{r})\cdot\mathbf{f_j}(\mathbf{r}')]\,G_0(\mathbf{r},\mathbf{r}')\,dv'dv. \tag{4.3.24}$$

The effect of magnetic currents on electric volumes, i.e. $\nabla\times\mathbf{F}(\mathbf{r})$ in (4.2.21), are computed using the Biot-Savart law:

$$(F_e)_{i,j} = \frac{1}{4\pi}\int_{v_{e_i}}\int_{v_{m_j}} \frac{[\mathbf{w_i}(\mathbf{r})\cdot\mathbf{f_j}(\mathbf{r}')]\times(\mathbf{r}-\mathbf{r}')}{|\mathbf{r}-\mathbf{r}'|^3}\,dv'dv. \tag{4.3.25}$$

and the effect of electric currents on magnetic volumes, i.e. $\nabla\times\mathbf{A}(\mathbf{r})$ in (4.2.22),

$$(F_m)_{i,j} = \frac{1}{4\pi}\int_{v_{m_i}}\int_{v_{e_j}} \frac{[\mathbf{w_i}(\mathbf{r})\cdot\mathbf{f_j}(\mathbf{r}')]\times(\mathbf{r}-\mathbf{r}')}{|\mathbf{r}-\mathbf{r}'|^3}\,dv'dv. \tag{4.3.26}$$

The scalar potentials in (4.3.20) are approximated using the Galerkin approach, by enforcing an average potential over each surface panel (*boundary* face). Thus, the entries on the potential coefficient matrices can be calculated as:

$$(P_e)_{i,j} = \frac{1}{a_i a_j\epsilon_0}\int_{s_{e_i}}\int_{s_{e_j}} G_0(\mathbf{r},\mathbf{r}')\,ds'ds. \tag{4.3.27}$$

and

$$(P_m)_{i,j} = \frac{1}{a_i a_j\mu_0}\int_{s_{m_i}}\int_{s_{m_j}} G_0(\mathbf{r},\mathbf{r}')\,ds'ds, \tag{4.3.28}$$

where a_i and a_j are the area of the *boundary* faces i and j.

4.3.3 Volume Loop Basis Functions with Half-SWG

As discussed in Section 2.3.3 of Chapter 2, volume loop (VL) basis functions [42] can be used to ensure divergence free currents within homogenous regions. However, VL basis functions, consisting of Full-SWG functions, cannot account for the charge accumulation at material interfaces. To overcome this, VL basis functions have to be divided into several VL basis functions, each consisting of Half-SWG functions, as shown in Fig. 4.3.3.

Figure 4.3.2 shows the electric currents, J_{p1} and J_{q1}, flowing across a *boundary* face that connects two Half-SWG functions. Charge accumulation on *boundary* faces are modeled as capacitors connected to a ground terminal.

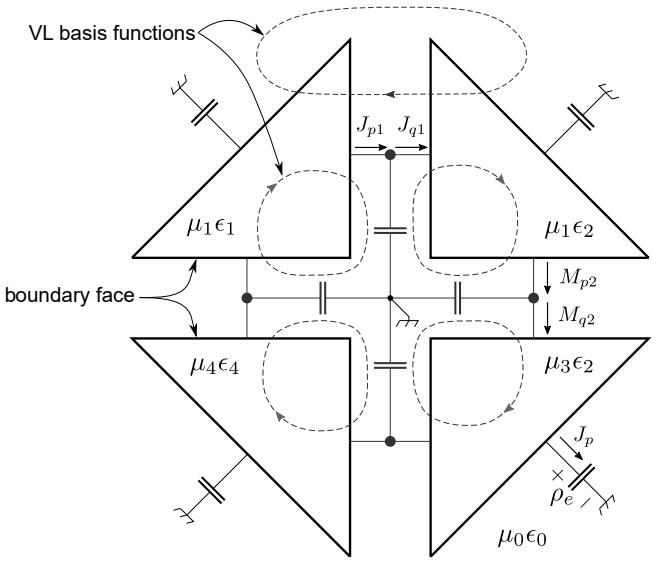

Figure 4.3.3: VL basis functions, consisting of Half-SWG basis functions, constructed around an edge; connecting four tetrahedrons with different dielectric and magnetic constants.

This approach is similar to the methods described in [88, 24, 3]. The difference between J_{p1} and J_{q1}, as given in (4.3.7), will flow through the capacitor and represents the electric charge accumulation on the *boundary* face. The same holds for the magnetic currents M_{p2} and M_{q2}. The electric and magnetic charges on the capacitors will collectively produce the electric and magnetic scalar potentials given in (4.3.17) and (4.3.18), respectively.

The two sets of linear equations, (4.3.19) and (4.3.20), can now be transformed into a single set of linear equations, using VL basis functions:

$$\begin{bmatrix} A_E Z_e A_E^T & A_E F_e A_M^T & W_E P_e & 0 \\ A_M F_m A_E^T & A_M Z_m A_M^T & 0 & W_M P_m \\ D_E(j/\omega) & 0 & -I & 0 \\ 0 & D_M(j/\omega) & 0 & -I \end{bmatrix} \begin{bmatrix} J_l \\ M_l \\ q_e \\ q_m \end{bmatrix} = \begin{bmatrix} A_E V_e \\ A_M V_m \\ 0 \\ 0 \end{bmatrix}, \tag{4.3.29}$$

where

$$Z_e = R_e + j\omega L_e, \tag{4.3.30}$$

$$Z_m = R_m + j\omega L_m, \tag{4.3.31}$$

and I is an identity matrix. The electric and magnetic currents, J_l and M_l, are the *mesh* currents circulating in volume loop l. The matrices, A_E and A_M, are index matrices that transforms the electric and magnetic *branch* currents into *mesh* currents, see Section 2.3.3. The index matrices, W_E and W_M, determine which electric and magnetic scalar potentials are added to each VL basis function, respectively. The index matrices, D_E and D_M, determine which electric and magnetic currents contribute to each electric and magnetic charge, as given in (4.3.11)-(4.3.12).

The number of unknowns in the linear system (4.3.29) can be reduced, by eliminating the electric and magnetic charges, q_e and q_m, from the solution vector. The linear system (4.3.29) can then be transformed as follow,

$$\begin{bmatrix} A_E Z_e A_E^T + (j/\omega) W_E P_e D_E & A_E F_e A_M^T \\ A_M F_m A_E^T & A_M Z_m A_M^T + (j/\omega) W_M P_m D_M \end{bmatrix} \begin{bmatrix} J_l \\ M_l \end{bmatrix} = \begin{bmatrix} A_E V_e \\ A_M V_m \end{bmatrix}. \tag{4.3.32}$$

4.3.4 Multiple Dielectrics

In order to support multiple dielectric interfaces, the equivalent charge method [89] can be used. The advantage of this method is the support for multiple dielectric layers between arbitrary shaped inductors. It has also proven to be effective for PEEC modeling [24]. Using the equivalent charge method, dielectric interface charges can be added to the linear system in (4.3.29),

$$\begin{bmatrix} A_E Z_e A_E^T & A_E F_e A_M^T & W_E P_e & 0 & W_E [P_e]_{cd} \\ A_M F_m A_E^T & A_M Z_m A_M^T & 0 & W_M P_m & 0 \\ D_E(j/\omega) & 0 & -I & 0 & 0 \\ 0 & D_M(j/\omega) & 0 & -I & 0 \\ 0 & 0 & E_{dc} & 0 & E_{dd} \end{bmatrix} \begin{bmatrix} J_l \\ M_l \\ q_e \\ q_m \\ q_d \end{bmatrix} = \begin{bmatrix} A_E V_e \\ A_M V_m \\ 0 \\ 0 \\ 0 \end{bmatrix}, \tag{4.3.33}$$

where q_d is the vector containing the charge densities at dielectric-dielectric interface [24]. The potential coefficient matrix $[P_e]_{cd}$ has the same format given in (4.3.27). The matrices E_{dc} and E_{dd} contain the electric field coefficients, which ensures continuity of the displacement current across dielectric interfaces [89],

$$\epsilon_{r1} \mathbf{E_1}(\mathbf{r}) \cdot \mathbf{n} = \epsilon_{r2} \mathbf{E_2}(\mathbf{r}) \cdot \mathbf{n}, \qquad \mathbf{r} \in S, \tag{4.3.34}$$

where ϵ_{r1} and ϵ_{r2} are the relative permittivity of the two dielectrics at the interface. The vector $\mathbf{n}$ is the unit vector normal to the interface surface, S. It is shown in [89, 24], that the diagonal entries of E_{dd} can be calculated as,

$$(E_{dd})_{i,i} = \frac{\epsilon_{r1} + \epsilon_{r2}}{2 a_i \epsilon_0}, \tag{4.3.35}$$

and the off-diagonal entries of E_{dd},

$$(E_{dd})_{i,j} = \frac{\epsilon_{r1} - \epsilon_{r2}}{a_i a_j 4\pi\epsilon_0} \int_{s_{m_i}} \int_{s_{e_j}} \frac{\mathbf{r} - \mathbf{r'}}{|\mathbf{r} - \mathbf{r'}|^3} \cdot \mathbf{n}(\mathbf{r}) \, ds' ds. \tag{4.3.36}$$

Both the diagonal and off-diagonal entries of E_{dc} are evaluated using (4.3.36). Although not shown here, the equivalent charge method can also be used to model multiple magnetic interfaces.

However, the evaluation of (4.3.33) requires additional unknowns to be solved. Computing (4.3.36) is also time consuming, since an additional FMM setup will be required to solve the additional matrix-vector products, i.e. $[E_{dc}]q_e$ and $[E_{dd}]q_d$, for each GMRES iteration. It was shown in [36], that the equivalent charge method is not necessary, if the integral kernels of the vector and the scalar potentials are independent of the material parameter, $\kappa(\mathbf{r})$. Fortunately, this is the case for both vector potentials, (4.3.13)-(4.3.14), and scalar potentials, (4.3.17)-(4.3.18). Similar to the method described in [36], (4.3.7) and (4.3.8) directly relate the surface charges to volume currents and do not require the evaluation of $\nabla\kappa(\mathbf{r})$ to obtain the surfaces charges, as in [34]. Therefore, the evaluation of (4.3.33) is not required for multiple dielectric interfaces; instead the linear system in (4.3.29) will suffice.

4.4 Solving the Linear System

Solving the complex linear system in (4.3.29), using Gaussian elimination, can become computationally intractable. The computational time scales with the number of tetrahedrons and *boundary* faces, which is equal to $N_e^v + N_m^v + N_e^s + N_m^s$. Instead, the GMRES algorithm is used, as described in [44] and in Section 2.5.1.

The dominant cost of the GMRES algorithm will be the computation of the matrix-vector products in (4.3.29). The computation of the matrix-vector products, $Z_e J_l$, $Z_m M_l$, $P_e q_e$ and $P_m q_m$, can be accelerated using the electrostatic analogy and the FMM, described in Section 2.4.2. Accelerating the computation of $F_e M_l$ and $F_m J_l$ can be accomplished, using the FMM with the Biot-Savart kernel, as discussed in Chapter 6.

4.4.1 Preconditioner

As discussed in Section 2.5.2, the convergence rate of the GMRES iterative method can be improved, by implementing a right preconditioned linear system,

$$ZPx' = y, \tag{4.4.1}$$

where Z, x and y are respectively the matrix, the left-hand and the right-hand side of the linear system, given in (4.3.29). The inverse of the preconditioning matrix, P^{-1}, is an approximation of the matrix Z. This is accomplished by sparsifying the matrix Z and using incomplete LU (ILU) factorization,

$$P^{-1} = Z_{\text{sp}} \approx LU. \tag{4.4.2}$$

The sparse approximation of matrix Z is calculated as follow:

$$Z_{\text{sp}} = \begin{bmatrix} A_E[Z_e]_{\text{sp}}A_E^T + (j/\omega)W_E[P_e]_{\text{sp}}D_E & 0 \\ 0 & A_M[Z_m]_{\text{sp}}A_M^T + (j/\omega)W_M[P_m]_{\text{sp}}D_M \end{bmatrix}$$

(4.4.3)

where

$$[Z_e]_{\text{sp}} = R_e + j\omega[L_e]_{\text{sp}}, \tag{4.4.4}$$
$$[Z_m]_{\text{sp}} = R_m + j\omega[L_m]_{\text{sp}}. \tag{4.4.5}$$

As stated in Section 2.5.2, two types of non-zero patterns for $[L_e]_{\text{sp}}$ are evaluated. The *Diagonal-L* preconditioner, which consist the diagonal values of L_e, or the *Pattern-R* preconditioner, which uses the non-zero pattern of R_e. The same patterns are used for $[L_m]_{\text{sp}}$. The sparse matrices $[P_e]_{\text{sp}}$ and $[P_m]_{\text{sp}}$ consist of the diagonal values of their corresponding matrices, P_e and P_m.

Figure 4.4.1 shows the convergence rate of the GMRES for the copper spiral in Fig. 4.5.1, with no preconditioning, *Diagonal-L* and *Pattern-R* preconditioning. It evident that both the *Diagonal-L* and *Pattern-R* preconditioners significantly improve the rate of converges, compared to solving the linear system without preconditioning. The same improvement in converge rate is obtained, as shown in Fig. 4.4.2, when simulating the permeable cylinder in Fig. 4.6.4.

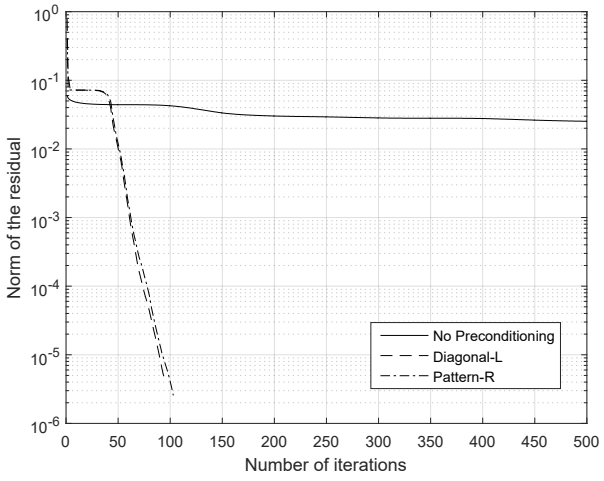

Figure 4.4.1: Convergence rate of GMRES for the copper spiral

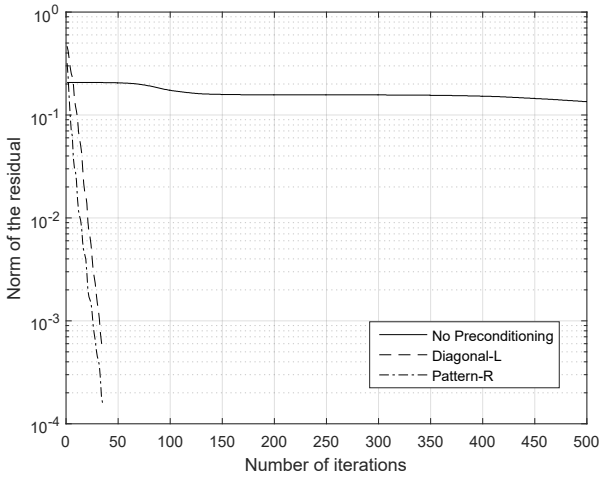

Figure 4.4.2: Convergence rate of GMRES for the permeable cylinder

4.5 Impedance Extraction

4.5.1 EMQS Analysis

When structures are small compared to the smallest wavelength of interest, electro-magneto-quasi-static (EMQS) analysis can be used, which is significantly faster than Full-Wave analysis. In EMQS analysis, the phase term of the free-space Green function, (4.2.33), can be approximated as,

$$j\omega k_0|\mathbf{r}-\mathbf{r}'| \ll 1 \Rightarrow e^{j\omega k_0|\mathbf{r}-\mathbf{r}'|} \approx 1. \tag{4.5.1}$$

The advantage of this approximation is that the kernel in the integral operators, $\frac{1}{|\mathbf{r}-\mathbf{r}'|}$, becomes frequency independent.

4.5.1.1 Copper Spiral in Free-Space

Figure 4.5.1 shows the tetrahedral mesh of a copper ($\sigma = 5.8 \times 10^7\, S/m$) spiral with three rotations, which is given to TTH as input. The FastImp [25] model, with the same dimensions and consisting of rectangular filaments, is shown in Fig. 4.5.2. In this example, the relative permeability and permittivity of the coil is taken to be the same as the surrounding free-space, i.e. $\epsilon = \epsilon_0$ and $\mu = \mu_0$. Therefore, electric charge only accumulates on the boundary of the structure. An AC voltage is applied to the two-terminal structure and the impedance is extracted, for a frequency range of 0.5 GHz to 30 GHz, using EMQS analysis.

The magnitude of the extracted impedance of both TTH and FastImp is shown in Fig. 4.5.3a. The MQS results corresponds exactly with FastImp, including the EMQS results, with a slight deviation near the 20 GHz and 26 GHz resonant peaks. This deviation can be explained by the difference in mesh

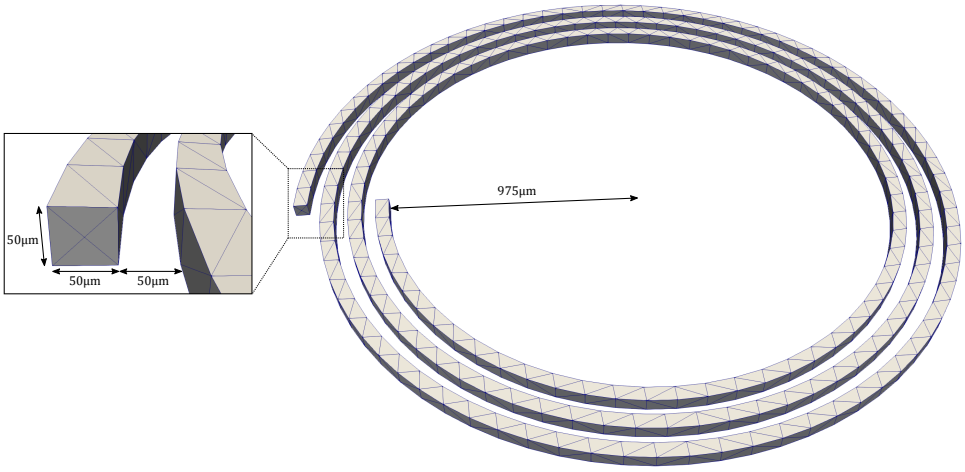

Figure 4.5.1: Tetrahedral mesh of the copper spiral with three rotations.

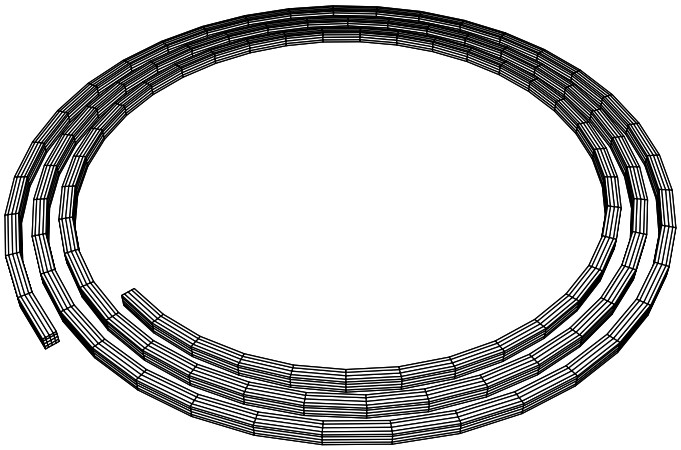

Figure 4.5.2: FastImp model of the copper spiral consisting of rectangular filaments.

types; one consisting of tetrahedral elements and the other consisting of rectangular filaments. Fig. 4.5.3b show the phase of the impedance, which also corresponds with FastImp.

This example used approximately the same number of unknowns for both solvers; with TTH requiring 13920 unknowns and FastImp requiring 14338 unknowns. The calculation time of TTH is significantly lower, compared to FastImp. Using the same computer with an i7-6700HQ processor and 8-GB memory, the calculation time of TTH for 10 sampling frequency points is 33.48 s, whereas the calculation time of FastImp is 151 s.

4.5.2 Full-Wave Analysis

When structures become larger than the wavelength of interest, EMQS analysis is no longer sufficiently accurate and Full-Wave analysis is required. The

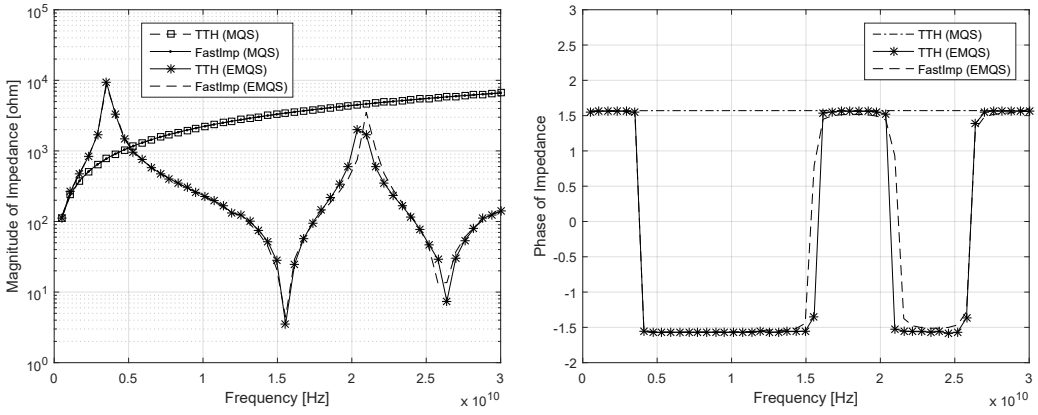

(a) (b)

Figure 4.5.3: (a) Extracted impedance of the copper spiral for both MQS and EMQS analysis. (b) Phase of the impedance.

phase term of the free-space Green function can no longer be approximated as $e^{j\omega k_0|\mathbf{r}-\mathbf{r}'|} \approx 1$, instead (4.2.33) must be used as the kernel for all integral operators. The integration of the kernel, (4.2.33), is accelerated using the ExaFMM library [76, 6]. ExaFMM uses the Full-Wave FMM to evaluating the Helmholtz equations in (4.2.25)-(4.2.28). Assuming uniform current density over each tetrahedron, the time-harmonic vector potentials in (4.2.31) and (4.2.32) are proportional to,

$$\int_V \frac{e^{j\omega k_0|\mathbf{r}-\mathbf{r}'|}}{|\mathbf{r}-\mathbf{r}'|}\,dV' = \int_V \frac{e^{j\omega k_0|\mathbf{r}-\mathbf{r}'|}-1}{|\mathbf{r}-\mathbf{r}'|}\,dV' + \int_V \frac{1}{|\mathbf{r}-\mathbf{r}'|}\,dV'. \tag{4.5.2}$$

The first integral on the right-hand side of (4.5.2) is evaluated numerically, using numerical quadrature, see Section 2.4.3. The second integral on the right-hand side is evaluated analytically, using the method given in [1]. The same holds for the time-harmonic scalar potentials in (4.2.29) and (4.2.30), assuming uniform charge density over each *boundary* face.

4.5.2.1 Transmission Line in Free-Space

Using Full-Wave analysis, the impedance of a copper transmission line, shown in Fig. 4.5.4, is extracted at discrete frequency points. The cross section of each conductor in the transmission line is $37\,\mu\text{m} \times 15\,\mu\text{m}$, separated by a distance, d. The length of the transmission line is 2 cm, which makes the structure two wavelength long, at 20 GHz. The dimensions of transmission line is the same as the model used in [3].

The impedance was extracted, at discrete frequency points, for a separation distance of $d = 0.01$ cm between the two conductors. Figure 4.5.5a shows the extracted impedance between 1 GHz and 30 GHz, using EMQS and Full-Wave analysis. The phase of the impedance and the relative error between

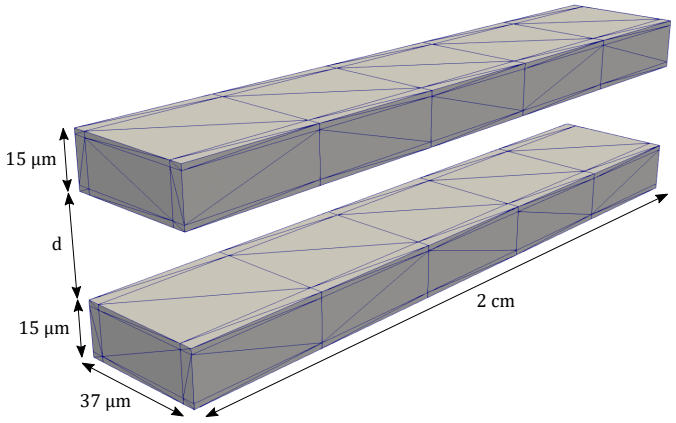

Figure 4.5.4: Scaled version of a two conductor transmission line ($\sigma = 5.8 \times 10^7\ S/m$).

EMQS and Full-Wave analysis are shown in Fig. 4.5.5b and 4.5.5c, respectively. The extracted impedance corresponds with the results obtained in [3]. For a separation distance of 0.01 cm, the average error between EMQS and Full-Wave analysis is well below 1 %. The relative error increases near the resonant peaks, but remains below 10 %. Hence, EMQS analysis is still sufficiently accurate for structures separated by a relatively small distance, which corresponds with the findings in [3].

Figure 4.5.6a and 4.5.6b show respectively the extracted impedance and the phase, for a separation distance of 1 cm between the two conductors. It is evident, from the relative error in Fig 4.5.6c, that EMQS analysis is no longer sufficiently accurate and captures the behavior of the transmission line only qualitatively. The error of the phase becomes significant at higher frequencies and the height of the resonant peaks are underestimated, which corresponds with the analysis done in [3]. As suggested in [3], if an error of a few percent is tolerated, EMQS analysis can be used to calculate the impedance of structures on the order of a wavelength, given that the separation between the structures are small relative to the wavelength. For larger structures, EMQS analysis captures the behavior of the transmission line only qualitatively.

4.5.2.2 Probe-Fed Patch Antenna

To demonstrate a multilayer dielectric structure, the probe-fed patch antenna in Fig. 4.5.7 is simulated with TTH. A dielectric volume, ϵ_d, is placed between the patch antenna and the ground plane, separated by 7 mm. Copper ($\sigma = 5.8 \times 10^7\ S/m$) is used for the patch antenna and the ground plane, and the surrounding space is taken as free-space, ϵ_0. The dimensions of the patch antenna correspond with the dimensions used in [90, 39]; however, the ground plane in Fig. 4.5.7b has finite dimensions (165 mm × 165 mm) and the thickness of the patch antenna and the ground plane is 0.5 mm. The extracted

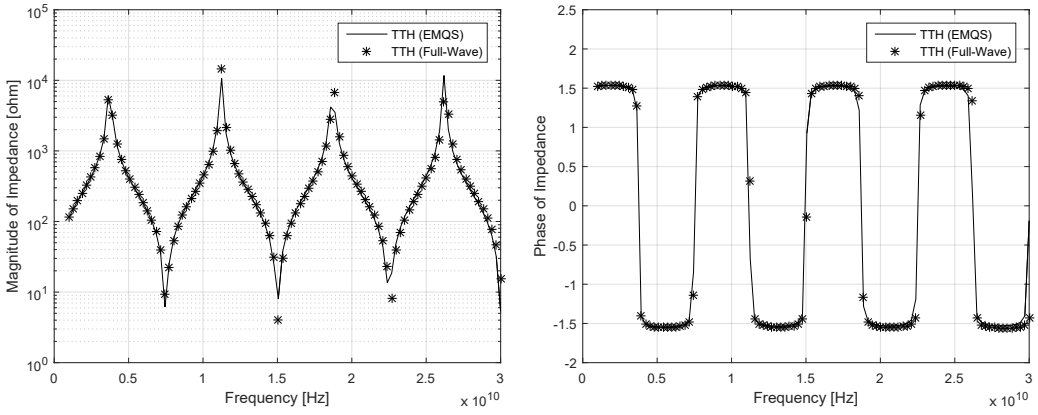

(a)

(b)

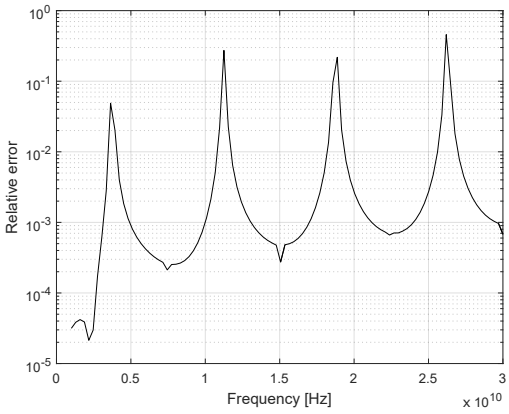

(c)

Figure 4.5.5: (a) Extracted impedance of the transmission line for both EMQS and Full-Wave analysis. The two conductors are separated by 0.01 cm. (b) Phase of the impedance. (c) Relative error between EMQS and Full-Wave analysis.

impedance, over a frequency range of 1.3 to 1.7 GHz, is shown in Fig. 4.5.8. As expected, the higher the permittivity of the dielectric volume, the lower the resonant frequency of the antenna. The impedance calculated with TTH, correspond with the results calculate and measured in [90, 39]. However, the resonant frequencies and amplitudes slightly deviate from the results in [39]. This may be due to two reasons: an infinite ground plane is used in [39] and the thickness of both the patch antenna and the ground plane is taken as infinitely thin sheets.

4.5.3 Superconducting Transmission Line with Vias

To evaluate the effects of displacement current on a superconducting structure, the impedance of a superconducting transmission line is extracted, using

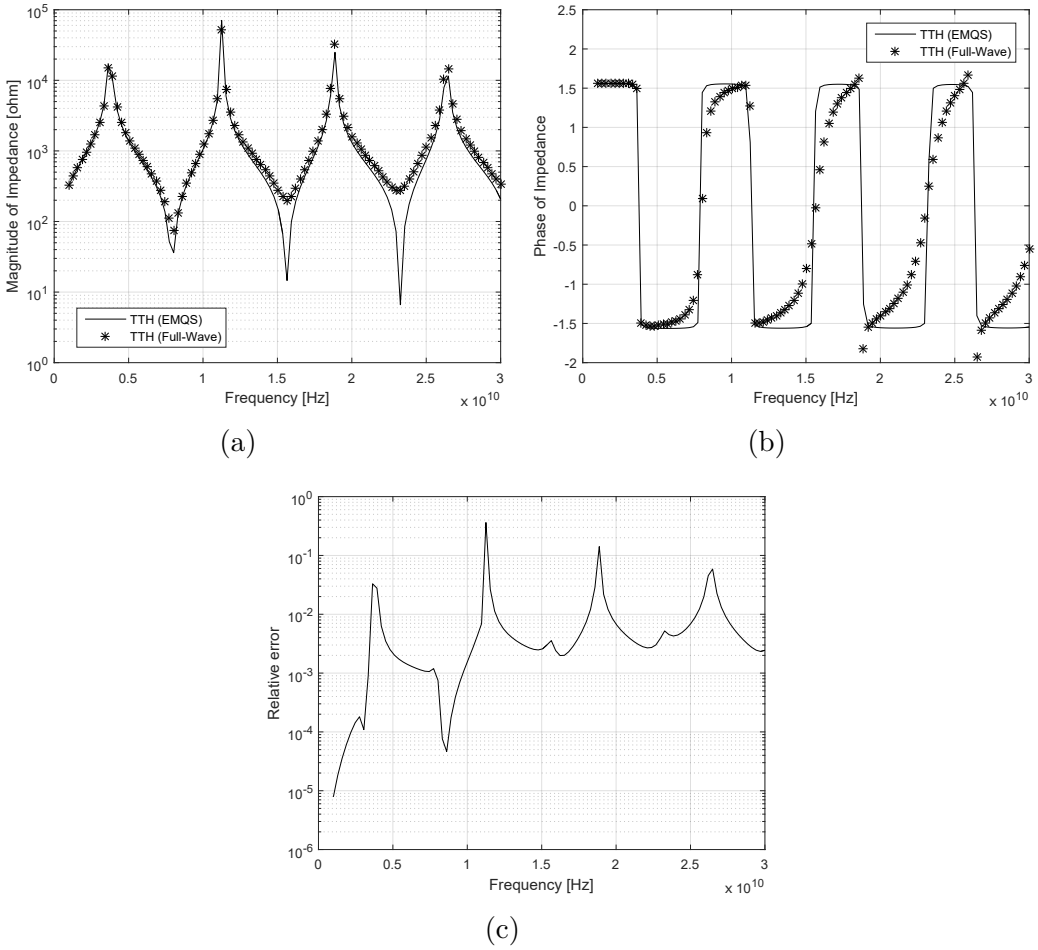

Figure 4.5.6: (a) Extracted impedance of the transmission line for both EMQS and Full-Wave analysis. The two conductors are separated by 1 cm. (b) Phase of the impedance. (c) Relative error between EMQS and Full-Wave analysis.

EMQS analysis. Two transmission line models were created, using the GDS layouts shown in Fig. 4.5.9. The first transmission line, see Fig. 4.5.9a, has vias punching through the ground plane and the second transmission line, see Fig. 4.5.9b, remains above the ground plane. The GDS layout was converted to a GMSH geometry, using InductEx [21, 2]. The transmission lines have a thickness of 135 nm and are 400 nm above and below the ground plane. The thickness of the ground plane is 300 nm. All structures have a London penetration depth of 90 nm.

Figure 4.5.10a show the magnitude of the impedance of the two superconducting transmission lines. Different dimensions where used for the holes in the ground plane surrounding the via pillars: $7\,\mu\text{m} \times 7\,\mu\text{m}$ and $13\,\mu\text{m} \times 13\,\mu\text{m}$. The phase of the impedance is given in Fig. 4.5.10b. The first resonant peak of the transmission line, without vias, occurs at 140 GHz. The resonant peaks of the transmission lines, with vias, occur at lower frequencies: 132 GHz for

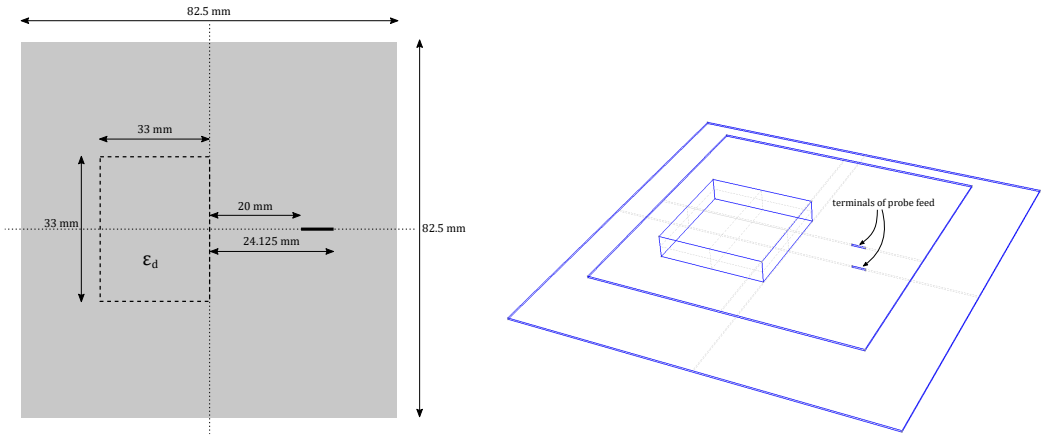

(a) (b)

Figure 4.5.7: Probe-fed patch antenna over a finite ground plane. (a) Dimensions of patch antenna. (b) 3D geometry with finite ground plane (165 mm × 165 mm)

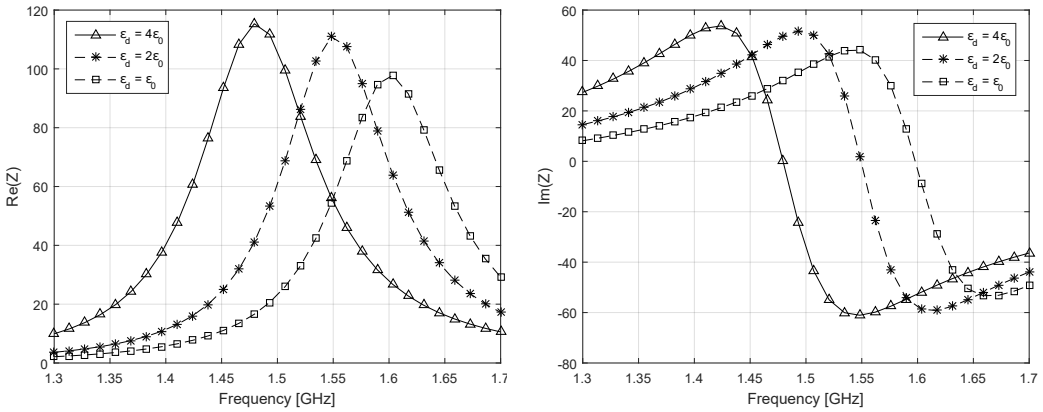

(a) (b)

Figure 4.5.8: Extracted impedance of patch antenna for different permittivity for the dielectric volume. (a) Real part of impedance. (b) Imaginary part of impedance

the smaller vias and 116 GHz for the larger vias. At higher frequencies, the difference in resonant peaks become more apparent.

Although not discussed here, the results from Fig. 4.5.10a and 4.5.10b can be used to construct an equivalent circuit model for the via in the ground plane. The results obtained with TTH for superconducting structures, still has to be verified experimentally, but this falls outside the scope of this dissertation.

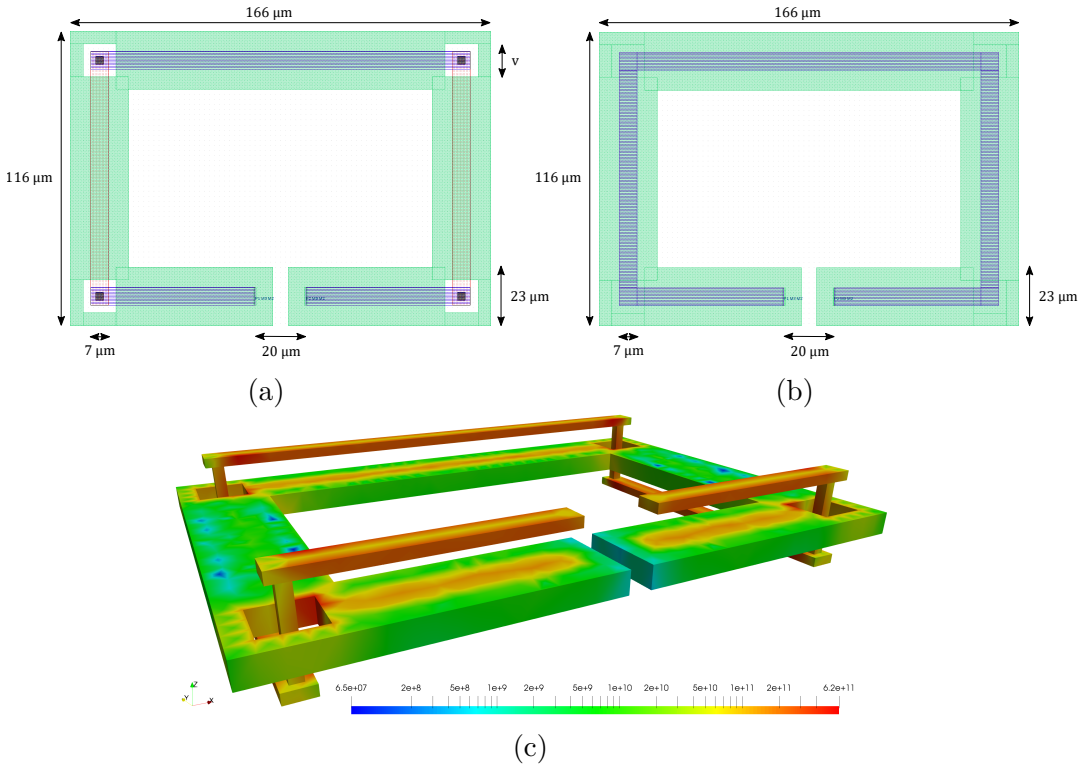

Figure 4.5.9: GDS layout of superconducting transmission line, (a) with vias punching through the ground plane and (b) without vias. (c) 3D model and current distribution of the transmission line with vias generated by TTH (scaled vertically).

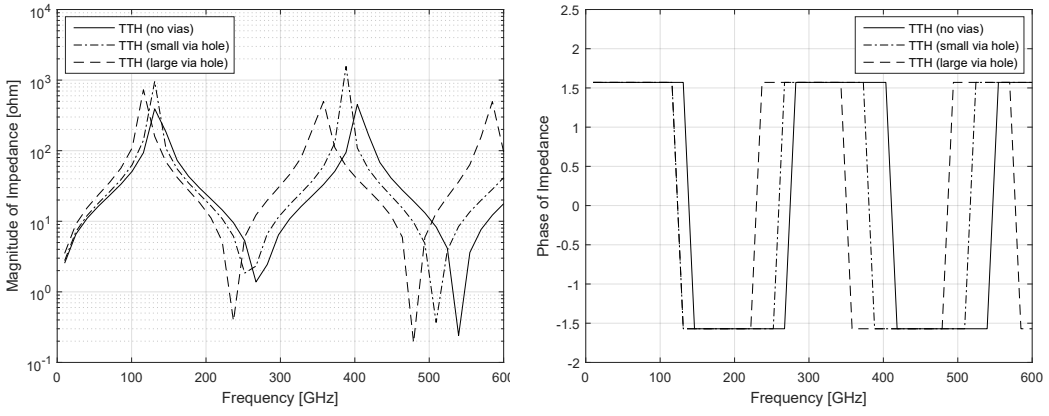

Figure 4.5.10: (a) Extracted impedance of the superconducting transmission lines, with vias punching through the ground plane and without vias. (b) Phase of the impedance.

4.6 Magnetic Materials

The VJIE method described in this chapter was implemented in TTH and can now be used to extract the inductance of structures in the presence of permeable materials. In order to demonstrate the accuracy the method described in this chapter, the results of TTH is compared to existing results for non-superconducting structures [91, 92, 93, 94, 95, 96] and simulated results obtained from *CST Studio* [97].

4.6.1 Permeable cylinder

Figure 4.6.1 shows an example of a permeable cylinder surrounded by an copper coil ($\sigma = 5.8 \times 10^7\, S/m$). The the top and bottom layers of the permeable cylinder have the same relative permeability, μ_{r1}.

To compare the accuracy TTH with the numerical results in [94], the permeable cylinder in Fig. 4.6.1 was kept homogenous, i.e. $\mu_{r1} = \mu_{r2}$. Figure 4.6.2 shows the inductance calculated with TTH at discrete relative permeability points, which is also compared with the numerical results in [94] and with the numerical results obtained with *CST Studio* [97]. The same number of tetrahedrons was used for both TTH and *CST Studio*. It is important to note that the structure in [94] is a factor 10^6 larger than the structure in Fig. 4.6.1 and that the results had to be scaled accordingly. Table 4.6.1 shows the calculated inductance values of TTH and *CST Studio*, for a relative permeability of $\mu_{r1} = \mu_{r2} = 10^4$, including the results of the *qualocation* and *collocation* methods given in [94]. The inductance calculated with TTH corresponds with *CST Studio*, with less than 2 % error.

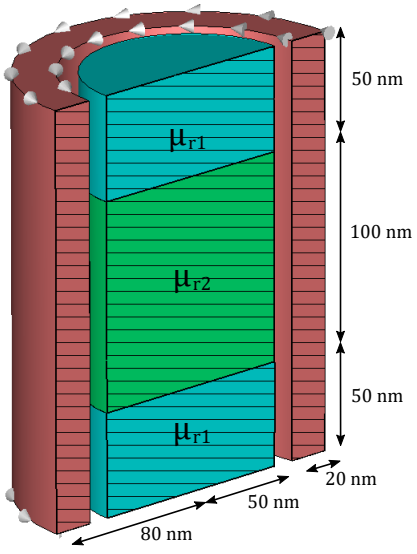

Figure 4.6.1: Cross section of permeable cylinder surrounded by a copper coil.

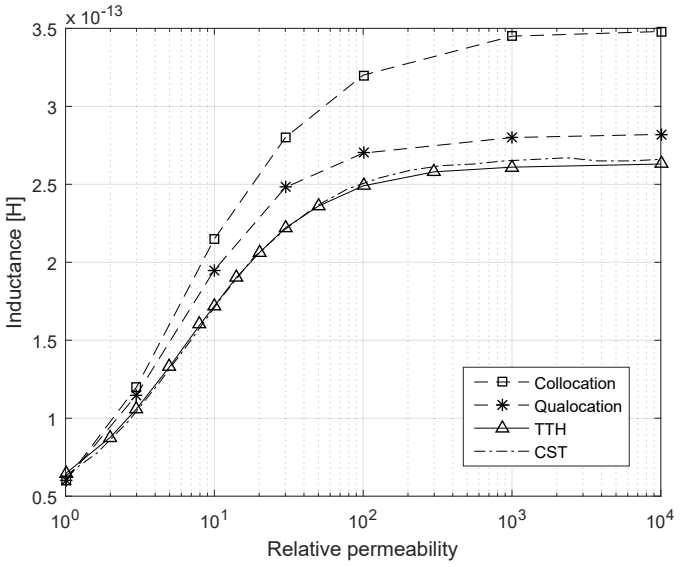

Figure 4.6.2: Inductance of permeable cylinder in Fig. 4.6.1. The relative permeability of the entire cylinder is changed equally, i.e. $\mu_{r1} = \mu_{r2}$.

Table 4.6.1: Inductance of the copper coil in Fig. 4.6.1 with $\mu_{r1} = \mu_{r2} = 10^4$.

Method	Inductance [pH]	Error compared to *CST Studio*
Collocation [94]	0.348	30.8 %
Qualocation [94]	0.282	6.02 %
TTH	0.263	1.13 %
CST Studio	0.266	0 %

To demonstrate the accuracy of TTH for piece-wise homogenous permeable materials, the relative permeability of each layer in Fig. 4.6.1 was changed independently. The relative permeability of the center layer was kept constant, $\mu_{r2} = 10^4$, while the relative permeability of the top and bottom layers, μ_{r1}, were adjusted. Figure. 4.6.3 shows the extracted inductance and compares it with the results from Fig. 4.6.2. For low values of μ_{r1}, the inductance is higher, compared to the permeable cylinder with $\mu_{r1} = \mu_{r2}$. This is due to the high permeability of the center layer. As μ_{r1} increases and becomes equal to μ_{r2}, the inductance converge to the same inductance value given in Table 4.6.1. Once again, TTH produces the same results as CST with less than 2 % error.

The permeable cylinder in Fig. 4.6.4 is similar to the to structure in Fig. 4.6.1, but the top and bottom layers are connected by a small cylinder, with a radius of 20 nm. The relative permeability of the two materials were chosen as $\mu_{r1} = 100$ and $\mu_{r2} = 10$. Figure 4.6.5a shows the magnetic current density inside the permeable cylinder, calculated with TTH, which closely matches the magnetic field calculated with *CST Studio*, see Fig. 4.6.5b. Using the same

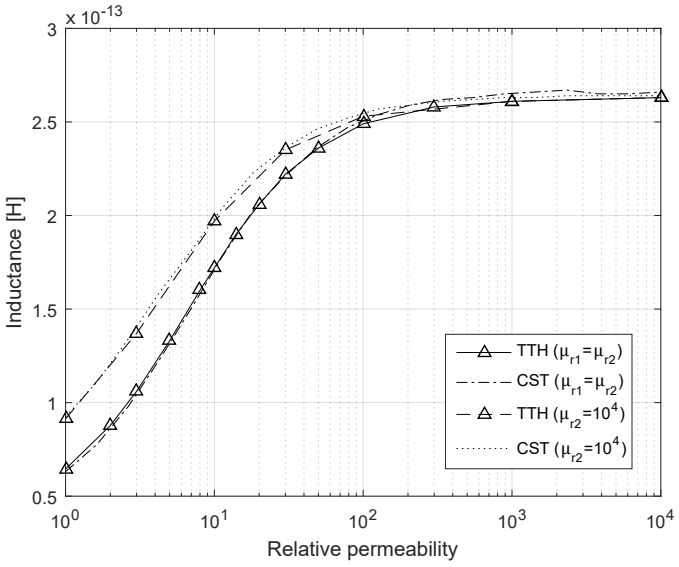

Figure 4.6.3: Inductance of permeable cylinder in Fig. 4.6.1, calculated with TTH and *CST Studio*. The relative permeability of the center layer is kept constant at $\mu_{r2} = 10^4$, while μ_{r1} was adjusted. For comparison purposes, the results are also shown for μ_{r1}=μ_{r2}.

mesh size, the inductance calculated with TTH and *CST Studio* are respectively 2.25 pH and 2.28 pH, which differs less than 2 %.

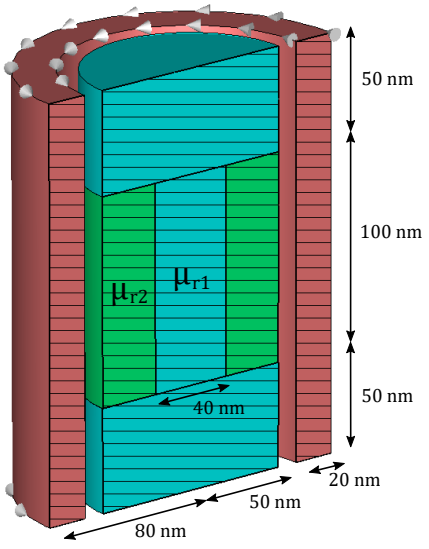

Figure 4.6.4: Cross section of permeable cylinder surrounded by a copper coil, with top and bottom layers connected by a small cylinder.

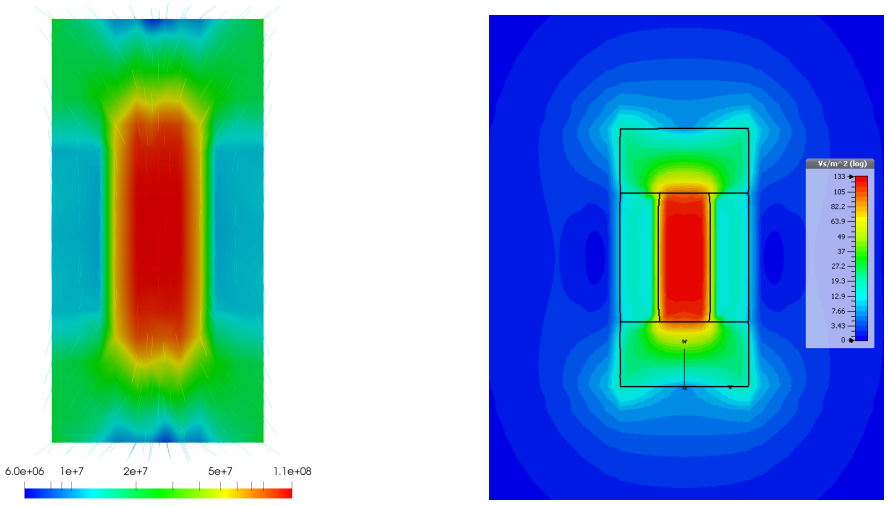

(a) (b)

Figure 4.6.5: Cross section of magnetic current and magnetic field inside the permeable cylinder of Fig. 4.6.4. (a) The magnetic current density calculated with TTH with the coil excited with 1 V. (b) The magnetic field calculated with *CST Studio* with 1 A inside the coil.

4.6.2 Coil Above Permeable Substrate

Figure 4.6.6 shows a circular inductor above a multilayer permeable substrate. The circular inductor has a diameter of 280 μm and a cross section of 10 μm $\times$ 10 μm. The relative permeability of the bottom layer is kept constant at $\mu_{r2} = 10^3$.

Figure 4.6.7 shows the inductance of the coil, calculated with TTH and *CST Studio*. The relative permeability of the top layer (μ_{r1}) was adjusted, while the bottom layer (μ_{r2}) was kept constant. As the number of tetrahedrons increase, the inductance calculated with *CST Studio* converge toward the values calculated with TTH. For a relative permeability below 3×10^3, TTH requires 3820 tetrahedrons to obtain the same results as *CST Studio*, which requires approximately 40000 tetrahedrons. As the relative permeability exceeds 3×10^3, the inductance calculated with TTH starts to deviate; even when higher expansion orders (P) are used for the FMM, see Chapter 6. This is due to the large magnetic charges forming on the surface of the permeable structure. As the relative permeability increase, it becomes increasingly difficult to accurately calculate the small magnetic currents inside the permeable volume. Although not discussed here, this calculation error can be overcome, using a method that is solely based on fictitious magnetic surface charges [80, 81, 93].

This example is also similar to the spiral inductor in [92]. If the inductance is scaled by a factor of 2, it will closely match the extracted inductance of the spiral inductor in [92], which consist of two turns.

The cross section of the multilayer permeable substrate is shown in Fig. 4.6.8,

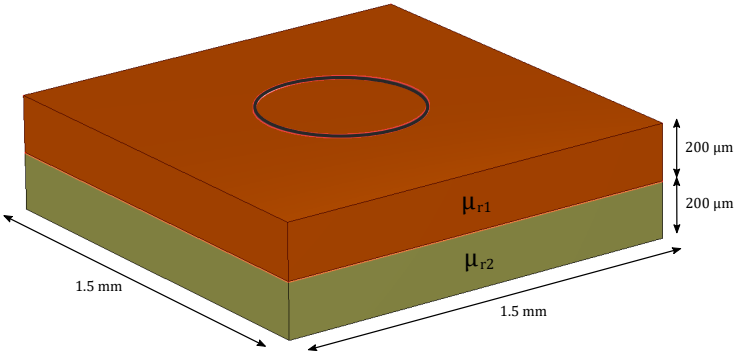

Figure 4.6.6: Copper coil above a multilayer permeable substrate.

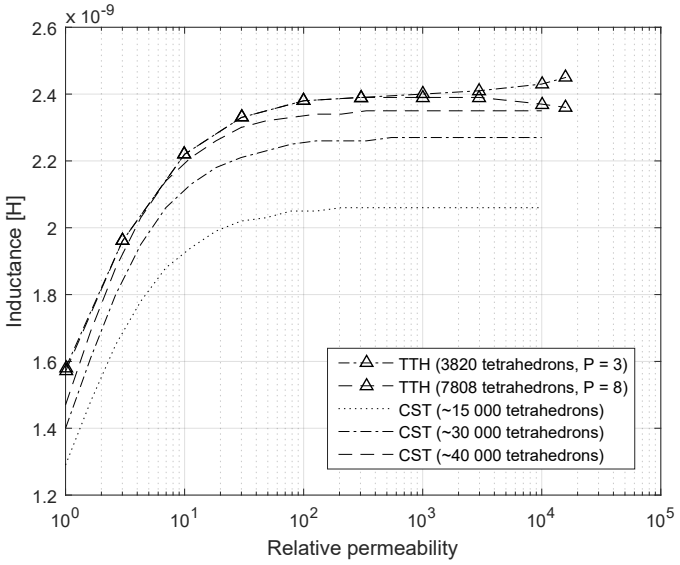

Figure 4.6.7: Inductance of the coil above the permeable substrate. The relative permeability of the bottom layer is kept constant at $\mu_{r2} = 10^3$.

with $\mu_{r1} = 10$ and $\mu_{r2} = 1000$. The magnetic current density was calculated with TTH and the magnetic field was calculated with *CST Studio*. Both field distributions were generate by exciting the coil with 1 V, at 1 MHz. Fig. 4.6.8c shows the vector field of the magnetic current inside the permeable substrate, which was generated by TTH and plotted in ParaView [5].

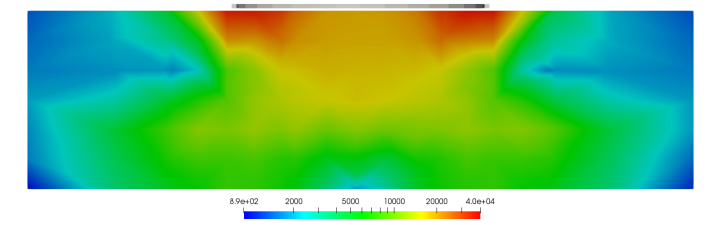

(a)

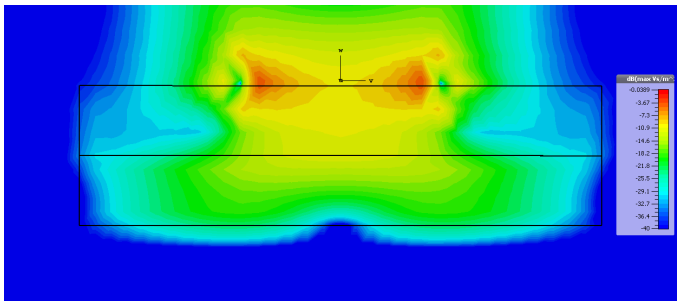

(b)

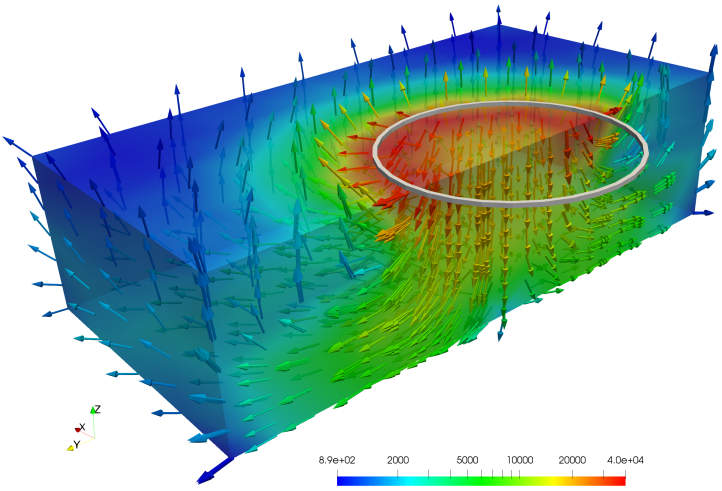

(c)

Figure 4.6.8: Cross section of the structure in Fig. 4.6.6. (a) Magnetic current density calculated with TTH. (b) Magnetic field calculated with *CST Studio*. (c) Vector field of the magnetic current density calculated with TTH.

4.6.3 Superconducting Microstrip Line with Permeable Substrate

Now that it has been shown that the inductance of non-superconducting metals, in the presence of permeable materials, can be calculated accurately with TTH, the effects of magnetic materials on superconducting structures are evaluated. Superconductivity and the London penetration depth is taken into account using the complex dielectric constant defined in (4.2.6).

To demonstrate the use of permeable materials, the inductance of a super-

conducting microstrip line, shown in Fig. 4.6.9, is calculated. A $32\,\mu\text{m} \times 22\,\mu\text{m}$ permeable rectangle is sandwiched between the microstrip line and the ground plane. InductEx was used to construct a 3D model from the GDS layers, using the Hypres $4.5\,\text{kA/cm}^2$ Nb fabrication process [4], as shown in Fig. 4.6.10. Layer $M2$ is used for the microstrip line and layer $M0$ for the ground plane. Two possible scenarios are tested: one where layer $M1$ is assumed magnetic and one where layer $R2$ is assumed magnetic. The inductance of the microstrip line was calculated for a range of μ_r values, as shown in Fig. 4.6.11, with an excitation voltage of 1 V at 10 GHz.

The electric current density, $\mathbf{J}$, calculated with TTH, is shown in Fig. 4.6.10. Figure 4.6.12a and 4.6.12b show respectively the direction of current flow of both the electric, $\mathbf{J}$, and magnetic, $\mathbf{M}$, current densities. From Fig. 4.6.10 and 4.6.12a, it is evident that the electric current in the ground plane is displaced by the magnetic layer. The electric current no longer flows directly beneath the microstrip, but around the permeable rectangle. Consequently, the total inductance is higher, see Fig.4.6.11, since the total path of the current has increased. This effect is similar to a hole being placed in the ground plane, directly below a microstrip, as demonstrated in [98].

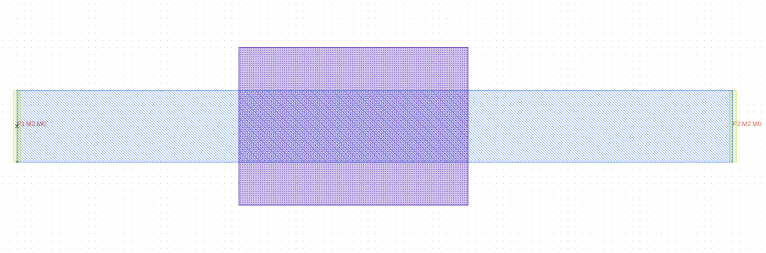

Figure 4.6.9: GDS layout of a $100\,\mu\text{m} \times 10\,\mu\text{m}$ microstrip line with a $32\,\mu\text{m} \times 22\,\mu\text{m}$ permeable rectangle sandwich between layers $M2$ and $M0$ of the Hypres $4.5\,\text{kA/cm}^2$ Nb fabrication process [4].

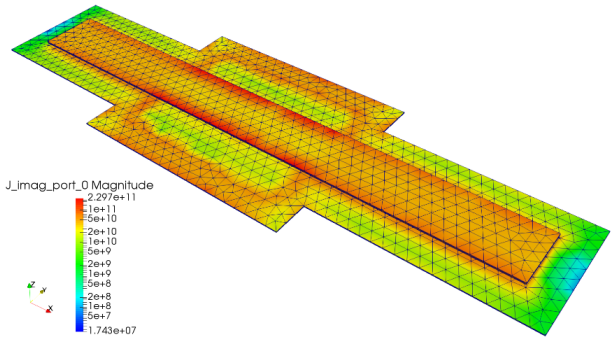

Figure 4.6.10: Electric current density of a superconducting microstrip line above a ground plane. The relative permeability of layer $M1$ is $\mu_r = 1000$.

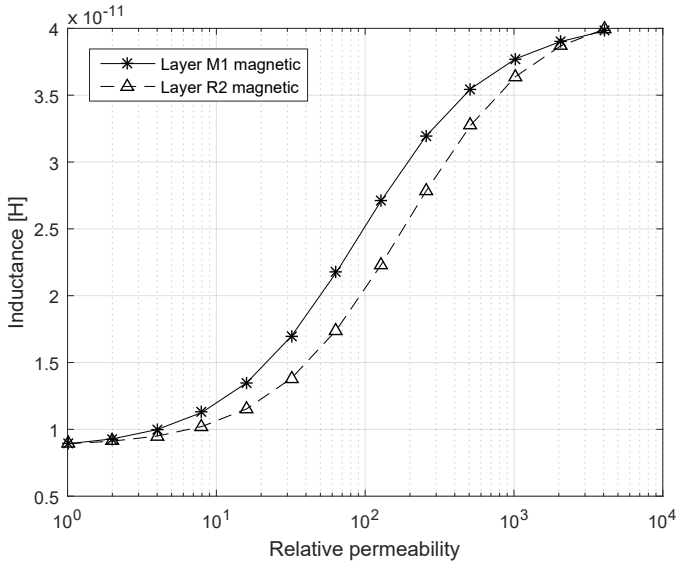

Figure 4.6.11: Extracted inductance of the microstrip line example for a range of relative permeability values for layer $M1$ and $R2$.

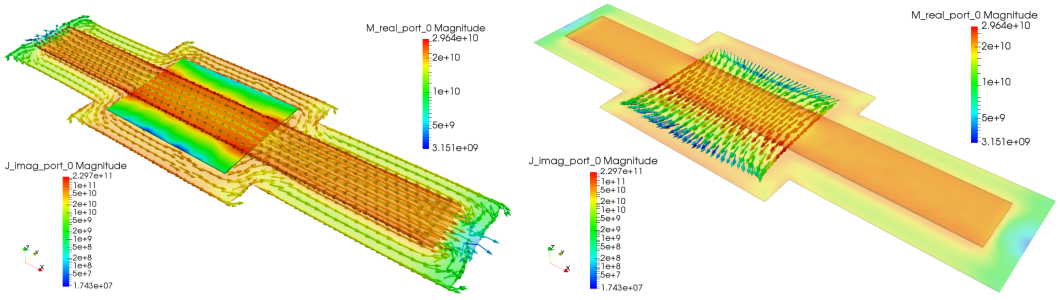

(a) (b)

Figure 4.6.12: Superconducting microstrip line with relative permeability of $\mu_r = 1000$ for layer $M1$. (a) Vector field of electric current density, $\mathbf{J}$, and the magnetic current density, $\mathbf{M}$, within the permeable material. (b) Vector field of magnetic current density, $\mathbf{M}$, within permeable material.

4.6.4 Inductive Coupling Using Permeable Layer

In single-flux-quantum (SFQ) circuits, the ground plane can severely limit the coupling factor between adjacent inductors. If higher coupling factors are required, ground plane holes can be place directly below the adjacent microstrip lines [99]. However, when using multiple ground planes, punching holes through all the layers is not always possible. In this section, it is shown

that permeable materials can be used to increase the mutual coupling (k) between two inductors, without creating a hole in the ground plane.

Figure 4.6.13 shows the GDS layout of two superconducting microstrip lines, with a $44\,\mu\text{m} \times 38\,\mu\text{m}$ permeable rectangle sandwiched between the lines and the ground plane. Using InductEx and the Hypres $4.5\,\text{kA/cm}^2$ Nb fabrication process, a 3D model is constructed from the GDS layers, as shown in Fig. 4.6.15. Layer $M2$ is used for the microstrip line, layer $M0$ for the ground plane, and layer $M1$ was changed to a permeable (magnetic) layer.

The inductance and mutual inductance between the two mictrostrip lines were calculated for a range of μ_r values, as shown in Table 4.6.2, with an excitation voltage of 1 V at 10 GHz. The coupling factor increases several order as the relative permeability increases, as can be seen in Fig. 4.6.14. Figure 4.6.15a and 4.6.15b show respectively the direction of current flow of both the electric, **J**, and magnetic, **M**, current densities. Once again, the current in the ground plane is displaced by the magnetic layer, which increases the total inductance and mutual inductance, similar to a hole being placed in the ground plane [99]. These results still have to be verified experimentally for superconducting structures, but this falls outside the scope of this dissertation.

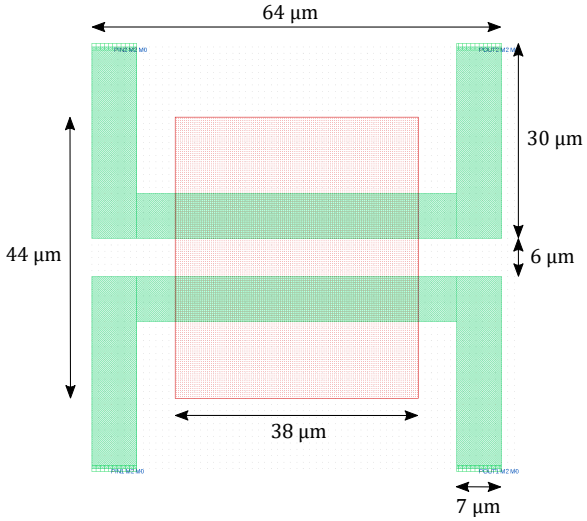

Figure 4.6.13: GDS layout of a two microstrip lines with a $44\,\mu\text{m} \times 38\,\mu\text{m}$ permeable rectangle sandwich between layers $M2$ and $M0$ of the Hypres $4.5\,\text{kA/cm}^2$ Nb fabrication process.

Table 4.6.2: Inductance and mutual inductance between microstrip lines in Fig. 4.6.13.

μ_r	Inductance [pH]	Mutual inductance [pH]	Coupling factor (k)
1	12.01	0.094	0.008
10	15.99	0.435	0.027
10^2	33.95	6.631	0.195
10^3	58.69	23.901	0.407
10^4	65.01	29.343	0.451

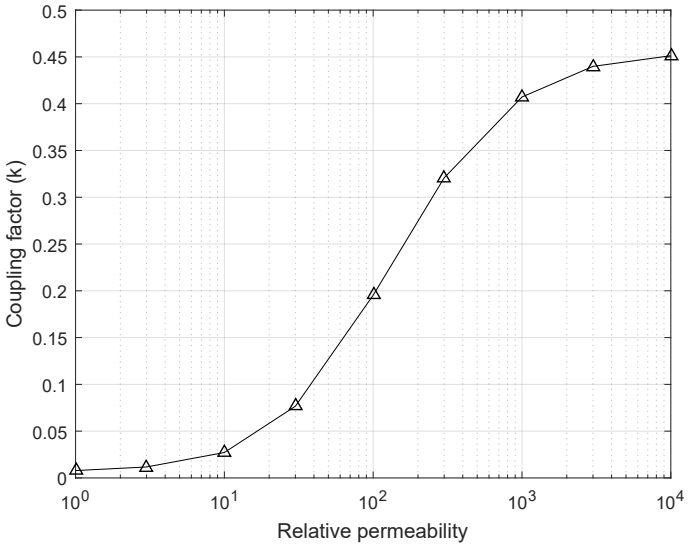

Figure 4.6.14: Coupling factor between the two microstrip lines for a range of relative permeability values.

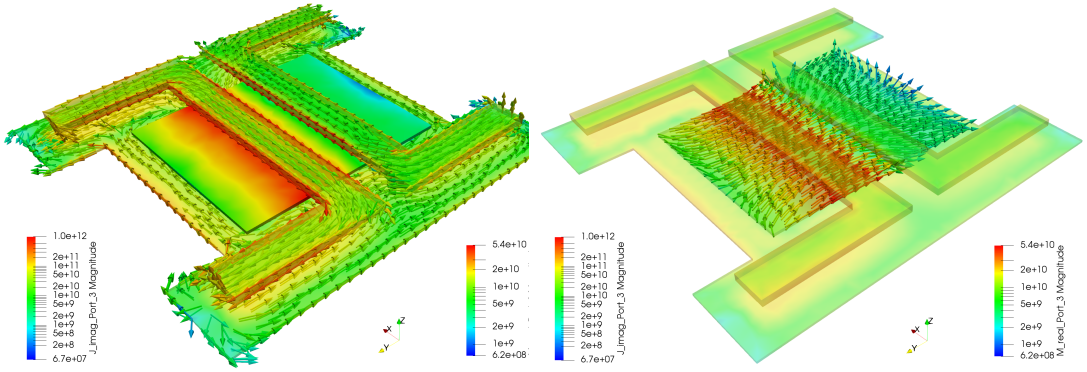

(a) (b)

Figure 4.6.15: Microstrip lines above substrate with relative permeability of $\mu_r = 1000$. (a) Vector field of electric current density, $\mathbf{J}$. (b) Vector field of magnetic current density, $\mathbf{M}$, within permeable material.

4.7 Conclusion

Modification were made to TetraHenry (TTH) to support electric and magnetic currents inside inhomogeneous dielectric and magnetic materials. The integral equations, required for EMQS and Full-wave analysis, with support for superconductivity, are presented. VL basis functions, consisting of Half-SWG functions, are used to account for charge accumulation at material interfaces of both dielectric and magnetic materials. The FMM is used to accelerate the computation of vector and scalar potential fields. It is shown that *Diagonal-L* and *Pattern-R* preconditioners are still effective at accelerating the convergence rage of the GMRES iterative solver.

Numerical results confirm the accuracy of TTH for non-superconducting structures, when extracting impedance over a wide range of frequencies. EMQS analysis can be used to accurately calculate the impedance of structures on the order of a wavelength, given that the separation between the structures are small relative to the wavelength. For larger structures, Full-Wave analysis should be used. The calculation time of TTH is also significantly faster, compared to FastImp, when using EMQS analysis.

It is shown that the frequency behaviour of a superconducting transmission line is affected, if the transmission line has vias punching through the ground plane. The frequency behaviour also depends on the size of the hole in the ground plane.

The effect of magnetic materials on non- and superconducting materials are analysed. It is shown that magnetic materials can significantly increase the self- and mutual inductance of non- and superconducting structures. The inductance extracted with TTH for non-superconducting structures, in the presence of permeable materials, correspond with existing results and with *CST Studio*. The results obtained with TTH for superconducting structures, in the presence of permeable materials, still has to be verified experimentally, but this falls outside the scope of this dissertation.

Chapter 5

External Magnetic Field

5.1 Introduction

When superconducting integrated circuits are exposed external magnetic fields, currents are induced inside the superconductors to expel the magnetic field. This phenomenon is known as the Meissner effect [26]. Due to the high order of sensitivity of these circuits, any small current can lead to a catastrophic failure. Understanding the limitations and operating margins of the circuits, in the presence of magnetic fields, can help designers optimize layouts and prevent circuit failure.

Obtaining the operating margins of a superconducting integrated circuits, in the presence of magnetic fields, requires simulating the structure for each possible angle and amplitude of the field. This can be time consuming when using VIE-based solvers, such as TTH. A better approach would be to use the VIE-based solver to derive an equivalent circuit model for each x-, y- and z-component of the field. This circuit model can then be reused to rapidly simulate magnetic fields at different amplitudes and obtain the operating margins.

5.2 Implementing Magnetic Fields

Before an equivalent circuit model can be derived, support for magnetic fields have to be implemented in TTH. The external magnetic field can be modeled as a uniform vector field with variable magnitude in the x-, y- and z-directions,

$$\mathbf{B_{ext}}(\mathbf{r}) = \begin{bmatrix} B_x \\ B_y \\ B_z \end{bmatrix}. \tag{5.2.1}$$

Magnetic field excitation can be added to the Gauge invariant integral equation given in [37], see Appendix A, by including an additional magnetic vector

potential, $\mathbf{A_{ext}}$,

$$\mu\lambda^2\mathbf{J_s}(\mathbf{r}) + \mathbf{A}(\mathbf{r}) + \mathbf{A_{ext}}(\mathbf{r}) = -\frac{\Phi_0}{2\pi}\nabla\theta(\mathbf{r}), \tag{5.2.2}$$

where $\mathbf{A}(\mathbf{r})$ is the magnetic vector potential induced by the currents $\mathbf{J}(\mathbf{r})$ and $\mathbf{A_{ext}}$ is the magnetic vector potential induced by the external magnetic field, $\mathbf{B_{ext}}$. Next, and expression for $\mathbf{A_{ext}}$ has to be obtained that will produce the same magnetic field vector given in (5.2.1). Using the relation between magnetic field and magnetic vector potential,

$$\mathbf{B_{ext}}(\mathbf{r}) = \nabla \times \mathbf{A_{ext}}(\mathbf{r}) = \begin{bmatrix} \frac{\partial}{\partial x} \\ \frac{\partial}{\partial y} \\ \frac{\partial}{\partial z} \end{bmatrix} \times \begin{bmatrix} A_x \\ A_y \\ A_z \end{bmatrix} = \begin{bmatrix} \frac{\partial A_z}{\partial y} - \frac{\partial A_y}{\partial z} \\ \frac{\partial A_x}{\partial z} - \frac{\partial A_z}{\partial x} \\ \frac{\partial A_y}{\partial x} - \frac{\partial A_x}{\partial y} \end{bmatrix}, \tag{5.2.3}$$

an expression for $\mathbf{A_{ext}}(\mathbf{r})$ can now be obtained in terms of B_x, B_y and B_z,

$$\mathbf{A_{ext}}(\mathbf{r}) = \begin{bmatrix} B_y\, z \\ B_z\, x \\ B_x\, y \end{bmatrix}. \tag{5.2.4}$$

Using the Method of Moments and taking the inner product of (5.2.2) with the weighting function, $\mathbf{w_n}(\mathbf{r})$, the vector potential can be integrated over each tetrahedron,

$$\begin{aligned} A_n &= < \mathbf{w_n}(\mathbf{r}), \mathcal{L}\left(\mathbf{A_{ext}}(\mathbf{r})\right) > \\ &= \int_{v_n} \mathbf{w_n}(\mathbf{r}) \cdot \mathbf{A_{ext}}(\mathbf{r})\, dv. \end{aligned} \tag{5.2.5}$$

where $\mathbf{w_n}(\mathbf{r})$ is a Full-SWG basis function of tetrahedron, T_n, and A_n is the vector entry corresponding to the SWG basis function m. Equation (5.2.5) must be evaluated for both tetrahedrons of the Full-SWG basis function, see T_n^+ and T_n^- in Fig. 2.3.2. Using the same approach described in Section 2.4.1, (5.2.5) can be separated into two components:

$$A_n = A_n^+ + A_n^-, \tag{5.2.6}$$

where

$$A_n^+ = \int_{T_n^+} \mathbf{w_n}(\mathbf{r}) \cdot \mathbf{A_{ext}}(\mathbf{r})\, dv, \tag{5.2.7}$$

and

$$A_n^- = \int_{T_n^-} \mathbf{w_n}(\mathbf{r}) \cdot \mathbf{A_{ext}}(\mathbf{r})\, dv. \tag{5.2.8}$$

To accelerate the integration of (5.2.5), an analytical solution can be obtained for both (5.2.7) and (5.2.8). The same approach that is used to evaluate A_n^+, can be applied to A_n^-. Starting with the definition of the SWG basis

function, (2.3.16), and the vector potential defined in (5.2.4), the following expression for A_n^+ is obtained,

$$\begin{aligned} A_n^+ &= \int_{T_n^+} \left(\frac{1}{3|v_n^+|} \rho_{\mathbf{n}}^+(\mathbf{r}) \right) \cdot \mathbf{A_{ext}}(\mathbf{r})\, dv. \\ &= \frac{1}{3|v_n^+|} \int_{T_n^+} (\mathbf{r} - \mathbf{r_n^+}) \cdot \mathbf{A_{ext}}(\mathbf{r})\, dv. \\ &= \frac{1}{3|v_n^+|} \int_{T_n^+} \begin{bmatrix} x - x_n^+ \\ y - y_n^+ \\ z - z_n^+ \end{bmatrix} \cdot \begin{bmatrix} B_y\, z \\ B_z\, x \\ B_x\, y \end{bmatrix} dv, \end{aligned} \tag{5.2.9}$$

where $\mathbf{r_n^{c+}}$ is the free-vertex of $\rho_{\mathbf{n}}^+(\mathbf{r})$, see Fig. 2.3.3. In order to obtain an analytical solution for (5.2.9), the origin of the coordinate system has to be shifted towards the center of tetrahedron T_n^+,

$$\mathbf{r_n^{c+}} = \begin{bmatrix} x_n^c \\ y_n^c \\ z_n^c \end{bmatrix}, \tag{5.2.10}$$

Writing the magnetic vector potential in terms of the new coordinate system,

$$\mathbf{A_{ext}}(\mathbf{r}) = \begin{bmatrix} B_y\,(z + z_n^c) \\ B_z\,(x + x_n^c) \\ B_x\,(y + y_n^c) \end{bmatrix}, \tag{5.2.11}$$

where (x, y, z) is a point in the Cartesian coordinate system with origin $\mathbf{r_n^{c+}}$. Using the integration formula for a tetrahedron [57], an analytical solution for (5.2.9) can now be obtained,

$$\begin{aligned} A_n^+ &= \frac{1}{3|v_n^+|} \int_{T_n^+} \begin{bmatrix} x - x_n^+ \\ y - y_n^+ \\ z - z_n^+ \end{bmatrix} \cdot \begin{bmatrix} B_y\,(z + z_n^c) \\ B_z\,(x + x_n^c) \\ B_x\,(y + y_n^c) \end{bmatrix} dv \\ &= \frac{1}{3|v_n^+|} \int_{T_n^+} B_y\,(xz - x_n^+ z_n^c) + B_z\,(yx - y_n^+ x_n^c) + B_x\,(zy - z_n^+ y_n^c)\, dv \\ &= \frac{1}{3|v_n^+|} \left\{ \frac{|v_n^+|}{20} \Big[B_y\,(x_1z_1 + x_2z_2 + x_3z_3 + x_4z_4) \right. \\ &\qquad + B_z\,(x_1y_1 + x_2y_2 + x_3y_3 + x_4y_4) \\ &\qquad + B_x\,(y_1z_1 + y_2z_2 + y_3z_3 + y_4z_4) \Big] \\ &\qquad \left. - |v_n^+| \left[B_y\,(x_n^+ z_n^c) + B_z\,(y_n^+ x_n^c) + B_x\,(z_n^+ y_n^c) \right] \right\}, \end{aligned} \tag{5.2.12}$$

where $(x_1, ..., x_4;\, y_1, ..., y_4$ and $z_1, ..., z_4)$ are the coordinates of the four nodes of tetrahedron T_n^+, with the same origin $\mathbf{r_n^{c+}}$. Equation 5.2.12 is an exact solution

and can easily be implemented in code. Storing the vector potential, A_n, of each SWG basis function in the vector,

$$A_{branch} = \begin{bmatrix} A_1 \\ A_2 \\ \vdots \\ A_n \end{bmatrix}, \tag{5.2.13}$$

and using the matrix M, defined in Section 2.3.3, the vector potential can be computed for each VL basis function,

$$A_{mesh} = MA_{branch}, \tag{5.2.14}$$

where the columns index of M determines which vector potentials from A_{branch}, form part of each VL basis function. Using the same approach to obtain the linear system in Section 2.3.3, (5.2.2) can be converted to a system of linear equations,

$$\left(MZM^T\right) I_{mesh} = P_{mesh} - A_{mesh}, \tag{5.2.15}$$

where P_{mesh} is the amount of flux through each VL function, i.e. right-hand side of the linear system derived in [37], see Appendix A.

The mesh currents, I_m, induced by an external magnetic field can now be extracted by enforcing zero flux, $P_{mesh} = 0$, through each inductive loop (VL basis function),

$$\left(MZM^T\right) I_{mesh} = -A_{mesh}. \tag{5.2.16}$$

Given the self-inductance of an inductive loop, L_m, and the current induced by the external magnetic field, I_m, the total flux inside the inductive loop can be obtained,

$$\Phi_m = L_m I_m, \tag{5.2.17}$$

if zero mutual inductance is assumed.

5.2.1 Superconducting Washer in External Magnetic Field

Support for external magnetic fields was implemented in TTH using the method described in Section 5.2. The accuracy of this method can be determined by applying an external magnetic field to a thin square superconducting washer, as shown in Fig. 5.2.1. If the inductance of the washer is known, the total magnetic flux, Φ_w, through the inner surface of the washer can be approximated as,

$$\Phi_w \approx d^2(\mathbf{n_w} \cdot \mathbf{B_{ext}}) \approx L_w I_B, \tag{5.2.18}$$

for and applied external magnetic field, $\mathbf{B_{ext}}$. The vector $\mathbf{n_w}$ is the normal vector of the inner surface of the hole, with size $d \times d$, as shown in Fig. 5.2.1. The value L_w is the inductance of the washer and I_B is the circulating current induced by the external magnetic field. The thickness of the washer, t, was kept constant at $0.5\,\mu$m. The field penetrating the washer is not taken into account; therefore, the approximation in (5.2.18) is only valid if $t << d$. The amount of field penetrating the washer, depends on the London penetration depth and forms part of the kinetic inductance, i.e. the first term of (5.2.2), and not the geometric inductance.

Figure 5.2.2 shows the extracted magnetic flux, Φ_w, trough the inner surface calculated with TTH, which corresponds with the approximation in (5.2.18). The angle, θ, of the magnetic field is measured relative to the z-axis and the magnitude is kept constant at $50\,\mu$T. The error of the approximation in (5.2.18) is less than 1% when $d > 50\,\mu$m, i.e. $t < 100d$. It is also evident that the error of the approximation, (5.2.18), will never reach zero as t increases, since the kinetic inductance is not taken into account.

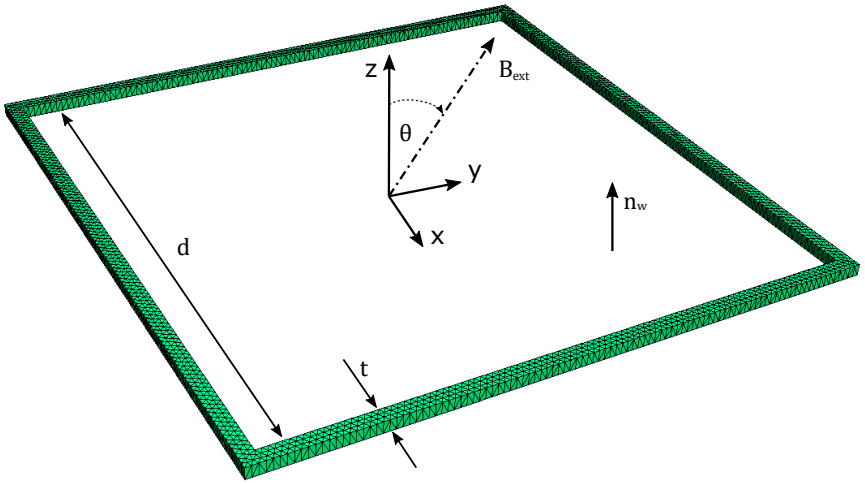

Figure 5.2.1: A superconducting washer (size $= d \times d$ and constant thickness $= 0.5\,\mu$m) with an applied external magnetic field.

5.2.2 Penetration Depths of Superconducting Slab

The accuracy of the magnetic field implementation can also be determined by applying a z-directed magnetic field, H_0, to a superconducting slab, as shown in Fig. 5.2.3a. The penetration depth of the slab is taken as: $\lambda = 90\,$nm; and the magnitude of the magnetic field: $H_0 = \frac{10^{-6}}{\mu_0}$A/m. The following thicknesses for the slab are evaluated: $2a = 500\,$nm, $2a = 1000\,$nm and $2a = 2000\,$nm. The current density inside the superconducting slab, calculated with TTH, is shown in Fig. 5.2.3b, including the analytical solution discussed in Section 2.6.1. The

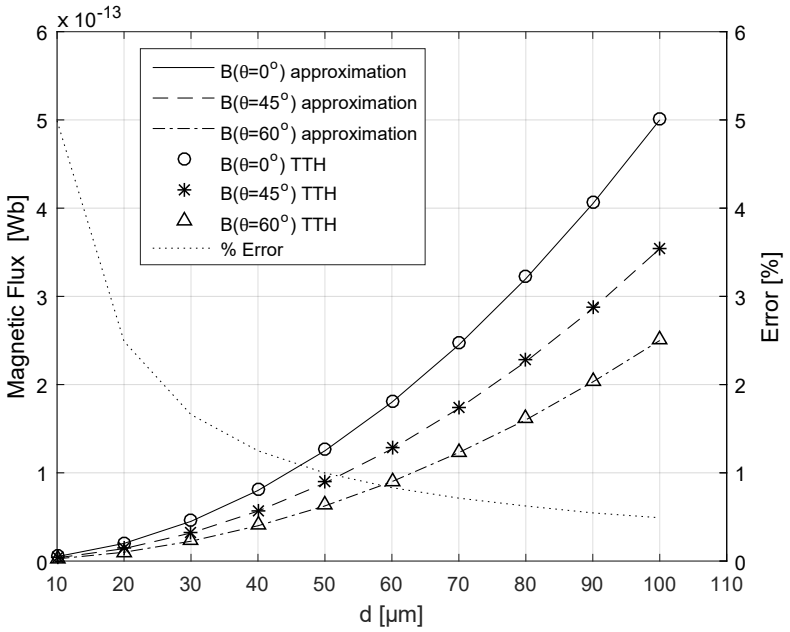

Figure 5.2.2: Computed magnetic flux through a thin superconducting washer. TTH results are compared to the approximation.

non-uniform current density, for each thicknesses of the superconducting slab, closely match the analytical solutions. Therefore, it is evident that both the magnetic field and London penetration depth are modeled correctly by TTH.

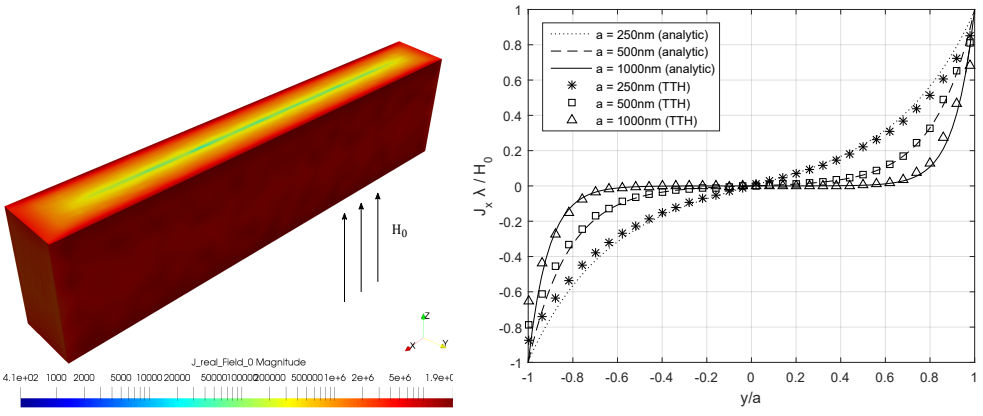

(a) (b)

Figure 5.2.3: (a) Superconducting slab (thicknesses $= 2a$ and $\lambda = 90\,\text{nm}$) in a z-directed magnetic field, H_0. (b) Normalised current density, J_x, inside superconducting slab, along the y-axis.

5.3 Equivalent Circuit Model for Magnetic Field

Now that support for external magnetic field is implemented in TTH, the magnetic coupling between a field and the inductors in a superconducting circuit can be obtained. Both the orientation and the magnitude of the field will determine the amount of current induced in each inductor. These magnetic couplings can then be used within equivalent SPICE models. A SPICE model has to be calculated for each angle of the magnetic field, but the same model can be used for different field magnitudes. This will allow to rapidly compute the operating margins of a circuit in the presence of an external magnetic field.

The inductance of each inductor can be extracted using the method described in Section 2.3.5 and InductEx [21, 2]. To obtain the mutual inductance between the magnetic field and each inductor in the circuit is not trivial, since the self-inductance of the magnetic field can be any arbitrary value. Generating a uniform vector field given in (5.2.1) can be approximated using Helmholtz coils [100, 101, 102], tetra coils [103], saddle coils [104, 105] or planar coils [106]. Although these methods will reach high field uniformity, the generated field will not offer a theoretically perfect uniform magnetic field, as given in (5.2.1). Instead ellipsoidal structures [107] or spheroidal helical coils [108] can be used to obtain a perfect uniform field, but calculating the self-inductance of such structures is challenging.

A simpler approach would be to assume that the magnetic field is generated by a fictitious coil (circular loop) of vanishing cross-section. The axis of such a coil should be in the same direction as the desired magnetic field, B_{ext}, as shown in Fig. 5.3.1. The radius of the coil, r_c, can be any arbitrary value, but must be large enough to ensure low mutual coupling between the coil and the inductors in the circuit. The reason for this is that all the currents inside the circuit will induce a small current inside the coil. Since this is a fictitious coil, extracting these induced currents is not possible.

One option is to assume that the current induced by the field in each inductor is equal to the current induced by the corresponding inductor in the fictitious coil. The currents induced in the fictitious coil will not have any effect on the external magnetic field, because it is defined as a constant in (5.2.1). Therefore, for this to be a valid assumption, the induced currents must be several orders smaller than current in the fictitious coil, I_c. This can be achieved by assuming that the radius of the fictitious coil is several orders larger than maximum dimension of the circuit, r_d.

If the test structure (circuit) is placed at the center of a circular coil, the circulating current can be calculated using the Biot-Savart law,

$$I_c = \frac{2r_c}{\mu_0} B_{ext}, \tag{5.3.1}$$

where B_{ext} is the magnitude of the applied magnetic field at the center of the

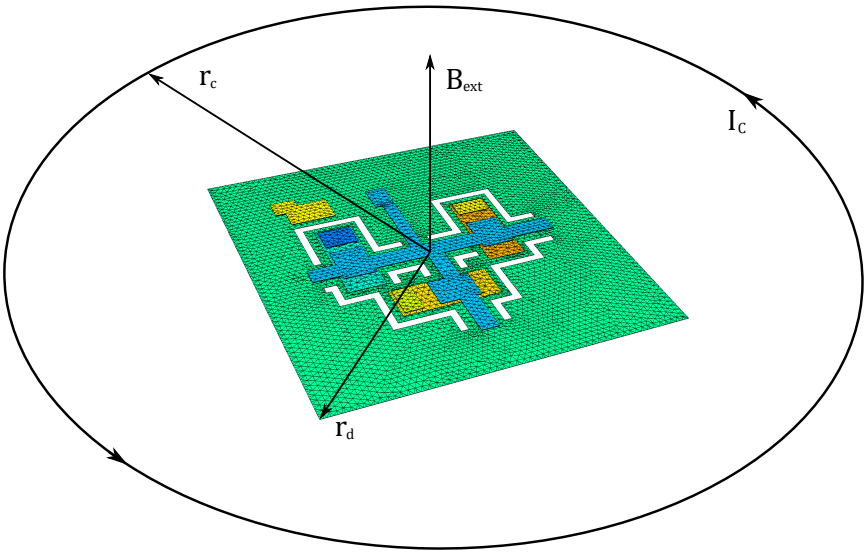

Figure 5.3.1: Magnetic field induce by a circulating current in a fictitious coil with radius r_c around a SFQ pulse splitter.

coil in the same direction of the coil's axis. An equivalent circuit can be used to modeled the magnetic field as an inductor, L_c, connected to a current source that magnetically couples with other inductors, as shown in Fig. 5.3.2.

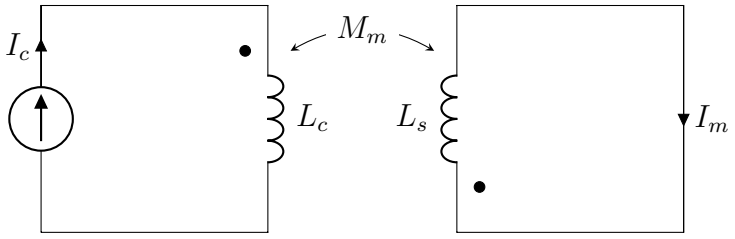

Figure 5.3.2: An equivalent circuit of the fictitious coil, L_c, magnetically coupling with an inductor, L_s, in the superconducting circuit.

The current, I_c, through the current source is calculated using (5.3.1). The inductor L_m represents an inductor in the superconducting circuit and M_m is the mutual inductance with the fictitious coil, L_c. The current induced by the external magnetic field, I_m, can be calculated using the method described in Section 5.2. From the equivalent circuit in Fig. 5.3.2, the total flux penetrating the inductive loop can be calculated as follow,

$$\Phi_m = L_m I_m - M_m I_c, \tag{5.3.2}$$

When applying an external magnetic field to a superconducting circuit, the current I_m is calculated using (5.2.16) and zero flux is enforced through each

inductive loop. Therefore, (5.3.2) becomes,

$$M_m I_c = L_m I_m. \tag{5.3.3}$$

The coupling factor can now be calculated as,

$$k_m = \frac{L_m I_m}{I_c \sqrt{L_c L_m}}. \tag{5.3.4}$$

The self-inductance, L_m, is calculated using the method described in [37], see Appendix A. Although the inductance of the fictitious coil, L_c, can be any arbitrary value, it must be chosen large enough to ensure that k_m is smaller than 1.0. Some SPICE engines do not allow coupling factors larger than 1.0. Using (5.3.4), the minimum value for L_c can be calculated when $k_m = 1$,

$$\min\left(L_c\right) = \min_{i \in [1,\ldots,m]} \frac{L_i I_i^2}{I_c^2}. \tag{5.3.5}$$

where L_i is the i^{th} inductor in the superconducting circuit and I_i is current induced in L_i by the applied magnetic field.

5.3.1 Superconducting Washer in Magnetic Field

To verify the accuracy of the equivalent circuit in Fig. 5.3.2, a magnetic field is applied to a $10\,\mu\text{m} \times 10\,\mu\text{m}$ washer, shown in Fig. 5.2.1, with a magnitude of $1\,\mu\text{T}$ at an angle of $\theta = 0^o$. The maximum radius of the washer is $r_d \approx 7\,\mu\text{m}$ and the radius of the fictitious coil is chosen to be 100 times larger than r_d, i.e $r_c = 0.7\,\text{mm}$. Using (5.3.1), the current through L_c can be estimated as $I_c = 1.11\,\text{mA}$. The self-inductance of the washer, $L_m = 41.8\,\text{pH}$, and the current induced by the magnetic field, $I_m = 2.51\,\mu\text{A}$, are calculated using the methods described in [37] and Section 5.2. The inductance of the coil is chosen as $L_c = 2.12\,\text{pH}$, which is 10000 times larger than the minimum value calculated in (5.3.5). For this value of L_c, the coupling factor is $k_m = 0.01$. Now that all the parameters are known, the equivalent circuit in Fig. 5.3.2 can be simulated using JSIM [109].

Figure 5.3.2 shows the current induced in the washer, I_m, as a function of the magnetic field's amplitude. The current calculated with JSIM, corresponds exactly with the current calculated with TTH, with no observable error. Therefore, the equivalent circuit in Fig. 5.3.2 can accurately model the magnetic coupling of the magnetic field with inductors in a superconducting circuit.

5.3.2 SFQ Pulse Splitter in Magnetic Field

To evaluate this method on a large-scale circuit, a magnetic field, $B_{ext} = 1\,\mu\text{T}$, is applied to the SFQ pulse splitter given in Fig. 2.7.5 in Chapter 2. The

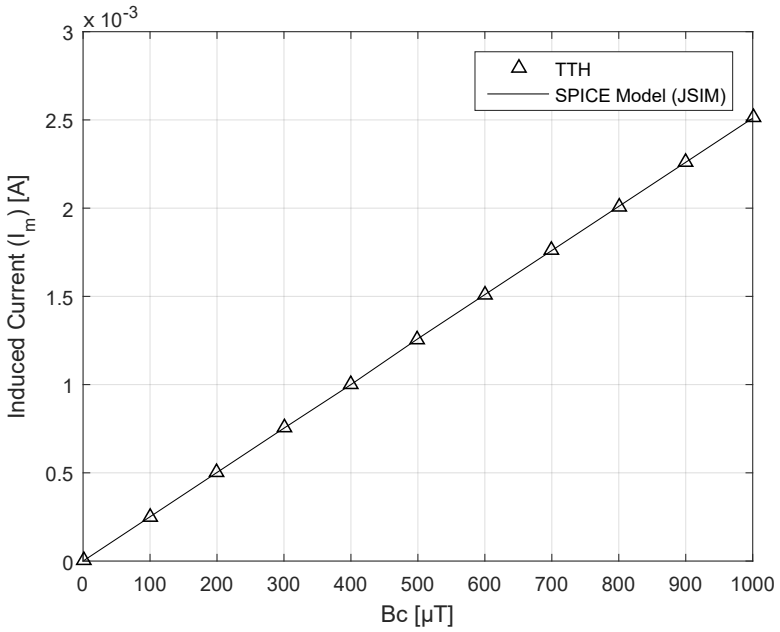

Figure 5.3.3: Current induced in the washer, I_m, as a function of the magnetic field's amplitude.

current distribution for the applied field is shown in Fig. 5.3.4. As expected, the current circulates along the edges of the ground plane for a z-directed magnetic field.

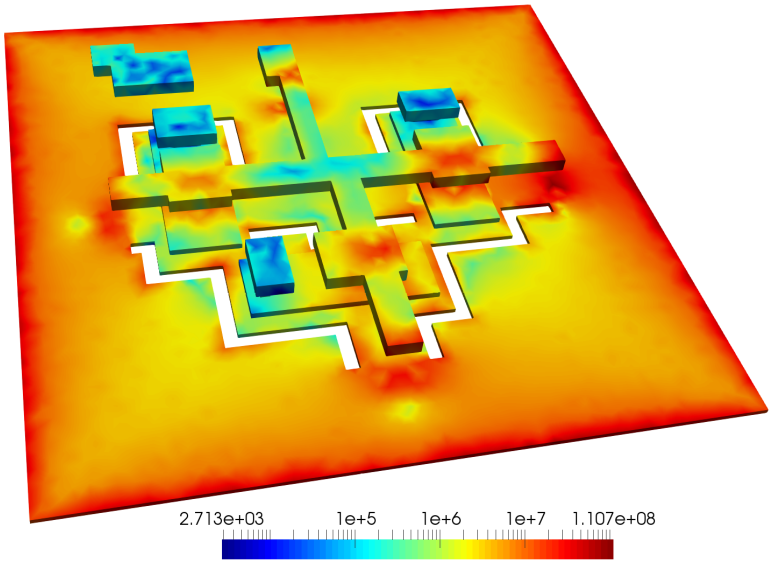

Figure 5.3.4: Current induced inside SFQ pulse splitter due to an external magnetic field in the z-direction.

The maximum dimension of the layout is 140 μm and the maximum dis-

tance from the center is $r_d = 70\,\mu$m. The radius of the fictitious coil is chosen to be 100 times larger than r_d, i.e $r_c = 7\,$mm. Given a field of $1\,\mu$T at the center of the fictitious coil, the current through the coil can be estimated as $I_c = 11.14\,$mA, using (5.3.1). The minimum value of L_c, as defined in (5.3.5), can not yet be calculated, since the self-inductance of each inductor is still unknown. As discussed in Chapter 2, the value of each inductor in the SFQ pulse splitter can be calculated using TTH and InductEx, see Fig. 2.7.5b. Table 5.3.1 shows the calculated inductance values. Since TTH uses a single fluxon to excite each inductive loop, a single fluxon can also be used to calculate the inductance of the fictitious coil, $L_c = \Phi_0/I_c = 0.186\,$pH. From the inductance values in Table 5.3.1, it can be shown that L_c is several orders larger than the minimum value given by (5.3.5).

Next, the current through each port is calculated for the applied magnetic field, using TTH and the method given in Section 5.2. These port currents, including the circuit netlist in Fig. 2.7.5b, are given to InductEx as input. The coupling factors (k) with the magnetic field (fictitious coil) in the x-, y- and z-direction are calculated, as shown in Table 5.3.1.

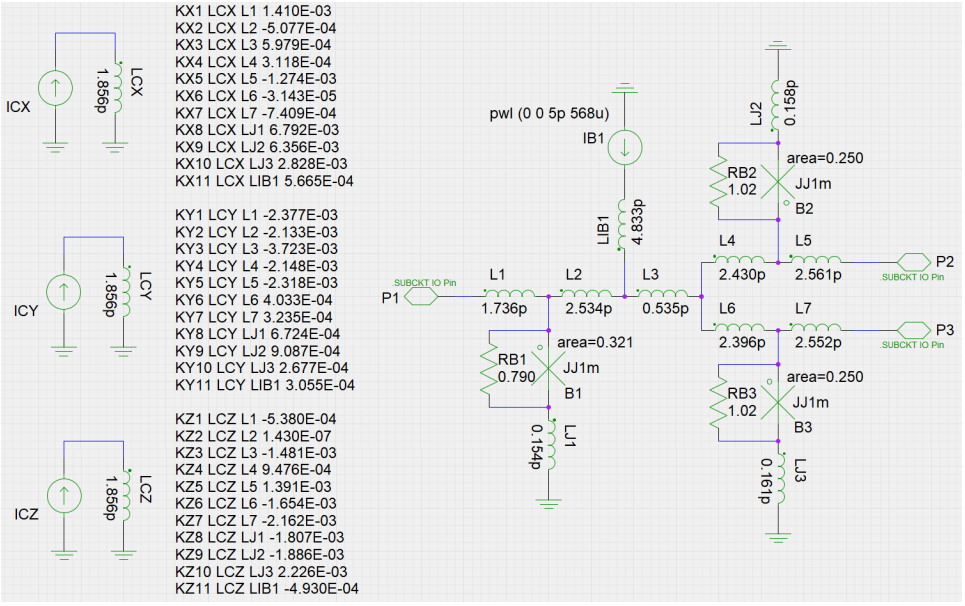

Figure 5.3.5: Circuit schematic of the SFQ pulse splitter. Magnetic fields (x-, y- and z-direction) are modeled as inductors connected to current sources.

Figure 5.3.5 shows the circuit schematic of the SFQ pulse splitter, with the magnetic fields modeled as inductors connected to current sources, similar to the model in Fig. 5.3.2. Coupling factors between the magnetic field and each inductor are added to the circuit schematic and the entire circuit is simulated using JSIM [109]. The operating margins of the SFQ pulse splitter is calculated for the three magnetic fields (x-, y- and z-direction), by sweeping the

magnitudes of the field, i.e. changing the magnitude of I_c. Figure 5.3.6 shows the operating margins of the three magnetic fields. The operating margins are determined by the component with the lowest margins, i.e. the maximum percentage deviation from its nominal value. As expected, the circuit is less sensitive to the magnetic field in the z-direction, compared to the x- and y-directed fields. The fields in x- and y-direction are perpendicular to the areas between the junctions and, therefore, have higher coupling effects. The area between junction "J1" and "J2" in Fig. 2.7.5a is approximately $60\,\mu\text{m} \times 700\,\text{nm}$. The field required for a single fluxon to be trapped between the junctions can be calculated as $\Phi_0/(60\,\mu\text{m} \times 700\,\text{nm}) \approx 50\,\mu\text{T}$, which corresponds with the maximum magnetic field in the y-direction.

Table 5.3.1: Coupling factors (k) between fictitious magnetic field coil ($L_c = 0.186\,\text{pH}$) and the inductors in Fig. 2.7.5b. The coupling factors are calculated for the magnetic field in the x-, y- and z-direction.

Inductor	Self-inductance [pH]	Coupling B_x	Coupling B_y	Coupling B_z
L1	1.7361	1.410e-03	-2.377e-03	-5.380e-04
L2	2.5339	-5.077e-04	-2.133e-03	1.430e-07
L3	0.5351	5.979e-04	-3.723e-03	-1.481e-03
L4	2.4298	3.118e-04	-2.148e-03	9.476e-04
L5	2.5609	-1.274e-03	-2.318e-03	1.391e-03
L6	2.3965	-3.143e-05	4.033e-04	-1.654e-03
L7	2.5522	-7.409e-04	3.235e-04	-2.162e-03
LJ1	0.1541	6.792e-03	6.724e-04	-1.807e-03
LJ2	0.1579	6.356e-03	9.087e-04	-1.886e-03
LJ3	0.1611	2.828e-03	2.677e-04	2.226e-03
LIB1	4.8334	5.665e-04	3.055e-04	-4.930e-04

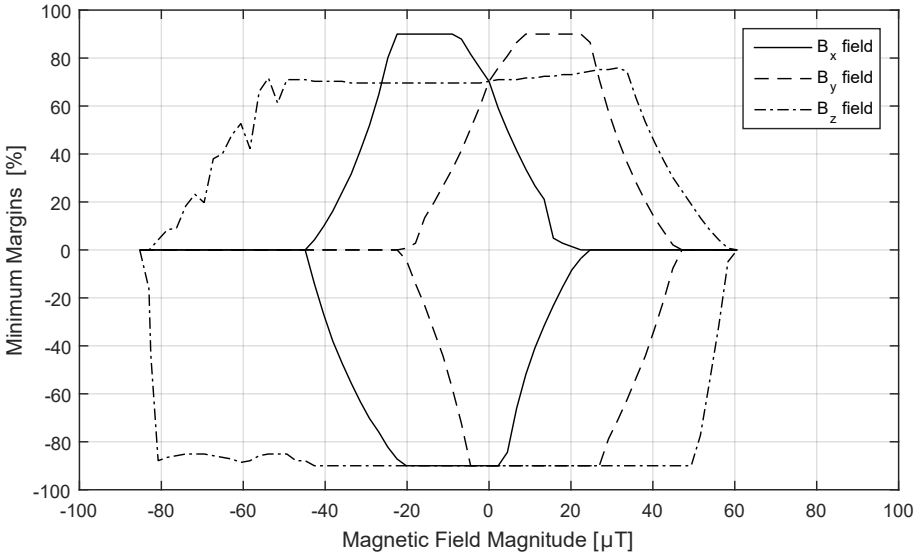

Figure 5.3.6: Operating margins of SFQ pulse splitter for magnetic fields in the x-, y- and z-directions.

5.4 Conclusion

Support for uniform external magnetic fields were implemented in TTH. The full derivation of the integral equation, with external magnetic field, is shown and demonstrated to be accurate. An equivalent circuit model is derived for external magnetic fields. This model is shown to be accurate and can be used, in SPICE engines, to rapidly analyse the performance of a superconducting circuit, in the presence of a magnetic field. The effects of external magnetic fields on the operating margins of a large SFQ pulse splitter are demonstrated.

Chapter 6

Fast Multipole Method for Biot-Savart Law

6.1 Introduction

When solving field problems containing magnetized materials in the presence of free electric currents, Biot-Savart law is often used to compute the magnetic field interaction between volumes containing magnetic and electric current densities [83, 82]. The computation time required to calculate the magnetic field of free currents increases exponentially as the number of volume elements increase and becomes infeasible for large scale structures.

Several methods [110, 76] have been developed to accelerate the computation of Biot-Savart law using the fast multipole method (FMM). The method proposed in [110] is discussed briefly and a detailed description of its implementation is not provided. The method proposed in [76] was developed for N-body simulations consisting of dynamic bodies and is mainly used in fields such as astrophysics and molecular dynamics. However, in many electromagnetic field solvers the problem domains are discretized into stationary volume or surface elements. The positions of these elements remain constant, whereas the field is the only dynamic component. This allows for substantial portions of the FMM to be precomputed and reused for a given set of discrete points. These precomputed parts of the FMM can then be used to replace direct multiplication in iterative solvers and has proven to be very efficient for solving large-scale problems, as demonstrated in FastCap [111] and FastHenry [20].

A FMM algorithm, referred to as BiotFMM, have therefore been developed to replace the direct multiplication of Biot-Savart law in iterative solvers. A full description of our algorithm and its implementation into the FMM code developed for FastCap and FastHenry is provided.

6.2 Far-Field Approximation

Given a volume, V, containing free electric currents, $\mathbf{J}$, the magnetic field, $\mathbf{H}$, can be calculated using Biot-Savart law:

$$\mathbf{H}(\mathbf{r}) = \frac{1}{4\pi} \int_V \mathbf{J}(\mathbf{r}) \times \nabla' G(\mathbf{r}, \mathbf{r}')\, dV' \tag{6.2.1}$$

where $\mathbf{r}$ and $\mathbf{r}'$ is respectively the evaluation and charge points, and $\nabla' G(\mathbf{r}, \mathbf{r}')$ is the gradient of Green's function,

$$\nabla' G(\mathbf{r}, \mathbf{r}') = \frac{\mathbf{r} - \mathbf{r}'}{|\mathbf{r} - \mathbf{r}'|^{\mathbf{3}}}. \tag{6.2.2}$$

The location of current vectors are referred to as charge points, since the three components of each current vector can be interpreted as charges when using the electrostatic analogy described in [20]. The evaluation of (6.2.1) can be accelerated using the FMM, which splits the field computation into two parts:

$$\mathbf{H}(\mathbf{r}) = \mathbf{H}_{\mathbf{near}}(\mathbf{r}) + \mathbf{H}_{\mathbf{far}}(\mathbf{r}) \tag{6.2.3}$$

where $\mathbf{H}_{\mathbf{near}}(\mathbf{r})$ is due to charges close to the evaluation points and $\mathbf{H}_{\mathbf{far}}(\mathbf{r})$ is due to charges far from the evaluation points. A full description of the hierarchical octree algorithm that divides the problem domain into near- and far-field regions is given in [111]. The near-field is computed directly, whereas the far-field can be approximated arbitrarily accurately by expanding the Green's function into a series of spherical harmonics, $Y_n^m(\theta, \phi)$,

$$G(r, \theta, \phi) \approx \sum_{n=0}^{l} \sum_{m=-n}^{n} \frac{r'^n}{r^{n+1}} Y_n^m(\theta, \phi) Y_n^{-m}(\theta', \phi'), \tag{6.2.4}$$

where r, θ and ϕ are the spherical coordinates of the evaluation points and l is the order of expansion [110, 112].

6.2.1 Multipole Expansion

When the radius of a sphere enclosing a group of charges is sufficiently smaller than the nearest evaluation point, the group of charges can be replaced by a single charge at the center of the sphere. This approximation is known as monopole approximation [111]. Substituting $G(\mathbf{r}, \mathbf{r}')$ in (6.2.1) with (6.2.4), the magnetic field can be approximated by a truncated multipole expansion:

$$\mathbf{H}(r, \theta, \phi) \approx \frac{1}{4\pi} \sum_{n=0}^{l} \sum_{m=-n}^{n} \mathbf{M}_{\mathbf{n}}^{\mathbf{m}} \frac{1}{r^{n+1}} Y_n^m(\theta, \phi). \tag{6.2.5}$$

The multipole coefficient vectors, $\mathbf{M}_{\mathbf{n}}^{\mathbf{m}}$, contain the complex weights of the series expansion and can be computed as proposed in [110],

$$\mathbf{M}_{\mathbf{n}}^{\mathbf{m}} = \int_V \mathbf{J}(\mathbf{r}') \times \nabla_{\mathbf{r}'} \left[r'^n \, Y_n^{-m}(\theta', \phi') \right] \, dV'. \tag{6.2.6}$$

In order to account for the gradient operator, $\nabla_{\mathbf{r}'}$, vector spherical harmonics (VSH) are used. Several conventions for VSH have already been defined [7]-[113]. Given the scalar spherical harmonic, $Y_n^m(\theta, \phi)$, and using the convention defined in [7], a vector field can be expressed as a linear combination of VSH:

$$\mathbf{Y}_{\mathbf{n}}^{\mathbf{m}}(\theta, \phi) = Y_n^m(\theta, \phi) \, \hat{\mathbf{e}}_{\mathbf{r}}, \tag{6.2.7}$$

$$\mathbf{\Psi}_{\mathbf{n}}^{\mathbf{m}}(\theta, \phi) = r \, \nabla Y_n^m(\theta, \phi), \tag{6.2.8}$$

$$\mathbf{\Phi}_{\mathbf{n}}^{\mathbf{m}}(\theta, \phi) = \hat{\mathbf{e}}_{\mathbf{r}} \times \mathbf{Y}_{\mathbf{n}}^{\mathbf{m}}(\theta, \phi), \tag{6.2.9}$$

where $\hat{\mathbf{e}}_{\mathbf{r}}$ is the unit vector along the radial direction. As stated in [7], if a scalar function, F, is expanded with spherical harmonics,

$$F(r, \theta, \phi) \approx \sum_{n=0}^{l} \sum_{m=-n}^{n} F_n^m(r) \, Y_n^m(\theta, \phi), \tag{6.2.10}$$

the gradient of F can be expressed as:

$$\nabla F(r, \theta, \phi) \approx \sum_{n=0}^{l} \sum_{m=-n}^{n} \nabla \left[F_n^m(r) \, Y_n^m(\theta, \phi) \right], \tag{6.2.11}$$

where

$$\nabla \left[F_n^m(r) \;\; Y_n^m \right] = \left(\frac{d}{dr} F_n^m(r) \right) \mathbf{Y}_{\mathbf{n}}^{\mathbf{m}} + \frac{F_n^m(r)}{r} \mathbf{\Psi}_{\mathbf{n}}^{\mathbf{m}}. \tag{6.2.12}$$

Using (6.2.12) and taking $F_n^m(\rho) = \rho^n$, the multipole coefficients, $\mathbf{M}_{\mathbf{n}}^{\mathbf{m}}$, can be expressed as a linear system of VSH:

$$\mathbf{M}_{\mathbf{n}}^{\mathbf{m}} \equiv \sum_{i=1}^{k} \mathbf{I}_i \times \rho_i^{n-1} \left[n \, \mathbf{Y}_{\mathbf{n}}^{-\mathbf{m}}(\alpha_i, \beta_i) + \mathbf{\Psi}_{\mathbf{n}}^{-\mathbf{m}}(\alpha_i, \beta_i) \right]. \tag{6.2.13}$$

The constant k represents the number of currents, $\mathbf{I}_i$ is the current vector, and ρ_i, α_i and β_i is the spherical coordinates of the ith element.

6.2.2 Local Expansions

When the radius of a sphere enclosing a group of evaluation points is sufficiently smaller than the nearest charge, the field calculated at these evaluation points are approximately equal to the field calculated at the center of the sphere. This approximation is known as local expansion [111]. Substituting $G(\mathbf{r}, \mathbf{r}')$

in (6.2.1) with (6.2.4), the magnetic field can be approximated by a truncated local expansion [110]:

$$\mathbf{H}(r,\theta,\phi) \approx \frac{1}{4\pi} \sum_{n=0}^{l} \sum_{m=-n}^{n} \mathbf{L}_{\mathbf{n}}^{\mathbf{m}}\, r^n\, Y_n^m(\theta,\phi), \tag{6.2.14}$$

The local coefficient vectors $\mathbf{L}_{\mathbf{n}}^{\mathbf{m}}$ contain the complex weights of the local series expansion and can be computed as follow:

$$\mathbf{L}_{\mathbf{n}}^{\mathbf{m}} = \int_V \mathbf{J}(\mathbf{r}') \times \nabla_{\mathbf{r}'} \left[\frac{1}{r'^{n+1}}\, Y_n^{-m}(\theta',\phi') \right] dV'. \tag{6.2.15}$$

Using (6.2.12) and taking $F_n^m(\rho) = 1/\rho^{n+1}$, the local coefficients $\mathbf{L}_{\mathbf{n}}^{\mathbf{m}}$ can be expressed as a linear system of VSH:

$$\mathbf{L}_{\mathbf{n}}^{\mathbf{m}} \equiv \sum_{i=1}^{k} \mathbf{I}_i \times \frac{1}{\rho_i^{n+2}} \left[-(n+1)\, \mathbf{Y}_{\mathbf{n}}^{-\mathbf{m}}(\alpha_i,\beta_i) + \mathbf{\Psi}_{\mathbf{n}}^{-\mathbf{m}}(\alpha_i,\beta_i) \right]. \tag{6.2.16}$$

6.3 Real Coeficient Multipole Algorithm

The reader will notice that the multipole coefficient vectors, $\mathbf{M}_{\mathbf{n}}^{\mathbf{m}}$, and local coefficient vectors, $\mathbf{L}_{\mathbf{n}}^{\mathbf{m}}$, consist of complex values. Using the algorithm described in [111], the complex coefficients can be replaced with real coefficients, $\bar{\mathbf{M}}_{\mathbf{n}}^{\mathbf{m}}$ and $\bar{\mathbf{L}}_{\mathbf{n}}^{\mathbf{m}}$. This eliminates the need for square root calculations and the storage of complex values. Starting with the Schmidt semi-normalized spherical harmonics, a formula for $\mathbf{Y}_{\mathbf{n}}^{-\mathbf{m}}(\theta,\phi)$ can be easily obtained and computed directly,

$$Y_n^{-m}(\theta,\phi) = \sqrt{\frac{(n-|m|)!}{(n+|m|)!}}\, P_n^{|m|}(\cos\theta)\, e^{-jm\phi}. \tag{6.3.1}$$

The function $P_n^m(\cos\theta)$ is the associated Legendre-function of the first kind with degree n and order m. Taking the gradient of Y_n^{-m} in spherical coordinates,

$$\begin{aligned} \nabla Y_n^{-m}(\theta,\phi) = \sqrt{\frac{(n-|m|)!}{(n+|m|)!}}\, e^{-jm\phi} \Bigg\{ & \frac{1}{r} \frac{\partial}{\partial\theta} P_n^{|m|}(\cos\theta)\, \hat{\mathbf{e}}_\theta \\ & -j \frac{m}{r\,\sin\theta}\, P_n^{|m|}(\cos\theta)\, \hat{\mathbf{e}}_\phi \Bigg\}, \end{aligned} \tag{6.3.2}$$

and inserting (6.3.2) into (6.2.8), we obtain an expression for $\mathbf{\Psi}_{\mathbf{n}}^{-\mathbf{m}}$,

$$\begin{aligned} \mathbf{\Psi}_{\mathbf{n}}^{-\mathbf{m}}(\theta,\phi) = \sqrt{\frac{(n-|m|)!}{(n+|m|)!}}\, e^{-jm\phi} \Bigg\{ & \frac{\partial}{\partial\theta} P_n^{|m|}(\cos\theta)\, \hat{\mathbf{e}}_\theta \\ & -j\, \frac{m}{\sin\theta}\, P_n^{|m|}(\cos\theta)\, \hat{\mathbf{e}}_\phi \Bigg\}. \end{aligned} \tag{6.3.3}$$

The vectors $\hat{\mathbf{e}}_\theta$ and $\hat{\mathbf{e}}_\phi$ represent the unit vectors of the spherical coordinate system. Table (6.3.1) presents a few explicit values for the vector spherical harmonics $\mathbf{\Psi}_\mathbf{n}^\mathbf{m}$. From (6.3.1) and (6.3.3) it is evident that the following relations are satisfied:

$$\mathbf{Y}_\mathbf{n}^{-\mathbf{m}}(\theta,\phi) = \mathbf{Y}_\mathbf{n}^\mathbf{m}(\theta,\phi)^*, \tag{6.3.4}$$

and

$$\mathbf{\Psi}_\mathbf{n}^{-\mathbf{m}}(\theta,\phi) = \mathbf{\Psi}_\mathbf{n}^\mathbf{m}(\theta,\phi)^*. \tag{6.3.5}$$

From (6.3.4) and (6.3.5) it is now evident that $\mathbf{M}_\mathbf{n}^{-\mathbf{m}}$ is always the complex conjugate of $\mathbf{M}_\mathbf{n}^\mathbf{m}$ and $\mathbf{L}_\mathbf{n}^{-\mathbf{m}}$ is the complex conjugate of $\mathbf{L}_\mathbf{n}^\mathbf{m}$. It can, therefore, be shown that the imaginary parts of the series expansions (6.2.5) and (6.2.14) will cancel out when $m \in [-n, n]$.

Table 6.3.1: Normalised vector spherical harmonics $\mathbf{\Psi}_\mathbf{n}^\mathbf{m}(\theta,\phi)$ [7]

n	$m=0$	$m=1$	$m=2$	$m=3$
0	0			
1	$-\sin\theta\,\hat{\mathbf{e}}_\theta$	$-\sqrt{\frac{1}{2}}e^{j\phi}$ $\cdot(\cos\theta\,\hat{\mathbf{e}}_\theta + j\hat{\mathbf{e}}_\phi)$		
2	$-\sqrt{\frac{9}{2}}$ $\cdot(\sin\theta\ \cos\theta)\hat{\mathbf{e}}_\theta$	$-\sqrt{\frac{3}{2}}e^{j\phi}$ $\cdot\ [\cos 2\theta\,\hat{\mathbf{e}}_\theta\ + j\ \cos\theta\,\hat{\mathbf{e}}_\phi]$	$\sqrt{\frac{3}{2}}\sin\theta\,e^{2j\phi}$ $\cdot(\cos\theta\,\hat{\mathbf{e}}_\theta + j\hat{\mathbf{e}}_\phi)$	
3	$-\frac{3}{2}[5\ \sin\theta\ \cos^2\theta$ $-\sin\theta]\hat{\mathbf{e}}_\theta$	$\sqrt{\frac{3}{16}}e^{j\phi}$ $\cdot[\cos\theta(15\ \cos^2\theta - 11)\hat{\mathbf{e}}_\theta$ $-j(5\ \cos^2\theta - 1)\hat{\mathbf{e}}_\phi]$	$\sqrt{\frac{15}{2}}\sin\theta\,e^{2j\phi}$ $\cdot[\frac{1}{2}(3\ \cos^2\theta + 1)\hat{\mathbf{e}}_\theta$ $-j\ \cos\theta\,\hat{\mathbf{e}}_\phi]$	$-\sqrt{\frac{45}{16}}\sin^2\theta\,e^{3j\phi}$ $\cdot[\cos\theta\,\hat{\mathbf{e}}_\theta + j\hat{\mathbf{e}}_\phi]$

6.3.1 Multipole Expansion Matrices (Q2M)

Starting with the multipole expansion approximation of the magnetic field given in (6.2.5) and substituting the spherical harmonics using (6.3.1), the magnetic field at location $(r,\ \theta,\ \phi)$ can be computed as follow:

$$\mathbf{H}(r,\theta,\phi) \approx \frac{1}{4\pi}\sum_{n=0}^{l}\sum_{m=-n}^{n}\mathbf{M}_\mathbf{n}^\mathbf{m}\,\frac{1}{r^{n+1}}\sqrt{\frac{(n-|m|)!}{(n+|m|)!}}\,P_n^{|m|}(\cos\theta)\,e^{jm\phi}. \tag{6.3.6}$$

Using the definition (A1) and (A2) in [111], (6.3.6) can be transformed into the real coefficient multipole expansion,

$$\begin{aligned}\mathbf{H}(r,\theta,\phi) \approx \frac{1}{4\pi}\sum_{n=0}^{l}\frac{1}{r^{n+1}}\sum_{m=0}^{n}\frac{(n-m)!}{(n+m)!}\,P_n^m(\cos\theta)\\ \cdot\left[\bar{\mathbf{M}}_\mathbf{n}^\mathbf{m}\ \cos(m\phi) + \tilde{\mathbf{M}}_\mathbf{n}^\mathbf{m}\ \sin(m\phi)\right].\end{aligned} \tag{6.3.7}$$

Given the multipole expansion coefficients defined in (6.2.13) for k currents at the spherical coordinates (ρ_i, α_i, β_i), the real multipole expansion coefficients $\bar{\mathbf{M}}_{\mathbf{n}}^{\mathbf{m}}$ and $\tilde{\mathbf{M}}_{\mathbf{n}}^{\mathbf{m}}$ can be computed,

$$\bar{\mathbf{M}}_{\mathbf{n}}^{\mathbf{m}} = \begin{cases} 2\sum_{i=1}^{k} \mathbf{I}_i \times \rho_i^{n-1} \Big[n\, P_n^{|m|}(\cos\alpha_i)\, \cos(m\beta_i)\, \hat{\mathbf{e}}_{\mathbf{r}} \\ \qquad + \dfrac{\partial}{\partial\alpha} P_n^{|m|}(\cos\alpha_i)\, \cos(m\beta_i)\, \hat{\mathbf{e}}_{\theta} \\ \qquad - \dfrac{m}{\sin\alpha_i} P_n^{|m|}(\cos\alpha_i)\, \sin(m\beta_i)\, \hat{\mathbf{e}}_{\phi} \Big], & m > 0, |m| \le n \\ \sum_{i=1}^{k} \mathbf{I}_i \times \rho_i^{n-1} \Big[n\, P_n^{0}(\cos\alpha_i)\, \hat{\mathbf{e}}_{\mathbf{r}} \\ \qquad + \dfrac{\partial}{\partial\alpha} P_n^{0}(\cos\alpha_i)\, \hat{\mathbf{e}}_{\theta} \Big], & m = 0, m \le n \\ 0, & \text{otherwise} \end{cases} \tag{6.3.8}$$

and

$$\tilde{\mathbf{M}}_{\mathbf{n}}^{\mathbf{m}} = \begin{cases} 2\sum_{i=1}^{k} \mathbf{I}_i \times \rho_i^{n-1} \Big[n\, P_n^{|m|}(\cos\alpha_i)\, \sin(m\beta_i)\, \hat{\mathbf{e}}_{\mathbf{r}} \\ \qquad + \dfrac{\partial}{\partial\alpha} P_n^{|m|}(\cos\alpha_i)\, \sin(m\beta_i)\, \hat{\mathbf{e}}_{\theta} \\ \qquad + \dfrac{m}{\sin\alpha_i} P_n^{|m|}(\cos\alpha_i)\, \cos(m\beta_i)\, \hat{\mathbf{e}}_{\phi} \Big], & |m| > 0, |m| \le n \\ 0, & \text{otherwise.} \end{cases} \tag{6.3.9}$$

6.3.2 Local Expansion Matrices (Q2L)

Starting with the local expansion approximation of the magnetic field given in (6.2.14) and substituting the spherical harmonics using (6.3.1), the magnetic field at location (r, θ, ϕ) can be computed as follow:

$$\mathbf{H}(r,\theta,\phi) \approx \frac{1}{4\pi} \sum_{n=0}^{l} \sum_{m=-n}^{n} \mathbf{L}_{\mathbf{n}}^{\mathbf{m}}\, r^n \sqrt{\frac{(n-|m|)!}{(n+|m|)!}}\, P_n^{|m|}(\cos\theta)\, e^{jm\phi}. \tag{6.3.10}$$

Using the definition (A1) and (A2) in [111], (6.3.10) can be transformed into the real coefficient local expansion,

$$\begin{aligned} \mathbf{H}(r,\theta,\phi) \approx \frac{1}{4\pi} \sum_{n=0}^{l} r^n \sum_{m=0}^{n} \frac{(n-m)!}{(n+m)!} P_n^m(\cos\theta) \\ \cdot \Big[\bar{\mathbf{L}}_{\mathbf{n}}^{\mathbf{m}} \cos(m\phi) + \tilde{\mathbf{L}}_{\mathbf{n}}^{\mathbf{m}} \sin(m\phi) \Big]. \end{aligned} \tag{6.3.11}$$

Given the local expansion coefficients defined in (6.2.16) for k currents at the spherical coordinates $(\rho_i,\ \alpha_i,\ \beta_i)$, the real local expansion coefficients $\bar{\mathbf{L}}_{\mathbf{n}}^{\mathbf{m}}$ and $\tilde{\mathbf{L}}_{\mathbf{n}}^{\mathbf{m}}$ can be computed,

$$\bar{\mathbf{L}}_{\mathbf{n}}^{\mathbf{m}} = \begin{cases} 2\sum_{i=1}^{k} \mathbf{I}_i \times \frac{1}{\rho_i^{n+2}} \Big[-(n+1)\, P_n^{|m|}(\cos\alpha_i)\, \cos(m\beta_i)\, \hat{\mathbf{e}}_{\mathbf{r}} \\ \qquad + \frac{\partial}{\partial\alpha} P_n^{|m|}(\cos\alpha_i)\, \cos(m\beta_i)\, \hat{\mathbf{e}}_{\theta} \\ \qquad - \frac{m}{\sin\alpha_i} P_n^{|m|}(\cos\alpha_i)\, \sin(m\beta_i)\, \hat{\mathbf{e}}_{\phi}\Big], & m > 0, |m| \le n \\ \sum_{i=1}^{k} \mathbf{I}_i \times \frac{1}{\rho_i^{n+2}} \Big[-(n+1)\, P_n^{0}(\cos\alpha_i)\, \hat{\mathbf{e}}_{\mathbf{r}} \\ \qquad + \frac{\partial}{\partial\alpha} P_n^{0}(\cos\alpha_i)\, \hat{\mathbf{e}}_{\theta}\Big], & m = 0, m \le n \\ 0, & \text{otherwise} \end{cases} \tag{6.3.12}$$

and

$$\tilde{\mathbf{L}}_{\mathbf{n}}^{\mathbf{m}} = \begin{cases} 2\sum_{i=1}^{k} \mathbf{I}_i \times \frac{1}{\rho_i^{n+2}} \Big[-(n+1)\, P_n^{|m|}(\cos\alpha_i)\, \sin(m\beta_i)\, \hat{\mathbf{e}}_{\mathbf{r}} \\ \qquad + \frac{\partial}{\partial\alpha} P_n^{|m|}(\cos\alpha_i)\, \sin(m\beta_i)\, \hat{\mathbf{e}}_{\theta} \\ \qquad + \frac{m}{\sin\alpha_i} P_n^{|m|}(\cos\alpha_i)\, \cos(m\beta_i)\, \hat{\mathbf{e}}_{\phi}\Big], & |m| > 0, |m| \le n \\ 0, & \text{otherwise.} \end{cases} \tag{6.3.13}$$

6.4 Implementation of FMM Algorithm

The real expansion coefficients defined in Section 6.3 have the same format as (A11), (A12), (A17) and (A18) defined in [111]. By treating each vector component of (6.3.7) and (6.3.11) as a scalar potential, the standard FMM implementation in FastCap and FastHenry can be used. The algorithm has to be called three times, once for each component of $\mathbf{H}(r, \theta, \phi)$. It is important to note that the vectors in (6.3.8), (6.3.9), (6.3.12) and (6.3.13) are given in spherical coordinates and must be transform back to the Cartesian coordinate system.

Although the implementation of $P_n^m(\cos\theta)$ has already been defined in [111], special care has to be taken when implementing $\frac{\partial}{\partial\theta}P_n^m(\cos\theta)$ and $\frac{m}{\sin\theta}P_n^m(\cos\theta)$, especially for cases where $\theta = 0$. Using the recurrence properties of the associated Legendre polynomials,

$$(x^2-1)\frac{d}{dx}P_n^m(x) = \sqrt{1-x^2}\,P_n^{m+1}(x) + mx\,P_n^m(x), \tag{6.4.1}$$

and

$$(x^2-1)\frac{d}{dx}P_n^m(x) = -(n+m)(n-m+1)\sqrt{1-x^2}P_n^{m-1}(x) - mxP_n^m(x), \tag{6.4.2}$$

and substituting x with $\cos\theta$, the derivative of $P_n^m(\cos\theta)$ can be computed for $m \geq 0$,

$$\frac{\partial}{\partial\theta}P_n^m(\cos\theta) = \frac{\partial P_n^m(\cos\theta)}{\partial\cos\theta}\cdot\frac{\partial\cos\theta}{\partial\theta}$$

$$= \begin{cases} P_n^{m+1}(\cos\theta) + \frac{m\cos\theta}{\sin\theta}P_n^m(\cos\theta), & m > 0, m < n \\ -(n+m)P_n^{m-1}(\cos\theta) - \\ \qquad \frac{m\cos\theta}{\sin\theta}P_n^m(\cos\theta), & m > 0, m = n \\ P_n^1(\cos\theta), & m = 0. \end{cases} \tag{6.4.3}$$

A simple implementation of $\frac{m}{\sin\theta}P_n^m(\cos\theta)$ can also be obtained starting with the following recurrence property,

$$\frac{1}{\sqrt{1-x^2}}P_n^m(x) = \frac{-1}{2m}\left[P_{n+1}^{m+1}(x) + (n-m+1)(n-m+2)\,P_{n+1}^{m-1}(x)\right]. \tag{6.4.4}$$

Substituting x in (6.4.4) with $\cos\theta$ and assuming $m \geq 0$,

$$\frac{m}{\sin\theta}P_n^m(\cos\theta) = \begin{cases} -\frac{1}{2}\left[P_{n+1}^{m+1}(\cos\theta) + (n-m+1)\right. & \\ \qquad \left.\cdot(n-m+2)P_{n+1}^{m-1}(\cos\theta)\right], & m > 0, m \leq n \\ 0, & m = 0. \end{cases} \tag{6.4.5}$$

6.5 Numerical Results

The magnetic field surrounding a $50\mu m \times 5\mu m$ superconducting microstrip line [114] is shown in Fig 6.5.1. The magnetic field was calculated using the

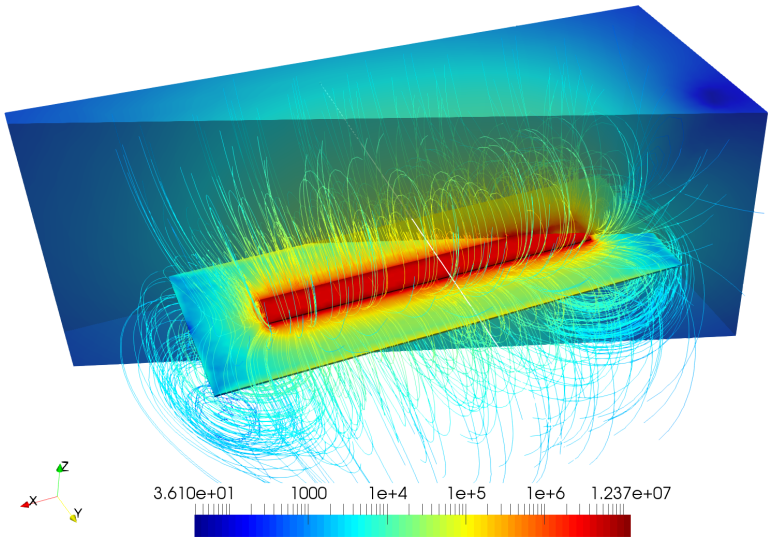

Figure 6.5.1: Magnetic field, H, surrounding a superconducting microstrip line. Streamlines were generated using ParaView [5, 6].

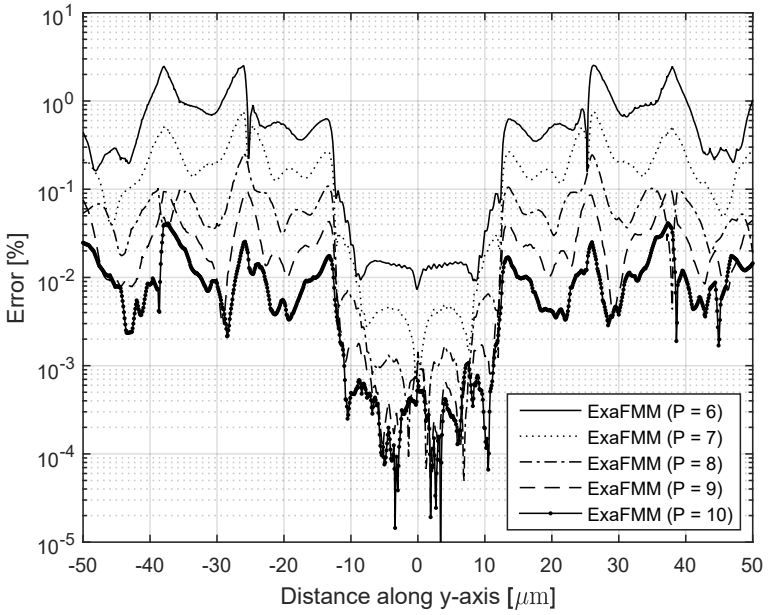

Figure 6.5.2: Relative error (%) along y-axis for ExaFMM (MAC = 0.3).

proposed FMM (BiotFMM) at observation points distributed throughout an enclosing volume. The current distribution was generated using TTH [114].

To evaluate the efficiency of BiotFMM, we compared the accuracy and computation time with ExaFMM [76, 6]. For ExaFMM, the multipole acceptance criterion (MAC) [76] and the maximum number of particles per leaf was chosen as 0.3 and 64, respectively. BiotFMM divides the problem domain into

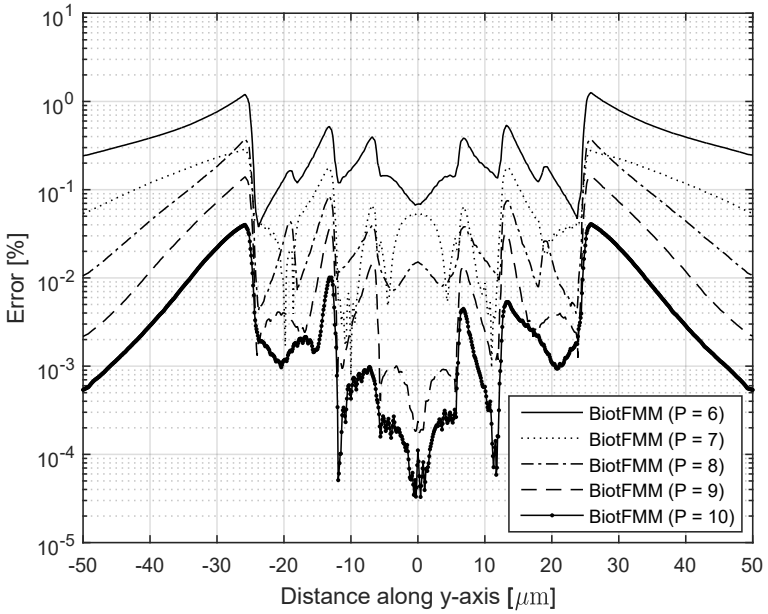

Figure 6.5.3: Relative error (%) along y-axis for BiotFMM.

a hierarchy of cubes [111], which was kept constant at 6 levels for all expansion orders. These values were chosen in such a way that the two algorithms produced similar error plots. Figure (6.5.3) and (6.5.5) show the relative error of the magnetic field along the y-axis, $40\mu m$ above the microstrip, for ExaFMM and BiotFMM, respectively. The relative error (L2-norm) was computed by comparing the vector fields of the FMM algorithms to the direct computation in (6.2.1). From Fig. 6.5.3 it is evident that the error of BiotFMM is far below 1% when the order of series expansions is 7 and decreases for higher expansion orders.

The computation time of BiotFMM and the direct approach is plotted in Fig. 6.5.4 as a function of problem size. Figure 6.5.5 and 6.5.6 show the computation time of BiotFMM and ExaFMM as a function of expansion order (P) and problem size, respectively. All experiments were performed on the same computer with an i7-6700HQ processor and 8-GB memory. Both BiotFMM and ExaFMM was compiled with the same compiler settings and all optimization libraries were disabled. To prevent the direct interactions from dominating the computation time, it was pre-calculated and stored in matrices for both ExaFMM and BiotFMM. The setup time of the expansion coefficient matrices is not included in the calculation time for BiotFMM, since these matrices are computed only once and reused within iterative solvers. ExaFMM requires these matrices to be recalculated each time the far-field is computed, since it was originally developed for dynamic problems. It is therefore evident from Fig. 6.5.3, 6.5.5 and 6.5.6 that BiotFMM can significantly reduce computation time of electromagnetic field solvers that use iterative solvers [83, 82].

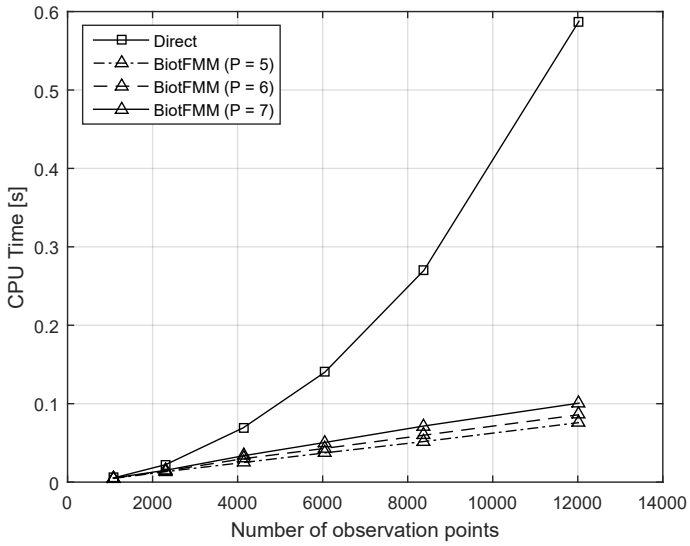

Figure 6.5.4: Calculation time of BiotFMM for different expansion orders (P) vs direct approach.

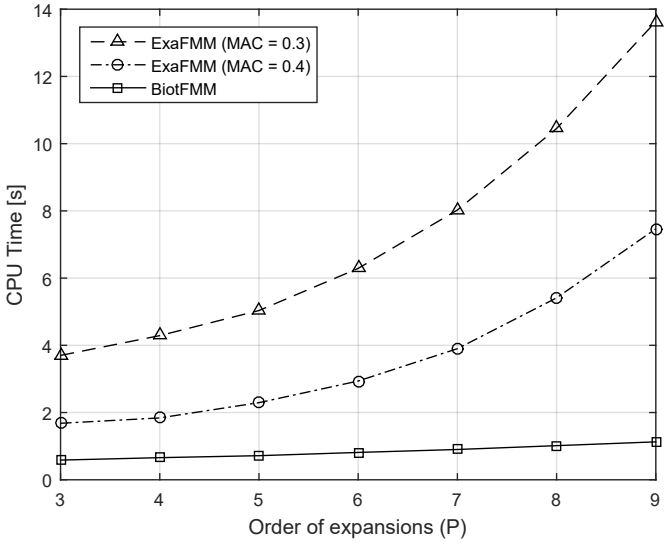

Figure 6.5.5: Calculation time of BiotFMM and ExaFMM for a problem consisting of $80,000$ observation points.

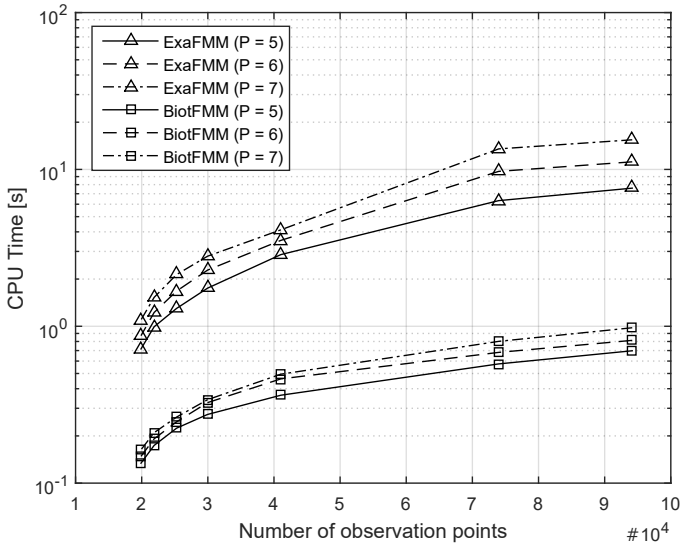

Figure 6.5.6: Calculation time of BiotFMM and ExaFMM as a function of problem size.

6.6 Conclusion

In this section an approach to evaluate the Biot-Savart law using the FMM was presented. It was shown that the derived algorithm can be implemented into existing FMM code developed for FastCap and FastHenry. Results are compared to ExaFMM and calculation errors below 1% are obtained. Computation time is drastically improved compared to direct computation and is reduced by an order of magnitude compared to ExaFMM. The growth in computation time is $O(N)$ for an increasing expansion order, whereas ExaFMM shows exponential growth.

Chapter 7

Conclusion

The dissertation describes the finite element numerical field solver that was developed, called TetraHenry (TTH), which uses tetrahedral volume elements to model current density within superconducting structures. Current through multiple ports are extracted, which can then be used to calculate the self- and mutual-inductance of a given SFQ circuit, using InductEx.

The VJIE formulation, with support for superconducting currents, is solved using the Full- and Half-SWG basis functions. The VJIE is discretised with VL basis functions and the Method of Moments transforms the boundary-value problem into a matrix equation. The matrix equation is solved with the GMRES iterative solver. Two types of preconditioners, *Diagonal-L* and *Pattern-R*, were developed to accelerate the convergence rate of the iterative solver. Analytical solutions were derived for the sparse resistance matrix. An electrostatic analogy was used to transform the dense inductance matrix into scalar fields, which can be solved using the FMM.

The existing VJIE was adapted for thin superconducting films on the same order as the London penetration depth. The number of unknowns were significantly reduced and computational speed gains of one order of magnitude were obtained, by replacing tetrahedral meshes with triangular meshes. The triangular method, in combination with hybrid basis functions, provides the capability to analyse large-scale SFQ circuits.

Support for inhomogeneous dielectric and magnetic materials were implemented in TTH. Impedance can be extracted, using either EMQS and Full-Wave analysis. EMQS was shown to be accurate for structures on the order of a wavelength; whereas Full-Wave analysis should be used for larger structures. The calculation time of TTH is also significantly faster, compared to FastImp, when using EMQS analysis. The effect of magnetic materials on non- and superconducting materials were analysed. It was shown that magnetic materials can significantly increase the self- and mutual inductance of non- and superconducting structures.

Support for uniform external magnetic fields was implemented in TTH. An equivalent circuit model was derived for external magnetic fields and was

shown to be accurate. This model can be used, in SPICE engines, to rapidly analyse the performance of SFQ circuits in the presence of magnetic fields. The effects of external magnetic fields on the operating margins of a large SFQ pulse splitter were demonstrated.

Calculation results of TTH correspond with FastHenry and FastImp, for small and large-scale superconducting structures. The inductance of holes and the mutual-inductance between holes were calculated and the results correspond with 3D-MLSI, with less than 1 % error. Closed VL basis function were used to specify the number of fluxons inside holes or moats. The energies of these fluxons, including the energy of an applied magnetic field, were then used to calculate the probability of flux trapping.

An approach to evaluate the Biot-Savart law using the FMM was presented. The algorithm can be implemented into existing FMM code developed for FastCap and FastHenry. Results were compared to ExaFMM and calculation errors below 1% were obtained. Computation time was drastically improved, compared to direct computation, and was reduced by an order of magnitude, compared to ExaFMM.

The work in this dissertation proves that TTH is a fast and accurate tool that can be used to extract inductance, impedance, and perform flux trapping analysis of complex three-dimension superconducting structures. TTH enables the analysis of modern superconducting IC cell layouts and makes chip-level extraction tractable on high-performance computers.

Bibliography

[1] D. Wilton, S. Rao, A. Glisson, D. Schaubert, O. Al-Bundak, and C. Butler, "Potential integrals for uniform and linear source distributions on polygonal and polyhedral domains," *IEEE Transactions on Antennas and Propagation*, vol. 32, no. 3, pp. 276–281, 1984.

[2] C. J. Fourie. (2015) InducteEx. [Online]. Available: http://www.inductex.info

[3] M. Kamon, "Fast parasitic extraction and simulation of three-dimensional interconnect via quasistatic analysis," Ph.D. dissertation, Massachusetts Institute of Technology, 1998.

[4] D. Yohannes, S. Sarwana, S. K. Tolpygo, A. Sahu, Y. A. Polyakov, and V. K. Semenov, "Characterization of HYPRES 4.5 kA/cm^2 and 8 kA/cm^2 Nb/AlOx/Nb fabrication processes," *IEEE transactions on applied superconductivity*, vol. 15, no. 2, pp. 90–93, 2005.

[5] A. Squillacote, "The ParaView Guide: A Parallel Visualization Application, Clifton Park, NY: Kitware," 2008.

[6] R. Yokota, "ExaFMM," https://github.com/exafmm/exafmm, 2017.

[7] R. G. Barrera, G. Estevez, and J. Giraldo, "Vector spherical harmonics and their application to magnetostatics," *European Journal of Physics*, vol. 6, no. 4, p. 287, 1985.

[8] R. Service, "Computer science. What it'll take to go exascale." *Science (New York, NY)*, vol. 335, no. 6067, p. 394, 2012.

[9] S. Borkar and A. A. Chien, "The future of microprocessors," *Communications of the ACM*, vol. 54, no. 5, pp. 67–77, 2011.

[10] B. D. Josephson, "Possible new effects in superconductive tunnelling," *Physics letters*, vol. 1, no. 7, pp. 251–253, 1962.

[11] K. Likharev and V. Semenov, "RSFQ Logic/Memory Family: A New Josephson Junction Technology for Sub-Terahertz-Clock-Frequency Digital Systems," *IEEE Transactions on Applied Superconductivity*, vol. 1, pp. 3–28, March 1991.

[12] N. Takeuchi, D. Ozawa, Y. Yamanashi, and N. Yoshikawa, "An adiabatic quantum flux parametron as an ultra-low-power logic device," *Superconductor Science and Technology*, vol. 26, no. 3, p. 035010, 2013.

[13] K. Inoue, N. Takeuchi, K. Ehara, Y. Yamanashi, and N. Yoshikawa, "Simulation and experimental demonstration of logic circuits using an ultra-low-power adiabatic quantum-flux-parametron," *IEEE Transactions on Applied Superconductivity*, vol. 23, no. 3, pp. 1 301 105–1 301 105, 2013.

[14] Q. Xu, Y. Yamanashi, C. Ayala, N. Takeuchi, T. Ortlepp, and N. Yoshikawa, "Design of an extremely energy-efficient hardware algorithm using adiabatic superconductor logic," in *Superconductive Electronics Conference (ISEC), 2015 15th International*. IEEE, 2015, pp. 1–3.

[15] K. K. Likharev, "Classical and quantum limitations on energy consumption in computation," *International Journal of Theoretical Physics*, vol. 21, no. 3-4, pp. 311–326, 1982.

[16] S. Nagasawa, K. Hinode, T. Satoh, M. Hidaka, H. Akaike, A. Fujimaki, N. Yoshikawa, K. Takagi, and N. Takagi, "Nb 9-layer fabrication process for superconducting large-scale SFQ circuits and its process evaluation," *IEICE Transactions on Electronics*, vol. 97, no. 3, pp. 132–140, 2014.

[17] S. Nagasawa, T. Satoh, K. Hinode, Y. Kitagawa, M. Hidaka, H. Akaike, A. Fujimaki, K. Takagi, N. Takagi, and N. Yoshikawa, "New Nb multilayer fabrication process for large-scale SFQ circuits," *Physica C: Superconductivity*, vol. 469, no. 15, pp. 1578–1584, 2009.

[18] K. Hinode, S. Nagasawa, M. Sugita, T. Satoh, H. Akaike, Y. Kitagawa, and M. Hidaka, "Pattern-size-free planarization for multilayered large-scale SFQ circuits," *IEICE transactions on electronics*, vol. 86, no. 12, pp. 2511–2513, 2003.

[19] S. Nagasawa, K. Hinode, M. Sugita, T. Satoh, H. Akaike, Y. Kitagawa, and M. Hidaka, "Planarized multi-layer fabrication technology for LTS large-scale SFQ circuits," *Superconductor Science and Technology*, vol. 16, no. 12, p. 1483, 2003.

[20] M. Kamon, M. J. Tsuk, and J. K. White, "FASTHENRY: A multipole-accelerated 3-D inductance extraction program," *IEEE Transactions on Microwave theory and techniques*, vol. 42, no. 9, pp. 1750–1758, 1994.

[21] C. J. Fourie and W. J. Perold, "Simulated inductance variations in RSFQ circuit structures," *IEEE transactions on applied superconductivity*, vol. 15, no. 2, pp. 300–303, 2005.

[22] C. J. Fourie, O. Wetzstein, T. Ortlepp, and J. Kunert, "Three-dimensional multi-terminal superconductive integrated circuit inductance extraction," *Superconductor Science and Technology*, vol. 24, no. 12, p. 125015, 2011.

[23] S. R. Whiteley. (2015) FastHenry-3.0wr. [Online]. Available: http://www.wrcad.com

[24] Y. Yi, P. Li, V. Sarin, and W. Shi, "A preconditioned hierarchical algorithm for impedance extraction of three-dimensional structures with multiple dielectrics," *IEEE Transactions on Computer-Aided Design of Integrated Circuits and Systems*, vol. 27, no. 11, pp. 1918–1927, 2008.

[25] Z. Zhu, B. Song, and J. K. White, "Algorithms in FastImp: a fast and wide-band impedance extraction program for complicated 3-D geometries," *IEEE Transactions on Computer-Aided Design of Integrated Circuits and Systems*, vol. 24, no. 7, pp. 981–998, 2005.

[26] T. P. Orlando and K. A. Delin, *Foundation of Applied Superconductivity.* Addison-Wesley, 1991.

[27] J. Pearl, "Current distribution in superconducting films carrying quantized fluxoids," *Applied Physics Letters*, vol. 5, no. 4, pp. 65–66, 1964.

[28] K. Morikawa, M. Tsuchimoto, T. Honma, H. Fujimoto, and M. Murakami, "Numerical evaluation of magnetization properties of a bulk HTSC with a hole," *IEEE Transactions on Magnetics*, vol. 33, no. 2, pp. 1576–1579, 1997.

[29] Y. Polyakov, S. Narayana, and V. K. Semenov, "Flux trapping in superconducting circuits," *IEEE Transactions on Applied Superconductivity*, vol. 17, no. 2, pp. 520–525, 2007.

[30] V. K. Semenov and M. M. Khapaev, "How moats protect superconductor films from flux trapping," *IEEE Transactions on Applied Superconductivity*, vol. 26, no. 3, pp. 1–10, 2016.

[31] M. Khapaev Jr, "Extraction of inductances of plane thin film superconducting circuits," *Superconductor Science and Technology*, vol. 10, no. 6, p. 389, 1997.

[32] M. M. Khapaev, A. Y. Kidiyarova-Shevchenko, P. Magnelind, and M. Y. Kupriyanov, "3D-MLSI: software package for inductance calculation in multilayer superconducting integrated circuits," *Applied Superconductivity, IEEE Transactions on*, vol. 11, no. 1, pp. 1090–1093, 2001.

[33] J. Phillips, H. Van der Zant, J. White, and T. Orlando, "Influence of induced magnetic fields on the static properties of Josephson-junction arrays," *Physical Review B*, vol. 47, no. 9, p. 5219, 1993.

[34] D. Schaubert, D. Wilton, and A. Glisson, "A tetrahedral modeling method for electromagnetic scattering by arbitrarily shaped inhomogeneous dielectric bodies," *IEEE Transactions on Antennas and Propagation*, vol. 32, no. 1, pp. 77–85, 1984.

[35] M. Li and W. C. Chew, "Applying divergence-free condition in solving the volume integral equation," *Progress In Electromagnetics Research*, vol. 57, pp. 311–333, 2006.

[36] L.-M. Zhang and X.-Q. Sheng, "Solving volume electric current integral equation with full-and half-SWG functions," *IEEE Antennas and Wireless Propagation Letters*, vol. 14, pp. 682–685, 2015.

[37] K. Jackman and C. J. Fourie, "Flux Trapping Analysis in Superconducting Circuits," *IEEE Transactions on Applied Superconductivity*, vol. 27, no. 4, pp. 1–5, 2017.

[38] ——, "Fast multicore FastHenry and a tetrahedral modeling method for inductance extraction of complex 3D geometries," in *Superconductive Electronics Conference (ISEC), 2015 15th International*. IEEE, 2015, pp. 1–3.

[39] Y. Schols and G. A. Vandenbosch, "Separation of horizontal and vertical dependencies in a surface/volume integral equation approach to model quasi 3-D structures in multilayered media," *IEEE transactions on antennas and propagation*, vol. 55, no. 4, pp. 1086–1094, 2007.

[40] J. Markkanen, P. Ylä-Oijala, and S. Järvenpää, "Volume integral equation methods in computational electromagnetics," in *Electromagnetics in Advanced Applications (ICEAA), 2013 International Conference on*. IEEE, 2013, pp. 880–883.

[41] J. Markkanen, P. Ylä-Oijala, and A. Sihvola, "Discretization of volume integral equation formulations for extremely anisotropic materials," *IEEE Transactions on Antennas and Propagation*, vol. 60, no. 11, pp. 5195–5202, 2012.

[42] H.-G. Wang and B. Zhao, "Combing multilevel Green's function interpolation method with volume loop bases for inductance extraction problems," *Progress In Electromagnetics Research*, vol. 80, pp. 225–239, 2008.

[43] R. F. Harrington and J. L. Harrington, *Field computation by moment methods*. Oxford University Press, 1996.

[44] Y. Saad and M. H. Schultz, "GMRES: A generalized minimal residual algorithm for solving nonsymmetric linear systems," *SIAM Journal on scientific and statistical computing*, vol. 7, no. 3, pp. 856–869, 1986.

[45] L. Greengard and V. Rokhlin, "A fast algorithm for particle simulations," *Journal of computational physics*, vol. 73, no. 2, pp. 325–348, 1987.

[46] C. Geuzaine and J.-F. Remacle, "Gmsh: A 3-D finite element mesh generator with built-in pre-and post-processing facilities," *International journal for numerical methods in engineering*, vol. 79, no. 11, pp. 1309–1331, 2009.

[47] ——. (2017) Gmsh: A 3-D finite element mesh generator with built-in pre-and post-processing facilities. [Online]. Available: http://gmsh.info/

[48] M. M. Botha, "Solving the volume integral equations of electromagnetic scattering," *Journal of Computational Physics*, vol. 218, no. 1, pp. 141–158, 2006.

[49] L. E. Sun and W. C. Chew, "A novel formulation of the volume integral equation for electromagnetic scattering," *Waves in Random and Complex Media*, vol. 19, no. 1, pp. 162–180, 2009.

[50] J.-M. Jin, *Theory and computation of electromagnetic fields*. John Wiley & Sons, 2011.

[51] H.-Y. R. Chao, *A multilevel fast multipole algorithm for analyzing radiation and scattering from wire antennas in a complex environment*. University of Illinois at Urbana-Champaign, 2002.

[52] S. Antenor de Carvalho and L. de Souza Mendes, "Scattering of EM waves by inhomogeneous dielectrics with the use of the method of moments and 3-D solenoidal basis functions," *Microwave and Optical Technology Letters*, vol. 23, no. 1, pp. 42–46, 1999.

[53] S. Kulkarni, R. Lemdiasov, R. Ludwig, and S. Makarov, "Comparison of two sets of low-order basis functions for tetrahedral VIE modeling," *IEEE transactions on antennas and propagation*, vol. 52, no. 10, pp. 2789–2795, 2004.

[54] H. Mahawar, V. Sarin, and W. Shi, "A solenoidal basis method for efficient inductance extraction," in *Proceedings of the 39th annual Design Automation Conference*. ACM, 2002, pp. 751–756.

[55] N. Deo, *Graph theory with applications to engineering and computer science*. Courier Dover Publications, 2017.

[56] E. W. Dijkstra, "A note on two problems in connexion with graphs," *Numerische mathematik*, vol. 1, no. 1, pp. 269–271, 1959.

[57] O. Zienkiewicz and R. Taylor, *The Finite Element Method: The basis*, ser. Fluid Dynamics. Butterworth-Heinemann, 2000, vol. 1.

[58] L. Zhang, T. Cui, and H. Liu, "A set of symmetric quadrature rules on triangles and tetrahedra," *Journal of Computational Mathematics*, pp. 89–96, 2009.

[59] S. S. Rao, *The Finite Element Method in Engineering*. Butterworth-heinemann, 2004.

[60] Y. Saad, *Iterative methods for sparse linear systems*. SIAM, 2003.

[61] H. C. Elman, "Iterative methods for large, sparse, nonsymmetric systems of linear equations," Ph.D. dissertation, Yale University New Haven, Conn, 1982.

[62] X. S. Li, "An overview of SuperLU: Algorithms, implementation, and user interface," *ACM Transactions on Mathematical Software (TOMS)*, vol. 31, no. 3, pp. 302–325, 2005.

[63] X. S. Li, J. W. Demmel, J. R. Gilbert, L. Grigori, M. Shao, and I. Yamazaki, "SuperLU Users' Guide," Lawrence Berkeley National Laboratory, Tech. Rep. LBNL-44289, September 1999, http://crd.lbl.gov/~xiaoye/SuperLU/. Last update: March 2016.

[64] J. W. Demmel, J. R. Gilbert, and X. S. Li, "An Asynchronous Parallel Supernodal Algorithm for Sparse Gaussian Elimination," *SIAM J. Matrix Analysis and Applications*, vol. 20, no. 4, pp. 915–952, 1999.

[65] C. J. Fourie, O. Wetzstein, T. Ortlepp, and J. Kunert, "Three-dimensional multi-terminal superconductive integrated circuit inductance extraction," *Superconductor Science and Technology*, vol. 24, no. 12, p. 125015, 2011.

[66] C. Teh, M. Kitagawa, and Y. Okabe, "Inductance calculation of 3D superconducting structures with ground plane," *Superconductor Science and Technology*, vol. 12, no. 11, p. 921, 1999.

[67] S. Narayana, Y. Polyakov, and V. K. Semenov, "Evaluation of Flux trapping in superconducting circuits," *Applied Superconductivity, IEEE Transactions on*, vol. 19, no. 3, pp. 640–643, 2009.

[68] M. M. Khapaev, "Inductance extraction of multilayer finite-thickness superconductor circuits," *IEEE Transactions on Microwave Theory and Techniques*, vol. 49, no. 1, pp. 217–220, 2001.

[69] M. Khapaev and M. Y. Kupiyanov, "Sparse Approximation of FEM Matrix for Sheet Current Integro-Differential Equation," in *2nd International Conference On Matrix Methods And Operator Equations, Moscow, Russia*, 2007, p. 37.

[70] B. Guan, M. J. Wengler, P. Rott, and M. J. Feldman, "Inductance estimation for complicated superconducting thin film structures with a finite segment method," *Applied Superconductivity, IEEE Transactions on*, vol. 7, no. 2, pp. 2776–2779, 1997.

[71] W. H. Chang, "Measurement and calculation of Josephson junction device inductances," *Journal of Applied Physics*, vol. 52, no. 3, pp. 1417–1426, 1981.

[72] S. M. Rao, D. R. Wilton, and A. W. Glisson, "Electromagnetic scattering by surfaces of arbitrary shape," *Antennas and Propagation, IEEE Transactions on*, vol. 30, no. 3, pp. 409–418, 1982.

[73] J. Wang, "A new surface integral formation of EMQS impedance extraction for 3-D structures," Ph.D. dissertation, Massachusetts Institute of Technology, 1999.

[74] N. A. Marques, M. Kamon, L. M. Silveira, and J. K. White, "Generating compact, guaranteed passive reduced-order models of 3-D RLC interconnects," *IEEE transactions on advanced packaging*, vol. 27, no. 4, pp. 569–580, 2004.

[75] A. E. Ruehli, "Equivalent circuit models for three-dimensional multiconductor systems," *IEEE Transactions on Microwave theory and techniques*, vol. 22, no. 3, pp. 216–221, 1974.

[76] R. Yokota, "An FMM based on dual tree traversal for many-core architectures," *Journal of Algorithms & Computational Technology*, vol. 7, no. 3, pp. 301–324, 2013.

[77] L. Ye, D. Gopman, L. Rehm, D. Backes, G. Wolf, T. Ohki, A. Kirichenko, I. Vernik, O. Mukhanov, and A. Kent, "Spin-transfer switching of orthogonal spin-valve devices at cryogenic temperatures," *Journal of Applied Physics*, vol. 115, no. 17, p. 17C725, 2014.

[78] S. Aradhya, G. Rowlands, J. Oh, D. Ralph, and R. Burman, "Nanoscale-timescale low energy switching of in-plane magnetic tunnel junctions through dynamic oersted-field-assisted spin-hall effectM," *Nano Lett.*, vol. 16, pp. 5987–5992, June 2016.

[79] I. Vernik, A. Kirichenko, O. Mukhanov, and T. Ohki, "Energy-efficient and compact ERSFQ decoder for cryogenic RAM," *IEEE Transactions on Applied Superconductivity*, vol. 27, no. 4, pp. 1–5, 2017.

[80] B. Krstajic, Z. Andelic, S. Milojkovic, S. Babic, and S. Salon, "Nonlinear 3D magnetostatic field calculation by the integral equation method with surface and volume magnetic charges," *IEEE transactions on magnetics*, vol. 28, no. 2, pp. 1088–1091, 1992.

[81] S. Babic, C. Akyel, and M. M. Gavrilovic, "Calculation improvement of 3D linear magnetostatic field based on fictitious magnetic surface charge," *IEEE transactions on magnetics*, vol. 36, no. 5, pp. 3125–3127, 2000.

[82] Y. Massoud and J. White, "FastMag: a 3-D magnetostatic inductance extraction program for structures with permeable materials," in *Computer Aided Design, 2002. ICCAD 2002. IEEE/ACM International Conference on.* IEEE, 2002, pp. 478–484.

[83] Y. Yi, R. Wenzel, V. Sarin, and W. Shi, "Inductance extraction for interconnects in the presence of nonlinear magnetic materials," *IEEE Transactions on Computer-Aided Design of Integrated Circuits and Systems*, vol. 28, no. 7, pp. 1106–1110, 2009.

[84] C. Balanis, "Advanced Enginerring Electromechanics," 1989.

[85] L. Mendes and S. Carvalho, "Scattering of EM waves by homogeneous dielectrics with the use of the method of moments and 3D solenoidal basis functions," *Microwave and Optical Technology Letters*, vol. 12, no. 6, pp. 327–331, 1996.

[86] G. L. James, *Geometrical theory of diffraction for electromagnetic waves.* IET, 1986, no. 1.

[87] O. Ergul and L. Gurel, *The multilevel fast multipole algorithm (MLFMA) for solving large-scale computational electromagnetics problems.* John Wiley & Sons, 2014.

[88] X. Hu, "Full-wave analysis of large conductor systems over substrate," Ph.D. dissertation, Massachusetts Institute of Technology, 2006.

[89] T. Sarkar and R. Harrington, "The electrostatic field of conducting bodies in multiple dielectric media," *IEEE Transactions on Microwave Theory and Techniques*, vol. 32, no. 11, pp. 1441–1448, 1984.

[90] G. A. Vandenbosch and A. R. Van de Capelle, "Mixed-potential integral expression formulation of the electric field in a stratified dielectric medium-application to the case of a probe current source," *IEEE Transactions on Antennas and Propagation*, vol. 40, no. 7, pp. 806–817, 1992.

[91] W. Roshen, "Effect of finite thickness of magnetic substrate on planar inductors," *IEEE Transactions on magnetics*, vol. 26, no. 1, pp. 270–275, 1990.

[92] Y. Massoud and J. White, "Improving the generality of the fictitious magnetic charge approach to computing inductances in the presence of permeable materials," in *Proceedings of the 39th annual Design Automation Conference*. ACM, 2002, pp. 552–555.

[93] ——, "FastMag: a 3-D magnetostatic inductance extraction program for structures with permeable materials," in *Computer Aided Design, 2002. ICCAD 2002. IEEE/ACM International Conference on*. IEEE, 2002, pp. 478–484.

[94] Y. Massoud, J. Wang, and J. White, "Accurate inductance extraction with permeable materials using qualocation," in *in Proceedings of the International Conference on Modeling and Simulation of Microsystems*. Citeseer, 1999.

[95] W. Rucker, C. Magele, E. Schlemmer, and K. Richter, "Boundary element analysis of 3-D magnetostatic problems using scalar potentials," *IEEE transactions on magnetics*, vol. 28, no. 2, pp. 1099–1102, 1992.

[96] C. Magele, H. Stogner, and K. Preis, "Comparison of different finite element formulations for 3D magnetostatic problems," *IEEE Transactions on Magnetics*, vol. 24, no. 1, pp. 31–34, 1988.

[97] (2016) CST STUDIO SUITE. [Online]. Available: https://www.cst.com

[98] C. J. Fourie, O. Wetzstein, J. Kunert, H. Toepfer, and H.-G. Meyer, "Experimentally verified inductance extraction and parameter study for superconductive integrated circuit wires crossing ground plane holes," *Superconductor Science and Technology*, vol. 26, no. 1, p. 015016, 2012.

[99] C. J. Fourie, O. Wetzstein, J. Kunert, and H.-G. Meyer, "SFQ circuits with ground plane hole-assisted inductive coupling designed with InductEx," *IEEE Transactions on Applied Superconductivity*, vol. 23, no. 3, pp. 1 300 705–1 300 705, 2013.

[100] J. L. Kirschvink, "Uniform magnetic fields and double-wrapped coil systems: improved techniques for the design of bioelectromagnetic experiments," *Bioelectromagnetics*, vol. 13, no. 5, pp. 401–411, 1992.

[101] R. Merritt, C. Purcell, and G. Stroink, "Uniform magnetic field produced by three, four, and five square coils," *Review of Scientific Instruments*, vol. 54, no. 7, pp. 879–882, 1983.

[102] W. Franzen, "Generation of Uniform Magnetic Fields by Means of Air-Core Coils," *Review of Scientific Instruments*, vol. 33, no. 9, pp. 933–938, 1962.

[103] G. Gottardi, P. Mesirca, C. Agostini, D. Remondini, and F. Bersani, "A four coil exposure system (tetracoil) producing a highly uniform magnetic field," *Bioelectromagnetics*, vol. 24, no. 2, pp. 125–133, 2003.

[104] F. Bonetto, E. Anoardo, and M. Polello, "Saddle coils for uniform static magnetic field generation in NMR experiments," *Concepts in Magnetic Resonance Part B: Magnetic Resonance Engineering*, vol. 29, no. 1, pp. 9–19, 2006.

[105] J. Dinale and J. Vrbancich, "Generation of long prolate volumes of uniform magnetic field in cylindrical saddle-shaped coils," *Measurement Science and Technology*, vol. 25, no. 3, p. 035903, 2014.

[106] I. Sasada and Y. Nakashima, "Planar coil system consisting of three coil pairs for producing a uniform magnetic field," *Journal of applied physics*, vol. 99, no. 8, p. 08D904, 2006.

[107] J. C. Maxwell, "A Treatise on Electricity and Magnetism, vol. II. Clarendon," 1904.

[108] Y. Öztürk and B. Aktaş, "Generation of uniform magnetic field using a spheroidal helical coil structure," in *Journal of Physics: Conference Series*, vol. 667, no. 1. IOP Publishing, 2016, p. 012009.

[109] E. S. Fang and T. Van Duzer, "A Josephson integrated circuit simulator (JSIM) for superconductive electronics application," in *Extended Abstracts of ISEC'89, Tokyo, Japan*, 1989, pp. 407–410.

[110] W. Hafla, A. Buchau, and W. M. Rucker, "Application of fast multipole method to Biot-Savart law computations," in *Computational Electromagnetics (CEM), 2006 6th International Conference on*. VDE, 2006, pp. 1–2.

[111] K. Nabors and J. White, "FastCap: A multipole accelerated 3-D capacitance extraction program," *IEEE Transactions on Computer-Aided Design of Integrated Circuits and Systems*, vol. 10, no. 11, pp. 1447–1459, 1991.

[112] L. Greengard, *The rapid evaluation of potential fields in particle systems*. MIT press, 1988.

[113] B. Carrascal, G. Estevez, P. Lee, and V. Lorenzo, "Vector spherical harmonics and their application to classical electrodynamics," *European Journal of Physics*, vol. 12, no. 4, p. 184, 1991.

[114] K. Jackman and C. J. Fourie, "Tetrahedral modeling method for inductance extraction of complex 3-D superconducting structures," *IEEE Transactions on Applied Superconductivity*, vol. 26, no. 3, pp. 1–5, 2016.

Appendices

Appendix A

Journal Paper - Flux Trapping Analysis

- K. Jackman and C. J. Fourie, "**Flux trapping analysis in superconducting circuits**," *IEEE Transactions on Applied Superconductivity*, vol. 27, no. 4, pp. 1-5, 2017. [37]

Flux Trapping Analysis in Superconducting Circuits

Kyle Jackman, and Coenrad J. Fourie, *Member, IEEE*

***Abstract*—Flux trapping adversely affects superconducting electronic circuit operation. Circuit designers would benefit from a tool to analyze the probability and effects of flux trapping at critical locations for a given circuit layout. We show how our tetrahedral volume element numerical solver, TTH, can be used to model trapped fluxons in the presence of external magnetic fields. We also show how to extract the self-inductance around holes and the mutual-inductance between moats and other excitation ports. Understanding the coupling effects between moats and circuit elements such as signal lines or Josephson junctions can help determine the optimal size and placements of moats, preventing circuit performance degradation and operation malfunction.**

***Index Terms*—Flux pinning, inductance extraction, superconducting integrated circuits.**

I. Introduction

A SIGNIFICANT drawback of superconducting integrated circuits is the sensitivity to magnetic fields created by fluxons trapped in superconducting films. Pearl vortices [1] trapped in superconducting films magnetically interact with surrounding superconducting circuits, degrading circuit performance.

Several efforts have been made to analyze the effects and probability of flux trapping [2]-[5]. In a recent study the Gibbs potential of arbitrary shaped films was used for estimating the efficiency of different moat patterns [6]. It was shown that the Gibbs potential can be used to calculate the probability of flux trapping and the self- and mutual-inductance between moats, holes and external magnetic fields.

Existing software such as 3D-MLSI [7]-[8] can extract self- and mutual-inductances around holes in superconducting films, using 2D scalar stream functions. An extraction method for self- and mutual-inductance around holes has been developed for Josephson-junction arrays [9], but is limited to geometries consisting of rectangular filaments. To the best of our knowledge, software capable of extracting self- and mutual-inductances around holes for complex 3D models has not yet been developed. Our 3D numerical engine, TetraHenry (TTH) [10] has been modified to evaluate the effects of flux trapping in superconducting circuits. Tetrahedral volume elements allow for accurate discretization of complex geometries and modeling of uneven multidirectional current flow along curved structures [10]. This is especially important for multi-layer fabrication technologies [11] that do not necessary planarize the top layers, resulting in irregular topographies. Although 2D triangular meshing can be used to model these irregularities, it lacks the ability to accurately model stacked vias and non-uniform current density near the surface of structures larger that the penetration depth.

We will show how volume loop basis functions [12] are used to evaluate volume integral equations on closed contours around holes, i.e. Pearl vortices or moats. The circulating supercurrents, for a given number of fluxons threading each hole, can be computed by solving a Method of Moments matrix equation. Once the current around each hole is known, the magnetic interactions (mutual-inductance) with surrounding components and with the external magnetic field are computed. These magnetic interactions are then used to calculate the critical magnetic field. The extracted self- and mutual-inductances can also be used within circuit simulators, such as JSIM [13], to determine the operating margins of circuits for different combinations of flux quanta trapped within Pearl vortices and moats.

II. Overview

A. Model for frozen vortex

During the cooling process the superconducting film is transparent to magnetic field for temperatures above its critical temperature, T_C. As the temperature crosses below the critical temperature, the metal film starts transition into superconducting state. Near the critical temperature, the expulsion of the magnetic field is weak and the London penetration depth is strongly dependent on temperature:

$$\lambda_L(T) = \frac{\lambda_L(0)}{\sqrt{1-(T/T_C)^4}}. \quad (1)$$

Small islands of the film become superconductive, growing larger as the temperature decrease. As these superconducting islands merge, some normal areas will become surrounded. If the field trough the normal area exceeds $1/2\Phi_0$, the flux will adjust to the nearest number of quanta, resulting in a Pearl vortex [3].

Figure 1 shows a trapped flux vortex consisting of a normal region with radius equal to the coherence length ξ and the magnetic field concentrated in an area with radius $\xi+\lambda$. The flux quantum is maintained by a circulating supercurrent around the vortex. Following a similar approach as the one

This work was supported in part by the South African National Research Foundation under Grant 93568.

The financial assistance of the National Research Foundation (NRF) towards this research is hereby acknowledged. Opinions expressed and conclusions arrived at, are those of the author and are not necessarily to be attributed to the NRF.

K. Jackman is with Stellenbosch University, 7602 Stellenbosch, South Africa (e-mail: 16192044@sun.ac.za).

C. J. Fourie is with Stellenbosch University, 7602 Stellenbosch, South Africa (e-mail: coenrad@sun.ac.za).

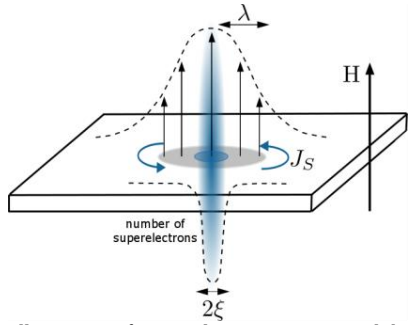

Fig. 1. An Illustration of a Pearl vortex maintained by a circulating supercurrent around the vortex. The magnetic field penetrates the superconducting film to a depth of λ.

described in [6], the Pearl vortex can be modeled as a hole in the superconducting film with a radius that is equal to the coherence length ξ.

B. Inductance extraction around Pearl Vortex

The original TTH engine was developed for inductance extraction using frequency-depended voltage excitation sources [10]. In order to model trapped fluxons and constant external magnetic fields, which are frequency-independent, the existing implementation of the volume electric current integral equation (VJIE) in TTH requires modification, as described in this section.

We assume that the superconducting media is homogeneous and isotropic. Starting with the London equations, the following Gauge invariant supercurrent equation can be derived [14]:

$$\mu_0\lambda^2\mathbf{J}_S(\mathbf{r})+\mathbf{A}(\mathbf{r})=-\frac{\Phi_0}{2\pi}\nabla\theta(\mathbf{r}) \tag{2}$$

where $\mathbf{J}_S(\mathbf{r})$ and $\theta(\mathbf{r})$ are respectively the superconducting current and its phase. The magnetic vector potential $\mathbf{A}(\mathbf{r})$ can be expressed in terms of the supercurrent:

$$\mathbf{A}(\mathbf{r})=\frac{\mu_0}{4\pi}\iint_{V'}\frac{\mathbf{J}_S(\mathbf{r}')}{|\mathbf{r}-\mathbf{r}'|}\cdot dv. \tag{3}$$

Next, the volume integral equation (2) is evaluated on a closed contour Γ around each hole (Pearl vortex) or moat:

$$\mu_0\lambda^2\oint_\Gamma\mathbf{J}_S(\mathbf{r})\cdot\mathbf{dl}+\oint_\Gamma\mathbf{A}(\mathbf{r})\cdot\mathbf{dl}=-\frac{\Phi_0}{2\pi}\oint_\Gamma\nabla\theta(\mathbf{r})\cdot\mathbf{dl}. \tag{4}$$

Equation (4) closely resembles the VJIE already implemented in TTH [10]. Closed Volume Loop (VL) basis functions [10]-[12] are then constructed around each hole using the tetrahedrons on the inner surface of the hole. The inner surface of each hole is specified by the user within the geometry file. Following the Method of Moments and using the closed VL basis functions, (4) can be converted into a system of m equations:

$$(\mathbf{M}\mathbf{L}_S\mathbf{M}^T)\mathbf{I}_m=\mathbf{P}_m. \tag{5}$$

The vectors $\mathbf{I}_m$ and $\mathbf{P}_m$ contain respectively the circulating current and the phase corresponding to each VL basis function [10]. The values in matrix $\mathbf{M}$ are either 0 or ±1, depending on the direction of the SWG basis functions [15]. The element at index (m, n) in matrix $\mathbf{L}_S$ consists of the volume integral over the two terms on the left-hand side of (4):

$$(\mathbf{L}_S)_{mn}=\mu_0\lambda^2\int_{V_m}\mathbf{w}_m(\mathbf{r})\cdot\mathbf{f}_m(\mathbf{r})dv + \frac{\mu_0}{4\pi}\int_{V_m}\int_{V_n}\frac{\mathbf{w}_m(\mathbf{r})\cdot\mathbf{f}_n(\mathbf{r}')}{|\mathbf{r}-\mathbf{r}'|}dv'dv. \tag{6}$$

The vectors $\mathbf{w}_m(\mathbf{r})$ and $\mathbf{f}_n(\mathbf{r})$ are the SWG basis functions over tetrahedrons m and n [10]. $\mathbf{P}_m$ is also a combination of SWG basis functions:

$$\mathbf{P}_m=\mathbf{M}\mathbf{P}_n \tag{7}$$

where element m in $\mathbf{P}_n$ can be calculated as:

$$(\mathbf{P}_n)_m=-\frac{\Phi_0}{2\pi}\int_{V_m}\mathbf{w}_m(\mathbf{r})\cdot\nabla\theta(\mathbf{r})dv. \tag{8}$$

It is shown in [16] that the entries of vector $\mathbf{P}_n$ will become zero for a closed VL basis function. In general, this is not true, since the phase is not well defined [14]. Even though an infinite number of possible values of the phase exist, the phase can only be specified within 2π of its principle value, which is restricted to $-\pi$ to π [14]. The value at index m in the vector $\mathbf{P}_n$ can, therefore, be only one of two values:

$$(\mathbf{P}_n)_m=\begin{cases}0, & \text{closed loop with zero flux}\\ n\Phi_0, & \text{closed loop with } n \text{ fluxons}\end{cases}. \tag{9}$$

The current vector $\mathbf{I}_m$ is computed by solving (5) iteratively using the GMRES method [17]. The supercurrent, I, circulating the Pearl vortex or moat can then be extracted from $\mathbf{I}_m$. Finally, the inductance is calculated using the given number of fluxons threading the hole:

$$L=n\Phi_0/I. \tag{10}$$

We evaluate the accuracy of our method by calculating the self- and mutual-inductances of two 4 μm x 1 μm moats inside a 50 μm x 30 μm film, shown in Fig. 2. The current density plot was generated with ParaView [18] using the VTK-formatted [19] output generated by TTH. The moats are separated by 8 μm and both are excited with a single fluxon, but with opposing polarities. Table 1 shows the comparison of the inductance values calculated using TTH and 3D-MLSI. Extracted values correspond with 3D-MLSI with less than 1% error.

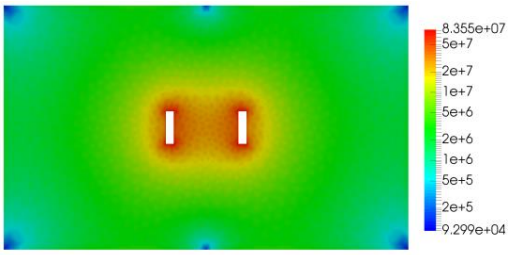

Fig. 2. The current density of two moats (4 μm x 1 μm) in a 50 μm x 30 μm film (thickness 100 nm and λ = 966.95 nm). The two moats are separated by 8 μm. Each moat traps one fluxon, but with opposing polarities.

TABLE I
EXTRACTED INDUCTANCE USING TTH AND 3D-MLSI

Inductance	3D-MLSI	TTH	% Difference
Moat (left)	38.260 pH	38.061 pH	0.5228 %
Moat (right)	38.280 pH	38.064 pH	0.5675 %
Moats (mutual)	-9.865 pH	-9.779 pH	0.8794 %

C. External Magnetic Threshold Field

Following the method described in [6], we define the threshold (critical) field as the magnetic field with 50% trapping probability. To calculate the threshold field, we need to calculate the Gibbs energy over the entire structure. Once the current density over the entire volume is known, i.e. the solution to (5), the Gibbs energy can be calculated:

$$E = \frac{1}{2}\int_V \mathbf{A}(\mathbf{r})\,\mathbf{J}_s^*(\mathbf{r})\,dv. \tag{11}$$

Evaluating (11) over the entire volume requires $O(N^2)$ operations. We reduce the operation count to $O(N)$ by utilizing the existing parallel implementation of the Fast Multipole Method (FMM) developed in [20].

Mutual-inductance between the Pearl vortex and the external magnetic field is also required to calculate the threshold field. First, we calculate the Gibbs energy, E_M, of the interaction between the Pearl vortex and the magnetic field [6]:

$$E_M = E - E_V - E_H \tag{12}$$

where E is the total Gibbs energy when both the Peal vortex and the magnetic field are excited. E_V and E_H are the Gibbs energy of the Pearl vortex and the magnetic field, respectively. Second, the currents I_V and I_H circulating the Pearl vortex are extracted by exciting the Pearl vortex and the external magnetic field separately. Finally, the mutual-inductance can be calculated:

$$M = \frac{E_M}{I_V \cdot I_H}. \tag{13}$$

Once the mutual-inductance is known, the threshold field, B_C, can be calculated when $E_V = -E_M$ [6]:

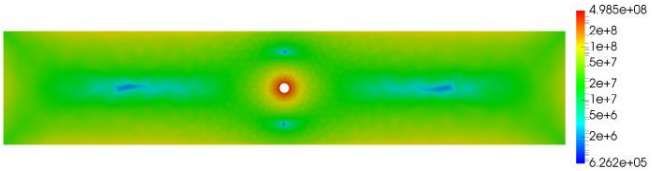

Fig. 3. Current density of single vortex (ξ = 0.43 μm) at absolutely stability trapped in 10 μm x 50 μm strip with 100 nm thickness and penetration depth of λ = 683.74 nm.

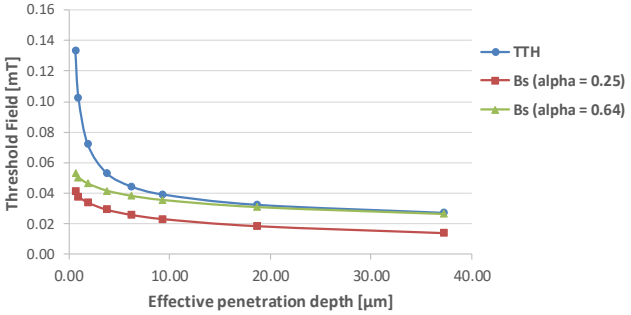

Fig. 4. Threshold field, B_C, calculated with TTH as a function of effective penetration depth. The theoretical absolute field, B_S, is also shown for α = ¼ and α = 2/π.

$$B_C = \frac{-\Phi_0 B_E}{2 I_H M} \tag{14}$$

where B_E is the magnitude of the applied external magnetic field used when calculating I_H and M.

III. FLUX TRAPPING IN MICROSTRIP

In this section, we reproduce known results to verify the accuracy of the threshold field calculated with TTH. We use the method described in Section II.C to determine the threshold field for a single vortex (ξ = 0.43 μm, dT = 0.02 and Λ = 9.35 μm) trapped in the center of a 10 μm-wide strip, as shown in Fig. 3. Although the dimensions of the structure might not be physically realizable, we use the same dimensions used in [6] to compare the accuracy of our theoretical results. Figure 4 shows the threshold field calculated with TTH and the theoretical field that is required for absolute stability [21] in a strip of infinite length:

$$B_S = \frac{2\Phi_0}{\pi W^2} \ln\left(\frac{\alpha W}{\xi}\right). \tag{15}$$

The value for the constant α was first suggested to be ¼ [21], and later suggested to be α = 2/π [22]. For unrealistically small effective penetration depths, Λ, the threshold field extracted with TTH differs from (15), but for larger and more realistic values of Λ, the extracted threshold field corresponds with (15) when α = 2/π. The calculated threshold field also corresponds with the results obtained in [6].

IV. COUPLING BETWEEN MICROSTRIP AND MOAT

It is known that the threshold field can be increased, i.e. the probability of flux trapping can be reduced, by placing moats or narrow cuts in the ground plane [23]-[25]. In this section,

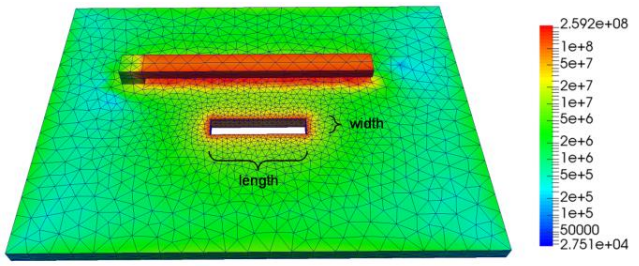

Fig. 5. Current density of a 5 µm x 50 µm strip (thickness 220 nm, 177.5 nm above ground plane and λ = 137 nm) and a moat in ground plane (300 nm thickness and λ = 86 nm). The strip and moat are excited with a single fluxon.

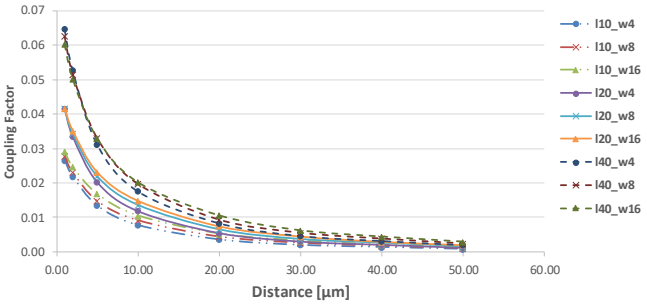

Fig. 6. Coupling between moat and microstrip. The distance is measured between the edge of the moat and the edge of the strip. The curve l10_w4 represents a moat with length = 10 µm and width = 4 µm.

we show that the density and patterns of these moats not only effluence the threshold field, but also the magnetic coupling with surrounding structures.

The current density of a 5 µm x 50 µm strip and a moat in the ground layer is shown in Fig. 5. Both the strip and the moat are excited with a single fluxon. The moat is placed at a distance *d* from the edge of the strip. We calculate the mutual coupling between the moat and the strip as a function of *d* for various dimensions of the moat, as shown in Fig. 6. As expected, the mutual coupling is indirectly proportional to the distance *d*. It is also evident that the mutual coupling is strongly dependent on the moat's length (parallel to the strip), whereas the moat's width (perpendicular to the strip) has little effect on the coupling.

Dividing a large moat into smaller moats has two advantages. First, the mutual coupling between the moat and the strip is reduced. Second, the repulsive force of a fluxon trapped in a smaller moat is reduced to a smaller area. Since moat efficiency reduces when a fluxon is trapped inside a moat [2], several smaller moats might be more effective than a single larger moat. One disadvantage of using smaller moats is the reduction of the threshold field, which is shown in the next section.

V. Threshold Field of Moat Patterns

To evaluate the effect of smaller moats on the threshold field, a single Pearl vortex (ξ = 0.43 µm, dT = 0.02 and Λ = 9.35 µm [6]) is placed in the center of a ground plane surrounded by moats, as shown in Fig. 7. The region between the moats represents a fictitious 20 µm-wide strip. An external magnetic field is applied perpendicular to the ground plane. The direction of the current circulating the vortex is in the opposite direction of the current induced by the external magnetic field.

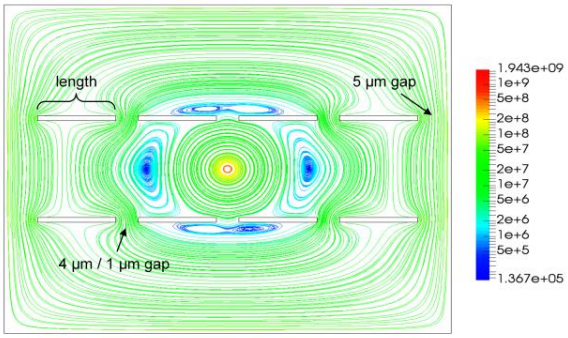

Fig. 7. Current density streamlines of single vortex (ξ = 0.27 µm) trapped in 60 µm x 80 µm film (thickness 100 nm) surrounded by 8 moats. An external field of 6.31 µT is applied perpendicular to the ground plane.

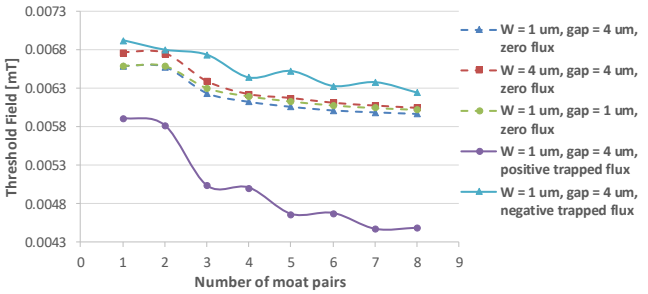

Fig. 8. Threshold field for different number of moat pairs. Each curve represents a moat of W = width, gap = separation and 2 or no trapped flux in the moats nearest to the vortex.

The threshold field was calculated when zero flux was trapped in the moats and when two fluxons was trapped in two of the moats. Figure 8 shows the threshold field as a function of the number of moats along the fictitious strip. The curves "positive trapped flux" (same polarity as the vortex) and "negative trapped flux" (opposing polarity) represent two fluxons trapped in two of the moats closest to the vortex; one at the top and one at the bottom. It is evident that the threshold field decreases as the number of moats increase, i.e. the length of each moat is decreased. However, the threshold field of the 4 µm-wide moats is only slightly larger than the 1 µm-wide moats and the distance (gap) between the moats has little effect on the threshold field. As expected, "positive" trapped fluxons in the moats significantly reduce the threshold field, whereas "negative" trapped fluxons slightly increase the threshold field. The former is more likely to occur, which reduces the efficiency of the moats [2] and, therefore, lowers the threshold field.

VI. Conclusion

Tetrahedral volume elements are used to evaluate the effects of flux trapping in 3D superconducting integrated circuit structures. We show that our numerical engine, TTH, can extract self- and mutual-inductances between moats and that the extracted values correspond with existing 2D numerical software with less than 1% error. Using tetrahedral volume elements opens the possibility to analyze the effects of flux trapping in complex 3D structures, such as stacked vias.

REFERENCES

[1] J. Pearl, "Current distribution in superconducting films carrying quantized fluxoids," *Appl. Phys. Lett.*, vol. 5, no. 4, pp. 65–66, Aug. 1964.

[2] S. Narayana, Y. A. Polyakov, and V. K. Semenov, "Evaluation of flux trapping in superconducting circuits," *IEEE Trans. Appl. Supercond.*, vol. 19, no. 3, pp. 640–643, Jun. 2009.

[3] Y. Polyakov, S. Narayana, and V. K. Semenov, "Flux trapping in superconducting circuits," *IEEE Trans. Appl. Supercond.*, vol. 17, no. 2, pp. 520–525, Jun. 2007.

[4] A. L. Fetter, "Flux-penetration in a thin superconducting disk," *Phys. Rev. B*, vol. 22, no. 3, pp. 1200–1213, Aug. 1980.

[5] G. Stan, S. Field and J. Martinis, "Critical Field for Complete Vortex Expulsion from Narrow Superconducting Strips", *Phys. Rev. Lett.*, vol. 92, no. 9, 2004.

[6] V. Semenov and M. Khapaev, "How Moats Protect Superconductor Films From Flux Trapping", *IEEE Trans. Appl. Supercond.*, vol. 26, no. 3, pp. 1-10, 2016.

[7] M. M. Khapaev, "Extraction of inductances of plane thin film superconducting circuits," *Supercond. Sci. Technol.*, vol. 10, no. 6, pp. 389–394, Jun. 1997.

[8] M. M. Khapaev, A. Y. Kidiyarova-Shevchenko, P. Magnelind, and M. Y. Kupriyanov, "3D-MLSI: Software package for inductance calculation in multilayer superconducting integrated circuits," *IEEE Trans. Appl. Supercond.*, vol. 11, no. 1, pp. 1090–1093, Mar. 2001.

[9] J. Phillips, H. van der Zant, J. White and T. Orlando, "Influence of induced magnetic fields on the static properties of Josephson-junction arrays", Phys. Rev. B, vol. 47, no. 9, pp. 5219-5229, 1993.

[10] K. Jackman and C. Fourie, "Tetrahedral Modelling Method for Inductance Extraction of Complex 3D Superconducting Structures", *IEEE Trans. Appl. Supercond.*, pp. 1-1, 2016.

[11] S. Nagasawa, K. Hinode, T. Satoh, M. Hidaka, H. Akaike, A. Fujimaki, N. Yoshikawa, K. Takagi, and N. Takagi, "Nb 9-Layer Fabrication Process for Superconducting Large-Scale SFQ Circuits and Its Process Evaluation," IEICE Trans. Electron., vol. 97, no. 3, pp. 132–140, 2014.

[12] M. Li and W. C. Chew, "Applying Divergence-Free Condition In Solving The Volume Integral Equation," *Progress In Electromagnetics Research PIER*, vol. 57, pp. 311–333, 2006.

[13] E. S. Fang and T. Van Duzer, "A Josephson integrated circuit simulator (JSIM) for superconductive electronics application," *Extended Abstracts of ISEC '89*, Tokyo, Japan, pp. 407-410, 1989.

[14] T. P. Orlando and K. A. Delin, *Foundations of applied superconductivity*. Reading, Mass.: Addison-Wesley, 1991, pp. 94–104.

[15] D. Schaubert, D. Wilton, and A. Glisson, "A tetrahedral modeling method for electromagnetic scattering by arbitrarily shaped inhomogeneous dielectric bodies," *IEEE Trans. Antennas Propagat.*, vol. 32, no. 1, pp. 77–85, 1984.

[16] H.-G. Wang and P. Zhao, "Combing Multilevel Green's Function Interpolation Method With Volume Loop Bases For Inductance Extraction Problems," *Progress In Electromagnetics Research PIER*, vol. 80, pp. 225–239, 2008.

[17] Y. Saad and M. H. Schultz, "GMRES: A Generalized Minimal Residual Algorithm for Solving Nonsymmetric Linear Systems," *SIAM J. Sci. and Stat. Comput.*, vol. 7, no. 2, pp. 856–869, 1986.

[18] U. Ayachit, "The paraview guide: a parallel visualization application," 2015.

[19] W. Schroeder, K. Martin and B. Lorensen, "The visualization toolkit," 2004.

[20] K. Jackman and C. J. Fourie. "Fast multicore FastHenry and a tetrahedral modeling method for inductance extraction of complex 3D geometries." Superconductive Electronics Conference (ISEC), 2015 15th International. IEEE, 2015.

[21] K. Likharev, "The formation of a mixed state in planar semiconductor films", *Radiophysics and Quantum Electronics*, vol. 14, no. 6, pp. 722-727, 1971.

[22] J. R. Clem (unpublished).

[23] M. Jeffery, T. Van Duzer, J. R. Kirtley, and M. B. Ketchen, "Magnetic imaging of moat-guarded superconducting electronics circuits," *Appl. Phys. Lett.*, vol. 67, no. 12, pp. 1769–1771, Sep. 1996.

[24] S. Nagasawa, H. Numata, C. Kato, and S. Tahara, "Evaluation of trapped magnetic flux for Josephson 4-Kbit RAMs," *in Extended Abstracts of ISEC '95*, Nogoya, 1995, pp. 192–195.

[25] S. Bermon and T. Gheewala, "Moat-guarder Josephson SQUIDs," *IEEE Trans. Magn.*, vol. MAG-19, pp. 1160–1164, May 1983.

[26] J. R. Clem, "Paper K36. 06." *Bull. Am. Phys. Soc*, vol. 43, pp. 411, 1998.

[27] G. Maksimova, "Mixed state and critical current in narrow semiconducting films", *Physics of the Solid State*, vol. 40, no. 10, pp. 1607-1610, 1998.

Appendix B

Conference Paper - Fast FastHenry (FFH)

- K. Jackman and C. J. Fourie, "**Fast multicore FastHenry and a tetrahedral modeling method for inductance extraction of complex 3d geometries**," in *Superconductive Electronics Conference (ISEC), 2015 15th International*. IEEE, 2015, pp. 1-3. [38]

DS-O04

Fast Multicore FastHenry and a Tetrahedral Modeling Method for Inductance Extraction of Complex 3D Geometries

Kyle Jackman
Department of Electrical and Electronic Engineering
Stellenbosch University
Stellenbosch, South Africa
16192044@sun.ac.za

Coenrad J. Fourie
Department of Electrical and Electronic Engineering
Stellenbosch University
Stellenbosch, South Africa
coenrad@sun.ac.za

***Abstract*— FastHenry is a powerful numerical engine with which to calculate inductance in superconducting structures, but modern high-end multilayer fabrication processes result in dense calculation problems for which it was not optimized. We identify these shortcomings for typical calculation problems and present algorithmic improvements and multicore parallelization to increase computational efficiency. We attain performance increases of one to two orders of magnitude for models of real circuit layouts. We also show that these multicore methods deliver similar performance increases when applied to an engine that uses tetrahedral elements.**

Keywords*— *Inductance, inductance extraction, numerical models, parallel processing, superconducting integrated circuits.

I. Introduction

FastHenry [1] remains a popular magnetoquasistatic solver for the calculation of inductance in three-dimensional structures. Energy-efficient superconducting digital electronics, from the single flux quantum (SFQ) pulse logic families [2] with clock frequencies in the 100 GHz range, to the adiabatic logic families [3] with zeptojoule bit energy dissipation, function through the exploitation of magnetic phenomena such as single flux quanta and inductance. It is thus not surprising that such electronics are very sensitive to magnetic fields and currents induced by stray coupling. Inductance calculation is therefore a crucial part of superconducting integrated circuit (IC) design. Of the available analytical and numerical inductance calculation tools FastHenry [1] adapted for superconductivity is still the most popular and versatile. It is also the numerical solver used by the multi-port IC inductance extraction software "InductEx" [4].

FastHenry was developed for printed circuit board layouts and chip package pins and works well for coils or other structures with slender conductors. However, we show that it is very inefficient for densely discretized IC structures. Fortunately speed can be improved significantly for dense structures through algorithm optimization and parallel processing. Here we briefly discuss the algorithmic improvements and parallelization methods that deliver impressive speed gains. Similar speed gains are achieved when discretizing complex geometries using tetrahedral elements.

This material is based upon work supported financially by the South African National Research Foundation, grant numbers 78789 and 92426.

II. FastHenry Overview

FastHenry was developed as a 3D inductance calculation program for general packaging structures [1]. It combines three components: mesh analysis, an iterative solver known as GMRES [5] and the Fast Multipole Method (FMM) [6] from which the name is derived. Calculation models for FastHenry are discretized into filaments in which currents and voltages are assumed to be sinusoidal and at steady state, so that

$$\mathbf{Z}\mathbf{I}_\mathbf{b} = (\mathbf{R} + j\omega\mathbf{L})\mathbf{I}_\mathbf{b} = \mathbf{V}_\mathbf{b}, \tag{1}$$

where $\mathbf{I}_\mathbf{b}$ and $\mathbf{V}_\mathbf{b}$ are vectors for the current and voltage phasors across filaments, and $\mathbf{Z}$ is the complex impedance matrix of which $\mathbf{R}$ is the diagonal matrix of dc resistances and $\mathbf{L}$ is the matrix of self-inductances of filaments on the diagonal and partial inductances between filaments everywhere else.

A structure that has been discretized into filaments can be represented as an equivalent circuit with branches for the filaments. The model topology is contained in matrix $\mathbf{M}$. If ideal voltage sources in vector $\mathbf{V}_\mathrm{S}$ are used to excite the circuit at a given frequency, it can be shown that

$$\mathbf{M}\mathbf{Z}\mathbf{M}^\mathrm{T}\,\mathbf{I}_\mathrm{m} = \mathbf{V}_\mathrm{S}, \tag{2}$$

where $\mathbf{I}_\mathrm{m}$ is the vector of mesh currents to be solved. This system of linear equations is intractable with Gaussian elimination when there are thousands of filaments, so that it is solved with an iterative method, GMRES [5].

The dominant cost during each GMRES iteration is the computation of the matrix-vector product $(\mathbf{M}\mathbf{Z}\mathbf{M}^\mathrm{T})\mathbf{I}_\mathrm{m}^k$, where $\mathbf{I}_\mathrm{m}^k$ is the basis vector for the Krylov subspace computed at the k^{th} iteration [5]. FastHenry reduces this cost by using the Fast Multipole Method [6] to form an approximation to the matrix-vector product whenever needed, without ever computing $\mathbf{M}\mathbf{Z}\mathbf{M}^\mathrm{T}$ explicitly. GMRES solves $\mathbf{x}$ in the equation

$$\mathbf{A}\mathbf{x} = \mathbf{b}, \tag{3}$$

where **A** is a square matrix and **b** a vector, with $\mathbf{A} = \mathbf{M}\mathbf{Z}\mathbf{M}^T$ and $\mathbf{b} = \mathbf{V}_S$ in (2). The equation $\mathbf{APx'} = \mathbf{b}$ has the same solution as (3) for some square matrix **P** with the same dimension as **A**, if we set $\mathbf{x} = \mathbf{Px'}$. The matrix **P** is a preconditioner [7] that is used to improve the convergence speed of GMRES. A good preconditioner should be quick to form and apply, and let GMRES solve a system quickly. Many preconditioning techniques exist, and most aim to make **P** as close as possible to $\mathbf{A}^{-1}$. FastHenry supports sparsified preconditioners, one where the matrix **L** of partial inductances in (1) is sparsified by dropping all mutual inductances outside of cubes formed during FMM, the other by using only the diagonal of **L**. We refer to these as Cube and DiagL respectively. Sparsification is a quick operation, but then the sparsified **A** is essentially inverted, which is hard and costly.

III. FastHenry Improvements

We can define the three costliest steps of a Fast-Henry calculation, in order of execution, as the multipole setup (MPS), the formation of the preconditioner, and GMRES. Parallelization is implemented using the OpenMP API, i.e. shared memory parallelization.

A. Multipole setup

The multipole to local expansion operators and the near-part matrices, used in the FMM, are calculated during the MPS. The dominant cost of MPS is the construction of the near-part matrices, which store the near-field interactions (self- and partial inductances) between filaments. The entire circuit is divided into cubes. The near-field interactions within the finest cubes are calculated independently, allowing for easy parallelization with negligible thread management overheads. Constructing the near-part matrix of a single cube requires $O(n^2)$ operations, where n is the number of nearby filaments surrounding that cube. We group these cubes together to ensure even load balance between threads.

B. Construction of the preconditioner

The preconditioner **P** is sparse and, therefore, it is only necessary to store the non-zero values. FastHenry uses linked lists, but this significantly increases the time required to add and modify values. The construction of the **P** matrices for the DiagL and Cube preconditioner is replaced with routines from the CXSparse library [8], which uses the Compressed Column (CC) format for storing sparse matrices. These routines reduce run time and memory usage.

The next step is the LU decomposition of $\mathbf{P}^{-1}$, for which the SuperLU_MT library [9] is ideal. We call library routines directly from FastHenry. SuperLU_MT implements an asynchronous parallel supernodal algorithm for sparse Gaussian elimination [10]. Together, the routines from the CXSparse and SuperLU_MT libraries reduce the construction time of the preconditioner by a factor of 50 to 130 for all our examples. The result is an overall time reduction even before parallel processing is implemented, as seen in Table 1. Despite faster GMRES convergence when using the Cube preconditioner, its construction time is 7 times larger than the DiagL preconditioner and delivers a lower overall speed gain.

C. GMRES

The dominant computation cost of the GMRES is the matrix-vector product. FMM uses more than 90% of this time. With a preconditioner, the matrix-vector product also requires the solution to $\mathbf{x} = \mathbf{Px'}$; now done with the LU matrices computed earlier with SuperLU_MT.

FastHenry implements the FMM through an electrostatic analogy by integrating the vector potential across each filament [1]. The vector potential is decomposed into its x, y, and z components; each component considered a scalar electrostatic potential. Instead of evaluating the FMM separately for each dimension, a separate set of *updating vectors* are created for each dimension, including the real and imaginary parts. Updating vectors are used for storing the results of each FMM stage and require negligible memory. This modification delivers a speed increase of nearly 4 times when computing the matrix-vector product. Furthermore, duplicating the updating vectors and assigning a set to each thread, several matrix-vector products (one for each GMRES) can be computed in parallel with negligible memory increase per additional thread.

Finally, typical superconducting IC models use many excitation ports. GMRES is executed once for every port, so that most gain is obtained for multi-port calculations when each GMRES is executed in a separate thread.

IV. Superconducting IC Structures

We show the efficiency of improvements to the solver on densely discretized IC structures with one or more ground planes. These are typical of multi-terminal superconducting circuit inductance calculations with InductEx [4], such as that in Fig. 1(a).

We selected 4 practical examples with increasing complexity from real IC layouts. The first is a set of coupled coils [11]. It has 2 ports and a slender line geometry, and uses 7,635 filaments. The second is an 8 port AQFP cell [12] with 23,090 superconductive and normal filaments. The third is a 21 port RSFQ toggle flip-flop (TFF) [13] with 37,247 filaments. The fourth is an eSFQ TFF (eTFF) [14] with 47,341 filaments and 17 ports, shown in Fig 1. Results are listed in Table 1.

V. Tetrahedral Modeling Method

The filaments model used by FastHenry makes it difficult to model uneven multidirectional current flow along curved structures. InductEx can model complex 3D structures for FastHenry, but the limitations imposed by rectangular uniaxial filaments can result in very inefficient models. We have

TABLE I
CALCULATION TIMES FOR ORIGINAL FASTHENRY AND FAST FASTHENRY (FFH) WITH DIFFERENT PRECONDITIONER OPTIONS AND CORE COUNTS.

Layout model	Original FH, Cube	Original FH, DiagL	Original FH, no preconditioner	FFH, DiagL 1 core	FFH, DiagL 2 cores	FFH, DiagL 4 cores
Coupled coils (2 ports)	9 s	8 s	35 s	4.7 s	3.1 s	2.4 s
AQFP cell (8 ports)	1,692 s	548 s	764 s	60 s	37 s	23 s
RSFQ TFF (21 ports)	47,632 s	6,627 s	14,457 s	273 s	181 s	131 s
eTFF (17 ports)	106,706 s	14,138 s	12,069 s	399 s	255 s	162 s

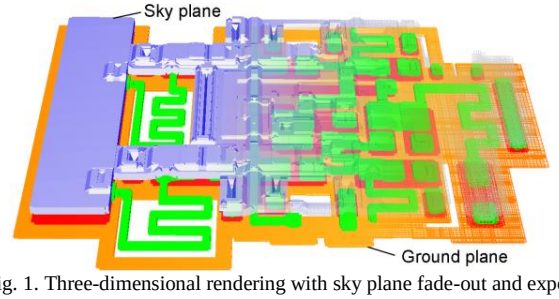

Fig. 1. Three-dimensional rendering with sky plane fade-out and exposed mesh detail of eTFF circuit [14].

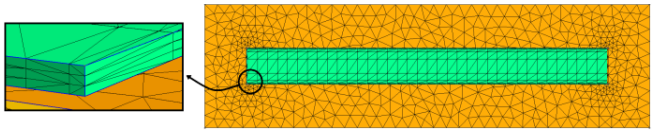

Fig. 2. Tetrahedral meshing detail of a 5 µm × 50 µm stripline (thickness = 220 nm and penetration depth = 137nm) 177.5 nm above ground plane (overhang = 6 µm, thickness = 300 nm, and penetration depth = 86 nm). Note: segment size and height division is for illustration purposes only.

developed a 3D numerical engine, TetraHenry (TTH), which uses tetrahedral volume elements to discretize complex geometries. Volume Loop basis functions [15] are used to discretize the volume integral equation to obtain the Method of Moments matrix equation. The FMM developed in FastHenry has been modified to support conventional SWG basis functions [16]. The methods discussed in Section III have also been modified and implemented in TetraHenry.

VI. Results

Fast FastHenry (FFH) with the DiagL preconditioner is used to solve the example calculations, and compared to results with different preconditioners in the original FastHenry. The results are listed in Table 1. FFH on a single processor core is significantly faster than the original, with immense gains for the more complex models. Calculation time scales well as more cores are used. The calculation time is reduced by a factor of 30 on a single core and a factor of 75 with 4 processing cores. The resulting inductances computed show zero loss of accuracy compared to the original FastHenry. The memory allocated for the eTFF example running on 1 core is 1.2 GB with an increase of 5.2% for each additional core.

The performance of TetraHenry is demonstrated by simulating a stripline above a ground plane with 106,296 superconducting tetrahedral elements, as shown in Fig. 2. The stripline has the same dimensions and penetration depth as one of the examples in [17]. The stripline example is solved within 181 s running on 4 processing cores. Total number of unknowns solved is 195,568; requiring 3.2 GB of memory. The inductance extracted is 4.409 pH and corresponds with the method used in [17] with less than 1% error. FastHenry yields 4.44 pH for similar a discretization size.

VII. Conclusion

Although demonstrated here for superconducting circuits, the presented speed improvements hold for normal conductor calculations of similar complexity. Parallelization of all the dominant calculation steps allows further gains that scale with increased processor count for modest memory increase. This allows inductance extraction of modern superconducting IC cell layouts within minutes on personal computers, and makes chip-level extraction tractable on high-performance computers.

Acknowledgment

The authors thank Mark Volkmann and Thomas Weighill for helpful suggestions.

References

[1] M. Kamon, M. J. Tsuk and J. K. White, “Fasthenry: a multipole accelerated 3-d inductance extraction program,” IEEE Trans. Microwave Theory Tech., vol. 42, pp. 1750-1758, 1994.

[2] O. A. Mukhanov, “Energy-efficient single flux quantum technology”, IEEE Trans. Appl. Supercond., vol. 21, no. 3, pp. 760 -769, 2011.

[3] N. Takeuchi, Y. Yamanashi and N. Yoshikawa, “Measurement of 10 zJ energy dissipation of adiabatic quantum-flux-parametron logic using a superconducting resonator,” Appl. Phys. Lett., vol. 102, 052602, 2013.

[4] C. J. Fourie, O. Wetzstein, T. Ortlepp, and J. Kunert, “Three-dimensional multi-terminal superconductive integrated circuit inductance extraction,” Supercond. Sci. Technol., vol. 24, 125015, 2011.

[5] Y. Saad and M. H. Schultz, “GMRES: A generalized minimal residual algorithm for nonsymmetric linear systems,” SIAM J. Sci. Stat. Comput., vol. 7, pp. 856-869, 1986.

[6] L. Greengard and V. Rokhlin, “A fast algorithm for particle simulations,” J. Comp. Phys., vol. 73, pp. 325-348, 1987.

[7] M. Benzi, “Preconditioning techniques for large linear systems: a survey,” J. Comp. Phys., vol. 182, pp. 418-477, 2002.

[8] T. A. Davis, “Direct Methods for Sparse Linear Systems,” Philadelphia, PA, USA: Society for Industrial and Applied Mathematics, 2006.

[9] X. Li, J. Demmel, J. Gilbert, iL. Grigori, M. Shao, and I. Yamazaki. (1999, September). “Superlu users’ guide,” Lawrence Berkeley National Laboratory, Tech. Rep. LBNL-44289. [Online]. Available: http://crd.lbl.gov/~xiaoye/SuperLU/. Last update: August 2011.

[10] J. W. Demmel, J. R. Gilbert and X. S. Li, “An asynchronous parallel supernodal algorithm for sparse Gaussian elimination,” SIAM J. Matrix Anal. Appl., vol. 20, pp. 915-952, 1999.

[11] I. Haverkamp, O. Wetzstein, J. Kunert, T. Ortlepp, R. Stolz, H.-G. Meyer and H. Toepfer, “Optimization of a digital SQUID magnetometer in terms of noise and distortion,” Supercond. Sci. Technol., vol. 25, 065012, 2012.

[12] N. Takeuchi, T. Ortlepp, Y. Yamanashi and N. Yoshikawa, “Novel latch for adiabatic quantum-flux-parametron logic,” J. Appl. Phys., vol. 115, 103910, 2014.

[13] C. J. Fourie, O. Wetzstein, J. Kunert, H. Toepfer and H.-G. Meyer, “Experimentally verified inductance extraction and parameter study for superconductive integrated circuit wires crossing ground plane holes,” Supercond. Sci. Technol., vol. 26, 015016, 2013.

[14] I. V. Vernik, S. B. Kaplan, M. H. Volkmann, A. V. Dotsenko, C. J. Fourie and O. A. Mukhanov, “Design and test of asynchronous eSFQ circuits,” Supercond. Sci. Technol., vol. 27, 044030, 2014.

[15] M. Li and W. C. Chew, “Applying divergence-free condition in solving the volume integral equation,” Progress In Electromagnetics Research, PIER, vol. 57, pp. 311–333, 2006.

[16] D. H. Schaubert, D. R. Wilton and A. W. Glisson, “A tetrahedral modeling method for electromagnetic scattering by arbitrarily shaped inhomogeneous dielectric bodies", IEEE Trans. Antennas Propag., vol. AP-32, pp. 77 -85, 1984.

[17] C. K. Teh, M. Kitagawa and Y. Okabe, “Inductance calculation of 3D superconducting structures with ground plane,” Supercond. Sci. Technol., vol. 12, pp. 921–924, 1999.

Appendix C

TTH User's Manual

TetraHenry (TTH)

User's Manual

3D Numerical Engine using

Tetrahedral and Triangular Meshing

Version 0.170807 (beta) – 2017

Kyle Jackman

Stellenbosch University

This document dated 07 August 2017

Contents

1 Credits

TTH (the code base, file translators, pre-processor and post-processing algorithms and visualisation tools) is the product of the combined research and development efforts of:

- Kyle Jackman
- Coenrad Fourie
- Ruben van Staden

2 Introduction

TetraHenry (TTH) [1] is a 3D numerical engine that was developed for inductance extraction of superconducting structures using tetrahedral volume elements to discretize complex geometries. The engine is a volume integral equation (VIE)-based solver that uses the magneto-quasistatic (MQS) Maxwell equations to obtain sinusoidal steady-state solutions.

2.1 Port excitations

The inductance between terminals are extracted by computing the complex frequency-dependent impedance matrix of a multi-terminal system, similar to the method used in FastHenry [7]. The problem is solved under the magnetoquasistatic approximation [7]. This requires solving the following linear equation at a given excitation frequency ω:

$$\mathrm{Z_m}(\omega)\tilde{\mathrm{I}}_\mathrm{m}(\omega) = \tilde{\mathrm{V}}_\mathrm{m}(\omega)$$

where $\tilde{\mathrm{I}}_\mathrm{m}, \tilde{\mathrm{V}}_\mathrm{m} \in \mathbb{C}^\mathrm{m}$ are vectors containing the current and voltage phasors at the terminals, respectively. The complex impedance matrix $\mathrm{Z_m} \in \mathbb{C}^{\mathrm{m}\times\mathrm{m}}$ for the two-conductor example in Fig. 1 will be of the form:

$$\begin{aligned}\mathrm{Z_m}(\omega) &= \mathrm{R}_m(\omega) + j\omega\mathrm{L_m}(\omega) \\ &= \begin{bmatrix}\mathrm{R}_{11}(\omega) + j\omega\mathrm{L}_{11}(\omega) & \mathrm{R}_{12}(\omega) + j\omega\mathrm{L}_{12}(\omega) \\ \mathrm{R}_{21}(\omega) + j\omega\mathrm{L}_{21}(\omega) & \mathrm{R}_{22}(\omega) + j\omega\mathrm{L}_{22}(\omega)\end{bmatrix}\end{aligned}$$

where $\mathrm{R_m}, \mathrm{L_m} \in \mathbb{C}^\mathrm{m}$ are the resistance and inductance matrix, respectively. The value L_{11} is the self-inductance of conductor 1 and $\mathrm{L}_{12} = \mathrm{L}_{21}$is the mutual inductance between the two conductors. If the vectors $\tilde{\mathrm{I}}_\mathrm{m}$ and $\tilde{\mathrm{V}}_\mathrm{m}$ is known, the i column of $\mathrm{Z_m}$ can be calculated when computing the voltage vector $\tilde{\mathrm{V}}_\mathrm{m}$. Set the value at index i in $\tilde{\mathrm{I}}_\mathrm{m}$ equal to and the rest to zero.

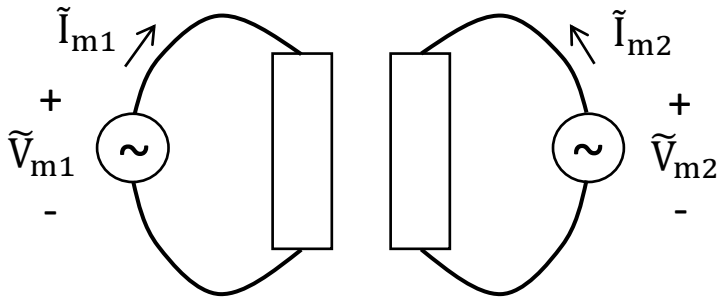

Fig. 1. Port excitation of two conductors.

Fig. **2** shows an example of a voltage port connected to a tetrahedral mesh. The two yellow surfaces define the positive and negative terminals of the voltage port. An example of a hole excitation is

shown in Fig. **3**, with the yellow surfaces defining the perimeter of the hole. The geometry (.geo) files of these two examples are provided at the end of this document.

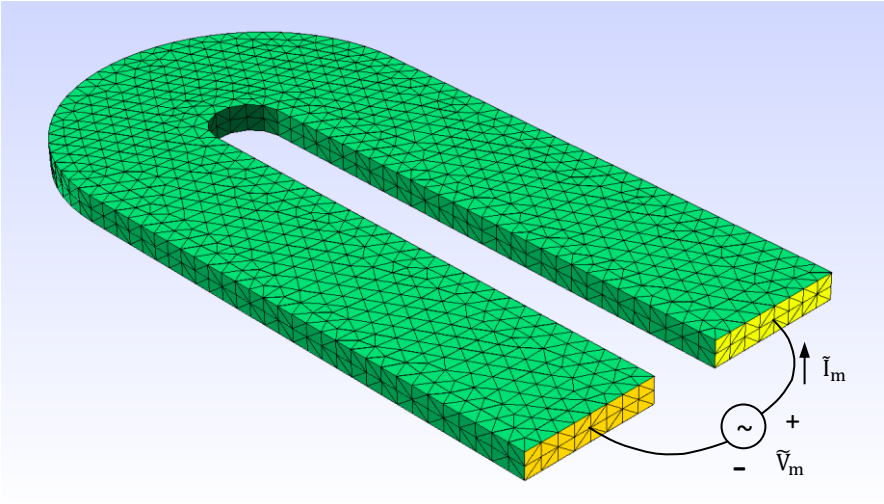

Fig. 2. Single voltage port defined by two surface terminals (yellow) connected to a tetrahedral mesh.

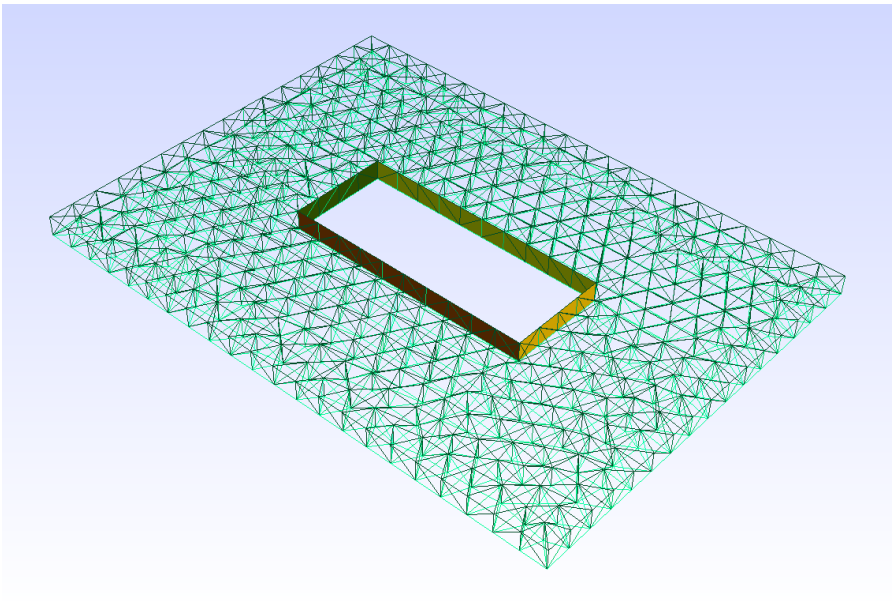

Fig. 3. A hole excitation port defined by the surfaces on the perimeter of the hole.

3 Input file requirements

Currently, TTH uses Gmsh [6] as the primary finite element mesh generator. All the geometrical and mesh instructions are prescribed in a ASCII text file (.geo file) using Gmsh's own scripting language, see Gmsh's reference manual (http://gmsh.info/). Creating 3D geometrical models are not discussed in this manual.

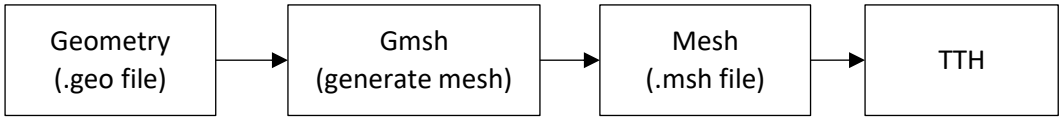

The following Gmsh commands must be used to specify the properties of volumes, surfaces and lines:

- `Physical Point("string label") = {};`
- `Physical Volume("string label") = {};`
- `Physical Surface("string label") = {};`
- `Physical Line("string label") = {};`

These properties are specified in the form of "string labels" and are read by TTH from the mesh (.msh) file. The format of these "string labels" are discussed in this section.

3.1 Global settings

Global frequency sweep settings are specified using the `Physical Point(".f")` command, e.g.:

```
Physical Point(".f -s 10E9 -e 10E9 -n 1") = {};
Physical Point(".f -s 1E9 -e 100E9 -l 10") = {};
```

Global external magnetic field settings are specified using the `Physical Point(".b")` command, e.g.:

```
Physical Point(".b 1 -m [50u 0 20u]") = {};
Physical Point(".b 2 -m [0 0 60E-6]") = {};
```

Flag	Value	Description	Example
Frequency Specifications			
.f		**Specify the global frequency sweep settings for all ports/holes when using voltage excitations (see -v under port excitations). If fluxon excitations are used (see -f under port excitations), frequency settings are ignored.**	**`.f`**
-s	start frequency	The starting frequency. If this value is the same as the end frequency, no frequency sweep will be performed.	`.f -s 1E9`
-e	end frequency	The end frequency. If this value is the same as the start frequency, no frequency sweep will be performed.	`.f -s 1E9 -e 10E9`
-n	number of linear steps	Linear sweep between start and end frequencies. If this value is 1, only the start frequency will be used.	`.f -s 10E9 -e 100E9 -n 20`
-l	number of log steps	Logarithmic sweep (base 10) between the start and end frequencies. If this value is 1, only the start frequency will be used.	`.f -s 2E9 -e 100E9 -l 10`
External magnetic field excitation			
.b id		**External magnetic field**	**`.b 2`**
-m	[x y z]	Magnetic field vector [Tesla] in x, y, z-direction (default: [0 0 0]).	`.b 0 -m [0 0 0.25u]`

3.2 Material properties

Material properties for volumes are specified using `Physical Volume(".v")` command, e.g.:

```
Physical Volume(".v 0 -s 0.0 -l 137E-9") = {volume id};
Physical Volume(".v 1 -s 0.0 -l 86E-9 -t [0 0 50E-9]") = {volume id};
Physical Volume(".v 2 -s 0.0 -l 86E-9 -t [200E-9 200E-9 50E-9]") = {volume id};
```

Material properties for surfaces are specified using `Physical Surface(".s")` command, e.g.:

```
Physical Surface(".s 1 -s 0.0 -l 137E-9 -h 220E-9") = {surface id/s};
Physical Surface(".s 2 -s 0.0 -l 86E-9 -h 300E-9") = {surface id/s};
Physical Surface(".s 3 -s 0.0 -l 86E-9 -h 300E-9") = {surface id/s};
```

Flag	Value	Description	Example
Volume material properties			
.v id		**Set volume material properties. The same id cannot be used for other volumes or surfaces.**	**`.v 0`**
-s	conductivity	Volume conductivity (units: Siemens per meter [S/m]) [default = 0.0]	`.v 0 -s 5.8E7`
-l	depth	London penetration depth (units: meter [m]) [default = 0.0]	`.v 0 -l 80E-9`
-u	Relative permeability	Specify the relative permeability, μ_r, of the volume.	`.v 1 -u 1.2E1`
-e	Relative permittivity	Specify the relative permittivity, ε_r, of the volume.	`.v 1 -e 3.9`
-t	[x y z]	Set the boundary layer thickness in the x-, y- and z-direction (units: meter [m]). When simulating structures with "vias", it is important to specify the thickness in all directions. [default = 0 0 0]	`.v 0 -t [200E-6 200E-6 50E-9]`
Surface material properties			
.s id		**Set 2D surface material properties. The same id cannot be used for other volumes or surfaces.**	**`.s 1`**
-s	conductivity	Volume conductivity (units: Siemens per meter [S/m]) [default = 0.0]	`.s 1 -s 5.8E7`
-l	depth	London penetration depth (units: meter [m]) [default = 0.0]	`.s 1 -l 80E-9`
-h	height	Height of the surface. The surface is projected height/2 in the positive and negative directions of the surface's normal. The surface should be place at the centre of its height. (units: meter	`.s 1 -h 220E-9`

		[m]) [default = 0.0] 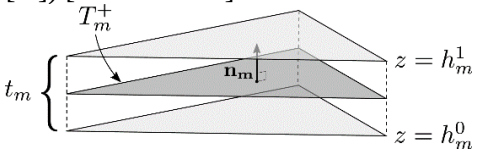	

3.3 Port excitation

Voltage ports are specified using the `Physical Point(".e")` command, e.g.:

```
Physical Point(".e 0 -p 0 -n 1") = {};
Physical Point(".e 1 -v 2.0 -p 2 -n 3 -e off") = {};
Physical Point(".e 3 -f 1.0 -p 4 -n 5") = {};
```

Hole (moat) excitations are specified using the `Physical Point(".h")` command, e.g.:

```
Physical Point(".h 0 -p 1") = {};
Physical Point(".h 1 -v 0.0 -p 2 -e off") = {};
Physical Point(".h 3 -f 1.0 -p 0") = {};
```

Surface terminals are specified using the `Physical Surface(".t")` command, e.g.:

```
Physical Surface(".t 0") = {Surface id/s};
Physical Surface(".t 1") = {Surface id/s};
Physical Surface(".t 2") = {Surface id/s};
```

Line terminals are specified using the `Physical Line(".t")` command, e.g.:

```
Physical Line(".t 0") = {Line id/s};
Physical Line(".t 1") = {Line id/s};
Physical Line(".t 2") = {Line id/s};
```

Terminals can specify the positive or negative terminals of a port or the perimeter of a hole. Surface terminals should only be used for 3D volume structures and line terminals only for 2D surface structures.

Flag	Value	Description	Example
Port excitation			
.e id		**Excitation port connected to two terminals. If not specified, the flags -v and -f are automatically set to 1.0 depending on whether voltages or fluxons are used.**	`.e 0`
-v	voltage	Constant voltage (default: 1.0V). If this value is set 0.0, then the current of this port will not be extracted.	`.e 0 -v 2.0`

	[t1 v1 t2 v2 ...]	Time dependent excitation voltage.	`.e 1 -v [0.0u 0.3m 0.2u 1.3m 0.5u 2.4m]`
-i	current	Constant current (default: 1.0A). If this value is set 0.0, then the voltage of this port will not be extracted.	`.e 0 -i 2.0`
-f	fluxons	Constant number of fluxons (default: 1.0 fluxon). Voltages, current or fluxons cannot be used simultaneously. Either voltages, current or fluxons should be used for all holes and ports. If this value is set 0.0, then the current/voltage of this port will not be extracted.	`.e 2 -f 1.0`
-p	id	Positive terminal id. If the id is 2, then there must exist a terminal with id 2, e.g. `Physical Surface(".t 2").`	`.e 5 -p 2`
-n	id	Negative terminal id. If the id is 3, then there must exist a terminal with id 3, e.g. `Physical Surface(".t 3").`	`.e 5 -p 2 -n 3`
-e	on	Make zero when exciting other ports/holes. The current of this port will be extracted. [Default]	`.e 5 -p 2 -n 3 -e on`
	off	Keep port excited at the specified voltage/current/fluxons when exciting other ports/holes. The current/voltage of this port will not be extracted. This option is automatically selected when voltage/current/fluxons is set to zero ("-v 0.0" or "-f 0.0").	`.e 5 -p 2 -n 3 -e off`
Hole excitation			
.h id		**Excitation hole connected to one terminal. If not specified, the flags -v and -f are automatically set to 1.0 depending on whether voltages or fluxons are used.**	**`.h 1`**
-v	voltage	Constant voltage (default: 1.0V). If this value is set 0.0, then the current of this hole will not be extracted.	`.h 0 -v 2.0`
	[t1 v1 t2 v2 ...]	Time dependent excitation voltage.	`.h 1 -v [0.0u 0.3m 0.2u 1.3m 0.5u 2.4m]`
-f	fluxons	Constant number of fluxons (default: 1.0 fluxon). If this value is set 0.0, then the current of this hole will not be extracted.	`.h 2 -f 1.0`
-p	id	Positive hole perimeter (terminal) id. The direction of the path around the hole will be **anticlockwise** around the z-axis. All the surfaces/lines on the hole's perimeter must form part of the terminal. If the id is 2, then there must exist a terminal with id 2 that contain all the surfaces/lines on the hole's	`.h 4 -p 2`

		perimeter, e.g. `Physical Surface(".t 2").`	
	[id1 id2 id3 id4]	The 4 terminal id's that specify the direction of the path around the hole. The 4 surfaces/lines on the hole's perimeter must be specified in the correct order.	`.h 5 -p [2 3 4 5]`
-n	id	Negative hole perimeter (terminal) id. The direction of the path around the hole will be **clockwise** around the z-axis. If the id is 3, then there must exist a terminal with id 3 that contain all the surfaces/lines on the hole's perimeter, e.g. `Physical Surface(".t 3").`	`.h 5 -n 3`
	[id1 id2 id3 id4]	The 4 terminal id's that specify the direction of the path around the hole, in the **reverse order** (-n). The 4 surfaces/lines on the hole's perimeter must be specified in the correct order.	`.h 5 -n [6 7 8 9]`
-e	on	Make zero when extracting other ports/holes. The current of this hole will be extracted. [Default]	`.h 4 -p 2 -e on`
	off	Keep hole excited at the specified voltage/fluxons when exciting other ports/holes. The current of this hole will not be extracted. This option is automatically selected when voltage/ fluxon is set to zero ("-v 0.0" or "-f 0.0").	`.h 4 -p 2 -e off`

3.4 Metric prefixes

SI Prefixes					
Name	**Symbol**	**Decimal**	**Name**	**Symbol**	**Decimal**
deci	d	0.1	yotta	Y	1E+24
centi	c	0.01	zetta	Z	1E+21
milli	m	0.001	exa	E	1E+18
micro	µ	1E-06	peta	P	1E+15
nano	n	1E-09	tera	T	1E+12
pico	p	1E-12	giga	G	1E+09
femto	f	1E-15	mega	M	1000000
atto	a	1E-18	kilo	k	1000
zepto	z	1E-21	hecto	h	100
yocto	y	1E-24	deca	da	10

4 NASTRAN Format

The NASTRAN file defines nodes (`GRID`), triangles (`CTRIA3`), tetrahedrons (`CTETRA`), etc. using a specific format. Although this format is fixed, additional properties can be mapped to each surface/tetrahedron using labels, e.g. HyperMesh uses the label "`$HMNAME PROP`" to define generic properties.

HyperMesh example with generic properties:

The NASTRAN file must contain all the terminal and material properties:

```
$HMNAME PROP              1".f -s 1.0E9 -e 1.0E9 -n 1"
$HMNAME PROP              2".v 0 -s 0.0E7 -l 0.09E-6 -u 1.0 -e 1.0"
$HMNAME PROP              3".t 0"
$HMNAME PROP              4".t 1"
$HMNAME PROP              5".e 0 -v 1.0 -p 0 -n 1"
```

The label "`$HMNAME PROP`" is a specific label used by HyperMesh to define a generic property. The identification numbers (IDs labelled in red) maps material properties to specific tetrahedrons (`CTETRA`) and terminal properties to specific triangles (`CTRIA3`).

Material IDs (labelled in red) are mapped to volumes (tetrahedrons) as follow:

```
CTETRA      1489        2      104      685      599      598
CTETRA      1490        2      598      211       60      649
```

Terminal IDs (labelled in red) are mapped to surfaces (triangles) as follow:

```
CTRIA3       745        3      423      424       89
CTRIA3       746        3      424      425       90
...
CTRIA3       729        4      414      415       41
CTRIA3       730        4      415      416       42
```

The string labels (in blue) must have the following format:

Frequency settings: `".f -s 1.0E9 -e 1.0E9 -n 1"`

- `-s` starting frequency
- `-e` end frequency
- `-n` number of frequency steps [default: 1]

Volume material properties: `".v 0 -s 0.0E7 -l 0.09E-6 -u 1.0 -e 1.0"`

- The first number after "`.v`" (in this case `0`) is a unique ID for this material property. This can be any integer value larger or equal to 0.
- `-s` conductivity (σ) [default: 0.0]
- `-l` London penetration depth (λ) [default: 0.0]
- `-u` relative permeability (μ_r) [default: 1.0]
- `-e` relative permittivity (ε_r) [default: 1.0]

Surface terminal 1: `".t 0"`

- The number after "`.t`" (in this case `0`) is a unique ID for this terminal. This can be any integer value larger or equal to 0.

Surface terminal 2: `".t 1"`

- The number after "`.t`" (in this case `1`) is a unique ID for this terminal. This can be any integer value larger or equal to 0.

Port between terminal 1 and 2: `".e 0 -v 1.0 -p 0 -n 1"`

- The number after "`.e`" (in this case `0`) is a unique ID for this port. This can be any integer value larger or equal to 0.
- `-v` excitation voltage. [default: 1.0]
- `-p` positive terminal ID. In this case, the ID corresponds to terminal 1 (`".t 0"`).
- `-n` negative terminal ID. In this case, the ID corresponds to terminal 2 (`".t 1"`).

5 Command-line Options

Calling TTH from command line (options are case sensitive, ***n*** = integer, ***d*** = float, ***s*** = string):

```
TTH <mesh file> [<Options>]
```

Command-Line Options			
Option (long)	**Option (long)**	**Value**	**Description**
--help	-h		Display help menu.
--emqs	-c	on	Enables EMQS for dielectric and permeable materials.
		off	Disable EMQS and use MQS. [default]
		perm	Enable EMQS for permeable materials only.
--gmresIter	-g	***n***	where n = maximum GMRES iterations. [default: 400]
--gmresTol	-t	***d***	where t = gmres converge tolerance.
--exa	-E	on	Enable ExaFMM method.
		off	Use custom FMM. [default]
		full	Enable Full-Wave ExaFMM.
--expOrder	-P	***n***	Expansion order for FMM. n = [4,10] for ExaFMM. [default: 8] n = [1,10] for custom FMM. [default: 3]
--exaBasis	-B	C	ExaFMM: Cartesian Basis. [default]
		S	ExaFMM: Spherical Basis.
--exaNcrit	-N	***n***	ExaFMM: number of bodies per leaf. [default: 64]
--exaTheta	-T	***d***	ExaFMM: multipole acceptance criterion. [default: 0.4]
--quad	-q	***d***	Accurate integration acceptance criterion. [default: 0.0]
--current	-i	***s***	where s = current output file name.
--voltage	-Y	***s***	where s = port voltage output file name.
--energy	-e	***s***	where s = magnetic energy output file name.
--vtkI	-v	a	Write current density (3D VTK file) of all volumes.
		e	Write 3D VTK file of volumes containing electric current.
		m	Write 3D VTK file of volumes containing magnetic current.
		p	Write 3D VTK file of port paths.
		t	Write 3D VTK file of edge types (for debugging).
--vtkB	-b	on	Write magnetic field to 3D VTK file.
		off	Disable magnetic field output. [default]

--vtkA	-f	on	Write potential field to 3D VTK file.
		off	Disable potential field output. [default]
--zScale	-z	***d***	z-axis scaling factor for VTK output. [default: 1.0]
--output	-o	s	Write RHS solution output file.
--threads	-n	***n***	where n = number of parallel threads. [default: 1]
--prec	-p	on	Use R non-zero pattern preconditioner. [default]
		off	Disable preconditioner.
		rpat	Use R non-zero pattern preconditioner.
		diag	Use R diagonal preconditioner.
--luPerm	-L	mmd	Preconditioner LU column permutation: Multiple Minimum Degree.
		col	Preconditioner LU column permutation: Column Approximate Minimum. [default]
--luThres	-S	***d***	where d = minimum LU condition number. [default: 1E-25]
--license	-l	***s***	where s = license file name.

6 Gmsh Examples

6.1 Single voltage port example in Fig. 2

File name: singlePort.geo

```
/*********************************************************************
 *  Curve rectangular volume with single excitation port
 *********************************************************************/

// Discretization size of each point
lc1 = 1.0e-6;
lc2 = 1.0e-6;

// Rectangle's width, length and height
l1 = 30E-6;
w1 = 8E-6;
t1 = 1.5E-6;

dist = w1 + 4E-6;

// Points defining the bottom surface of the rectangle 1
Point(1) = {-l1/2.0, -w1/2.0 - dist/2, 0, lc1};
Point(2) = {-l1/2.0,  w1/2.0 - dist/2, 0, lc1};
Point(3) = { l1/2.0,  w1/2.0 - dist/2, 0, lc1};
Point(4) = { l1/2.0, -w1/2.0 - dist/2, 0, lc1};

// Points defining the bottom surface of the rectangle 2
Point(5) = {-l1/2.0, -w1/2.0 + dist/2, 0, lc1};
Point(6) = {-l1/2.0,  w1/2.0 + dist/2, 0, lc1};
Point(7) = { l1/2.0,  w1/2.0 + dist/2, 0, lc1};
Point(8) = { l1/2.0, -w1/2.0 + dist/2, 0, lc1};

// Curve Centre
Point(9) = { l1/2.0, 0, 0, lc1};

// Curved rectangle lines
Line(21) = {4,1};
```

```
Line(22) = {1,2};
Line(23) = {2,3};
Circle(24) = {3,9,8};
Line(25) = {8,5};
Line(26) = {5,6};
Line(27) = {6,7};
Circle(28) = {4,9,7};

// Curved rectangle surface loop
Line Loop(41) = {21,22,23,24,25,26,27,-28};

// Curved rectangle bottom surface loop
Plane Surface(51) = {41};

// Create volume by extruding surface in z-direction
info[] = Extrude {0,0,t1} {Surface{51}; Layers{{1},{1}};};

/*****************************************************************
* TTH Properties
*****************************************************************/
// Frequencies (-s = start, -e = end, -n = steps)
Physical Point(".f -s 10.0E9 -e 10.0E9 -n 1") = {};

// Volume conductivity (-s) and penetration depth (-l):
Physical Volume(".v 1 -s 0.0E7 -l 0.09E-6") = {info[1]};

// Port with positive (-p) and negative (-n) terminals
// Excitation voltage: 2.0 V (-v)
Physical Point(".e 0 -v 2.0 -p 1 -n 2") = {};

// Surface of positive Terminal
Physical Surface(".t 1") = info[3];

// Surface of negative Terminal
Physical Surface(".t 2") = info[7];
```

6.2 Hole example in Fig. 3

File name: hole.geo

```
/*****************************************************************
 *  Rectangle volume with hole port
 *****************************************************************/

// Discretization size of each point
lc1 = 0.5E-6;
lc2 = 0.5E-6;

// Rectangle's width, length and height
w1 = 8E-6;
l1 = 11E-6;
t1 = 0.4E-6;

// Hole's width and length
w2 = 2E-6;
l2 = 5E-6;

// Points defining bottom surface of rectangle
Point(1) = {-l1/2.0, -w1/2.0, 0, lc1};
```

```
Point(2) = {-l1/2.0,  w1/2.0, 0, lc1};
Point(3) = { l1/2.0,  w1/2.0, 0, lc1};
Point(4) = { l1/2.0, -w1/2.0, 0, lc1};

// Points defining bottom surface of hole
Point(5) = {-l2/2.0, -w2/2.0, 0, lc2};
Point(6) = {-l2/2.0,  w2/2.0, 0, lc2};
Point(7) = { l2/2.0,  w2/2.0, 0, lc2};
Point(8) = { l2/2.0, -w2/2.0, 0, lc2};

// Rectangle lines
Line (11) = {1,2};
Line (12) = {2,3};
Line (13) = {3,4};
Line (14) = {4,1};

// Hole lines
Line (15) = {5,6};
Line (16) = {6,7};
Line (17) = {7,8};
Line (18) = {8,5};

// Rectangle surface loop
Line Loop(21) = {11,12,13,14};

// Hole surface loop
Line Loop(22) = {15,16,17,18};

// Remove hole's surface from larger rectangle
Plane Surface(31) = {21,22};

// Create volume by extruding surface in z-direction
info1[] = Extrude {0,0,t1} {Surface{31}; Layers{{1},{1}};};

/*************************************************************
 * TTH Properties
 *************************************************************/
// Frequencies (-s = start, -e = end, -n = steps)
Physical Point(".f -s 1.0E9 -e 1.0E9 -n 1") = {};

// Volume conductivity (-s) and penetration depth (-l):
Physical Volume(".v 0 -s 0.0E7 -l 0.4E-6") = {info1[1]};

// Hole port with anticlockwise (-p) excitation of 1 fluxon (-f)
Physical Point(".h 1 -v 1.0 -p 0") = {};

// Terminal defining perimeter surfaces of hole
Physical Surface(".t 0") = {info1[6], info1[7], info1[8], info1[9]};
```

7 References

[1] K. Jackman and C. Fourie, "Tetrahedral Modelling Method for Inductance Extraction of Complex 3D Superconducting Structures", *IEEE Trans. Appl. Supercond.*, pp. 1-1, 2016.

[2] M. Li and W. C. Chew, "Applying Divergence-Free Condition In Solving The Volume Integral Equation," *Progress In Electromagnetics Research PIER*, vol. 57, pp. 311–333, 2006.

[3] D. Schaubert, D. Wilton, and A. Glisson, "A tetrahedral modeling method for electromagnetic scattering by arbitrarily shaped inhomogeneous dielectric bodies," *IEEE Trans. Antennas Propagat.*, vol. 32, no. 1, pp. 77–85, 1984.

[4] Y. Saad and M. H. Schultz, "GMRES: A Generalized Minimal Residual Algorithm for Solving Nonsymmetric Linear Systems," *SIAM J. Sci. and Stat. Comput.*, vol. 7, no. 2, pp. 856–869, 1986.

[5] K. Jackman and C. J. Fourie, "Fast Multicore FastHenry and a Tetrahedral Modeling Method for Inductance Extraction of Complex 3D Geometries," *2015 15th International Superconductive Electronics Conference (ISEC)*, 2015, in print.

[6] C. Geuzaine and J. Remacle *Gmsh: A Three Dimensional Finite Element Mesh Generator*, [online]. Available: http://www.geuz.org/gmsh/.

[7] M. Kamon, M. Ttsuk, and J. White, "FASTHENRY: a multipole-accelerated 3-D inductance extraction program," *IEEE Trans. Microwave Theory Techn.*, pp. 1750–1758, 1994.